

5083

OBSERVATIONS OF NORMAL PRESSURE
ON WIND-GENERATED SEA WAVES

by

FREDERIC WILLIAM DOBSON

B.Sc., Dalhousie University, 1959

M.Sc., Dalhousie University, 1961

A THESIS SUBMITTED IN PARTIAL FULFILMENT OF THE
REQUIREMENTS FOR THE DEGREE OF
DOCTOR OF PHILOSOPHY
in the Department
of
Physics

We accept this thesis as conforming to the
required standard

THE UNIVERSITY OF BRITISH COLUMBIA

August, 1969

In presenting this thesis in partial fulfilment of the requirements for an advanced degree at the University of British Columbia, I agree that the Library shall make it freely available for reference and Study.

I further agree that permission for extensive copying of this thesis for scholarly purposes may be granted by the Head of my Department or by his representatives. It is understood that copying or publication of this thesis for financial gain shall not be allowed without my written permission.

Department of PHYSICS

The University of British Columbia
Vancouver 8, Canada

Date AUGUST, 1969

ABSTRACT

The process by which the wind makes sea waves grow is not well-understood, partly because of the lack of adequate observational information on the normal pressures which transfer energy to the waves. The principal object of this experiment has been to provide some of the missing data.

A system for making simultaneous measurements of normal pressure and wave height was developed and tested in the laboratory and in the field. The system consisted of a disc-shaped buoy 23 cm in diameter (in which was embedded the pressure sensor) which rode up and down on a vertical rod, which was the wave sensor. Careful attention was paid to rejecting so-called "dynamic" pressures associated with the distortion of the air flow by the buoy.

The results from the experiment are presented as power and cross-spectra of the pressure and wave signals. Spectra of Energy (E) and Momentum (τ_w) fluxes to the waves, and of ζ , the fractional energy increase of the waves per radian, are also presented.

Wave power spectra are found to be normal for the site; the pressure power spectra consist of a "basic" spectrum similar to that observed over land, on which is superimposed a wave-induced "hump".

The phase angle between the waves and the pressure at the frequency of the peak of the wave spectrum is found to be shifted from -180° (pressures high over wave troughs) by amounts which exceed the theoretical predictions of Miles (1957) by an average of $20 \pm 5^\circ$ over a wide range of

conditions.

The \bar{E} and $\bar{\tau}_w$ spectra are found to be sharply peaked at or above the frequency of the peak of the wave spectrum. The integrated energy fluxes \bar{E} show large scatter, indicating that the wave generation process varies considerably in time (and space). The integrated momentum fluxes $\bar{\tau}_w$ to the waves show no significant difference from total fluxes from air to water computed assuming a constant drag coefficient of 1.2×10^{-3} ; it appears that about 80% of the total drag of the water on the wind is caused by the wave generation process.

The ζ spectra exceed the predictions of Miles' (1957) theory by factors of 5 to 8, indicating that his "inviscid laminar" model is not adequate to explain observed rates of wave growth. The present results fall close to an empirical curve suggested by Snyder and Cox (1966) except at high frequencies, where they are considerably lower.

A dimensionless plot of ζ versus the ratio of wind speed to wave speed is presented; the observed data is fitted by the simple relation

$$\zeta(f) = \rho_a / \rho_w (U_2/c - 1),$$

where ρ_a / ρ_w is the ratio of the densities of air and water, U_2 is the mean wind speed at a height of two meters, and c is the phase velocity of the waves. This formula is only considered applicable for $U_5/c < 6$, where U_5 is the mean wind speed at 5 meters height.

Also presented are the results of a dry-land comparison of the buoy pressure sensor with two other pressure sensors; besides indicating that the buoy sensor was adequate, this comparison produced some interesting

preliminary information on the vertical and horizontal structure of the turbulent pressure field in the atmospheric boundary layer.

TABLE OF CONTENTS

	PAGE
Abstract	ii
Table of Contents	v
List of Tables	vi
List of Figures	viii
Acknowledgements	xiv
 Section 1: Introduction	 1
Section 2: Theories	4
Section 3: Observations	17
Section 4: Experiment	38
Section 5: Data Analysis and Interpretation	71
Section 6: Results	105
Section 7: Discussion of Results	133
Section 8: Conclusions	161
Appendix 1: Spike Removal	168
Appendix 2: The Boundary Bay Experiment	184
Appendix 3: Wave Damping by Adverse Winds	219
Bibliography	235

NOTE: A detailed table of contents precedes each of the Sections and the Appendices.

LIST OF TABLES

TABLE		PAGE
4.1	Predicted Phase Lag of Pressure Behind Wave Elevation over Wind-Generated Waves	40
4.2	Values of K/m for Six Wave Probe Calibrations	48
5.1	Summary of Information from Test Hand-Digitized Data . .	78
5.2	Expected Effects of Backscattering on Wave Power Spectrum	97
5.3	Expected Effects of Backscattering on Pressure-Waves Cross Spectrum	98
6.1	Summary of Information for Runs with Buoy on Waves: October-November 1967	108
6.2	Further Information for Runs with Buoy on Waves	109
6.3	Pressure Calibrations Used: October-November 1967 . .	110
6.4	Coherence Changes Caused by Removal of ρ_{237} in Pressure-Waves Cross Spectra	117
6.5	Mean Fluxes of Energy and Momentum from Wind to Waves .	124
7.1	Dimensionless Parameters c_p/u_* , Λ , and L for Runs with Buoy on Waves	138
7.2	Comparison of Observed Phase Angle of Pressure Relative to Waves at 0.6 Hz, with That Calculated from Miles' Inviscid Laminar Model	142
7.3	Comparison of Observed Values of \bar{E} with Those Obtained by Kolesnikov and Efimov (1962)	146
7.4	Fraction of the Wind Stress Supported by the Waves . .	149
7.5	Observed and Predicted Transition Fetches	152
7.6	Comparison of Observed and Predicted Values of $\bar{\xi} = \bar{E}/\omega \bar{E}$	156

LIST OF TABLES (continued)

TABLE		PAGE
A2.1	Information Summary for Boundary Bay Runs: September, 1968	193
A2.2	Summary of Results of u_x Analysis on Hot-Wire Anemometer Spectra	196
A2.3	Advection Velocity of Pressure-Generating Eddies	204
A2.4	Calculated Pressure Differences Between Air and Ground Sensors for Run 5e	214
A3.1	Corrected Phase Angles Between the Wave Signal and Pressure, Sonic "B", and Sonic "w"	225
A3.2	Comparison of Theoretical and Observed Pressure and Velocity Amplitude over Swell Moving Against the Wind	227

LIST OF FIGURES

FIGURE

1. Map of Site of Experiment
2. Available Fetch at Site
3. Photograph of Recording Platform and Instrument Masts
(Looking Northeast)
4. Wave Probe Calibration: Oscillator Frequency vs Immersion Depth
5. Wave Probe Calibration: (Frequency)⁻¹ vs Immersion Depth
6. Schematic Cross-Section of Microphone
7. Schematic Diagram of Pressure Measurement System
8. Pressure Recording Electronics: Block Diagram
9. Wiring Diagrams of Buoy Oscillator and Amplifier
10. FM Tuner Ratio Detector Response Curve
11. Pressure Sensor Calibration Setup
12. Laboratory Calibration of the Buoy Pressure Sensor
13. Diagram of the Buoy
14. Pressure Distribution over a Planetary Ellipsoid Similar to the
Buoy in Shape
15. Schematic Diagram of Wind Tunnel Setup
16. Profile of Buoy (To Scale)
17. Aerodynamic Calibration of Buoy: Pressure vs Distance from Bow
for Various Attack Angles
18. Aerodynamic Calibration of the Buoy: Pressure vs Distance from
Bow for $\pm 30^\circ$ Yaw Angles
19. Aerodynamic Calibration of the Buoy: Fraction of Stagnation
Head at Pressure Port vs Wind Speed

LIST OF FIGURES (continued)

FIGURE

20. Schematic Representation of the Effect of Attack Angle on the Pressure Measured by the Buoy
21. Effects on $p + \rho g \eta$ Phasor of 50% Error in Pressure Calibration
22. Phase Corrections for Time Shift of η Signal Compared with Full Correction Curve
23. Effects on $p + \rho g \eta$ Phasors of Low and High-Frequency Approximations to Full Phase Correction Curve
24. Power Spectra of p_s , $p_s + \rho g \eta$, η : Run 1
25. Power Spectra of p_s , $p_s + \rho g \eta$, η : Run 2a
26. Power Spectra of p_s , $p_s + \rho g \eta$, η : Run 2b
27. Power Spectra of p , $p + \rho g \eta$, η : Run 3
28. Power Spectra of p , $p + \rho g \eta$, η : Run 4a
29. Power Spectra of p , $p + \rho g \eta$, η : Run 4b
30. Power Spectra of p , $p + \rho g \eta$, η : Run 5
31. Power Spectra of p_s , $p_s + \rho g \eta$, η : Run 6
32. Coherence Spectra between p_s , η_s ; Phase Spectra between p_s , η_s and p_s , $p_s + \rho g \eta_s$: Run 1
33. Coherence Spectra between p_s , η_s ; Phase Spectra between p_s , η_s and p_s , $p_s + \rho g \eta_s$: Run 2a
34. Coherence Spectra between p_s , η_s ; Phase Spectra between p_s , η_s and p_s , $p_s + \rho g \eta_s$: Run 2b
35. Coherence Spectra between p_s , η_s ; Phase Spectra between p_s , η_s and p_s , $p_s + \rho g \eta_s$: Run 3
36. Coherence Spectra between p_s , η_s ; Phase Spectra between p_s , η_s and p_s , $p_s + \rho g \eta_s$: Run 4a

LIST OF FIGURES (continued)

FIGURE

37. Coherence Spectra between p_s, η_s ; Phase Spectra between p_s, η_s and $p_s, p_s + 0.9\eta_s$: Run 4b
38. Coherence Spectra between p_s, η_s ; Phase Spectra between p_s, η_s and $p_s, p_s + 0.9\eta_s$: Run 5
39. Coherence Spectra between p_s, η_s ; Phase Spectra between p_s, η_s and $p_s, p_s + 0.9\eta_s$: Run 6
40. Energy and Momentum Flux Spectra and Wave Power Spectrum: Run 1
41. Energy and Momentum Flux Spectra and Wave Power Spectrum: Run 2a
42. Energy and Momentum Flux Spectra and Wave Power Spectrum: Run 2b
43. Energy and Momentum Flux Spectra and Wave Power Spectrum: Run 3
44. Energy and Momentum Flux Spectra and Wave Power Spectrum: Run 4a
45. Energy and Momentum Flux Spectra and Wave Power Spectrum: Run 4b
46. Energy and Momentum Flux Spectra and Wave Power Spectrum: Run 5
47. Energy and Momentum Flux Spectra and Wave Power Spectrum: Run 6
48. Spectra of ζ : Comparisons with Snyder and Cox, Miles: Run 1
49. Spectra of ζ : Comparisons with Snyder and Cox, Miles: Run 2a
50. Spectra of ζ : Comparisons with Snyder and Cox, Miles: Run 2b
51. Spectra of ζ : Comparisons with Snyder and Cox, Miles: Run 3
52. Spectra of ζ : Comparisons with Snyder and Cox, Miles: Run 4a
53. Spectra of ζ : Comparisons with Snyder and Cox, Miles: Run 4b
54. Spectra of ζ : Comparisons with Snyder and Cox, Miles: Run 6
55. Dimensionless plot of ζ vs U_5/c
- 56 - 63 Power and cross-spectra of hypothetical sinusoidal "pressure" and "wave" signals $p(t)$ and $\eta(t)$; removal of a "spike" once per cycle is indicated by the subscript "s".

LIST OF FIGURES (continued)

FIGURE

56. Power Spectrum of $p_s(t)$
57. Coherence between $p_s(t)$ and $\eta(t)$
58. Phase Angle between $p_s(t)$ and $\eta(t)$
59. Power Spectrum of $\eta(t)$
60. Power Spectrum of $p_s(t)$
61. Coherence between $p_s(t)$ and $\eta_s(t)$
62. Phase Angle between $p_s(t)$ and $\eta_s(t)$
63. Power Spectrum of $\eta_s(t)$
64. Comparison of the $\eta(t)$ and $\eta_s(t)$ Power Spectra for Run 1
65. Comparison of the $\eta(t)$ and $\eta_s(t)$ Power Spectra for Run 2b
66. Comparison of the $\eta(t)$ and $\eta_s(t)$ Power Spectra for Run 3
67. Comparison of the $\eta(t)$ and $\eta_s(t)$ Power Spectra for Run 6
68. Comparison of p, η Phase Spectra from "Clear" and "Spike-Contaminated" data: Run 1
69. Comparison of p, η Phase Spectra from "Clear" and "Spike-Contaminated" data: Run 2b
70. Comparison of p, η Phase Spectra from "Clear" and "Spike-Contaminated" data: Run 3
71. Comparison of p, η Phase Spectra from "Clear" and "Spike-Contaminated" data: Run 6
72. Comparison of Energy Flux Spectra from "Clear" and "Spike-Contaminated" data: Run 1
73. Comparison of Energy Flux Spectra from "Clear" and "Spike-Contaminated" data: Run 2b
74. Comparison of Energy Flux Spectra from "Clear" and "Spike-Contaminated" data: Run 3

LIST OF FIGURES (continued)

FIGURE

75. Comparison of Energy Flux Spectra from "Clear" and "Spike-Contaminated" data: Run 6
76. Map of Site Area for Boundary Bay Experiment
77. Photograph of Equipment Deployment Prior to a Run
78. Buoy Sensor Calibration for Boundary Bay Experiment
79. Frequency Response of Calibration Drum
80. Typical Power Spectrum of Downwind Velocity Fluctuations
81. Comparison of the Power Spectra from Three Pressure Sensors:
Run 1a
82. Comparison of the Power Spectra from Three Pressure Sensors:
Run 5a
83. Non-dimensional Pressure Spectrum from Boundary Bay
84. Coherence between "Buoy" and "Air" Pressure Sensors
85. Phase Angle between "Buoy" and "Air" Pressure Sensors
86. Coherence between "Buoy" and "Reference" Pressure Sensors
87. Phase Angle between "Buoy" and "Reference" Pressure Sensors
88. Coherence between "Buoy" Pressure Sensor and Hot-Wire Air Speed
89. Phase Angle between "Buoy" Pressure Sensor and Hot-Wire Air Speed
90. Coherence between "Air" Pressure Sensor and Hot-Wire Air Speed
91. Phase Angle between "Air" Pressure Sensor and Hot-Wire Air Speed
92. Coherence between "Reference" Pressure Sensor and Hot-wire Air
Speed
93. Chart Recording of Wave, Pressure, and Sonic Anemometer Signals
during Passage of 4-Second Swell Group
94. Scale Drawing of Instrument Setup for Run 5

LIST OF FIGURES (continued)

FIGURE

95. Time Variation of U , θ from Sonic Anemometer (Means over Ten-Second Intervals) for Run 5
96. Coherence Spectra during Passage of Swell Group
97. Phase Spectra during Passage of Swell Group

ACKNOWLEDGEMENTS

This work has been part of the Air-Sea Interaction research program of the Institute of Oceanography at the University of British Columbia. It has been supported by the Office of Naval Research (U. S. A.), Grant No. NRO 83-207. During my stay at IOUBC I have been supported by the Institute of Oceanography, a UBC Graduate Fellowship, and a National Research Council Postgraduate Scholarship.

I would like to thank Dr. R. W. Stewart and Dr. R. W. Burling for many stimulating discussions, and Dr. Burling for his painstaking examination of my thesis.

All of the graduate students and staff of the Institute have helped me in my work one way or another, and I thank them collectively. In particular I am deeply indebted to John Garrett, who spent an inordinate amount of his time on my behalf, and to Ron Wilson, who hand-digitized a valuable piece of data for me. I also thank Jim Elliott, with whom I spent some of my most pleasant and productive scientific hours at Boundary Bay.

Lastly I thank my wife Evelyn, who lovingly typed this thesis so many times.

F. W. Dobson

SECTION 1:

INTRODUCTION

1.1	Purposes of the Research	1
1.2	Practical Considerations	2

SECTION 1: INTRODUCTION

1.1 Purposes of the Research

The principal concern of this thesis is with the determination of the correlation between fluctuations in surface pressure and surface elevation on wind-generated gravity waves. This permits the estimation of two important parameters: the vertical fluxes of mechanical energy and of momentum from the wind to the waves.

As such the research is in the most literal sense a study of the air-sea interaction, and therefore has been carried out as part of the Air-Sea Interaction program at the Institute of Oceanography of the University of British Columbia.

A knowledge of the energy flux from the wind to the waves provides insight into the wave generation process itself. Even today this process is not well-understood; the "classical" theory (the Miles-Phillips theory: Miles, 1960) is now thought to be inadequate to explain the observed growth of wind waves at sea. Both Miles and Phillips (1957) have stated that the least-known variable in their equations is $p(x,t)$, the pressure at the sea surface. The pressure measured in this experiment is $p(o,t)$, the time variation of pressure at one location.

The Miles theory deals with energy transfer from the mean flow in the air to the waves via a positive feedback process, whereby the mean flow streamlines are modified by existing waves so as to increase the energy transfer. The end result of the theory is a prediction for the energy transfer in terms of the magnitude and phase of the wave-induced normal pressure at the water surface. An object of this work is to

measure the energy transfer by measuring this pressure, and to compare it with the theoretical predictions.

Stewart (1961) has predicted that a large fraction of the total wind stress on the water surface goes directly into wave momentum. A knowledge of the energy flux to the waves implies, assuming they are almost irrotational, a knowledge of the momentum flux to them (see, for instance, Stewart 1961). Therefore a secondary object is to compare the momentum flux measured in this way with that either inferred from assumed logarithmic vertical profiles of mean wind speed or measured by measuring the Reynolds stress $\tau = -\rho \overline{uw}$ and thus obtain an estimate of the size of Stewart's fraction.

In spite of a great deal of recent work (Miles 1957, 1959 a and b, 1960, 1962, 1965, 1967; Phillips 1957, 1966, 1967; Bryant 1966; Benjamin 1959; Lighthill 1962; Stewart 1967), no theory exists today which predicts within an order of magnitude the energy transfer from the wind to the waves it generates. A principal reason for the failure of the theories is the lack of good experimental information on the flow of the air over waves. The principal object of this experiment is to provide some of the missing information, and in so doing to throw some light on the basic mechanisms by which the wind generates waves on water.

1.2 Practical Considerations

The practical problems of putting a pressure sensor on the water surface and of getting it to measure normal pressures there are far from negligible. The first decision to be made is whether the buoy carrying the pressure sensor should be allowed to drift as freely as possible (Lagrangian measurement) or to be constrained to move only vertically

(quasi-Eulerian measurement). Because the analysis difficulties seem insurmountable in the former measurement, the latter is felt to be mandatory.

Unfortunately the quasi-Eulerian measurement is much more difficult; it fairly bristles with problems. The principal one is keeping water away from the pressure sensing port; a film of water 1 mm thick causes a spike in the pressure record larger by a factor of five than the largest air pressure amplitudes actually observed in the data. In a Lagrangian measurement it would be possible to keep water from the sensor 90% of the time in a fairly strong wind; with the quasi-Eulerian measurement it is not. Therefore special data processing must be used to extract useful information from a pressure signal on which are superimposed numerous water-induced spikes.

Another major cause for concern, separate from the Lagrangian-Eulerian problem, is the effect of the shape of the vehicle carrying the sensor on the pressures it measures. Care must be taken to ensure rejection of the so-called "dynamic" pressure $\frac{1}{2} \rho_a U^2$, where ρ_a is air density and U wind speed, caused by the streamline configuration set up as the air flows over the buoy.

The last problem to be mentioned is the one which haunts all oceanographers (except perhaps the Ivory-Tower breed): that of making sensitive electronics work in the presence of salt water.

SECTION 2: THEORIES

2.1	The Kelvin-Helmholtz Instability	4
2.2	Jeffreys' Sheltering Hypothesis	5
2.3	The Stability Analyses of Wuest and Lock	7
2.4	Eckart's Model	8
2.5	Phillips (1957)	9
2.6	Miles' (1957) Inviscid Laminar Model	11
	2.6.1 Assumptions	11
	2.6.2 Theory	12
2.7	Miles' (1962) Viscous Laminar Model	14

SECTION 2: THEORIES

From the beginning, man's encounter with the sea has been a stormy one. Extended sea voyages, for a long time only possible with the aid of the winds, were seriously impeded by the waves which those winds generated. That the wind generates sea waves has long been recognised. The question, "How?" has no satisfactory answer; in some sense this indicates the complexity of the process. In the following paragraphs theoretical progress made up to the time when this work was begun will be reviewed.

2.1 The Kelvin-Helmholtz Instability

The first to suggest the possibility of an instability on a density discontinuity between fluids moving relative to each other was H. Helmholtz (1868). The problem was tackled in more detail in 1874 by Sir W. Thomson (Lord Kelvin), who included the effects of surface tension. His solution is known as the "Kelvin-Helmholtz Instability", and was the first theory in which an attempt was made to predict the growth of sea waves.

The problem is taken up in Lamb (1932, § 268). Both fluids are considered as inviscid. The boundary layer between the two fluids is assumed to be of negligible thickness compared with wave heights to be considered. The mean flow of both fluids is taken to be uniform (no variation in speed U with distance from their common boundary), but different in the two media. For the case considered here the air speed is U_a and the water speed is zero. ρ_a is air density and ρ_w is water density; surface tension T is included in the analysis.

Solutions are looked for in the case for which the interface is

deformed with a travelling wave of the form $\exp ik(x-ct)$ where the wave number k is known and the wave phase velocity c is to be solved for.

The resulting c is complex in general:

$$c = \frac{\rho_a U_a}{(\rho_a + \rho_w)} \pm \left\{ \frac{g(\rho_w - \rho_a)}{k(\rho_w + \rho_a)} + \frac{\tau k}{(\rho_w + \rho_a)} - \frac{\rho_w \rho_a U_a}{(\rho_w + \rho_a)^2} \right\}^{1/2} \quad 2.1.$$

The waves will grow exponentially if for a given k the air speed U_a is large enough to make the c expression complex; the positive root sign produces growth. Because water waves have a minimum velocity C_m (see, for instance, Lamb 1932, § 267) there is a range of wind speeds which generate no waves of any wave length; substitution of C_m into the stability criterion yields the minimum wind speed at which this mechanism can be effective, about 650 cm/sec. Since naturally-occurring wind-generated waves are initiated at much lower speeds, and since in fact the assumption of a very thin interfacial boundary layer is unrealistic, this mechanism is not thought to be very effective over most of the ranges of wind speeds and wavelengths commonly observed at sea (see Miles 1959b).

The most telling argument against the efficacy of the Kelvin-Helmholtz mechanism has been given by Stewart (personal communication). If exponential wave growth is occurring then the bracketed term on the right hand side of equation 2.1 is pure imaginary. This means that the propagation velocity of the waves being generated is given by $\frac{\rho_a}{(\rho_a + \rho_w)} U_a$, which is very small for the case of air flowing over water. The wave must grow straight up and hardly propagate at all, a highly unrealistic state of affairs.

2.2 Jeffreys' Sheltering Hypothesis

Sir Harold Jeffreys (1925) re-examined the problem and produced

another mechanism which could generate waves. He assumed that as the air flows over the wavy water surface, separation occurs on the leeward side of the wave crests with re-attachment somewhere further down on the leeward slope of the wave. This produces low ambient pressures on the downwind slopes of the waves, and hence a pressure field coupled to the wave profile in such a way that the correlation $\overline{p\dot{\eta}}$ of pressure and wave vertical velocity is positive, producing a positive energy transfer from the air flow to the waves.

He assumed that transfers caused by shear stresses are negligible. In his calculations he replaced the sea surface with a single Fourier component, a long-crested sine wave. He then calculated the work done on this sine wave by the component of normal pressure in quadrature with $\dot{\eta}$, the wave height, which is given by

$$p^* = s \rho_a (U_a - c)^2 \partial \eta / \partial x \quad 2.2$$

where s is less than one and was called by Jeffreys a "sheltering coefficient". He calculated s by first calculating the rate of energy loss due to molecular viscosity and then the least wind U_{\min} that can maintain waves against this loss, and compared this with "observed" least winds which seemed just capable of generating waves.

Since in Jeffreys' theory his calculated s varies as $(U_{\min})^3$, his choice of the "correct" U_{\min} was critical; this represents a weak point in his argument. He chose U_{\min} to be 110 cm sec^{-1} , giving an s of 0.3.

Ursell (1956) reviews the data available at that time on pressure variations over solid model waves in wind tunnels: the works of Stanton et al (1932), Motzfeld (1937), and Thijssse (1951), and finds little evi-

dence to support a value for s as large as that suggested by Jeffreys: "The evidence of the three sets of measurements ... on the whole favours the conclusion that the pressure differences over a solid profile composed of a number of waves are an order of magnitude smaller than the differences postulated by Jeffreys." He goes on to point out that no experiments had been done (1956) over liquid profiles, and that therefore the question of the actual size of s is still open. There are now some such observations; they will be discussed in "Observations".

It is perhaps worth noting here that the type of separation suggested by Jeffreys is not the only type of separation which can exist over the waves and produce the necessary phase quadrature between waves and pressures. There is also the possibility, first clearly pointed out by Lighthill (1962), that flow reversal can occur over the waves in the co-ordinate system moving at the wave phase speed, and that this type of "separation" can produce the required phase quadrature.

2.3 The Stability Analyses of Wuest and Lock

Wuest (1949) and Lock (1954) both treated the problem of the laminar flow over a semi-infinite plate. Their work is reviewed by Ursell (1956). Although their analytical procedures differ, they both looked for the conditions necessary for the onset of instabilities in the flow.

They used the same physical model: air flows over deep water under the influence of gravity and with surface tension; the air flow has no pressure gradient. Viscosity causes boundary layers in air and water. Both layers are assumed to have instabilities which start at some location and grow downstream. Outside the boundary layer in the air the flow is initially uniform and the water at rest. The interface is then perturbed.

with a small (much smaller than the boundary layer thickness) sinusoidal disturbance of wavelength λ much less than the distance x from the start of the layer. The problem is then reduced to the determination of the stability of this flow for various wind speeds and values of λ and x .

Their results, as Ursell points out, are hard to relate to any field situation (or for that matter, to any simple laboratory experiment). What was predicted in fact was the condition for transition to turbulence from laminar flow, while the flow over wind-generated waves is invariably turbulent. The models, being determinations of the onset of instability, said nothing about the subsequent behaviour of the instabilities in the air or the water.

2.4 Eckart's Model

Eckart (1953) proposed a model which was the forerunner of Phillips' (1957) Theory.

He assumed an inviscid open ocean over which a theoretical circular "storm" exists. The storm consists of a stationary random distribution of similar "gusts" (regions of relatively high normal pressure). The model neglects shear stresses and any distortion of the flow by wave-produced feedback.

The pressure variations in the gusts are small enough so that the equations of motion can be made linear. The gusts are not directly coupled (i.e. through a feedback mechanism) to any waves already present; they move over the water at the wind speed, and have been present for long enough that conditions within the "storm" and outside it are stationary.

The problem was posed in terms of Fourier - Stieltjes integrals, and the results are statistical. He obtained an expression for mean-square wave height in terms of mean-square pressure at the "storm" centre, "storm" diameter, "gust" diameter, and distance from the storm. He then used known wave heights from a real storm to see what mean-square pressures his theory predicted. The pressures required are an order of magnitude too large (they would have to be greater than $\frac{1}{2} \rho_a U_a^2$, the full dynamic head for air moving at a speed U_a). This leads him to believe that randomly distributed normal pressures in the air are probably insufficient to generate waves. The weakest point in his conclusion is in the estimation of pressures; at that time, no measurements were available of the mean-square pressure over waves in the open ocean. In the light of recent measurements, his conclusions were correct.

2.5 Phillips (1957)

O. M. Phillips (1957) has developed a wave generation theory which along with that of Miles (1957) has received much attention over the past ten years. Since the predictions of the theory are not directly applicable to the present experimental results, only a brief outline is given below.

Phillips considers the subsequent motion on an initially flat water surface after the onset of a turbulent wind. The water motions are assumed to be inviscid and irrotational. Stated simply, he finds that as the turbulent pressure fluctuations in the air are carried over the water surface, forced oscillations are generated which travel in all directions and which have all the wave numbers present in the air pressure

spectrum. Of this initial broad wave spectrum, two components for each Fourier component in the pressure field correspond to free gravity wave oscillations: those two which move at angles to the wind such that their propagation speed in the wind direction equals the "advection velocity" of their generating pressure fluctuations. These components grow as long as the pressure fluctuations retain their phase relative to the waves; that is, they "resonate" with the pressure field.

The development of the waves falls into two stages, depending on whether the "time scale" for which the atmospheric pressure fluctuations exist and maintain their phase relative to the waves is greater or less than the elapsed time from the onset of the wind.

In the "initial" stage of development, the most prominent waves are those which travel at the minimum phase velocity of gravity-capillary waves $c_m = \left(\frac{4gT}{\rho_w} \right)^{1/4}$ (where g is the acceleration of gravity and T is the surface tension of the water, and ρ_w is its density). They move at angles to the wind given by $\theta_m = \cos^{-1}(c_m/U_{ad})$, where U_{ad} is the advection velocity of the generating pressure fluctuations.

In the "principal" development stage the phase of a given Fourier component of the pressure wanders relative to the wave phase, and as a result the wave amplitude grows as \sqrt{t} , as in a random walk problem. He derives for the mean-square wave amplitude the equation $\overline{a^2} \approx \overline{p^2} t / 2 \rho_w g U_{ad}$, where a is wave amplitude, p is atmospheric pressure, ρ_w is water density, and U_{ad} is the advection velocity of the pressure field.

To verify his theory he estimates the approximate size of the rms pressure fluctuations to be

$$\sqrt{\overline{p^2}} \approx 0.1 \rho_a U^2$$

where ρ_a is air density and U_a is mean wind speed at "anemometer height"--usually 10 meters. He finds that this estimate gives order-of-magnitude agreement of his theory with observed wave growth. The validity of the estimate 2.3 is discussed in "Discussion of Results", p. 139.

Miles (1960) has incorporated the above model into a composite one involving it and his own: Miles (1957). This will be discussed in the following paragraphs.

2.6 Miles' (1957) Inviscid Laminar Model

The present work provides a test of the wave generation theory proposed in 1957 by Miles; therefore, this theory will be discussed in more detail than the others mentioned so far.

2.6.1 Assumptions

The air is assumed to be inviscid and incompressible, as is the water; the air is given a prescribed mean shear flow (in the absence of waves) which varies with height above the surface only. It is assumed that there is a feedback from the waves such that wave-induced air velocity and pressure perturbations are two-dimensional and small enough to be unimportant in the nonlinear processes of the equations of motion. Turbulence in the air is neglected (except for the implicit assumption that it maintains the prescribed shear flow). Because of the last assumption, the flow is called "quasi-laminar".

Mean water currents are assumed to be absent. The water-wave motion is assumed to be irrotational, and wave amplitudes and slopes small enough that linear wave theory (see, for instance, Phillips, 1966, § 3.2) may be used. The magnitude of the speed of the waves is assumed to be

that of free gravity waves plus a second-order perturbation term which is caused by the component of aerodynamic pressure in phase with the wave slope.

2.6.2 Theory

The wave elevation of a given Fourier wave component is taken to be

$$\eta(x,t) = a \exp[ik(x-ct)] \quad 2.4,$$

where a is amplitude, $k = 2\pi/\lambda$ (λ is wavelength) is the wave number, x is horizontal distance (the waves are long-crested), c is the wave phase speed, and t is time. The perturbation aerodynamic pressure associated with the mean flow he takes to be

$$p' = (\alpha + i\beta) \rho_a U_i^2 k \eta \quad 2.5,$$

where ρ_a is air density, U_i is a "reference speed" (later defined as $2.5(\tau/\rho_a)^{1/2}$, where τ is the total momentum flux from air to water), and α and β are dimensionless coefficients.

The hydrodynamic equations are then solved for the wave velocity c , giving

$$c^2 = c_w^2 + \rho_a/\rho_w (\alpha + i\beta) U_i^2 \quad 2.6,$$

where c_w is the speed of free gravity waves ($c_w = \sqrt{g/k}$ for wave number k in deep water) and ρ_a/ρ_w is the ratio of the densities of air and water. He then assumes

$$c_w^2 \gg \left| \rho_a/\rho_w (\alpha + i\beta) U_i^2 \right|$$

and expands c about c_w , keeping only the first two terms. This gives

$$c \simeq c_w \left\{ 1 + \frac{1}{2} \rho_a / \rho_w (\alpha + i\beta) (U_1 / c_w)^2 \right\} \quad 2.7.$$

Substituting 2.7 into 2.4 gives for the surface elevation

$$\eta(x,t) \simeq a \exp \left\{ \frac{1}{2} \rho_a / \rho_w \beta k c_w (U_1 / c_w)^2 t \right\} \exp[ik(x - c_w t)] \quad 2.8,$$

where it is assumed that

$$|\alpha + i\beta| \ll \rho_w / \rho_a (c_w / U_1)^2 \quad 2.9.$$

Miles then defines

$$\mathcal{J} = (1/\omega \bar{E}) \partial E / \partial t \quad 2.10$$

as the fractional increase in wave energy E per radian. From 2.8 this is

$$\mathcal{J} = (\rho_a / \rho_w) \beta (U_1 / c_w)^2$$

In a later paper (Miles 1960) the relation is generalized for arbitrary wave propagation angle (relative to the wind) θ to $\mathcal{J} = (\rho_a / \rho_w) \beta (U_1 \cos \theta / c_w)^2$.

In the same paper his own model is generalized to include that of Phillips (1957).

He finds that to obtain \mathcal{J} he must solve the inviscid form of the Orr-Sommerfeld equation (see, for instance, Lin, 1955, Equation 1.3.15). He finds that the growth rate of a given Fourier component of the wave field is a direct function of the curvature of the vertical wind shear at the height (the "critical" height z_c) above the wave where $U = c_w$.

The inviscid Orr-Sommerfeld equation is integrated numerically (Conte and Miles, 1959) for the commonly-observed logarithmic profile

$$U(z) = U_1 \log(z/z_0) = 2.5 u_* \log(z/z_0) \quad 2.11$$

where $u_* = (\tau / \rho_a)^{1/2}$ is the "friction velocity", τ the Reynolds stress, and

z_0 is a "roughness length" (see, for example, Lumley and Panofsky, p. 103). The equation has also been solved for several different wind profiles and including viscous effects by Benjamin (1959), using an orthogonal sinusoidal co-ordinate system which follows the unperturbed flow streamlines.

The result of Miles' computations is a curve (Miles 1959a) relating β to c_w/u_1 for various values of the wind profile parameter

$$\Omega = g z_0 / u_1^2 \quad 2.12.$$

Other curves presented in the same paper represent his predictions of the energy input rate from the wind to the waves and of the phase angle between air pressure and wave elevation. Some of the predicted phase angles have been calculated for profile parameters expected in the experiments done at the present site, and they have been presented in Table 4.1.

2.7 Miles' (1962) Viscous Laminar Model

Miles (1962), in studying the growth of short-wavelength waves on shallow water, is led to propose a theory whereby energy may be transferred by "viscous Reynolds stresses" from the wind to the waves when the height of the critical layer is so small that it is in the so-called "viscous sublayer" immediately above the water surface, where the curvature of the mean wind profile is linear and so the inviscid laminar mechanism, which depends for its action on the existence of profile curvature, is ineffective. The term "viscous Reynolds stresses" implies that the energy transfer occurs through the action of pressures in quadrature with the waves. The theoretical model described in the paper is referred to as the "viscous laminar" model.

The theory considers the growth of two-dimensional waves on the surface of a slightly viscous liquid (which we will call the water) of finite depth which is subjected to prescribed surface stresses. These normal and tangential stresses are calculated by solving the viscous Orr-Sommerfeld equation for the air above the wavy water surface in the orthogonal sinusoidal co-ordinate system used by Benjamin (1959).

By subjecting the equations of motion for the water to boundary conditions which match the calculated normal and tangential stresses at the air-water interface, an eigenvalue equation for the complex wave phase speed is obtained and the imaginary part of the phase speed is computed to obtain the growth rate of the waves.

The solutions to the eigenvalue equation for the water waves are composed of two parts: the first solution gives free surface water waves damped by the action of viscous stresses at the surface and at the bottom; the second solution is for Tollmien-Schlichting waves in the air perturbed by the wavy motion of the water. Miles points out that although the two classes of waves are independent at most wind speeds and wavelengths, there is a possibility of resonance between them at a physically realizable combination of wind speed and wavelength ($u_* = 5 \text{ cm sec}^{-1}$ and $\lambda \approx 5 \text{ cm}$, where u_* is the friction velocity as defined in equation 2.11). The growth of the first class of waves is discussed in some detail. Approximate solutions are found for the growth rate and growth rate curves are presented.

Since the measurements made in the present set of experiments are almost completely outside the range of validity of the viscous laminar model, its predictions will not be discussed in any more detail. The

range of validity of the model will be given, however, so that the results may be discussed in terms of the various wave generation theories.

The thickness of the laminar sublayer is

$$\delta_s \approx 5 \nu_a / u_* \quad 2.13$$

where ν_a is the kinematic viscosity of the air. Miles defines a characteristic length δ_c for the thickness of the critical layer according to

$$\delta_c = (\nu_a / U_c' k)^{1/3}$$

where U_c' is the slope of the mean wind profile at the critical height and k is the wavenumber of the waves. He then defines a non-dimensional height

$$Z = z_c / \delta_c$$

and finds that the viscous laminar model applies over the range $0 < Z < 2.3$.

He computes numerical values for wave growth assuming a mean wind profile which is linear in the laminar sublayer and logarithmic above it. His predictions cover wavelengths from 1 - 10 cm and values of u_* from 5 - 30 cm sec⁻¹. The energy transfer is thus appreciable only for values of c/u_* less than about 8.

This concludes the outlines of theoretical progress on wave generation. The discussions given are far from exhaustive, and other theories have been advanced since the date of the 1962 Miles paper. Any of these newer ideas which are relevant to the present work are mentioned in context, during "Discussion of Results".

SECTION 3: OBSERVATIONS

3.1	Sverdrup and Munk (1947)	17
3.1.1	Comparisons with Theories of Miles (1957) and Phillips (1957)	18
3.2	Field Measurements of Normal Pressures over Waves	20
3.2.1	Kolesnikov and Efimov (1962)	20
3.2.2	Longuet-Higgins, Cartwright and Smith (1963) . . .	22
3.2.3	Summary	25
3.3	Recent Observations	26
3.3.1	Tests of Miles' Viscous Laminar Model	26
3.3.2	Field Tests of Miles' Inviscid Laminar Model . . .	27
3.3.2a	Snyder and Cox (1966)	27
3.3.2b	Barnett and Wilkerson (1967)	29
3.3.3	Laboratory Tests of Miles' Inviscid Laminar Model	31
3.3.3a	Wiegel and Cross (1966)	31
3.3.3b	Shemdin and Hsu (1967)	33
3.3.3c	Bole and Hsu (1969)	34
3.4	Summary of Observations	36

SECTION 3: OBSERVATIONS

The amount of available experimental data on pressures over waves and on rates of wave growth under the action of the wind has been increasing rapidly over the past ten years. Since so large a fraction of the total information has been published in the last three years, it has become necessary to divide the following reviews of the experiments most relevant to this work into two parts: those which were published prior to the inception and design of the present experiment (which was conceived in early 1965) and those which appeared in the literature from that time until late 1968. The latter form the background against which the final results of the experiment are discussed.

3.1 Sverdrup and Munk (1947)

The best summary of reliable observations available in 1957 when Miles and Phillips published their now-classical wave generation theories was that made by Sverdrup and Munk (1947) to produce a method of practical wave forecasting for the U. S. Navy. This summary drew heavily on those of Krummel (1911), Patton and Marmer (1932), and Cornish (1934) as well as others.

The relevance of the theory of wave forecasting and of the assumptions about how waves grow as discussed by Sverdrup and Munk need not be considered here--these points were discussed fully by Ursell (1956). The authors summarize the observations of wave growth on non-dimensional plots (a) of wave steepness H/L versus wave "age" c/U_a , (b) of wave velocity c/U_a and wave height gH/U_a^2 versus fetch gF/U_a^2 and duration gt/U_a , where H = peak to trough wave height of the "significant" waves,

L = wavelength of the "significant" waves,

c = wave phase velocity,

U_a = anemometer wind speed at 8 m height,

g = gravitational acceleration,

F = fetch: distance over which the wind blows over the water,

and t = duration: time for which wind has blown.

It should be noted that H and L do not refer to the long-crested sinusoids considered in potential theory and in the wave generation theories. Sverdrup and Munk define them as the "average height and period of the one-third highest waves", and as such their energy budget is not the same as that of long-crested sinusoids; they discuss the differences fully. The fact that H and L are not simply related to the a and λ of a simple sinusoidal wave should be borne in mind during the discussions which follow.

This work, basically empirical in nature, and the wave generation theories of Jeffreys (1925) and Eckart (1953), were the most recent available theories of wave generation when an article by Ursell (1956) turned the attention of theoretical fluid dynamicists to the complete inadequacy of the existing explanations of the process. As the direct result of the article two theories were published within a year, by Miles (1957) and Phillips (1957). These two theories, as unified by Miles in 1960, form the "classical" view of wave generation.

3.1.1 Comparisons with Theories of Miles (1957, 1960) and Phillips (1957)

Phillips (1957), having obtained a value for the mean square wave amplitude $\overline{a^2}$ in terms of the wind duration and speed and the mean square

fluctuations in normal pressure of the wind field (see pp. 9-11), estimated the size of $\overline{p^2}$ as

$$\overline{p^2} \simeq 0.1 (\rho_a U_a^2)^2 \quad 3.1,$$

and compared the resulting $\overline{\alpha^2}$ with that expected from the results in Sverdrup and Munk's paper; he found the points relating gH/U^2 to gt/U to be in good agreement with his theoretical curve. By 1960, however, Phillips concluded that his estimate of $\overline{p^2}$ was too large by as much as one order of magnitude.

Miles (1959a) made, besides an estimate of the minimum wind speed necessary to raise waves, a comparison with the Sverdrup-Munk data as well. He computed from his theory the value of the "sheltering coefficient" s (see Jeffreys' wave generation theory, pp. 5-9) by two different methods: first, by computing the mean energy transfer to the waves using his theory; and, secondly, by computing the mean theoretical momentum transfer. The latter computation involved the assumption of a directional distribution for the waves (one proportional to $\cos^2 \theta$ is used). Both assumed a wave spectrum of the functional form given by Neumann (1952). Wind profile parameters were taken from empirical results quoted by Ellison (1956).

From these two computations, his estimates for s were 1.1×10^{-2} and 0.9×10^{-2} ; the value found by Sverdrup and Munk to fit the observations is 1.3×10^{-2} . Munk (1955) also calculated a range of values for s from shearing stresses of the wind on the water inferred from some earlier measurements of Van Dorn, and its value of $0.8 - 1.2 \times 10^{-2}$ was also used by Miles as evidence of the validity of his theory.

Thus the "classical" theory of wave generation, the Miles-Phillips theory as unified by Miles (1960), relies heavily for the experimental

proof of its validity on the wave growth observations summarized by Sverdrup and Munk in 1947. At the time when the theories of Miles and Phillips were published, the only information on pressure fluctuations over waves was that contained in the three experiments done on variations in normal pressure on solid wave models by Stanton et al (1932), Motzfeld (1937), and Thijsse (1951), all of which were considered by Miles (1957) to be irrelevant to the study of the flow of air over water. The results obtained by these three experiments, reviewed by Ursell in 1956, are far from consistent, the first two experiments giving measured values for s ranging from 0.006 (Stanton) to 0.11 (Motzfeld); Thijsse's work indicates that the pressure distribution is such that the wave would grow as expected by Jeffreys, indicating an s nearer 0.27.

3.2 Field Measurements of Normal Pressures over Waves

In 1962 two accounts were published of measurements of pressure fluctuations over waves, both from freely floating buoys equipped with accelerometers for measuring the wave height simultaneously with the pressure. Each will be discussed below in the context of the present work.

3.2.1 Kolesnikov and Efimov (1962)

Kolesnikov and Efimov (1962) used a buoy about 30 cm in diameter--this figure is not given in the paper, but is obtained from a description of an earlier model (Kolesnikov and Kononkova, 1961). It was conical in shape underwater; the part which was in the air was a segment of a sphere. The pressure port was at the top of the segment on the vertical axis of the buoy, and was about 5 cm above the water when the buoy was level. Wave heights were obtained by twice integrating the output of a vertical

accelerometer located in the buoy.

The description of the experiment is terse in the extreme. A diagram of the inner workings of the buoy is not dimensioned. The reader must rely for credibility of the results on such statements as, "In measurements of the frequency dependence of pressure, surface, velocity and wave profile, the calibration curves of the microbarometer and the wave recorder were linear.". Further, the statement is made that an error exists in the pressure measurements caused by the failure of the buoy to remain parallel with the surface of the waves which, for the measurements made at sea, "was about 12%." The probable effects of this error are discussed more fully below.

A calculation of the mean input of energy \bar{E} to the waves is made for each run using the formula

$$\bar{E} = \frac{1}{T} \int_0^T p(t) w(t) dt \quad 3.2,$$

where T is the time interval over which the run was taken and $p(t)$ and $w(t)$ are the pressure at the surface and the vertical velocity of the waves. The values of \bar{E} and of U , the wind speed at 2.5 meters height, are presented--nothing else--for seven runs.

The first point to be made about the experiment concerns the measurement of pressure from a buoy which follows the orbital motions of the waves (Lagrangian measurement). The buoy contained a single accelerometer which measured vertical accelerations. Whether the first integral of the signal from this accelerometer can be considered an accurate representation of the true vertical velocity of the waves depends on the amount of motion the buoy describes relative to the orbital motion of the

surface water particles. Further, the pressure variation along a wave profile is distorted by the action of the buoy, which follows the wave surface orbital velocities. This distortion probably has little effect on the values of energy transfer to the waves computed by Kolesnikov and Efimov, since its effects are averaged out over a wavelength.

The principal source of error in the energy fluxes computed from pressure-wave correlations measured by the Kolesnikov-Efimov buoy arises from the contamination of the pressure signal with dynamic pressures associated with the flow of the air over the buoy. Its spherical above-water shape indicates that the dynamic fluctuations exerted on the buoy surface vary between about $p_d = +\frac{1}{2} \rho_a U^2$ at the junction of the buoy with the water and about $-p_d$ at the top of the buoy where the pressure measurement port is located (if the buoy is represented by a hemisphere embedded in a flat surface, potential flow theory gives $-\frac{5}{4} p_d$ for the dynamic pressure at the top of the hemisphere); here U is the mean wind velocity near the water surface. This means that as the buoy tilts relative to the water surface, an unknown spurious component will be added to the quadrature spectrum between the waves and the pressure, resulting in the computation of erroneous energy transfers. Without a detailed time history of the tilt fluctuations of the buoy, the spurious pressures could not be extracted from the recorded signal. In any case, the computed values of the energy flux from Kolesnikov and Efimov (1962) are compared with the present results where the wind speed was the same, in "Discussion of Results".

3.2.2 Longuet-Higgins, Cartwright and Smith (1963)

The buoy used by Longuet-Higgins, Cartwright, and Smith (1963) was

much larger than that of Kolesnikov and Efimov: it consisted of an aluminum disc about 1.7 meters in diameter and 0.6 meters deep, which when loaded floated with its top about 30 cm above the water surface (the 30 cm is an estimate from their Figure 1a; no figure is quoted). The pressure sensor was raised 6 cm above the top of the buoy and observed the pressure above a thin horizontal disc about 45 cm in diameter (estimated from the same figure) through twelve orifices, presumably near the centre of the disc. The cross-section of the part of the buoy above water was roughly concave with a flat top. The raised disc was located at the geometric centre of the buoy.

Since the principal object of the experiment was to measure the directional spectrum of wind-driven waves, the buoy was provided with three accelerometers which responded to rates of change of vertical motion, pitch and yaw. Thus this experiment theoretically provided enough information, assuming the buoy did not move relative to the water surface particles, to correct the observed pressure signal for the effect of the motion of the buoy along the wave profile (see p. 22); this correction was apparently not made.

Longuet-Higgins et al, having obtained directional spectra for the waves, then fit a number of theoretical angular distributions to them, finding that one proportional to $\cos^{2r}(\frac{1}{2}\theta)$ appears to fit their data best; r is found to vary from 7 to about 0.4 as U_1/c varies from 0.1 to 0.5, where $U_1 = 2.5 u_*$ and u_* is the friction velocity estimated from observed mean velocities. They then compute the in phase component of the total pressure predicted by Miles' theory as generalized by Benjamin (1959) to include viscosity and other wind profiles besides logarithmic ones.

They find that the observed ratios of their pressure spectra to their wave spectra are predicted moderately well by the theoretical ratios. This fact they take to indicate that the pressures measured by the buoy are almost entirely produced by "aerodynamical pressure changes due to the flow of the air over the undulating surface" together with the static pressure term $\rho g \eta$.

They also include a table of phase differences between the pressure and the waves as measured by the buoy for one of the runs. These phase angles become less and less reliable at high frequencies but are accurate to about $\pm 10^\circ$ below $\omega = 3$ rad/sec; the peak of the wave spectrum is at 0.6 rad/sec. The phase angles they get are about -180° (pressure lag behind waves) and this lag appears to increase with increasing frequency, although the measurements are deemed untrustworthy at the frequency (3 rad/sec) where the increase begins. Since an increase of pressure lag beyond 180° indicates that wave damping is occurring as the difference $U - c$ increases, the trend is inexplicable in terms of existing theories. The fact that the phase of the pressure signal remains -180° over the part of the wave spectrum containing most of the wave energy they take as further evidence of the validity of Miles' theoretical predictions (see "Experiment": Table 4.1) that the phase shifts of the pressure versus wave correlations should remain close to -180° . Where possible, comparisons with the data obtained from the present experiment are compared, in "Discussion of Results".

As was probably the case with the Russian buoy, it is expected that the pressure signal recorded by the English buoy was contaminated by dynamic pressure fluctuations. Since Longuet-Higgins et al only report information of the pressure-waves cospectrum, only the effects of dynamic

pressure contamination on the in-phase component of pressure will be discussed.

The height at which the English buoy floated relative to its diameter is considerably less than was apparently the case for the Russian buoy, and it is therefore expected that dynamic pressure contamination is of less significance. Two sources of contamination exist; that associated with tilting of the buoy relative to the water surface (pitching) and that arising from the dynamic pressure generated by the portion of the air flow relative to the buoy which is coherent with the waves. Unfortunately not enough is known either of the response of the buoy to the wave field or of the air flow which exists over real waves to estimate the size of either effect. It is expected that the first of the two will be more important, since the dynamic pressure at the sensor varies as $\rho_a U^2$ with the buoy pitch angle, where the relevant dynamic pressure for the second source of contamination is $\rho_a U u'$; in these expressions, U is the mean wind speed near the water surface and u' is the portion of the wind speed relative to the buoy which is coherent with the waves, which is at least one order of magnitude less than U ordinarily.

3.2.3. Summary

In summary, both the Kolesnikov and Efimov buoy and the buoy used by Longuet-Higgins et al appear to introduce into the pressure signals they record spurious dynamic pressures which may be as large as $1/2 \rho_a U^2$ for the Russian buoy and are somewhat smaller, but far from negligible, for the English buoy. The results from the two experiments cannot be compared, since Kolesnikov and Efimov report information of the pressure-waves quadrature spectrum and Longuet-Higgins et al are able to give information

only on the cospectrum. Of the two measurements the one by Longuet-Higgins et al must be considered the most significant because the buoy they used apparently had a lower profile on the water. For this reason their finding that the phase of their pressure signal is nearly -180° with respect to the waves suggests that Miles' (1957) inviscid theory gives at least a good first approximation to the air flow over the waves.

3.3 Recent Observations

A discussion of the observations published since 1962 must divide them into two classes: those which are relevant to the inviscid theory proposed by Miles in 1957, and those pertaining to the so-called viscous laminar theory (Benjamin 1959; Miles 1962). In the latter theory it is assumed that the height of the critical layer is so small that it is within the viscous sublayer, a thin stratum of air adjoining the water. In the theory, wave generation is presumed to occur through the action of viscous Reynolds stresses (see p. 14 ff.).

3.3.1 Tests of Miles' Viscous Laminar Model

Since the flow regime postulated by the latter theory is not that commonly observed for the range of wind-generated gravity waves at sea which contain most of the total energy, and since it probably never occurred during the present measurements, those experiments dealing with it will be mentioned but not commented on. The following list of works published up to late 1966 has been unabashedly extracted from Miles (1967); later references are the result of a literature search.

The experiments dealing with the viscous laminar theory have all been carried out in the laboratory in wind-water tunnels, where short-

wavelength waves are generated on smooth water under controlled turbulent boundary layers. Included in this category are the works of Hamada (1963),* Holmes (1963),* Hanratty and Woodmansee (1965), Cohen and Hanratty (1965), Hidy and Plate (1965, 1966), Plate and Hidy (1967), Hires (1967), and Plate, Chang and Hidy (1969). These were conducted in "normal" i.e. long, straight, narrow, wind tunnels; a novel, although entirely qualitative, approach has been taken using cylindrical geometry by Auerbach and Richardson (1967). With the exception of the first two and last two papers mentioned, all show more or less satisfactory agreement with the viscous laminar theory. The latest work, that of Plate, Chang, and Hidy produces conflicting results--experimental growth rates are found some of which exceed and some of which fall short of the theoretical predictions by amounts greater than the expected experimental errors.

3.3.2 Field Tests of Miles' Inviscid Laminar Model

The experiments relevant to Miles' inviscid model can be subdivided into two groups: field measurements, and those made in the laboratory in wind-wave tunnels. The field measurements will be discussed first.

3.3.2a Snyder and Cox (1966)

Since 1962 only two experiments have been published on observations of wave growth at sea under more or less carefully monitored conditions. The first is that of Snyder and Cox (1966), who towed behind their vessel an array of wave detectors tuned to waves of a single wavelength (17 m). It was towed downwind at the group velocity of these waves during offshore winds. The ship's speed was measured with a taffrail log, and wind speeds with an anemometer on the ship at a height of about 6 m above the

*Not available to the writer; comments are from Miles (1967).

water surface. From the resulting information the linear and exponential growth rates $\alpha(k_o, t)$ and $\beta(k_o, t)$ of the spectral intensity $F(k_o, t)$ of the 17 m waves have been calculated from (Hasselmann, 1960)

$$\frac{\partial F(k_o, t)}{\partial t} = \alpha(k_o, t) + \beta(k_o, t)F(k_o, t) \quad 3.3.$$

The time history of $F(t, k_o)$ was recovered from the observed spectra for a number of runs, and values of α and β were determined by fitting this time history with a regression of the form 3.3. If the spectrum of pressure fluctuations is assumed to be similar to one measured by Priestley (1965) over mown grass in Virginia, then the values of α found are consistent with those predicted by Phillips' (1957) theory. The fitted values of β are found to increase linearly with wind speed, although showing considerable scatter. The experimental points are found to be fitted quite well by the relation

$$\beta = (\rho_a/\rho_w)(k_o \cdot U - \omega_o) \quad 3.4,$$

where k is the wave number and ω_o the frequency of the 17 m waves, and U is the observed mean wind velocity. The measured values of β are compared with the predictions of the theories of Jeffreys (1925) assuming a sheltering coefficient of 0.27, and of Miles (1957) assuming a logarithmic profile, a profile parameter Ω (Equation 2.12) of 3×10^{-3} and a roughness length of 10^{-1} cm. This assumed roughness length appears to be high by a factor of about 20 (see Phillips 1966, or Smith 1967), which makes the Ω used too large and the theoretical growth rate computed from Miles (1957) too small by an unknown factor. β , however, is only a weak function of Ω ; this overestimate of Ω will thus cause an error in β which probably does not exceed 25%. Therefore the basic conclusion

reached by Snyder and Cox remains unaltered. Their measurements of spatial growth are about one order of magnitude greater than those predicted by Miles' (1957) theory.

They also made an estimate of the total momentum transfer to their wave field assuming equation 3.4 to hold and using a simple empirical spectrum; they obtained a wind drag coefficient of about 7×10^{-3} - considerably larger than the value of $1.0 - 1.4 \times 10^{-3}$ obtained from direct measurements, e.g. Smith (1967) or Weiler and Burling (1967). They assumed the discrepancy to be accounted for by the assumptions used to make the estimate, which "tend to give an overestimate of the momentum transfer by normal stress ...". Because they overestimated C_D by such a large amount, their conclusion that the major portion of momentum transfer at sea goes directly into waves must be regarded as highly speculative.

3.3.2b Barnett and Wilkerson (1967)

The second field experiment was that of Barnett and Wilkerson (1967). They measured profiles of the sea surface under the action of a well-established offshore wind in the upwind and downwind direction, using as their wave sensor a sensitive radar altimeter mounted in an airplane, which flew over the water at an altitude of 150 m over a distance of 340 km. The altimeter averaged heights over a circular area of ocean about 9 m in diameter, thus filtering out all wave frequencies greater than about 0.4 Hz. The large speed of the plane--about 100 m/sec--meant that the entire wave field was sampled twice within about two hours. Wind speeds near shore were extrapolated from concurrent values at land stations. Those further offshore were obtained by successive fixes with

Loran - C; wind profile information, as in the case of the Snyder and Cox measurements, was not taken.

Their results are presented first as two plots (their Figures 6 and 7): one for the upwind one and one for the downwind run, which show contours of equal spectral density on a graph with wave frequency as ordinate and distance from shore as abscissa; these graphs therefore show the development with fetch of the complete measured power spectrum, and in themselves present an immense amount of data in a very edifying manner.

They found, as expected, that the major spectral peak moves to lower frequencies as the fetch increases. They found "considerable" energy in their spectra at frequencies below the peak, indicating a broadband energy input mechanism which they presume to be that of Phillips. If attention is fixed on the behaviour with time of a particular spectral component for which $U/c > 1$, it is found to grow exponentially until it reaches a maximum and then to lose energy until it reaches an equilibrium energy 30 - 70% below that of the maximum: it "overshoots" its maximum values.

The finding of most interest here is the fact that their experimentally determined values of the exponential growth parameter γ (Equation 2.10, p. 13) are in close agreement, at least for their downwind run, with the empirical curve suggested by Snyder and Cox (Equation 3.4, p. 28.) They thus arrived at the same conclusion as did Snyder and Cox. The inviscid model proposed by Miles predicts wave growth rates smaller by an order of magnitude than those measured.

In their upwind run, they found positive growth rates at wave frequencies for which the wave phase speed exceeded the wind speed as they

measured it. They suggest possible reasons for this, but there seems little justification in making such suggestions in view of the scantiness of their wind speed information.

3.3.3 Laboratory Studies

Three laboratory studies since 1962 have attempted to match conditions in wind-water tunnels with Miles' inviscid laminar theory. The first, Wiegel and Cross (1966), was carried out at the Department of Civil Engineering, University of California, Berkeley; the other two, Shemdin and Hsu (1967) and Bole and Hsu (1969) used the extensive wind-wave facilities available at the Department of Civil Engineering at Stanford University.

3.3.3a Wiegel and Cross (1966)

Wiegel and Cross (1966) measured air speed and normal pressure above mechanically-generated waves in three different wind-water tunnels, for a variety of wave speeds and wind speeds. They measured air velocity and normal pressure at the same downwind position as a resistance wire wave gauge, using a total-head tube for air speed and a pitot-static tube for the normal pressures. The tubes were placed as close as possible to the surface of the waves, but were always above the critical height z_c for the waves under study. The static holes of the pitot-static tube were at the same downwind position as the wave probe and the tip of the total head tube.

The frequencies of the mechanically-generated waves ranged from 1.5 to 2 Hz, giving wavelengths of 70 to 40 cm and wave speeds of 100 to 80 cm/sec; wind speeds used were 670 to 1340 cm/sec. The water depth in

their tunnels ranged from 15 to 45 cm. The results are presented in terms of coherence and phase cross-spectra and power spectra of the static pressure and wave elevation. Although some inconsistencies were observed (in one run observed phase lags of pressure behind wave height were zero throughout the spectral range, not $160 - 170^\circ$ as predicted by the inviscid theory), in general agreement with the inviscid theory was good.

There are two causes of uncertainty in their measurements. The first has been discussed in some detail by Shemdin and Hsu (1966), who found that by measuring pressures over waves with a probe fixed in space above the critical height z_c where $U = c$, (as was the probe used by Wiegel and Cross) they obtained results which were similar to those obtained by Wiegel and Cross but which differed sharply from results obtained when their probe stayed beneath z_c . They took this to mean that the validity of Miles' (1957) theory could not be checked with pressure measurements made above z_c .

The second cause of uncertainty is their use of a pitot-static tube to measure pressures in close proximity to the waves. As the wavelength of the waves used in the wind-wave tunnel decreased with increasing frequency, the pressure measured at the static ports of the tube would contain increasing fractions of the stagnation pressure $\frac{1}{2} \rho_a u'^2$, where U is the mean free-stream air speed and u' is the portion of the total air speed fluctuations which is coherent with the waves (the same defect besets the buoy measurement system used in the present experiments, and its effects are discussed in detail in "Data Analysis and Interpretation" on p. 91 ff). The influence of this dynamic pressure contamination on their

results cannot be estimated without a detailed knowledge of their measurement system.

3.3.3b Shemdin and Hsu (1967)

Shemdin and Hsu (1967) studied the pressure distribution over mechanically generated waves in a wind-water tunnel, using a static pressure probe which moved vertically with the water surface a short distance above it. The probe was a thin circular disc mounted parallel to a vertical plane containing the wind direction. Pressure was measured at the axis of the disc. Although such devices are notoriously sensitive to yaw, the small turbulence levels and accurately aligned flow available in the wind tunnel eliminated yaw effects, which might cause large errors if the same experiment were attempted in the field. In order to insure that the critical layer for the waves was sufficiently thick for the probe to remain within it, it was necessary to thicken the boundary layer over the water artificially using roughness elements located at a transition plate where the air first met the water. In this way they were able to obtain the required thicknesses for wind speeds up to 600 cm/sec.

For comparison of their results with Miles' (1957) theory, carefully measured vertical profiles of mean wind speed were made at each mean wind speed; they were found to be closely logarithmic, although a systematic deviation from a least-squares fit was found. This deviation was ignored for the calculation of the profile parameter Ω (Equation 2.12) required for comparison with Miles' theory.

To obtain the phase difference between pressure and waves, they superimposed chart recordings of the observed pressure on simultaneous wave recordings, and found least-square fit sinusoids for each wind speed.

The phase information obtained in each case is effectively equivalent to that which would be contained at one frequency in a cross-spectral analysis.

The final results were presented in a table showing measured and theoretical (predicted from Miles' 1957 theory) phase shifts, and measured and theoretical values of the perturbation pressure amplitude for 0.4 and 0.6 Hz waves over a range of wind speeds from 120 - 1160 cm/sec⁻¹. The Miles' inviscid theory was found by the authors to be satisfactorily verified by their observed phase shifts. Miles himself (1967) is not so sanguine--he finds that their phase measurements "... are in fair agreement with, although somewhat larger (to a statistically significant extent) than, the theoretical predictions of the inviscid laminar model...".

3.3.3c Bole and Hsu (1969)

The latest published account of observations relevant to Miles' inviscid laminar theory is that of Bole and Hsu (1969). They made careful observations with capacitance probes of the growth with fetch under the action of the wind of mechanically-generated waves. Vertical wind speed profiles were taken at numerous locations, both with the mechanically-generated waves present and absent. They used a modified version of the same wind-water tunnel used by Shemdin and Hsu (1967). Their waves varied in frequency from 0.9 to 1.4 Hz; the water depth was about 100 cm. Wind speeds used were 350 - 1350 cm/sec. Their boundary layer was not thickened (as was that of Shemdin and Hsu) and as a result, the thickness of the critical layer was small, ranging between .013 and .34 cm.

They doubted the existence of a laminar sublayer, noting that at the

wind speeds they used the standard deviations of surface roughness of the water caused by wind-generated ripples substantially exceeded the estimated thicknesses of both the laminar sublayer and of the critical layer. They also, therefore, doubted the existence of organized vortex motion below the critical layer. These two facts, taken together, appear to eliminate the direct application of their results to either the inviscid laminar model or the viscous model of Miles. They nevertheless applied their results to the former.

They found their mean velocity profiles to be logarithmic close to the water surface--this result being obtained in the absence of mechanically generated waves. When these waves were present the profiles were similar, but could no longer be extended as close to the water surface. They found evidence that ripples on the mechanically-generated waves were steep and sharp-crested, and appeared to "ride" the wave crests.

They computed spatial wave growth in a stepwise manner, since they observed that the boundary layer evolved with fetch. From their spatial growth curves they obtained measured values for the growth parameter (Equation 2.8, p. 13), and found that the ratios of these to values computed from Miles inviscid laminar model using measured profile parameters varied from 1 - 10, with a mean of about 3. They took this as evidence of the truth of Miles (1957) statement that his inviscid model would only give qualitative agreement with reality when the flow over the water surface could be taken as aerodynamically rough. They go on to suggest that the presence of sharp-crested ripples on the crests of the waves indicates the possibility that separation may indeed occur over their waves, and that this may account for the large ratios of observed to

predicted §.

Because of the small critical layer thicknesses existing in the measurement, it is problematical whether the results shown should be applied to the inviscid or the viscous laminar model. It should be possible with the data they obtained for Bole and Hsu to make the latter comparison; the results of such a comparison would be edifying.

3.4 Summary of Observations

In summary, there are available in the literature only four observations of fluctuations in static pressure over wind-generated gravity waves--two, those of Longuet-Higgins et al and Kolesnikov and Efimov--being field measurements and two, those of Wiegel and Cross and Shemdin and Hsu, being made in wind-water tunnels. Both field measurements are suspected of being strongly contaminated by dynamic pressure fluctuations, the latter probably somewhat more than the former. The measurements of phase made by the English buoy are not accurate enough to permit the computation of a pressure-wave quadrature spectrum.

Of the two wind-tunnel measurements only those of Shemdin and Hsu remain above suspicion, although strong reservations about their data analysis are expressed in Bole and Hsu (1969). Their results are equivocal when compared with Miles' inviscid laminar theory; phase shifts reported in Shemdin and Hsu (1967) are only slightly greater than those predicted by theory, while some results from the same experiment published later (Shemdin 1968) apparently indicate growth rates larger by a factor of about two than those predicted by Miles' inviscid model.

The two wave growth measurements made were both done in the field,

and were those of Snyder and Cox (1966) and Barnett and Wilkerson (1967). They both reached the same conclusion: observed rates of wave growth exceed those predicted by the inviscid laminar model by about one order of magnitude. In fact, the growth rates they observe are larger by more than a factor of two than the largest ones reported by Shemdin (1968).

Since real waves break, energy fluxes computed from field measurements of spatial growth should be smaller than those obtained from measurements of pressure fluctuations over sinusoidal waves in a wind tunnel. It can thus be seen that the experiments described leave our understanding of the mechanism of energy transfer from the wind to sea waves in some confusion.

SECTION 4: EXPERIMENT

4.1	Rationale	38
4.2	Design Criteria	39
4.2.1	The Pressure Measurement System	39
4.2.2	The Wave Measurement System	44
4.3	The Measurement Site	44
4.4	The Measurement of Wind Speed	45
4.5	The Wave Sensor	46
4.5.1	Calibration	46
4.6	The Pressure Sensor	47
4.7	The Pressure Measurement System	51
4.7.1	The Waterproofing Diaphragm	51
4.7.2	The Backup Volume	52
4.8	Electronics	53
4.8.1	Design Criteria	53
4.8.2	Description of System	55
4.9	Calibration of Pressure Sensor	57
4.9.1	Laboratory Calibrations	58
4.9.2	Field Calibrations	59
4.10	The Buoy	60
4.10.1	Underwater Shape	60
4.10.2	Upper Surface: Aerodynamics	62
4.11	Wind Tunnel Tests	64
4.11.1	The Wind Tunnel	65

SECTION 4: EXPERIMENT (continued)

4.11.2	Experimental Procedure	65
4.11.3	The Dynamic Pressure Rejection Ring	66
4.11.4	The Artificial Turbulent Boundary Layer	67
4.11.5	The Aerodynamic Calibration of the Buoy	68
4.11.6	Consequences of Attack Angle Variation	70

SECTION 4: EXPERIMENT

The preceding section has set the stage for this one; the theoretical and experimental evidence available up to mid-1965 formed the basis for the design criteria and experimental procedures described immediately below. These descriptions are followed by detailed accounts of apparatus and calibrations.

4.1 Rationale

As mentioned in the introduction, the first decision which had to be made in the design of the experiment was whether the buoy should be allowed to drift more or less freely on the waves (Lagrangian measurement), or be constrained to move only vertically (quasi-Eulerian measurement). Cross spectra between pressure and wave elevation were required, as well as the power spectra of each variable.

If the waves are measured with accelerometers on the buoy, then the relative phase of pressure and waves can be recovered correctly. The true frequency to which a given frequency in the recorded information is related cannot be extracted, unless motions of the buoy relative to the waves moving it are small with respect to the wave motions.

For this reason, and since two attempts at measuring pressure fluctuations with freely moving accelerometer-equipped buoys had already been made (see p.20ff), it was felt necessary that the next attempt--the one under discussion here--be quasi-Eulerian.

The experimental technique used was to measure the pressure at the surface of a disc-shaped styrofoam float with a gymbal-suspended bearing

on its vertical axis, which moved up and down on the wave sensor, a teflon-sheathed brass rod clamped vertically in the water.

4.2 Design Criteria

4.2.1 The Pressure Measurement System

The entire pressure measurement apparatus was designed so that as precise a measurement as possible could be made of the phase relation between surface elevation and pressure. Rather severe compromises were found necessary with amplitude measurements, as will become clear in subsequent paragraphs, but no such compromises were permitted in the phase measurements.

That the phase measurement is crucial can be seen in Table 4.1. The table shows theoretically predicted phase differences between pressure and wave elevation for representative wind speeds as computed by Miles (1959a) and used to obtain his Figure 6:

$$\theta = \tan^{-1} \left\{ -\beta (U_1/c)^2 / (1 - \alpha (U_1/c)^2) \right\} \quad 4.1$$

(this is a modification of Miles' calculation made by Longuet-Higgins et al, 1963; it includes the effect of the static pressure term $\rho_a g \eta$).

θ is the phase lead of pressure over wave elevation η , c is the wave phase speed, U_1 is a "characteristic" velocity given by

$$U_1 = (u_* / K) \simeq 2.5 u_* \quad 4.2,$$

where u_* is the friction velocity (see, for instance, Lumley and Panofsky, 1964) and K is von Karman's constant; α and β are numerical constants calculated by Miles (1959a) in his theory of wave generation.

TABLE 4.1

Predicted Phase Lag of Pressure Behind Wave Elevation
over Wind-Generated Waves

(Calculated from Miles, 1959; the static pressure
term $\rho_0 g \eta$ has been included in the pressure, as
in Longuet - Higgins et al, 1963)

Radian Frequency (Rad/sec)	$\frac{U_1}{c}$	$-\alpha$	β	$\frac{-\beta(U_1/c)^2}{1 - \alpha(U_1/c)^2}$	θ (Degrees)
0.5	0.025	-	-	-	-
1.	0.05	-	-	-	-
2.	0.1	7.2	0.42	-0.004	180.
4.	0.2	7.4	3.25	-0.1	174.
6.	0.3	12.0	3.44	-0.15	172.
8.	0.4	13.4	3.4	-0.17	170.
10.	0.5	14.5	3.4	-0.184	169.

Wind profile values used in the table are:

$$u_* = 20 \text{ cm/sec}$$

$$U_1 = 2.5 u_* = 50 \text{ cm/sec}$$

$$z_0 = 7 \times 10^{-2} u_*^{-1} = 3.5 \times 10^{-3} \text{ cm}$$

$$\Omega = g z_0 / U_1^2 = 3 \times 10^{-3} \quad (\Omega \text{ calculated from given } z_0, U_1 \text{ values is } 2.8 \times 10^{-3})$$

Using the estimates for the logarithmic profile for "moderate wind over wavy water" in Miles (1959a) ($u_* \approx 20$ cm/sec, $z_0 \approx 7 \times 10^{-2} u_*^{-1}$, $\Omega \approx 3 \times 10^{-3}$), α and β can be calculated, and the table displays the results for values of the radian wave-frequency ω between 0.5 and 10 rad/sec. Expected phase shifts are therefore small, requiring an accurate phase measurement.

A further calculation will give some idea of the expected amplitude of the pressure fluctuations. If the water surface elevation is given by

$$\eta = a \sin(kx - \omega t),$$

then the wave slope has amplitude

$$\left| \frac{\partial \eta}{\partial x} \right| \approx ka.$$

The momentum flux to the waves from p' , the part of the total pressure field in phase with the wave slope, is

$$\tau_w = \overline{p' \frac{\partial \eta}{\partial x}}$$

where the overbar denotes a time average. Root mean square slopes on wind driven waves have been measured (Cox and Munk, 1954a, b; Cox, 1958), and are

$$\left\{ \overline{(ka)^2} \right\}^{1/2} \approx 0.1.$$

If it is assumed that half of the total wind stress goes into waves, then for a 5 meter/sec wind,

$$\begin{aligned} \tau &= \rho_a C_D U^2 \approx 1.2 \times 10^{-3} \times 1.5 \times 10^{-3} \times 2.5 \times 10^5 \\ &\approx 0.5 \text{ dyne cm}^{-2}. \end{aligned} \tag{4.3}$$

$$\text{Then } |p'| \approx (\tau/2)(1/\overline{ka}) \approx 2.5 \text{ dyne cm}^{-2} \tag{4.4}$$

The size of the expected pressure amplitudes becomes even more important when the effect of the buoy shape on the air flow over it is

considered. The mean flow streamlines will be distorted by the buoy, the distortion being related to the shape chosen for the part of the buoy above the waterline. This distortion will cause the presence of dynamic pressures on the buoy surface, and their size will be a fraction F of the full stagnation pressure $\frac{1}{2} \rho_a U^2$, F being a function of position on the buoy surface and of the shape of the buoy. If a turbulent wind of speed $U + u'$, where u' is the fluctuating part of the total wind, blows over the buoy, then the fluctuations in dynamic pressure at the sensor would be

$$p_d = F \rho_a u' U \quad 4.5;$$

typical values obtained from wind tunnel tests for the shape of the buoys used and a 500 cm/sec wind give, assuming u to be given by $(\overline{u^2})^{1/2}$ for a situation similar to those observed at the measurement site,

$$\begin{aligned} p_{d(500)} &= 0.2 \times 1.2 \times 10^{-3} \times 60 \times 500 \\ &\simeq 7 \text{ dynes / cm}^2. \end{aligned} \quad 4.6.$$

This means that to achieve the modest signal to noise ratio of ten it became necessary to devise means for rejecting at least 96% of the dynamic pressure fluctuations.

The size of the buoy was of great importance. It had to be large enough to carry the required electronics and yet small enough to respond to high frequency waves beyond the peak of the spectrum.

One of the major factors which had to be considered is the ability of the buoy to keep water off its surface, and if water gets there to shed it rapidly. The effect of the water on the pressure signal has been mentioned (p. 3). It remains to note that water, once on the buoy

surface, could very easily then be blown by the wind to the sensor location. Also surface currents in the wind direction produced bow waves at the front of the buoy which were then blown over the sensor.

This consideration demanded buoy shapes diametrically opposed to the shapes suggested as good for rejecting dynamic pressures; therefore, a compromise had to be reached which satisfied as closely as is feasible each of the two criteria.

The frequency response of the pressure system was much harder to control at low than at high frequencies. The highest frequency at which waves could in practice be resolved by the wave probe used in the experiment was not more than 5 Hz, and most pressure measurement devices are quite capable of responding to such frequencies--indeed, many, such as microphones, are not usually designed to respond to such low frequencies! Therefore, the choice of the high-frequency cutoff of the system was one more of convenience than anything else. One consideration was the digital sampling rate. Frequencies above half this frequency had to be filtered out to avoid aliasing.

The low-frequency cutoff presented more problems. The pressure spectrum is at its largest there; in fact, it becomes thousands of times larger in the (lower) frequency range associated with the passage of storms and frontal systems. The lowest frequencies at which wind-driven waves were encountered at the experimental site were about 0.2 Hz, and the usual frequency at which the peak of the spectrum occurred was 0.5 Hz. Because accurate measurement of phase in the region of wave generation was so important, it became necessary to set the cutoff frequency at least a decade below this, at about 0.05 Hz, thus keeping phase

corrections less than 10^0 at 0.5 Hz. Setting the cutoff frequency this low introduced two problems. First the large, natural low-frequency components in the pressure signal introduced drifts; second, internal temperature variations in the sensor introduced spurious low-frequency noise. Both of these hide information at higher frequencies because of windows used in the spectral analysis.

4.2.2 The Wave Measurement System

Demands on the wave probe were less stringent than those on the pressure measurement system. Expected maximum wave excursions were about 100 cm, and the entire frequency band of interest within which all waves more than one or two millimeters in amplitude were found was 0.1 - 3.0 Hz. The probe itself had to be strong enough so that flexure caused by the extra drag of the buoy was kept small, although this flexure distorted only the observed shape of the waves; it did not affect the accuracy of the relative phase between pressure and waves. Absolute water depth accuracy was unimportant; only the resolution mattered.

The frequency response of the wave probe used was essentially flat from DC to a frequency somewhere between 3 and 5 Hz, covering completely the range of interest expected at the experimental site.

4.3 The Measurement Site

The location of the measurement site is shown in Figure 1. It is a tidal flat adjoining Point Grey, Vancouver, B. C. The available fetch (distance from shore to observation point) as a function of the direction from which the wind blows is shown in Figure 2. On the land to the south-east are apartment blocks ranging in height above sea level from 20 to

80 meters. Water depth at the site and over most of the sand flat ranges from 0 to 4 meters depending on the tide. There is a weak ($< 1\text{ m/sec}$) circular tidal current in English Bay. Figure 3 shows the measurement masts themselves and the platform on which the data were recorded. The distance from platform to mast is 60 meters in a Northerly direction.

4.4 The Measurement of Wind Speed

Wind speed was measured in two different ways during the course of the experiment, using cup anemometers, and using a sonic anemometer. For the first four of the six runs presented, mean wind speed and direction were measured with three "Thorntwaite" sensitive cup anemometers located at heights of 3, 4, and 5 meters above the water surface (anemometers were deployed at lower levels, but were destroyed just prior to the period during which the finally-used runs were made). Of these three anemometers the one at the 4 meter height read low consistently, and data from it was not used. Since only two reliable determinations of wind speed were therefore available, no attempt was made to estimate from them any characteristics of the wind profiles.

For the last two runs presented no cup anemometers were available, and wind speed was measured with a first-generation solid-state Kaijo-Denki 3-dimensional Sonic Anemometer (Mitsuta et al, 1967). This device was used to obtain the mean and fluctuating components of the downwind air velocity \vec{U} . From this quantity the mean wind speed \bar{U} , the mean direction $\bar{\theta}$, and the wind stress

$$\tau = -\rho_a \overline{uw} = \rho_a u_*^2$$

were extracted. The mean wind speed \bar{U}_5 at 5 meters height was extrapolated from the value of \bar{U} at the height of the sonic anemometer (about

1.5 meters) assuming a logarithmic wind profile as defined in Equation 2.11.

4.5 The Wave Sensor

The sensor used to measure waves was of the capacitance type, similar to that used by Gilchrist (1965). It consisted of a $\frac{1}{4}$ inch stock (0.635 cm O.D.) brass rod 180 cm in length covered with a teflon dielectric in the form of spaghetti tubing (0.719 cm O.D., 0.681 cm I.D.), sealed at the bottom and with an electrical connection to the brass rod at the top. This formed a cylindrical condenser when immersed in a conducting fluid such as sea water. It was connected to the frequency-determining network of a blocking oscillator similar to that used by Burling (1955), and Kinsman (1960). The frequency of the oscillator thus varied with changes in water level on the probe. This frequency-modulated (FM) signal was returned from the sensor location to the recording platform via coaxial cable. It was then either recorded directly on analog magnetic tape, or for monitoring purposes was first demodulated and then recorded. The demodulator used for this purpose was a "Vetter" Model 3 three channel FM recorder adaptor.

4.5.1 Calibration

The frequency-determining equation of the oscillator was

$$f = K / (C_p + mH) \quad 4.7,$$

where f is frequency, K is a constant including resistive elements in the frequency-determining network, C_p is a fixed "padding capacitance", H is the water depth to which the probe is immersed, and m is the (constant) rate of change of probe capacitance with immersion depth. Calibrations were static; that is, they were made by measuring the frequency of the

oscillator at various fixed immersion depths in salt water (salinity 4 - 10%).

The resulting calibration curve was quite nonlinear; a typical example is shown in Figure 4. The result of plotting H against $t = 1/f$ is shown in Figure 5; from this it can be seen that the signal from the probe is amenable to linearization during digital analysis, and this was in fact done (see "Data Analysis and Interpretation", p. 84).

The equation for H , from 4.7, is

$$H = K/mf - C_p/m \quad 4.8.$$

The second term in 4.8 in the system used had to be adjusted by as much as 30% from day to day. Since, however, it was only height differences which were required, these drifts were not important. Changes in K/m were important, and with this in mind, a series of six static calibrations of the probe was made which extended over three days, and for which the salinity in the testing tank was varied over a salinity range of 2 - 5.5‰. Air temperature was uncontrolled but varied over a range of 2 - 13°C. H was plotted against $1/f$ for all the tests, and the slopes (values of K/m) for all the lines are given in Table 4.2.

On the basis of this test neither air temperature nor water salinity caused the minor changes of slope which occurred, and the 95% confidence limits for wave height differences observed in the experiments were $\pm 3\%$ providing that the signal from the probe was linearized prior to spectral analysis.

4.6 The Pressure Sensor

The pressure sensor was a modified commercial capacitance microphone--

TABLE 4.2

Values of K/m for Six Wave Probe Calibrations

Date (Jan 1968)	Time of Day	Salinity (‰)	Air Temperature (°C)	$10^{-3}K/m$ (cm/sec)
Notes:			(1)	(2)
22	aft	2.0	13.3	1133
23	morn	4.0	10.0	1126
24	aft	4.5	6.7	1096
24	eve	5.0	4.4	1126
25	morn	5.2	2.2	1139
26	morn	5.5	3.9	1111

Notes:

1. Air temperature is that measured at Vancouver International Airport.
2. Mean $K \times 10^{-3}/m = 1122$ cm/sec; Std. Deviation = 15.8 cm/sec.

a schematic diagram (Figure 6) shows its construction. The pressure-sensing diaphragm was a gold-coated glass disc 1.27 cm in diameter and about 0.08 cm thick. It was clamped to a stainless steel casing, and its gold coating made electrical contact with the shell. Variations in its distance from a backing plate insulated from the shell caused capacitance variations which were a measure of the pressure difference across it. The microphone was mounted in the buoy so that the plane of its diaphragm was vertical, thus minimizing the effect on the signal of vertical accelerations.

When the microphone was first obtained, considerable time and effort were spent in trying to get the manufacturer (Altec Lansing, Inc.) to seal off a small leak which allowed air to pass from the front to the rear of the microphone diaphragm inside the stainless steel casing. The seal was deemed necessary in the present experiment so that the time constant of the microphone could be controlled. The time constant was six seconds for the microphone as received from the manufacturer, with the space behind its diaphragm sealed into a volume of 2 cm^3 ; a time constant of about 20 seconds was required. The attempt had to be abandoned when the manufacturer was unsuccessful in sealing the leak after three tries, each one entailing about a two-month delay. Therefore the time constant had to be lengthened by connecting the space at the rear of the diaphragm to a larger volume. This volume is referred to hereafter as the "backup" volume.

The pressure measurement port on the surface of the buoy could not be left open. Whenever water was shipped by the buoy it flooded the area of the port and clogged even 0.5 cm diameter holes for periods up to

ten seconds "after the flood". A number of different chemical agents for reducing surface tension were used in an attempt to reduce the size of the smallest "uncloggable" hole, but none were particularly successful. Therefore, the hole was sealed with a thin rubber diaphragm, sealing off a small forevolume (about 2 cm³) in front of the microphone diaphragm.

Because large ambient low-frequency pressures associated with weather systems existed it became necessary to provide some means for equalizing the internal pressure of the microphone-backup volume system with ambient pressures. This was achieved by venting the backup volume to atmosphere with a slow (period about 50 seconds) leak. This leak was also designed to eliminate as much as possible the effects of variations of ambient temperature on the pressure in the backup volume. In practice the latter effect was by far the most important, and was the source of the major component of noise at low (0.1 Hz) frequencies. A simple calculation shows its effect. If the backup volume changes temperature by an amount δT , then the associated pressure change (if the backup volume were sealed) would be

$$\delta P = P_0 \delta T / T_0 \quad 4.9,$$

where P_0 is ambient atmospheric pressure and T_0 is ambient temperature. Putting 1000 dyne cm⁻² for p_0 , 290° K for T_0 , and 0.1° K for T gives

$$\delta P \simeq 0.3 \text{ dyne cm}^{-2}$$

If this δT occurs in 10 seconds pressure drifts of the order of 2 dyne cm⁻² per minute can be expected; these are a small fraction of the observed pressure signals at these frequencies, but may be important in cases where the air-sea temperature difference was large and changing rapidly.

4.7 The Pressure Measurement System

A schematic diagram of the pressure system is shown in Figure 7. The enclosed space in front of the diaphragm had a resonant frequency of between 150 and 250 Hz depending on the tension of the rubber waterproofing diaphragm.

4.7.1 The Waterproofing Diaphragm

Many methods of keeping water out of the microphone were considered, and some were tried. The only successful one was to seal the microphone behind the aforementioned rubber diaphragm, and this was used in the experiment. Along with its obvious advantages came less obvious disadvantages; because it was mounted horizontally, flush with the measurement surface, it caused the sensor to become sensitive to vertical accelerations. Being thin natural rubber it changed its tension, and hence the pressure sensitivity of the system, as it aged with use. Further, treatments to make it shed water (see below) had to be chosen so as to not change its tension.

Because this diaphragm sealed the system except for a slow vent to atmosphere via the backup volume, any buildup of pressure inside the system was balanced by an increase in diaphragm tension, with a concomitant decrease in amplitude sensitivity of the instrument. Such pressure buildups occurred all too easily. Changes in ambient temperature (see p. 50) were their main source; another was the intermittent passage of water over the diaphragm. This could, if it happened frequently, cause the mean pressure on the diaphragm to differ from ambient enough to change the diaphragm tension.

Because in practise there was always water on the buoy surface, it

was necessary to prevent the formation of water drops which "nested" in the diaphragm and prevented pressure measurement. This "nesting" property of the water in fact determined the minimum practicable diaphragm tension and hence the maximum sensitivity of the system. This tension was determined by trial and error to be that which reduced the basic microphone sensitivity by a factor of 2 - 3.

To prevent this "nesting", and also to prevent the diaphragm from being wetted by the water (which increased its acceleration sensitivity and its tension by an unknowable amount), it was treated with a light silicone oil. The area immediately around it was, except for small areas, coated with a wetting agent, sodium silicate or water glass. This treatment remained effective for periods of up to two hours in conditions where the diaphragm was being inundated once every 10 - 15 seconds on the average.

4.7.2 The Backup Volume

The backup volume was an aluminum cylinder 4 cm long with a 3.5 cm inside diameter. It was connected to the rear of the microphone diaphragm by 10 cm of 1.5 mm I.D. polyethylene tubing. It was vented to atmosphere by 4 cm of 0.1 mm I.D. stainless steel tubing. Because the buoy was always wet, the vent itself was sealed into the buoy and an air passage provided via 10 cm of stainless steel tubing (1 mm I.D.) which was fixed vertically, so that its top did not often become blocked. The tubing from the backup volume to the microphone casing was cemented firmly in place in the buoy to prevent it from flexing as the buoy moved on the water. The backup volume was embedded in the styrofoam buoy. Other than this, it was not thermally insulated. Although this meant that temperature-

induced pressure drifts introduced some noise at frequencies less than 0.1 Hz, space and weight consideration precluded any more elaborate design. A dessicant was sealed into the backup volume to prevent condensation from occurring either on the microphone diaphragm or in the vent to atmosphere. Either would prevent the system from functioning in a predictable way; in fact, blockage of the vent proved to be the major source of equipment failure during the field experiments.

4.8 Electronics

The electronics system, with the exception of two components (tape recorder, FM tuner) had to be designed specifically for the experiment. The reasons for choosing the particular system used are first outlined; a more detailed account of the parts of the system follows.

4.8.1 The Design Criteria

The design criteria to be met by the electronics system were as follows:

1. Buoy electronics small, light, waterproof;
2. Pressure sensitivity greater than 2 millivolts per dyne cm^{-2} change in pressure. Electronics noise less than 0.2 mv p-p in the frequency range of interest (set by the tape recorder noise level);
3. Frequency and phase response nearly flat in the range 0.1 - 5.0 Hz;
4. Pressure signal free from contamination caused by the waves.

The requirements of No. 1 above are discussed later in this chapter (p. 60ff). Stated briefly they are: the physical dimensions of the buoy had to be less than one-half the wavelength of the shortest waves of interest--about 50 cm in this experiment; the displacement had to be

minimized to reduce the drag of the water on the buoy, which produces instability in the alignment of the buoy into the wind. The need for waterproofing led to the inclusion of the battery for the electronics in the buoy rather than bringing in DC power via the signal cable.

The lightest transducer with the required pressure sensitivity was a capacitance microphone. In order to get the required low frequency response, it was necessary to use frequency modulation rather than the usual DC signal conditioning system. Since the capacitance and the modulation of commercially available microphones was extremely small (typically 5 pf with $\pm 0.02\%$ modulation per microbar pressure difference across the diaphragm) it was necessary to use a high frequency carrier. The FM band (88 - 108 megahertz) was chosen, chiefly because components for this band were easily bought locally.

The undesirable contamination of the output signal by wave motions proved of major importance in the design in two separate areas: first, in the choice of methods of data transmission from the buoy; and second, in the design of shielding for the system.

It was originally intended to telemeter the 100 MHz carrier from the buoy to the hut. After considerable effort this idea, and even that of transmitting to the instrument mast had to be given up. The power received from the buoy, small to begin with because of weight limitations on the battery and size limitation on the antennae, varied over enormous ranges as the configuration of the water surface (the ground plane) varied with wave motions. As a result the receiver was not always fully limited, and wave-induced modulations of the amplitude of the carrier caused significant fluctuations in the demodulated tuner output.

An effect with a similar result occurred in the buoy oscillator. The movement of the ground plane caused large changes in loading on the carrier oscillator, which could not adequately be removed (within the limits on power consumption set by the battery) with a buffer amplifier.

The problem remained after it was decided to transmit from buoy to mast via a coaxial cable; however, it was solved by careful attention to shielding and grounding. The oscillator used in the experiment was enclosed in (and grounded to) a box milled from a block of aluminum, which was itself grounded only via the signal cable to the shield of the radio frequency (RF) amplifier on the instrument mast. A ground to the sea was considered, but not used when it was found to have no effect on the performance of the oscillator.

4.8.2 Description of System

A block diagram of the electronics system is shown in Figure 8. It can be separated into three parts: the transducer electronics in the buoy; an RF amplifier on the instrument mast; and an FM receiver, matching amplifier, and tape recorder in the hut (60 meters from the mast--see Figure 3).

Sealed into the buoy were a battery (15 volts, carbon-zinc) to power the transducer electronics, a small self-latching relay enabling the power to the electronics to be switched on or off by applying a DC voltage to terminals on the buoy, and the transducer electronics themselves. The electronics were potted with beeswax into the small aluminum box to which the microphone was attached. In this aluminum box, in shielded compartments, were the 110 mHz (Clapp) carrier oscillator and a small buffer stage consisting of a low -Q tuned amplifier which matched to the signal

cable, which was a seven meter length of 50 ohm coaxial cable (Amphenol RG - 174/u).

Circuit diagrams for the oscillator and amplifier are shown in Figure 9. Considerable care was taken to make the Q of the oscillator as large as possible. The tank circuit was temperature-compensated through the use of negative temperature coefficient capacitors; the coil was hand wound on a ceramic form (Miller 4300 - Y) and the coil wire was a strip of copper 1 mm wide and 0.05 mm thick. The beeswax potting further reduced temperature effects and provided an excellent waterproofing for the oscillator and buffer when it did ship some water. The transistors of both circuits were biased for low power drain, a total of less than 10 ma from the 15 v battery. The low-current biasing used in the buffer amplifier had the added advantage of increasing its input-to-output impedance ratio, thus improving its buffering capability.

The RF amplifier on the instrument mast was designed to receive the 100 mHz carrier, amplify it by 25 db, and drive a 75 meter length of shielded 300 ohm twin-lead cable. It was powered by two Mercury cells and used a commercially available integrated circuit (Motorola MC 1110) as a low -Q tuned amplifier. Its input was matched to the 50 ohm coaxial cable from the buoy and its (balanced) output matched to the 300 ohm twin-lead.

The twin-lead cable ran along the sand from the instrument mast to the hut, where it was connected directly to the antenna terminals of a commercially available FM tuner (EICO ST - 97). There the carrier was demodulated and the voltage analog of the pressure fed via an operational amplifier to an FM record channel of the tape recorder, which was a 14-

channel Ampex "CP - 100", or "FR - 1300". The tuner was modified in two ways to increase the stability of its local oscillator; the B⁺ power supply was replaced by a better-regulated one (Dressen - Barnes Model 32 - 101), and the ganged air-dielectric tuning capacitors were replaced with glass-dielectric variable capacitors.

These modifications and the special care taken with the carrier oscillator in the buoy reduced the reproduced noise of the system to less than 1 millivolt p-p over a frequency range of 0.01 - 10 Hz. This noise test was of necessity carried out with a fixed 5 pf capacitor replacing the microphone, to remove ambient pressure noise.

The dynamic range of the entire system was limited by the bandwidth of the Intermediate Frequency amplifier in the FM tuner. This amplifier was carefully tuned to give maximum bandwidth and good linearity. The output voltage of the tuner (from a ratio detector demodulator) is plotted against input frequency to the IF amplifier in Figure 10.

4.9 Calibration of Pressure Sensor

In the paragraphs that follow, descriptions will be given of the calibration techniques used in the determination of the sensitivity of the pressure sensor (the term "pressure sensor" will hereafter refer to the complete pressure measurement system). Both field and laboratory calibrations were done. The field tests determined amplitude sensitivity only, and were necessary because of day-to-day variations in sensitivity caused by the rubber waterproofing diaphragm covering the pressure port (see the description of the pressure measurement system on p. 51). The laboratory caliabrations were more precise and more elaborate, giving phase response as well as amplitude response.

4.9.1 Laboratory Calibrations

The setup for the calibrations is shown in Figure 11. The entire buoy was placed inside a "clean" ten-gallon oil drum at one end of which was a back plate, through which were led the cable attached to the buoy and a short length of 2.5 mm ID steel tubing, which was led via an O-ring fitting into one pressure port of a "Barocel" pressure sensor. The other port of the Barocel was at ambient atmospheric pressure. Both the pressure tube to the Barocel and the buoy cable were sealed carefully to the back plate of the drum.

The other end of the drum was closed with a thin, taut rubber membrane. Bearing on this membrane was a circular aluminum or perspex disc about 15 centimeters in diameter. This disc was made to oscillate along its (horizontal) axis by a linear driver (Ling Altec v47/3 Vibration Generator), which was controlled via a low-frequency power amplifier by a sine wave generator. By suitable adjustment of the pressure exerted by the membrane on the disc and of the amplitude and frequency of the signal to the driver, sinusoidal pressures with amplitudes from 10 to 500 dyne cm^{-2} (as measured with the Barocel) over a range of frequencies from 0.003 to 10 Hz could be generated in the drum. Amplitudes used in actual calibration runs were 30 - 100 dyne cm^{-2} (the reason for choosing these large amplitudes is discussed on p. 59); the accuracy of the Barocel sensor is better than $\pm 1\%$ of full scale, which meant ± 0.4 dyne cm^{-2} for the 30 dyne cm^{-2} amplitude and ± 1.3 dyne cm^{-2} for the 100 dyne cm^{-2} amplitude, over a frequency range 0 - 10 Hz.

The analog outputs from the buoy system and the Barocel were recorded on a two-channel chart recorder (for frequencies below 0.1 Hz). They were

also observed with an oscilloscope, phases being measured by the Lissajous figure technique. This method proved impractical at frequencies less than 1 Hz. At frequencies below 1 Hz the phase differences were measured directly from the sinusoidal traces on the chart recordings.

The principal source of error in making the calibrations was the variability of ambient atmospheric pressure in the room where the apparatus was set up. This was presumably due to fluctuations in the wind speed outside, and was on windy days large enough (up to 100 micro-bars) to preclude any calibrations at all. Hence the calibrations were done on calm days and with as large a pressure amplitude as possible in the drum. This upper amplitude limit was set by the dynamic range of the buoy system, which was in turn set by the bandwidth of the tuner IF amplifier (See "Electronics", p. 57). Since most of the noise arising from ambient pressure was at low frequencies the accuracy of the calibrations decreased rapidly below about 0.05 Hz, with amplitude accuracy falling off considerably faster than did phase accuracy. The laboratory calibration of the pressure system used in the field is shown in Figure 12. The 10% difference at the two amplitudes in the sensitivity is ascribed to a non-linear response of the rubber waterproofing diaphragm.

4.9.2 Field Calibrations

These were made necessary by the presence of the waterproofing diaphragm. Since it was natural rubber and was treated with a thin film of oil before the start of each run, it was felt necessary to carry out field calibrations, and these were done before and preferably after every run.

The method used was simple: the buoy was lifted from the water

(or from the bench, if the calibration was made before the run), and moved vertically a measured distance, usually about 100 centimeters. The voltage change resulting from this pressure change was recorded on the chart of an oscillograph and this divided by $\rho_a g \Delta h$, where ρ_a is air density, g is gravity, and Δh is the height change, gave the sensitivity. Usually the buoy was moved up and down a number of times and the average voltage change taken. The accuracy (about 10% in sensitivity) of this method was considerably less than the laboratory calibration. Inaccuracies were caused by the invariable presence of large ambient pressure fluctuations and by the measurement of the short distances over which the buoy could be raised and lowered.

4.10 The Buoy

4.10.1 Underwater Shape

The buoy was made from styrofoam; the basic shape was turned on a lathe and all further work was done by hand. After final shaping and cutting, the entire surface was coated with epoxy resin. The buoy had a diameter of about 23 centimeters and was about 3 centimeters thick. It is shown in Figure 13. Note in the figure that the part of the buoy containing the backup volume was attached to the front section.

The final underwater shape was arrived at primarily by trial and error. Slow-motion movies were taken of many "trial buoys" in a variety of conditions, and most of the information contained in this section was obtained from these movies. It was necessary to make the seakeeping characteristics of the buoy such that it would conform to the water surface for as large a percentage of the time as possible.

The most stringent experimental requirement for the buoy was that it be constrained to move only vertically. Since the buoy was free to tilt with the waves, being attached to the bearing on the wave probe with gymbals, it was therefore unstable to drag forces exerted on it by surface currents; that is, small tilts with respect to the water surface were amplified. Most early models of the buoy suffered from this instability. Not even the present model was immune, and it is to the credit of the microphone manufacturers that their product survived "dives" of as much as 10 cm below the surface of the water.

The diving propensity was minimized statically by putting as much buoyancy as possible at the bow of the buoy. This was aided dynamically by making the entry of the bow into the water vertical, by "fairing" the underwater surface, and by placing the gymbals as low as possible.

It was discovered early that in situations of active wave generation, the surface water current formed by the wind commonly doubles the orbital crest velocities of the waves. Thus whereas little care needed to be taken with the downwind side of the buoy, the shaping of the bow was of critical importance.

The effect on the buoy of this current, besides the diving propensity already mentioned, was the formation of a "bow wave" ahead of it which could with the aid of the wind be swept up and over the buoy, usually reaching the sensor. When this happened a large "spike" appeared in the pressure signal.

Because of the fairing of the bow the current caused it to ride up on the wave. This effect was counterbalanced in two ways: first, the centre of gravity of the buoy was kept well forward by judicious arrange-

ment of its "payload"; second, some of flotation of the front half of the buoy was located behind the gymbals, so that tilts associated with waves shorter than the radius of the buoy were resisted. The flotation under the bow was ended abruptly after 4 cm to cause flow separation, thus stalling the flow beneath the buoy and enhancing the lift of the bow fairing. In this way the configuration was designed to keep the bow of the buoy in a state of static and dynamic balance over a wide range of water motions.

The rear section of the buoy was hinged to allow the buoy to respond to waves with wave-lengths comparable with its radius. It had enough flotation to support a high-drag fin, which kept the buoy pointed within 20° of the wind direction. The sole function of the rear section of the buoy besides those mentioned, was to make the buoy symmetrical, thus avoiding the possibility of reversal of the buoy direction in cases where the wave orbital velocities in the troughs were greater than the wind-generated surface current. Because short wavelength waves have significant amplitudes in a wind-generated sea the tilting parts of the buoy had to be cut away (indicated by dotted lines in Figure 13) on either side of the hinges, allowing it to flex as much as $\pm 30^\circ$ from the horizontal. This contributed greatly to its seakeeping abilities.

4.10.2. Upper Surface: Aerodynamics

The upper surface of the buoy was a cover beneath which were sealed the pressure sensor and its electronics, the backup volume, a battery which powered the electronics, and a small relay which provided a means of switching off the battery current when the instrument was not in use.

Pressures were transmitted to the sensor through the thin rubber

diaphragm, which was glued over a 0.8 cm diameter hole in the perspex plate (8.2 cm x 3.9 cm x 0.3 cm--see Figure 13) which sealed the sensor and its electronics into its compartment.

The battery and the relay were held in place with a silicone rubber sealant. The upwind surface of the buoy was waterproofed with a sheet of thin polyethylene which covered all joints. This was held securely in place with a fast-setting rubber-base cement and masking tape. As a final protection the entire surface of the buoy except for the diaphragm was spray-painted white, to keep radiative heat transfer to the buoy, and in particular to the backup volume, to a minimum.

Prior to the design phase of the experiment, it was realized that the distortion of the mean streamlines of the air flow by the buoy could cause spurious pressure fluctuations at the pressure sensor, which if not rejected in some way could seriously affect the validity of the results.

To see how great this effect would be the solution (see, for instance, Lamb (1932), 103) for the potential flow over a planetary ellipsoid of revolution similar to the buoy in profile has been calculated. The resulting pressure distribution is shown in Figure 14.

From the figure, the dynamic pressures exerted on this shape are asymptotic to -0.2 times the stagnation pressure $\frac{1}{2} \rho_a U^2$. Although the shape used has a bow (left side of the figure) which is much less bluff than that used in the actual buoy, the figure of $-0.1 \rho_a U^2$ is probably within 50% of the actual figure at the pressure measurement port on the buoy. If $-0.1 \rho_a U^2$ is calculated for a 500 cm/sec wind it gives a value for the dynamic pressure which must be rejected at the pressure

port of about 7 dynes/cm^2 (see p. 42).

Further calculations show that this dynamic pressure can be reduced by increasing the eccentricity of the ellipse. Thus the best way to minimize shape effects is to make the part of the buoy above water as slim as possible.

It is easy to see on the other hand that if the pressure sensing point is to be kept relatively free from water, the best shape would have a bluff (vertical) bow with a small downward slope in the upwind direction. The bluff bow is also demanded to insure fast buoy response to changes in water level.

Of the two opposing requirements the latter was dominant. Without a bluff bow pressure measurements on the water surface were impossible.

This meant that the buoy distorted the air flow over it considerably, and that large dynamic pressures could be expected at the measurement point. It was necessary to reject these pressures; therefore, a series of wind tunnel tests described in the following section was carried out to find the best method for doing this.

4.11 Wind Tunnel Tests

Three series of tests were performed, all of them in the wind tunnel of the Department of Mechanical Engineering of the University. The first two series were developmental. The first was concerned with the determining an optimum aerodynamic shape for the buoy within the limitations stated in the last section; the second was taken up with the search for an adequate method for rejecting the dynamic pressure caused by the bow of the buoy. The third series of measurements were used to

"calibrate" the buoy aerodynamically.

4.11.1 The Wind Tunnel

The wind tunnel used for the tests was of the closed-return type. It generated wind speeds between 1 and 45 meters/sec, with low (0.1%) turbulence levels, and spatial variations in mean velocity in the test section less than 0.25%. The test section was rectangular and was 0.9 meters wide and 0.7 meters high. It was provided with tapering fillets, which partly compensated for boundary layer growth along its length.

Air speed in the test section was measured in terms of the pressure difference along a 7:1 contraction immediately upstream of the section. The speed calibration included the effect of variations in mean air density caused by ambient temperature and pressure. The pressure decrease along the contraction was measured with a micromanometer to an accuracy of ± 20 dynes/cm. This provided values for the free stream wind speed accurate to $\pm 1\%$ at 1 meter/sec and $\pm 0.5\%$ at 5 meters/sec.

4.11.2 Experimental Procedure

Wind tunnel testing was done directly on the buoy used in the field. The general setup is shown in Figure 15. The buoy was recessed in the floor of the test section at the same level at which it floated on the water; it was placed at the center of the test section floor on the tunnel axis. The bow of the buoy could be set at various pitch (attack) angles and yaw (orientation) angles by simple adjustments. In all cases, openings in the structure of the buoy and around its edges, where it met the tunnel floor, were carefully sealed with tape. The wave probe which would exist in the field measurements was replaced with a laboratory stand

of the same diameter, the base of which supported the buoy.

Pressures along the upstream horizontal axis of the buoy were measured at five carefully prepared pressure taps (0.75 mm holes). These were drilled in a slab of perspex which closely resembled the one which sealed the microphone and electronics into the buoy (see Figure 13). They were located at 0.53, 0.57, 0.63, 0.66, and 0.69 buoy radii (slant distance) from the bow of the buoy, and are shown in Figure 16.

Pressures were measured relative to the static pressure ring of the tunnel with a "Barocel" differential pressure transducer. The lines from the pressure taps and the static ring to the Barocel were pneumatically filtered to remove high-frequency pressure fluctuations present in the turbulent boundary layer. In spite of this, considerable low-frequency fluctuations (amplitudes of about 10 dynes/cm) remained; these were found to be smaller on calm days and so were presumed to be the result of wind-induced dynamic pressures on the building housing the tunnel. Therefore the wind tunnel work was done whenever possible on days when the winds were less than a few knots. To reduce these errors all measurements were averaged over a period (one minute) exceeding the range of periods containing most of the ambient pressure fluctuation energy (0 to 20 seconds).

4.11.3 The Dynamic Pressure Rejection Ring

During the early design stages of the experiment many methods were considered for cancelling the dynamic pressure, which in this case was a negative (suction) pressure caused by the flow over the boy. The method used in the actual experiment was by far the best. A thin half-ring (see plan view of Figure 13) 4.2 cm I.D. and 0.27 cm high was placed

on the surface of the buoy a short distance (1.9 cm) downstream of the pressure port, with its axis normal to the buoy surface and intersecting it just upstream of the port. This obstruction produced a positive pressure at the port which cancelled within $\pm 0.1 \text{ dyne cm}^{-2}$ the suction pressure from the bow when the buoy was sitting level in the tunnel. Because of its symmetry, the ring removed almost completely any sensitivity of the system to yaw (that is, rotation of the buoy about its vertical axis).

4.11.4 The Artificial Turbulent Boundary Layer

The air flow in the tunnel was laminar, while that in the field, in the atmospheric boundary layer, was turbulent. Since the atmospheric boundary layer is so thick (typically 100 - 300 meters), its Reynolds number cannot be matched in laboratory wind tunnels except at extremely high wind speeds. Therefore an artificial turbulent boundary layer was created in the wind tunnel using a trip 1.7 meters upstream of the buoy (see Figure 15). The trip consisted of a 2.5 cm square length of wood extending over the full width of the tunnel floor, into which were cut slots about 1.5 cm deep with widths varying from 0.5 to 2 cm, at separations of 1 - 2 cm. Velocity profiles in the turbulent boundary layer were measured with a small Pitot tube mounted on a remotely-controlled traversing mechanism which is part of the wind tunnel equipment. The mean wind profiles produced in this way followed the "Law of the Wall":

$$\bar{U}/u_* = f(zu_*/\nu_a) = f(y_*),$$

where u_* is the friction velocity and ν_a the kinematic viscosity of the air; they exhibit a straight line on a plot of \bar{U}/u_* versus $\log(y_*)$ over a range $2 \leq \log y_* \leq 3.6$. Because the transition to turbulence was artifi-

cially tripped, the friction velocity was larger and hence the line lay below that found experimentally for the smooth-transition Law of the Wall (see, for instance, Willmarth and Wooldridge 1962, Figure 3).

4.11.5 The Aerodynamic Calibration of the Buoy

Measurements of the pressure at all five taps were made over ranges of values of three different parameters: wind speed, pitch, and yaw. Of these three, wind speed and pitch were the most important; symmetry of the ring was effective in eliminating almost all sensitivity to yaw for measurements up to $\pm 45^\circ$. Three wind speeds: 3.5, 4.3, and 6.0 meter sec^{-1} , and five pitch angles: -5, 0, 5, 10, and 20 degrees, were used throughout the tests. The results, which constitute the aerodynamic calibration of the buoy, are shown in Figures 17, 18, and 19. These show the pressure distribution over the buoy under the most severe conditions expected in the field.

Figure 17 shows the difference between ambient pressure and that measured along the buoy surface as a function of distance from the bow in buoy radii; the pressure difference is not normalized to the stagnation pressure so that a better "feel" may be obtained for the size of the dynamic pressures existing on the surface of the buoy (at 6 meters per second the stagnation pressure $\frac{1}{2} \rho_a U^2$ is about 220 dyne cm^{-2}). The pressure variation along the buoy is shown for various attack angles of the buoy, which are taken to be positive if the bow of the buoy is tilted upwards. At attack angles less than -5° the bow of the buoy would be submerged if it were in the water. The arrow between tap positions 2 and 3 indicates the position chosen for the inlet to the pressure sensor used in the field experiments. It might be thought that the arrow should

be further from the ring than shown in view of the large sensitivity of the buoy to negative attack angles. This larger sensitivity is offset, however, by the response of the buoy to actual waves; positive attack angles occur more often (and are larger on the average) than do negative attack angles.

Figure 18 shows "worst-case" variation of pressure along the buoy for orientations of the buoy with respect to the wind ("yaw" angles) of $\pm 30^\circ$ for an attack angle of $+5^\circ$ in a 6 meter sec^{-1} wind. The total pressure variation at the buoy surface for a 60° change in yaw angle is less than 2 dyne cm^{-2} , or 1% of the stagnation pressure $p_d = \frac{1}{2} \rho_a U^2$.

Figure 19 shows the variation of the pressure at the "optimum" sensor inlet location versus wind speed for various angles of attack. It can be seen immediately in view of the design criteria (dynamic pressure rejection to less than 0.07 p_d ; see p. 42) that attack angles of more than $+10^\circ$ are unacceptable; it can also be seen that more than 95% of p_d is rejected if the buoy's attack angle is less than $+10^\circ$ and more than -5° in the wind speeds as high as 7 meters per second (one run was made in the field where the wind speed was 8 meter sec^{-1} ; from the figure it appears that about 6% dynamic pressure contamination occurred in this run). At attack angles greater than 10° , flow separation probably occurs at the bow of the buoy at wind speeds less than 6 m sec^{-1} ; during the tests separation appeared to be present at all wind speeds above 3 m sec^{-1} for a $+20^\circ$ attack angle. When selecting runs for subsequent analysis, all runs where the attack angle often exceeded 10 degrees or where the orientation angle exceeded 30 degrees were rejected.

4.11.6 Consequences of Attack Angle Variation

Figure 20 shows a schematic representation of the effect on the observed pressure of likely variations in the angle of attack of the buoy as it rides over a wave on an existing pressure signal in quadrature with the wave elevation. Although the shape of the signal, and hence its amplitude, is changed considerably, its phase is almost unaltered. The principal effect of angle of attack variations appears to be the introduction into the observed pressure signal of harmonics of the wave frequency, in particular of the first harmonic.

SECTION 5: DATA ANALYSIS and INTERPRETATION

5.1	Analysis	71
5.1.1	Analog Preconditioning	71
5.1.1a	Pressure	71
5.1.1b	Waves	73
5.1.1c	Playback and Selection of Data	73
5.1.1d	Rerecording	74
5.1.2	Digitization	75
5.1.2a	Hand Digitization	75
5.1.3	The IOUBC Fast Fourier Transform Package	79
5.1.3a	FTOR: The Fast Fourier Transformation Program	80
5.1.3b	The Spectral Analysis Program SCOR	81
5.1.4	Special Programming	84
5.1.4a	The Wave Height Signal	84
5.1.4b	The Pressure Signal	85
5.1.4c	The Sonic Anemometer Signals	86
5.1.4d	Special Programming in SCOR	87
5.2	Interpretation of the Spectra	88
5.2.1	Distortions Introduced by the Sensors Themselves	88
5.2.1a	The Pitching Action of the Buoy	88
5.2.1b	The Finite Size of the Buoy	91
5.2.1c	Backscattering	94
5.2.2	Distortions Introduced during Preparation and Analysis of Data	98
5.2.2a	Filtering of the Wave Signal	98
5.2.2b	The Pressure Signals	99
5.3	Summary	104

SECTION 5: DATA ANALYSIS AND INTERPRETATION

5.1 Analysis

The analysis of the data will be considered from the point of view of what is done to the signals between the time they originate at the sensors and the time when the final computer printout of spectra, cross-spectra, etc. is generated. For this reason, analog pre-conditioning and subsequent digitization will be discussed first. This will be followed by a brief resume of the digital computer programs made available to the Air-Sea Interaction Group through the labours of some of its members, which incorporate the Fast Fourier Transform technique of Cooley and Tukey (1965) into a practical scheme for obtaining digital spectra from digitized analog voltage signals. Next, the programming specifically designed for this project (and which is hence the work of the author) will be discussed in some detail. Finally, methods of presentation of the statistics of the spectra will be mentioned, as an aid in the interpretation of the spectra.

5.1.1 Analog Preconditioning

5.1.1a Pressure

The pressure recording system itself performed the first filtering of the signal. The amplitude of the signal "seen" by the microphone was reduced by about a factor of two by the presence of the waterproofing diaphragm; the frequency response of the microphone-waterproofing diaphragm combination is known to have been flat up to 10 Hz and was probably flat at 100 Hz, since the natural resonance of the volume enclosed by the waterproofing diaphragm and that of the microphone occurs at 300 Hz.

The combination of the leak around the microphone diaphragm and the backup volume acted as a high-pass pneumatic filter. Its measured low-frequency cutoff was at 50 ± 10 seconds.

All of these built-in filters caused the pressure measurement system to have an amplitude and phase response which varied with frequency. These responses were measured during calibration (see Experiment, Figure 12), and were corrected for if necessary in the analysis.

The FM pressure measurement system employed a phase-sensitive ratio detector for demodulation of the modulated 100 mc frequency which originated at the microphone. The slope of the frequency response curve of the ratio detector set the voltage sensitivity of the system and determined the voltage output from the FM tuner for a given input pressure amplitude. The frequency response of the demodulator was found to be flat over the entire frequency range of interest. The signal from the demodulator was then fed through a single operational amplifier, which acted as a buffer stage between the demodulator and the analog tape recorder and provided a gain which was variable from 0 - 2.5. This amplifier allowed optimum use to be made of the dynamic range of the tape recorder; its gain was set at the maximum level consistent with keeping the pressure signal within the limits (± 1.5 volts) of the tape recorder system.

Two tape recorders were used; Ampex models "CP - 100" and "FR - 1300". The FM record mode was used, at tape speeds of $1 \frac{7}{8}$ or $3 \frac{3}{4}$ inches per second (ips). Both recorders were set up to reproduce the signal as recorded--no amplification was attempted.

5.1.1b Waves

The wave signal was recorded as described under Experiment (p. 46) in one of two ways: either the FM output of the wave probe blocking oscillator was recorded in the Direct mode as an analog signal or it was first demodulated with a separate instrument and then recorded in the FM mode. In both cases it was played back in the FM mode.

5.1.1c Playback and Selection of Data

The signals were played back at the Institute to a chart recorder; the resulting chart records were compared with monitor chart records produced during the run. It is on the basis of these chart recordings that portions of data were chosen as suitable for further analysis.

Because the selection criteria for the runs were to some extent subjective, being sometimes the result of "feelings that the run looked right", they cannot be spelled out completely. The best way seems to be to enumerate reasons why actual runs were thrown out:

1. One of the faults of the protective diaphragm was that it sometimes "bulged out" or became "sucked in" under abnormal tension due to failure of the pressure equalisation system. The result was a rectified pressure signal, since the diaphragm in this condition could respond only to pressures which tended to decrease the pressure difference across it. Any runs in which this was known to occur or which showed any such rectification were disqualified.

2. If a drop of water "nested" in the diaphragm, a characteristic pressure signal at the bobbing frequency (2 Hz) of the buoy resulted. Runs where this happened were easily recognized and thrown out.

3. Because of the unavoidable presence of large pressure spikes caused by water splashing on or over the diaphragm, all runs except one calm-water case had to be examined closely. Only those with the fewest pressure "spikes" were analysed. In fact, analysis was postponed for some months while a (vain) attempt was made to gather more data, on the grounds that some of the best runs presented in this thesis were considered by the author (not his supervisor) as not worth analysing! Eventually the only runs thrown out because of spike problems were those where water remained on the diaphragm long enough to change the mean pressure in the backup volume, leading to the presence of large steps in the pressure records.

4. The last large source of "bad runs" was drift in the pressure system. Usually the gain of the buffer amplifier at the demodulator output was kept as high as possible, to maximize the signal to noise ratio. The practical upper limit to the gain was determined by drift, which if the gain was too high caused the signal to exceed the limits of the tape recorder FM system. Thus runs were rejected if the monitored pressure signals were even partially buried in noise or if voltage limits were exceeded during part of a ten minute period.

The remaining runs (there were six analysed, of which two were analysed in two parts; see "Results") were then prepared for digitization. One run which was hand-digitized will be discussed separately (p. 75 ff.).

5.1.1d Rerecording

The runs were rerecorded at twice the tape speed (thus reducing noise and time used for analysis) after preconditioning consisting of amplification and high-pass filtering. The low cutoff frequency (0.02 Hz)

of the filter was such that negligible ($\pm 1^\circ$) phase shift occurs at the lowest frequencies (0.05 Hz) of interest. To minimize the amount of data lost due to ringing in the filters a DC voltage equivalent to the mean signal value near the start of the run was applied to each filter; then when the run began the DC voltages were replaced by the signals themselves. This method effectively removed spurious low frequency components from both the wave and pressure signals. The amplifier gains were set to make optimum use of the dynamic range of the tape recorder.

5.1.2 Digitization

All signals except those processed by hand were digitized on a "Digital Equipment" Analog-to-Digital (A/D) converter, which is capable of digitizing as many as ten channels of data. This instrument is interfaced with a small computer (Control Data 8092 Teleprogrammer) which forms part of the computing facility of the U.B.C. Computing Centre. The 8092 was programmed to write digital (A/D) tapes for subsequent processing on the main computer at the Computing Centre, which was an IBM 7044 at the time the analyses were done.

The digitization was carried out in the same room in which the 8092 and the 7044 were housed. Signals from the analog tape recorder were passed through low-pass linear phase shift filters with a cutoff frequency of 6 Hz prior to digitization. A sampling frequency of approximately 50 Hz was used for all runs. In most cases a short section of the composite noise of the preamplifier, filters, and tape recorders was also digitized.

5.1.2a Hand Digitization

Runs 4a and 4b were digitized by hand from a chart paper recording

of the pressure and wave signals which was taken during the actual run made on October 30, 1967. The recorder used was a Sanborn Model 320 two-channel recorder. The digitizing was done by Mr. J. R. Wilson, a fellow graduate student, on a "Thomson Electronics" Model PF-10 Pencil Follower in the Canadian Oceanographic Data Centre in Ottawa.

Two separate pieces of data were analysed. The first of these (run 4a) was split into two parts in order that it might be analysed for stationarity. Since there proved to be no statistically significant difference between the parts they were subsequently merged, and are presented together as run 4a. In both runs, the spikes in the pressure signals were smoothed by hand before digitization by drawing smooth curves joining the "good" data on either side of them.

Two sources of error in the measurement of time must be considered: those which affect both channels equally and those which do not. The first type of error includes, besides chart variations, inaccuracies in the digitizer. The recorder chart drive speed of 5 mm/sec varies less than $\pm 4\%$; the claimed resolution in the digitizer is ± 0.1 mm, which corresponds to ± 0.02 seconds or $\pm 2\%$; so the total expected absolute time resolution is $\pm 4.5\%$.

The second type of error is the more serious of the two; it involves processes which produce time shifts between the data digitized from different channels at different times. There are two sources of such errors: those associated with the chart recorder and those arising from the digitization procedure. The chart drive of the recorder is arranged so that the paper is pulled over a ridge with sufficient strain to keep it taut; heated styli bearing on the ridge produce the trace. The

specified maximum misalignment is ± 0.25 mm across the paper which is 5 cm wide; this causes possible misalignments between the channels equivalent to ± 0.025 seconds. This sets an upper limit of $\pm 18^\circ$ at 2 Hz for errors due to this source. Another source of error may arise from differences in the high frequency response of the two stylus driver amplifiers. Since the wave signal is essentially zero by 10 Hz, and since the recorder specifications indicate that when properly compensated the amplifier responses are only down 3 db at 100 Hz, this error should be small. However amplifier compensation had not been adjusted for some time previous to the run; also the pressure of the stylus recording the waves increased markedly towards the end of the actual recording (which extended 40 minutes beyond the end of run 4b) causing an attenuation in its response which was visible at frequencies as low as 1 - 2 Hz. These facts led to a more careful consideration of the effects of the frequency response of the chart recorder. The wave signals at earlier parts of the chart record were visually compared with those at times later than the two data sections (runs 4a and 4b) chosen for analysis; since the high-frequency portion of the signal seemed identical in appearance both before and after the pieces chosen it was assumed that the effect of stylus pressure did not set in until well beyond the end of run 4b. Moreover the spectral shapes computed later for these runs were in no obvious way different at high frequencies from those for other runs.

A realistic estimate of the phase error introduced because of excess stylus pressure is difficult to make. Its action was that of a low-pass filter, and it visibly attenuated frequencies of 1 Hz 40 minutes beyond the end of run 4b; it had no apparent effect, however, 20 minutes beyond the end of run 4b. This means that its cutoff frequency was

decreasing with time. An extrapolation assuming the effect began at the beginning of run 4a gives 75 Hz for the cutoff frequency at the end of run 4b. If the filter associated with excess stylus pressure can be assumed to have a transfer function similar to that of a simple RC low-pass filter, then the phase lag produced by such a filter is less than 1° over the whole frequency range of interest in this work (0.05 - 5 Hz) and hence will be ignored as a source of phase error.

The digitization procedure introduces errors through misalignments of the time axis by the operator; for this reason, great care was taken to insure accurate alignment. As a further check a sum of three sine waves of different frequencies covering the range of interest was generated on a computer and plotted twice side by side by a Calcomp plotter to resemble the data as it appeared on the chart paper. These signals were then hand-digitized with the same care and analysed in the same way as the data. The phase between channels from one cross-spectrum computed from the two hand-digitized test signals are given below in Table 5.1.

TABLE 5.1

Summary of Information from Test Hand-Digitized Data

Frequency of Spectral Peak (Hz)	Spectral Estimate at peak $\ast(\text{dyne cm}^{-2})^2 \text{ Hz}^{-1}$	Relative Phase between Channels
0.3	36.0	-2.0°
0.59	23.0	-2.6°
1.27	32.5	-0.8°
2.54	10.5	4.2°

*Note: The signal is multiplied by the same calibration factor used for the pressure in runs 4a and 4b.

This is considered the best estimate of the phase errors caused by the digitization. It indicates that it is considerably less than the ± 0.1 mm, or ± 0.02 seconds, resolution specified for the digitizer.

The errors from all sources produce a maximum expected phase error of about $(18^2 + 6^2 + 4^2)^{\frac{1}{2}}$, or about $\pm 20^\circ$ at 2 Hz; the error decreases linearly as the frequency is decreased.

Amplitude errors in the wave signal other than those associated with the probe and its calibration are caused by errors in the gain of the chart recorder. The gain of both channels of the recorder has been checked in the field and on neither channel were errors greater than $\pm 2\%$. This is then the expected maximum error attributable to the hand-digitization process in the waves and pressure signal. It should be noted that while the error is about equal to calibration errors for the waves signal, the large uncertainties ($\pm 20\%$) in the pressure calibration swamp this error and it can safely be ignored.

5.1.3 The IOUBC Fast Fourier Transform Package

This package was written by J. F. Garrett and J. R. Wilson, students at the Institute. It is a series of programs, some in FORTRAN IV, and some in assembler language which instructs the IBM 7044 computer to read the tapes generated by the 8092, store the data in the computer memory, and perform a Fast Fourier Transform (FFT) on them; the Fourier coefficients resulting from the FFT process are used to compute spectra for all channels and cross-spectra between selected pairs of channels.

Included in the package are routines for plotting the digitized signals on a Calcomp plotter, calculating and printing out the distribution of digitized values over the range of the A/D converter for all

channels and the first four moments of these distributions (this program is run routinely on all digitized data and is extremely useful for detecting digital errors), and for plotting out the distribution of Fourier coefficient amplitudes versus frequency for all channels. Other more specialised programs, not used in the present investigation, are also available.

5.1.3a FTOR: The Fast Fourier Transformation Program

This program calls an assembler language program which causes the data tape generated by the A/D converter to be read. The maximum number of data points which can be read into the computer memory at a time is 10,240. Since the FFT subprogram PKFORT (Cooley and Tukey, 1966) accepts blocks of data in integral powers of two, the maximum number of data points per data block for a single channel is 8192 or 2^{13} ; if the number of data points per channel is made less than this more channels can be analysed simultaneously, up to a maximum of ten. Thus the program reads in for each channel to be analysed a group of 2^j data points hereafter called a "data block", where j is set by the user. The only restrictions are the maximum number of points which can be simultaneously stored in the computer memory and that the data blocks must contain a number of points which is a multiple of two.

When one data block has been stored in memory PKFORT is called. This subroutine replaces the data points in memory with 2^{j-1} complex Fourier coefficients which are the building blocks for the spectra. Each coefficient consists of a real and an imaginary part, and hence contains amplitude and phase information present in the signal at a given frequency. The highest frequency is the Nyquist frequency $f_s/2$, where f_s

is the A/D sampling frequency for the data, and the lowest frequency is $1/\tau$, where τ is the block length in seconds and equals $2^j/f_s$.

These Fourier coefficients are then written on a "coefficient" tape along with pertinent information such as an identification number, block number, sampling frequency, etc. Following this the next block is read in from the A/D tape; the sequence is repeated for as many blocks as requested on the input data cards or until an end-of-file mark is encountered on the A/D tape.

5.1.3b The Spectral Analysis Program SCOR

This program reads the coefficient tape generated by FTOR. Data cards provide information on number of channels and number of blocks to be done, block number at which the analysis is to begin, channels to be analysed and which are to have cross spectra, whether linear or logarithmic (approximately one-half octave) bandwidths are to be used, phase corrections, etc. The program then reads in Fourier coefficients a block at a time.

Provision is made in SCOR for smoothing the Fourier coefficients before the spectra are computed; smoothing is carried out at this point by a method (see, for example, Bingham and Tukey, 1967) often referred to as "hanning"; a three-point running average with weights $-1/4$, $1/2$, and $-1/4$ is applied to the Fourier coefficients. This is equivalent to convolving the spectra with a spectral window

$$32 \pi^4 / (3 [4 \pi^2 - (2 \pi f)^2 \tau^2])^2 \quad 5.1,$$

where τ is the duration of the data block in seconds and f is frequency. Since the spectra are already convolved with a spectral window associated

with the finite length of the data block which varies as δf^{-2} , where

δf is the frequency interval from the centre frequency (see Appendix 1, Equation A1.11), hanning of the coefficients has the effect of producing a composite spectral window which falls off as δf^{-6} . It also has the effect of spreading the energy of sharp peaks in the unhanned spectra and of confining to the two lowest frequencies of the smoothed spectra any energy associated with large mean values in the data.

The Fourier coefficients of all the spectra analysed in this experiment have been hanned. This procedure should insure that the large falloff rates (δf^{-5} approximately) observed in the wave spectra are real, and that the energy introduced into the low-frequency regions of the spectra by large mean values or drifts in the original data are confined to the first three or four spectral estimates. In fact it will be seen when the results of the spectral analysis of the field data are presented that the four-lowest-frequency spectral estimates are unreliable.

If the individual Fourier coefficients for two channels are $R_1 + iI_1$ and $R_2 + iI_2$, where $i = (-1)^{\frac{1}{2}}$ and τ equals the block length in seconds (and equals $1/\Delta f$ where Δf is the bandwidth between Fourier coefficients) then the power spectra are given by

$$\begin{aligned}\phi_{11}(f) &= \tau \frac{(R_1^2 + I_1^2)}{2} = \frac{R_1^2 + I_1^2}{2 \Delta f} \\ \text{and } \phi_{22}(f) &= \tau \frac{(R_2^2 + I_2^2)}{2} = \frac{R_2^2 + I_2^2}{2 \Delta f}\end{aligned}\quad 5.2;$$

the cross spectra are

$$C_{12}(f) = \tau \frac{(R_1 R_2 + I_1 I_2)}{2} = \frac{R_1 R_2 + I_1 I_2}{2 \Delta f} \quad 5.3.$$

$$Qu_{12}(f) = \tau \frac{(R_2 I_1 - R_1 I_2)}{2} = \frac{(R_2 I_1 - R_1 I_2)}{2 \Delta f} \quad 5.3.$$

The factor of two in the above equations makes the integral under the power spectrum over positive frequencies equal to the signal variance. Phase corrections are made at this point by calculating the phase $\theta(f) = \tan^{-1} \left(\frac{Qu(f)}{Co(f)} \right)$, correcting this angle for instrumental responses, and then recalculating Co and Qu from

$$\begin{aligned} Co(f) &= \sqrt{Co^2(f) + Qu^2(f)} \cos \theta_c, \\ \text{and } Qu(f) &= \sqrt{Co^2(f) + Qu^2(f)} \sin \theta_c, \end{aligned} \quad 5.4$$

where θ_c is the corrected phase and the uncorrected estimates are under the square root sign.

After all the required power and cross spectra for a given block and other required information on the block statistics have been stored, the sequence is repeated until all the blocks asked for have been processed or an end-of-file mark is encountered on the coefficient tape. Then at each frequency the program averages the spectral estimates over the number of blocks processes and computes the standard error of each mean and the average trend over the blocks. The standard error of the mean is computed from

$$\sigma = \left\{ \frac{\sum_N (S_N - \bar{S})^2}{N-1} \right\}^{\frac{1}{2}} \quad 5.5$$

for N realizations (blocks) of the quantity S_N . Also computed for each frequency are

$$\text{Coherence} = \left[\frac{Co^2(f) + Qu^2(f)}{\Phi_{11} \Phi_{22}} \right]^{\frac{1}{2}} \quad 5.6$$

$$\text{and} \quad \text{Phase} = \tan^{-1} \left[Q_u(f) / Co(f) \right] \quad 5.7.$$

The program also computes the variance of the zeroth harmonics (the means of the individual blocks) and their trend. This information is then printed out in tabular form.

5.1.4 Special Programming

The programming which was designed specifically for this project can conveniently be grouped into two sectors: that concerned with the computation of Fourier coefficients (FTOR), and that concerned with spectra (SCOR).

The first sector is by far the largest; it performed all digital conditioning of the signal. In the description of the programs actual computational details are not discussed; instead an attempt is made to describe what the programs did to the signals. Since the digitized data were brought into the computer in blocks, the conditioning was done on one block at a time; the description that follows is of what was done to a single block of data. Conditioning of signals from three sensors--wave height, buoy pressure, and sonic anemometer--will be described. The subroutine in which this conditioning was carried out is named FIDDLE.

5.1.4a The Wave Height Signal

The wave signal on transfer from FTOR consisted of variations in tape recorder output voltage about some mean voltage. In FIDDLE it had applied to it the nonlinear wave probe calibration given in Equation 4.8. It emerged from this calibration as deviations in centimeters about the

known immersion depth of the wave probe. Two separate wave signals were returned from FIDDLE to FTOR; the first was the wave signal as described above and the second was the same signal multiplied by a "Spike Function" which was one except during the times that spikes occurred in the pressure signal, in which case it was set to zero. The reasons for analysing these two wave signals are outlined in Appendix 1.

5.1.4b The Pressure Signal

In FTOR, a calibration factor which includes all analog gains, inversions and instrument amplitude calibrations was applied to the pressure signal which was then stored as variations in pressure in units of dyne cm^{-2} . FTOR generated if required an extra channel called S, for Spike Function, all the data points of which were at this stage set equal to 1.0.

The pressure signal was next transferred from FTOR to FIDDLE along with the S channel. In FIDDLE the first operation performed on the pressure signal was to add to each of its data points an amount $R\rho_a g\eta$, where R is a factor which could be preset to any number including zero, ρ_a is air density, g is the acceleration due to gravity, and η is the value of the wave signal at the time of zero, one or two samples in advance of the pressure signal. The number of samples by which η preceded the pressure signal could be preset. The reason for choosing an earlier wave signal is that in the actual measurements the wave probe was downwind of the pressure sensor; the advance is an approximation to the phase correction required by the spatial separation of the sensors. This correction is discussed in some detail in "Data

Analysis and Interpretation", on p. 102 ff.

The pressure signal, if it had spikes in it, was next transferred from FIDDLE to the spike removal subroutine SPKSKP; the S channel of ones was also transferred at this time. The actual mechanics of SPKSKP are somewhat complicated and their discussion is deferred to Appendix 1, in which the effects of spike removal on the pressure spectra is also discussed.

SPKSKP detected the presence of spikes on the basis of rate of change of the pressure signal; information was previously read into a data card on threshold values and number of points to be skipped after the signal drops below the threshold. SPKSKP replaced the pressure data points and the ones in the S channel by zero during spikes. If more than a preset fraction of the data points in a block were replaced by zeros, SPKSKP caused the "defective" block to be ignored in the analysis of "clear" blocks, which may however be separated widely in time, and was used to investigate the effect of the spikes on the pressure spectra: see Appendix 1, p. 178 ff.

Following processing by SPKSKP the pressure signal with spikes removed was averaged and the Fourier transform performed on deviations from this average.

5.1.4c The Sonic Anemometer Signals

The sonic anemometer produced three signals: vertical velocity (w) and two horizontal velocities (A and B). These are related trigonometrically to u and v , the fluctuating components of the wind velocity in directions along and at right angles to \bar{U} , the mean wind

vector for the run (see Experiment, p. 45); the two velocities were used in FIDDLE to compute u and v .

5.1.4d Special Programming in SCOR

The cross-spectra between the pressure and the wave elevations were used as described in the following paragraphs to compute the mean flux of energy \bar{E} and of momentum from the air to the waves via fluctuations in pressure. It is these calculations which were special to this program, and the modification of SCOR which performed them was called SCORF.

The mean flux of energy from the wind to the waves is given by the covariance

$$\bar{E} = \overline{p(t) \frac{\partial \eta(t)}{\partial t}} \quad 5.8.$$

SCORF first computed the spectrum of energy flux $\dot{E}(f)$ and then integrated under this to get \bar{E} . Because the pressure and wave signals were composed almost entirely of noise above 3 Hz (see p.104 of this section) the integration was truncated at this frequency. The computation done in SCORF was

$$\langle \dot{E} \rangle = \sum_{f_i = .05}^{3.0} E(f_i) \Delta f_i = \sum_{.05}^{3.0} 2\pi f_i \text{Qu}_{p, \eta_s}(f_i) \Delta f_i \quad 5.9,$$

where the lower frequency limit of 0.05 Hz is the frequency for which there is one complete cycle in a 1024-point data block; $\langle \dot{E} \rangle$ is the integrated energy flux for one block, Δf_i is the bandwidth of the spectral estimates, and $\text{Qu}_{p, \eta_s}(f_i)$ is the quadrature spectrum of the spike-contaminated pressure and wave signals. The quantities shown in Equation 5.9 were computed separately for each data block. The mean

energy flux \bar{E} over the number of blocks in the run and the standard error in this mean were then computed.

The spectrum at a frequency f_i of the momentum flux from the wind to the waves is given by

$$\tau_w(f_i) = \dot{E}(f_i)/C_i = 2\pi f_i \dot{E}(f_i)/g \quad 5.10,$$

where $C_i = g/2\pi f_i$ is the phase velocity of the wave component of frequency f_i . SCORF computed, for each data block,

$$\langle \tau_w \rangle = 1/g \sum_{.05}^{3.0} 4\pi^2 f_i^2 \text{Qu } \tau_s(f_i) \Delta f_i \quad 5.11;$$

the integral under $\tau_w(f_i)$ was truncated at the same frequencies as the integral under $\dot{E}(f_i)$. As for $\dot{E}(f)$, SCORF computed $\bar{\tau}_w$, the mean of $\langle \tau_w \rangle$ over the blocks, and the standard error in this mean for the run.

5.2 Interpretation of the Spectra

This section contains fairly detailed discussions of the effects on the spectra presented in "Results" of various instrumental shortcomings, and also gives brief accounts of the filtering processes performed on the pressure and wave data prior to and during spectral analysis. The purpose of the section is to describe processes which may introduce significant distortions in the spectra and give wherever possible a quantitative estimate of their effect, so that these spectra may be interpreted objectively.

5.2.1 Distortions Introduced by the Sensors Themselves

5.2.1a The Pitching Action of the Buoy

The forced response of the buoy (which is hinged so that it can

respond to steep, short waves--see Figure 13) to the motions of the water surface is a complex motion which is not easily described analytically. Observations of the movements of the buoy have been made with the aid of slow-motion movies, and these indicate that most of the changes in the angle that the bow of the buoy makes with respect to the instantaneous water surface (this angle is referred to hereafter as the "pitch angle") are associated with oscillations of the front section (bow) of the buoy about its hinge. A resonance in this pitching mode occurs at 2 ± 0.2 Hz. It is thought that the largest distortions of the pressure signal (and to some extent the wave signal) which can be directly attributed to the motion of the buoy are the result of these oscillations.

The pressure signal is affected by the oscillations since the efficiency of the dynamic pressure rejection arrangements varies with the pitch angle of the buoy (see figure 19); positive pitch angles (bow tilted up) produce spurious negative dynamic pressures to appear at the measurement location, so that pitch angle and pressure are 180° out of phase.

Because of the resonance at 2 Hz the effect of the pitching of the buoy varies with frequency. At resonance the pitching will be in phase with the waves; consequently the spurious pressures produced should be in antiphase with the waves and will increase the magnitude of the p, η cospectrum as well as producing a "bump" in the pressure power spectrum. The effect on the wave spectrum should be negligible.

At lower frequencies, the pitch fluctuations of the buoy can be expected to lag the waves by 90° . This case has been mentioned

("Experiment"; p. 70); the expected quadrature pressures generated by such fluctuations are shown in Figure 20. It can be seen that the most important effect is the generation of a large spurious first harmonic of the pressure signal coherent with the first harmonic of the waves. This spurious pressure signal will cause a false observed p, η correlation at twice the fundamental frequency of the waves. It will be largest at $2 f_p$, which is twice the frequency of the peak of the wave spectrum. Because of the phase relation between the natural ("Stokes") first harmonic in the waves and the fundamental, the spurious pressure signal will lead the Stokes' harmonic and its effects will be an apparent shift in the observed phase towards -180° and a decrease in the $\dot{E}(f)$ and $\tau_w(f)$ spectra at $2 f_p$.

It is possible to estimate the size of this effect. The amplitude of the Stokes' first harmonic is $ka^2/2$, where k and a are the wave-number and amplitude of the fundamental; here the fundamental frequency will be taken to be f_p . Run 2a is taken as a "typical" run. For $f_p \simeq 0.6$ Hz, $k_p \simeq 1.4 \times 10^{-2} \text{ cm}^{-1}$ and the wave power spectrum $\Phi_\eta(f)$ at f_p is $40 \text{ cm}^{-2} \text{ Hz}^{-1}$. If these waves occupy a bandwidth of 0.1 Hz they are equivalent to a single sinusoidal wave at 0.6 Hz of amplitude $(2 \times 40 \times 0.1)^{\frac{1}{2}} \simeq 3 \text{ cm}$; therefore $ka^2/2 \simeq 6 \times 10^{-2} \text{ cm}$. The prediction for the contribution to $\Phi_\eta(1.2 \text{ Hz})$ of the Stokes' harmonic is therefore $(6 \times 10^{-2} \text{ cm})^2 / (2 \times 0.1 \text{ Hz}) \simeq 2 \times 10^{-2} \text{ cm}^2 \text{ Hz}^{-1}$. The maximum expected amplitude of the pressure harmonics generated by the pitch fluctuations of the buoy is about 2.5 dyne cm^{-2} ; if a pressure amplitude (for a 3 cm amplitude wave) of 1 dyne cm^{-2} is assumed and if it is further assumed that about one half of this is in quadrature with the Stokes' first

harmonic of the waves, then the contribution to the p, η quadrature spectrum in a 0.1 Hz bandwidth caused by this effect is given by

$$\begin{aligned} \text{Qu}_{p\eta}(f) &= \left\{ \left(2 \times 10^{-2} \frac{\text{cm}^2}{\text{Hz}} \times \frac{1}{2} \frac{\text{dyne}}{\text{cm}^2} \right) / (2 \times 0.1 \text{ Hz}) \right\}^{\frac{1}{2}} \\ &\approx 0.2 \text{ dyne cm}^{-1} \text{ Hz}^{-1}. \end{aligned}$$

The observed size of $\text{Qu}_{p\eta}(f)$ at 1.2 Hz in run 2a is $3 \text{ dyne cm}^{-1} \text{ Hz}^{-1}$; it is therefore expected that the effect of this contamination of the energy and momentum fluxes to the Stokes harmonics by the pitching action of the buoy may be 5 - 10% of the total p, η quadrature spectrum at $2 f_p$. This may show up in the $\text{Qu}_{p\eta}(f)$ as a slight reduction in their magnitudes near $2 f_p$; as mentioned earlier it may also appear as a slight "hump" at $2 f_p$ in the pressure power spectra. Since the magnitude of the quadrature spectra is reduced by the effect, the $\dot{E}(f)$ and $\tau_w(f)$ spectra would also be reduced at $2 f_p$, and this should be looked for in these spectra.

5.2.1b The Finite Size of the Buoy

The second source of contamination of the spectra is caused by the finite size of the buoy. The wavelength of the high-frequency waves becomes comparable with the size of the buoy at frequencies above 1 Hz. At 1.2 Hz the ratio of buoy radius to wavelength is 0.1; it reaches 0.33 at 2 Hz and 1 at 3.7 Hz. As a result, the scales of variations in the wind speed associated with the wave motion are comparable with the buoy, and so the wind speed at the bow of the buoy may differ significantly from that at the pressure port and at the ring downwind of the port. This means that the fraction of the stagnation pressure appearing

at the port due to the air flow over the bow may not be exactly cancelled by the effect of the ring (see "Experiment", p. 66).

If the fluctuations in wind velocity associated with the waves are assumed to be approximately those of the orbital velocities of the water particles at the surface of the waves then their amplitude is kac , where k is wave number, a is wave amplitude, and c wave phase speed. Therefore in a mean wind speed U_0 the stagnation pressure varies along the wave profile (in the x direction) according to

$$p_s \approx \frac{1}{2} \rho_a \cdot 2U_0 kac \sin(kx) \quad 5.12.$$

Some fraction F of p_s appears at the pressure port of the buoy as a suction pressure; in an air flow over the buoy, which is uniform in the x direction, this is cancelled by a positive pressure Fp_d due to the presence of the ring downwind from the port. If a wind is present which varies as $\sin kx$ over the buoy and if d and e are respectively the distances from the ring and the bow to the pressure port, then the pressure at the port is given approximately by

$$\begin{aligned} p_p &\approx p_{\text{ring}} + p_{\text{bow}} \\ &\approx F \rho_a U_0 kac (\sin k(x-d) - \sin k(x+e)) \\ &= F \rho_a U_0 kac (\delta^2 + \gamma^2)^{\frac{1}{2}} \sin(kx - \xi) \end{aligned} \quad 5.13,$$

$$\begin{aligned} \text{where } \delta &= \sin kd + \sin ke \\ \gamma &= \cos kd - \cos ke, \text{ and} \\ \xi &= \tan^{-1} (\delta / \gamma) \end{aligned} \quad 5.14.$$

That gives, for sufficiently small values of k , d , and e

$$p_p = -F \rho_a U_0 k^3 ac (d+e)^2 \cos kx \quad 5.15,$$

indicating that the spurious pressures caused by the buoys failure to completely cancel out the stagnation pressures will be in quadrature with the waves, lagging them by 90° .

Run 2a is chosen to estimate the size of the effect. The estimate will be made at two frequencies: 0.6 Hz, and 2 Hz. For the buoy

$$F \approx 0.1 \text{ (see "Experiment", Figure 16),}$$

$$d \approx 2 \text{ cm, and}$$

$$e \approx 7.5 \text{ cm.}$$

For the run, $U_0 \approx 3 \times 10^2 \text{ cm sec}^{-1}$.

The wave slope ka will be taken to be

$$ka \approx 0.1;$$

$$c = g/\omega \approx 2.6 \times 10^2 \text{ cm sec}^{-1}, \text{ and}$$

$$k = \omega^2/g \approx 1.45 \times 10^{-2} \text{ cm}^{-1}.$$

Taking $d + e \approx 10 \text{ cm}$ gives, from Equation 5.15,

$$p_p = -2.0 \times 10^{-2} \text{ dyne cm}^{-2}.$$

If this is spread over a bandwidth of 0.1 Hz, the resulting power spectral estimate for p_p gives

$$\begin{aligned} \Phi_{p_p}(0.6) &= (2 \times 10^{-2})^2 / (2 \times 0.1) \\ &\approx -2 \times 10^{-3} (\text{dyne cm}^{-2})^2 \text{ Hz}^{-1}. \end{aligned}$$

To find the observed quadrature pressure spectral estimate coherent with the waves, the square of the $p_r \eta$ quadrature spectrum must be divided by the wave spectral estimate at 0.6 Hz:

$$\begin{aligned} \Phi_{p_o}(0.6) &= Qu^2_{p_r \eta}(0.6) / \Phi_{\eta}(0.6) \\ &= (22)^2/40 \\ &\approx 12 (\text{dyne cm}^{-2})^2 \text{ Hz}^{-1}. \end{aligned} \tag{5.16}$$

Since $\Phi_{p_p}(0.6) / \Phi_{p_o}(0.6) < 2 \times 10^{-4}$ the effect of the finite size of the buoy can be neglected at 0.6 Hz.

At 2 Hz neither kd nor ke can be assumed small, and so Equation 5.13 must be used. At 2 Hz, $Qu_{p\eta}(2) \simeq -.04 \text{ dyne cm}^{-1}\text{Hz}^{-1}$, and $\Phi_{\eta}(2) \simeq 0.063 \text{ cm}^2\text{Hz}^{-1}$; using Equation 5.16 this gives

$$\Phi_{p_o}(2) \simeq -2.5 \times 10^{-2} (\text{dyne cm}^{-2})^2 \text{ Hz}^{-1}.$$

Equation 5.13 gives for $\Phi_{p_p}(2)$

$$\Phi_{p_p}(2) \simeq -6.5 \times 10^{-3} (\text{dyne cm}^{-2})^2 \text{ Hz}^{-1}.$$

Thus $\Phi_{p_p}(f)$ is about 30% of $\Phi_{p_o}(f)$ at 2 Hz, which is the upper frequency limit beyond which errors in the measurement of the phase between pressure and waves become large.

Therefore the probable distortions introduced by the finite size of the buoy are small at f_p (the frequency at the peak of the wave spectrum); they increase with frequency and may add as much as 30% to the magnitude of the p, η quadrature spectrum by 2 Hz. Since, however, the waves and hence the pressures coherent with them at this frequency are quite small, it is not expected that the effect will show up in the pressure power spectra. The \dot{E} and τ_w spectra will be affected by the same percentage as $Qu_{p\eta}(f)$, since they are derived from it; they will tend to be too large at high frequencies.

5.2.1c Backscattering

The last source of distortion in the spectra to be dealt with is backscattering of waves from the mast which supports the wave probe, which is 10 cm in diameter. The backscattered waves travel against the

wind and are hence damped by it. The pressure distribution over the incident wave is influenced by that over the reflected wave; the resulting spurious phase shift in the pressure can be in the direction of either damping or added generation (towards -180° or towards -90°) depending on the relative phase of the incident and reflected waves. This relative phase depends on the length λ of the waves being scattered, and hence on their frequency through the dispersion relation

$$f^2 = \frac{gk}{4\pi^2} = \frac{g}{2\pi\lambda} \quad 5.17.$$

The mast which supports the wave probe is a vertical cylinder; the backscattering from such an object can be calculated from potential flow theory (Havelock, 1940). Assuming that the incident and scattered waves are the only waves present and that the incident wave is a plane wave proceeding in the $-x$ direction with the potential

$$\Phi_i = Ae^{i(\omega t + kx)}e^{kz} = \phi_i e^{i\omega t}e^{kz} \quad 5.18$$

where x is the horizontal and z the vertical dimension and the motion is two-dimensional (uniform in the third direction).

The potential for the flow in the presence of a scatterer can then be written

$$\begin{aligned} \Phi &= \Phi_i + \Phi_r \\ &= e^{i\omega t}e^{kz} (\phi_i + \phi_r) \end{aligned} \quad 5.19.$$

In polar cylindrical coordinates ϕ_i can be expanded as an infinite sum of Bessel functions and ϕ_r as an infinite sum of Hankel functions of the second kind. The origin of the coordinate system is taken to be

at the geometric centre of the scatterer. Introducing the boundary condition that the velocities normal to the scatterer must vanish results in an expression for the ratio ϕ_i / ϕ_r in terms of the above-mentioned sums of Bessel and Hankel functions. The wave elevation η is given (to the first order) by

$$\begin{aligned} & \frac{1}{g} \left[\frac{\partial \phi}{\partial t} \right]_{z=0} \\ &= \frac{i\omega}{g} (\phi_i + \phi_r) e^{i\omega t} e^{kz}; \end{aligned}$$

$$\text{therefore } \eta_r / \eta_i = \phi_r / \phi_i \quad 5.20.$$

A computer program written by J. F. Garrett, a fellow student, has been used to compute ϕ_i and ϕ_r in terms of the above-mentioned sums of Bessel and Hankel functions for various values of k , for the particular radius of the mast used and the (fixed) distance from the mast to the wave probe. The Garrett program truncates the sums of Bessel functions at a point where the truncation error becomes negligible. It computes three quantities: $\langle \phi_i \rangle$, $\langle \phi_r \rangle$, and $\langle \phi_r \rangle / \langle \phi_i \rangle$. The quantity $\langle \alpha \rangle$ is

$$\langle \alpha \rangle = \text{Max} \left| \alpha e^{i\tau} \right| \quad \text{for } 0 \leq \tau \leq 2\pi ;$$

thus the $\langle \rangle$ denote "maximum value over a full cycle". $\langle \phi_i \rangle$ and $\langle \phi_r \rangle$ are complex and vary with the wave number k ; the relative phase of the incident and reflected waves can be determined from them. The total amplitude of reflected plus backscattered waves can also be computed and compared with the amplitude of the incident wave. It must however be noted that such calculations assume that the incident and

backscattered waves are coherent. It has been found by Garrett (personal communication) that at the Spanish Banks site in a southeast wind the waves become essentially incoherent at frequencies greater than 1 Hz at downwind wave probe separations of 2 m (2 m is twice the distance from the wave probe to the supporting mast). If the incident and reflected waves are coherent, their total (incident plus reflected) energy must be found by adding them vectorially before squaring; if they are incoherent their total energy is given by the sum of the squares of their amplitudes.

The relative phase of the incident and reflected waves has been calculated at a number of frequencies; the ratio of total to incident energy has also been calculated, on the assumption that incident and reflected waves are coherent at frequencies below 1 Hz and incoherent above 1 Hz.

The energy ratio for coherent waves

$$R_c = (\langle \phi_i \rangle + \langle \phi_r \rangle)^2 / (\langle \phi_i \rangle)^2 \quad 5.21$$

is displayed for frequencies from 0.35 to 1.7 Hz in Table 5.2; the corresponding ratio for incoherent waves

$$R_{ic} = (|\langle \phi_i \rangle|^2 + |\langle \phi_r \rangle|^2) / |\langle \phi_i \rangle|^2 \quad 5.22$$

is displayed in the same table for frequencies from 0.85 to 2.0 Hz.

From the table it is clear that at frequencies near 1 Hz spurious wave energy amounting to as much as 15% of the incident wave energy may be present in the wave spectrum. The effect of the backscattering on the pressure power spectrum cannot be estimated without a knowledge of the pressure distribution over the reflected waves, which are being damped.

TABLE 5.2

Expected Effects of Backscattering on Wave Power Spectrum

f (Hz)	R_c	$100(R_c-1)$ (%)	R_{ic}	$100(R_{ic}-1)$ (%)
<u>Notes:</u>	(1)		(2)	
0.35	.998	0.2	-	-
0.5	.982	2.0	-	-
0.85	1.06	6.0	1.00	0
1.0	9.91	-9.0	1.00	0
1.2	.872	-14.0	1.01	1
1.4	.923	-8.0	1.02	2
1.7	1.4	40.0	1.03	3
2.0	-	-	1.03	3

- Notes: 1. R_c is computed from Equation 5.21; it is the ratio of total to incident energy for coherent incident and reflected waves.
2. R_{ic} is computed from Equation 5.22; it is the corresponding energy ratio for incoherent incident and reflecting waves.

A qualitative estimate of the effect of the backscattering on the cross-spectrum between pressure and waves can be made. As the wave number $k = 2\pi/\lambda$ of the waves changes by 1 m^{-1} , the relative phase θ_{ir} of the incident and reflected waves changes 1 radian (57.3°). The relative phase at any frequency can thus be found if the phase at one frequency is computed from the backscattering formula. The relative phase of incident and reflected waves was calculated and plotted versus wave number to find the wavenumbers where the phase was 0° , 90° , 180° and 270° ; these wavenumbers were then converted to frequencies using the dispersion relation for water waves, given by Equation 5.17. The qualitative effect on $\text{Co}_{pz}(f)$, $\text{Qu}_{pz}(f)$, and Phase $\theta_{pz}(f) = \tan^{-1}(\text{Qu}_{pz}(f)/\text{Co}_{pz}(f))$ of a damped reflected wave is determined at each of the four phase angles mentioned above, assuming that the pressure over the reflected wave leads it by 90° . The results of the determination are displayed in Table 5.3 in conjunction with a tabulation of the frequencies at which each of the phases θ_{ir} occur. A "+" in the Co, Qu and $\theta(f)$ columns means the relevant spectrum is increased by the effect of the backscattering, and a "-" means a decrease (thus, since Co, Qu and $\theta(f)$ are commonly negative, the magnitudes of Co and Qu are increased and the angle of $\theta(f)$ moved towards -180° in the columns where "-" signs occur). A zero means "not affected". The backscattering effect is assumed to be unimportant at frequencies above 1 Hz, since at this frequency incident and reflected waves are assumed to be essentially incoherent.

5.2.2 Distortions Introduced during Preparation and Analysis of Data

5.2.2a Filtering of the Wave Signal

The wave signal is filtered in three ways. First, it is filtered

TABLE 5.3

Expected Effects of Backscattering on Pressure-
Waves Cross Spectrum

f (Hz)	θ_{ir} (Degrees)	Co(f) (dyne cm ⁻¹ Hz ⁻¹)	Qu(f) (dyne cm ⁻¹ Hz ⁻¹)	θ (f) (Degrees)
Notes:		(1)	(1)	(2)
0.22	90	+	0	+
0.52	180	0	+	-
0.69	270	-	0	-
0.82	0	0	-	+
0.94	90	+	0	+
1.02	180	0	+	-
1.12	270	-	0	-
1.20	0	0	-	+
1.38	90	+	0	+

- Notes:
1. A "+" in the Co or Qu columns indicates that positive energy is added to the relevant spectrum by the backscattering.
 2. A "+" in the θ (f) column indicates that the phase angle between pressure and waves is increased by the effect of the backscattering.

by the buoy itself which rides vertically on the wave probe. The exact form of distortion introduced is not known; it is felt that it only becomes significant above the frequency (about 2 Hz) where the wavelength of the waves is comparable with the diameter of the buoy. Because of the physical dimensions of the bearing, errors caused by surging of the water between the bearing and the probe are not expected to exceed 1 mm in observed wave amplitude. Typically the standard deviation of the wave signal for frequencies above a low-frequency cutoff of 2 Hz exceeds 1 mm, so the error caused by the presence of the bearing on the wave probe can almost certainly be neglected at frequencies less than 2 Hz. Second, the wave signal is analog filtered, as mentioned earlier, prior to digitization; in addition a digital filter is applied during analysis by taking an unweighted three point running mean of the sample points. The latter filter is designed principally to reduce high frequency noise when the wave signal is differentiated digitally; it is applied to all the waves signals for the sake of consistency.

The wave power spectrum is thus the convolution of the original wave spectrum with the transfer functions of the above three filters, and of the resulting unsmoothed spectrum with the hanning window as given by Equation 5.1, p. 81.

5.2.2b The Pressure Signals

Since the pressure signals $p_s(t) = p(t)S(t)$, where $S(t)$ is defined by Equation A1.2, Appendix 1, and $p_s(t) + \rho g \eta(t)$, the pressure plus static head, are treated differently in some parts of the analysis, they will be discussed separately.

As mentioned earlier, the "raw" pressure signal recorded at the time of the run is subjected to some filtering and conditioning prior to digitization. During rerecording it is passed through a high-pass filter with a 50-second time constant, which removes DC offsets and slow drifts from the data. During digitization the signal is passed through a linear phase shift low-pass filter with a 3 db point at 6 Hz and a fall-off rate of 12 db per octave.

During digital conditioning prior to Fourier transformation sections of data points where spikes occur are replaced with zero, and any residual mean value is removed from the signal. It should be noted that in run 4, the hand-digitized run, the spikes were removed by hand by drawing smooth curves from the beginning to the end points of the spikes. After the Fourier transformation has been performed the resulting Fourier coefficients are smoothed by a digital filter which is equivalent to hanning the spectra.

The $p_s + p_{a97}$ signal is generated during the digital analysis, after all filtering and averaging on the pressure and wave signals is complete but before the Fourier transform is computed. p_a is computed from

$$p_a = 1.29 \frac{(273)}{\bar{T}} \left(\frac{\bar{P}}{1000} \right) \quad 5.23,$$

where \bar{T} is mean air temperature in degrees Kelvin, and

\bar{P} is mean sea level pressure in millibars.

\bar{T} and \bar{P} are available for most of the runs (see Table 6.1); where they are not reasonable estimates are used.

There are two important sources of error in the computation of

$p_s + \rho g \eta$. First, over the range of frequencies where the size of p_s and $\rho g \eta$ are comparable any calibration errors in p_s and η are proportionately greater in their difference. This error is found to be significant in both the power spectra and the cross spectra. The second source of error (in $p_s + \rho g \eta$) involves the physical separation of the pressure and wave sensors; the latter is 3.8 cm downwind of the former. Because of this the phase of the wave signal must be advanced in time digitally prior to transformation. The digital time shift has the effect of introducing a phase shift in the wave signal which increases linearly with frequency. The phase error which the time shift is meant to correct varies with the ratio of the sensor separation to the wavelength of the waves; this ratio varies as the frequency squared through the dispersion relation for gravity waves. Therefore the time shift will only correct the η phase over a range of frequencies, on either side of which large phase errors in the $p_s + \rho g \eta$ signal may occur.

The possible effects of each of these two sources of error will be discussed in the following paragraphs.

Figure 21 shows the effect on the $p + \rho g \eta$ phasor of a 50% underestimate in the pressure calibration for two situations which commonly occur in the data: $|p| \gg \rho g |\eta|$ (top) and $|p| \approx \rho g |\eta|$ (bottom). In the figure the phasor P is the hypothetical "correct" pressure measured by an ideal sensor at the exact location of the wave probe. P_m is the "correct measured" phasor, i.e. that measured by the actual sensor located about 4 cm upwind of the wave probe, and for which the calibration is correct. P_{mu} is the measured pressure with the underestimated calibration. η_m is the measured wave phasor and η_c is the

wave phasor corrected for the 4 cm sensor separation so that it has the proper phase with P_m . The diagrams show that if $|p| \gg \rho_a g |\eta|$ the amplitude of the $p + \rho_a g \eta$ signal is most strongly affected by the calibration error, while if $|p| \approx \rho_a g |\eta|$ the amplitude of $p + \rho_a g \eta$ is affected little, but the phase error is large.

The full phase correction curve for the pressure sensor, which includes both the effect of the phase response of the sensor (Figure 12) and the full nonlinear effect of the spatial separation of the pressure and wave sensors as discussed on the preceding page, is exhibited in Figure 22. It is this curve which must be approximated by the time shift of the η signal prior to the addition of $\rho_a g \eta$ to the pressure. For this reason the (linear) phase correction curves for an advance of the wave signal in time by one and two samples (at a sampling frequency of 50 Hz the advances are 0.02 and 0.04 seconds) are included in Figure 22.

During analysis, the size of the advance to be used was chosen separately for each run on the basis that the phase correction be as small as possible near the peak in the spectrum of energy flux to the waves.

The effect of the phase errors introduced by approximating the full pressure phase correction curve by a straight line is shown in Figure 23 for four different situations which appear in the results: wave generation (p lags η by 90°) and wave damping (p leads η by an angle of 90° to 180°), for $|p| \gg \rho_a g |\eta|$ and $|p| \approx \rho_a g |\eta|$. On all the diagrams P and P_m are, as for Figure 21, the pressures observed by

ideal (at the wave probe) and actual (3.8 cm upwind of wave probe) sensors respectively. η is the wave phasor corrected using the full pressure phase correction curve and η_a is that corrected using the linear approximation resulting from the simple time advance of the wave signals. It will be seen that at high frequencies the approximate phase correction underestimates the actual one while it overestimates it at low frequencies, as indicated in Figure 22 (at very low frequencies the approximation underestimates the phase correction, but this is not considered here).

The first point to be noticed is that at both high and low frequencies the phase of $p + \rho_a g \eta$ and its amplitude are affected strongly if $|p| \simeq \rho_a g |\eta|$, while neither the amplitude nor the phase of $p + \rho_a g \eta$ are greatly affected if $|p| \gg \rho_a g |\eta|$. The second point to note is that in all cases the effect of the approximation on the phase angle between η_c and $p_m + \rho_a g \eta_c$ (which is the required phase difference) is to underestimate its magnitude.

Since in general in the results $|p| \simeq \rho_a g |\eta|$ at the lower frequencies and $|p| \gg \rho_a g |\eta|$ at the higher frequencies, the overall effect on the signal of the approximation of the proper phase correction by a linear time shift of η is at low frequencies, to cause an overestimation of its power spectrum and an underestimate of any damping or generation which may occur. At high frequencies neither the $p + \rho_a g \eta$ power spectrum nor the phase with respect to η are affected greatly by the approximation.

It should perhaps be noted that the phase angles given by the cross-spectra between p and η and between $p + \rho_a g \eta$ and η differ by the errors

mentioned on the preceding page, since the phase of p is corrected using the full correction curve for the cross-spectrum between p and η . With the application of the full correction curve, the expected accuracy of the p, η phase angles to be presented is $\pm 5^\circ$ from 0.05 to 0.1 Hz, $\pm 1^\circ$ from 0.1 to 1 Hz, and $\pm 5^\circ$ from 1 to 2 Hz (see Experiment, p. 58 ff). The accuracy of the $(p + \rho_{\eta} \eta), \eta$ phases is harder to define, since scatter caused by low coherences is also present. A reasonable estimate of the accuracy also depends on the expected accuracy of the pressure calibrations (these are given in Table 6.3), which vary from run to run. Therefore only a rough estimate can be given: ± 10 to 20° in the frequency range from 0.1 to 1 Hz, and larger outside this range. These estimates do not include the expected effects of the sensors themselves mentioned on p. 88 ff.

5.3 Summary

The data analysis is seen to be fairly straightforward; not so the interpretation of the results in some frequency ranges. The safest course (that chosen in discussing the results) is to treat only circumspectly the frequency ranges 0.05 to 0.1 Hz and 1.0 to 2.0 Hz in all spectra except perhaps $\Phi_{\eta}(f)$, extracting from these "suspect" ranges only corroborative information. If it is necessary to examine the data in these frequency ranges more closely, then the "Interpretation" section should be referred to extensively.

SECTION 6: RESULTS

6.1	Introduction	105
6.2	Method of Presentation	105
6.3	Summary of Runs	106
6.4	The Power Spectra	107
6.5	The Cross-Spectra	113
6.5.1	The Pressure-Waves Cross-Spectra	114
6.5.1a	Coherence	115
6.5.1b	Phase	118
6.5.2	The Fluxes of Energy and Momentum to the Waves .	122
6.5.2a	Summary of Mean Values of \dot{E} and τ_w . .	122
6.5.2b	The Spectra of Energy and Momentum Flux	125
6.5.3	The Spectra of ζ	130

SECTION 6: RESULTS

6.1 Introduction

The principal results of the thesis are presented in this section. They consist of power spectra of wave elevation and normal pressure at the sea surface; they contain information heretofore not available on the processes of wave growth and momentum transfer from the air to the sea.

The measurements from which the above-mentioned spectra have been computed were made under conditions which taxed the design and use of the instrumentation to their limits; they cannot be repeated easily. In order to ensure confidence in the results the data have been analysed in several different ways, and a comparison experiment has been made (called the "Boundary Bay" experiment and discussed in detail in Appendix 2) in which the performance of the buoy pressure sensor was tested against that of other types of pressure sensors. The comparison experiment turned up no serious discrepancies between the results from the buoy sensor and those from the sensors against which it was compared, in the frequency range considered to be of interest in the results to be presented below (0.1 to 2 Hz, as indicated in "Data Analysis and Interpretation", p. 104).

6.2 Method of Presentation

The data will be presented in various ways to bring out different points. First, a summary of the important facts about each of the runs will be given. This will be followed by the power spectra of waves and

pressure. Then the cross spectra will be shown, first as coherence and phase plots of the correlations of pressure versus wave elevation and pressure plus static head $\rho_a g \eta$ versus wave elevation. Finally, the spectra $\dot{E}(f)$ and $\tau_w(f)$ of computed energy and momentum fluxes from the wind to the waves will be presented, along with spectra of the negative damping ratio $\zeta = \dot{E}/\omega E$, defined by Miles (1960) as the fractional increase in wave energy per radian. Where possible the mean momentum flux $\overline{\tau}_w$ found from these computations will be compared with that ($\overline{\tau}_s$) obtained from measured \overline{uw} covariances. Where this is not possible, the mean wind speed will be used to calculate an approximate mean momentum flux from

$$\overline{\tau}_c = \rho_a C_D U_5^2 \quad 6.1$$

where C_D , the drag coefficient, will be taken as 1.2×10^{-3} ; U_5 , the mean wind speed at 5 meters, was measured with cup anemometers.

6.3 Summary of Runs

Most of the accessory information for the six runs is presented in order of increasing wind speed in Tables 6.1, 6.2, and 6.3. The runs cover a range of wind speeds (extrapolated to 5 m height) of 150 - 800 cm sec^{-1} and a range of values of $(U_5 - c_p)$, the difference between wind speed at 5 m and wave phase velocity at the peak of the wave spectrum, of -150 to 535 cm sec^{-1} . At least two and sometimes three cup anemometers were present for the first four runs; during the last two runs a sonic anemometer was used. The accuracy of wind speed extrapolation was not maintained to better than $\pm 5\%$; hence the wind speeds at 5 meters, which are extrapolated from assumed logarithmic profiles, are only meant to be

this accurate. In every case except one (run 1) the winds blew from the S-E quadrant; the variation of fetch with azimuth for this quadrant has been computed by Gilchrist (1965; his Figure 2) and is reproduced in Figure 2. The fetch in the westerly direction was about 40 km. Currents were measured by timing tissue paper floating 1 - 10 cm below the water surface over known distances. In general the observed mean tidal drift current was opposing the wind; this arose from the fact that the buoy only operated successfully in these conditions. If the tidal current was slack or aiding the wind, the small "bow wave" formed by the buoy was continually driven by the wind over its surface to the pressure diaphragm, causing an unacceptable number of spikes in the data.

With one exception (run 5) the air was $0.5 - 1.5^{\circ}\text{C}$ ($\pm 0.4^{\circ}$) cooler than the water at a depth of 5 - 10 cm, indicating unstable or neutrally stable conditions. The runs were taken in the fall of the year at the start of coastal British Columbia's "winter monsoons"--successions of lows reaching the coast from the west and dropping their moisture against the coastal mountains. For this reason skies were overcast for all runs--it was raining lightly during run 6.

6.4 The Power Spectra

Three power spectra are presented for each run in Figures 24 - 31. p_s denotes the pressure measured by the buoy and contaminated by spikes, η the wave height, and $p_s + \rho_a g \eta$ the pressure with $\rho_a g \eta$, the static pressure head caused by the vertical excursions of the buoy, added to it. The latter provides an indication of the spectrum which would be measured by a hypothetical sensor fixed at the mean water level.

All the power spectra have logarithmic (roughly half-octave) band-

TABLE 6.1

Run No.	Time/Date 1967	Length of Run (min.)	Fetch (km)	U_5 (cm sec ⁻¹)	$\bar{\theta}$ (° true)	\bar{U}_w (cm sec ⁻¹)	\bar{T}_a (°C)	\bar{T}_w (°C)	\bar{P} (mb)	Comments
Notes:	(1)			(3)		(4)	(5)	(5)	(6)	
5	1545/XI/17	12.0	1.0	150(s)	135	-	10.2	8.9	1015.2(f)	Tide slack. Water depth 3.0 m.
1	1940/X/16	16.3	40.	220(c)	260	5(SW)	9.8	11.2	1027.6(u)	Tide slack. Water depth 2.4 m. Just after sunset.
2b	2030/X/19	15.5	2.4	310(c)	115	18(E)	9.8	11.2	1023.9(f)	Tide falling. Water depth 2.0 m. Dark.
2a	2010/X/19	11.0	2.4	320(c)	115	18(E)	10.0	11.2	1023.9(f)	Tide falling. Water depth 2.1 m. Dark.
3	1435/X/20	16.8	6.7	340(c)	80	5(W)	10.4	11.0	1010.7(f)	Tide rising. Water depth 2.8 m. T_a rising.
6	1225/XI/23	10.5	1.6	570(s)	120	8(W)	7.8	8.2	1015.9(f)	Tide slack. Fine rain. Water depth 3.4 m.
4b (2)	1200/X/30	3.1	2.4	700(c)	ESE	30(W)	-	-	1020.8(f)	Tide falling. Water depth 2.7 m.
4a	1150/X/30	4.0	2.4	800(c)	ESE	30(W)	-	-	1020.8(f)	Tide falling. Water depth 2.7 m.

TABLE 6.1 (continued)

Notes: 1. Time/Date months in Roman numerals.

2. Run 4 wind speed and water current information from memory; original data destroyed.

3. \overline{U}_5 : (c) following wind speed means "measured with cup anemometers"; three cups were used of which two were considered accurate enough to use their results.

(s) following wind speed means "measured with 3-component sonic anemometer".

4. \overline{U}_w : observed surface drift and tidal current; direction in brackets.

5. \overline{T}_a , \overline{T}_w : mean air and water temperatures, measured to $\pm 0.2^\circ\text{C}$ with a thermistor bead at the recording platform.

6. \overline{P} : pressure at time of run as measured at Vancouver International Airport, corrected to mean sea level; trends are (u) unchanged, (f) falling, and (r) rising.

TABLE 6.2

Run No.	U_5 (cm sec ⁻¹)	c_p (cm sec ⁻¹)	f_k (Hz)	z_{cp} (cm)
Notes:		(1)	(2), (4)	(3), (4)
5	150	332	1.25	$> 10^4$
1	220	370	0.93	$> 10^4$
2b	310	275	0.62	145
2a	320	270	0.58	83
3	340	225	0.54	9.7
6	570	270	0.29	1.2
4b	700	305	0.22	0.7
4a	800	265	0.19	0.2

- Notes:
1. c_p is wave phase velocity at the peak of the locally-generated wave spectrum.
 2. f_k is the frequency at which the phase speed c of the waves is equal to the mean wind speed U_k at $1/k = \lambda / 2\pi$ above the mean water level.
 3. z_{cp} is the Miles' critical height for the peak of the locally-generated wave spectrum: the height were $c_p = U$.
 4. The mean wind speeds used in the calculation of f_c and z_{cp} are extrapolated values from logarithmic profiles with C_D , the drag coefficient, set equal to 0.0012.

TABLE 6.3

Run	Pressure Calibration Used (mv/dyne cm ⁻²)	Estimated Accuracy of Calibration (%)
Notes	(1)	
5	1.32	20
1	4.0	10
2b	4.0	10
2a	4.0	10
3	3.8	10
6	1.67	20
4b	1.75	30
4a	1.75	30

- Notes: 1. All calibrations used (Column 2) were made in the field immediately following the run for which they are used.
2. The same waterproofing diaphragm was used for all the runs; its laboratory calibration is shown in Figure 12, and was 2.4 mv/dyne cm⁻².

widths. The spectra have been smoothed by hanning so that they are not distorted in regions which change less rapidly than f^5 or f^{-5} (the window falls off as δf^{-6}). In addition aliasing has been avoided by analog filtering prior to digitization. For more detailed discussions of these points and those following, see "Data Analysis and Interpretation", pp. 71 ff.

The wave spectra, marked with an " η " in the figures, appear normal for the site; they show high-frequency slopes between -4.5 and -5. One interesting feature is the presence in some of the spectra of two separate "peaks"; these are particularly noticeable in runs 2a, 2b, and 3. The low-frequency peaks occur near 0.2 Hz, indicating a phase speed in deep water of about 8 m sec^{-1} . These "peaks" near 0.2 Hz were almost certainly not locally generated, and were probably caused by marine traffic in the approaches to Vancouver harbour; many freighters were observed passing the experimental site during the period when the runs were made.

The most striking feature of the p_s spectra is the presence of regions of excess pressure energy at frequencies where the wave spectra are large; in runs where the wave spectra show two peaks, the p_s spectra show corresponding "humps" at both frequencies. This is not so in the $p_s + p_{a9\eta}$ spectra; the removal of $-p_{a9\eta}$ has the effect of almost completely eliminating the low-frequency regions of excess pressure energy. The higher-frequency "humps" in the pressure spectra remain, but their center of mass is moved to slightly higher frequencies.

The lowest-frequency parts of the pressure spectra (near $\log(f) = -1$) are the only regions of the entire 0.05 - 2.0 Hz bandwidth covered by the

pressure spectra presented which appear to contain information not directly associated with waves. The small number of low-frequency spectral estimates which are available here suggest that the pressure spectra have a shape near f^{-2} , at variance with the f^{-1} form suggested by similarity considerations (Stewart, R. W.; personal communication). The results of the Boundary Bay experiment indicate that the f^{-2} shape may in fact be spurious, since the low-frequency shapes of the power spectra obtained from the two sensors used in the comparison are closer to f^{-1} than f^{-2} . For this reason the shapes of the pressure spectra shown in Figures 24 - 31 can be assumed to be at best heavily contaminated with noise, and are not discussed further.

From 0.2 Hz to the upper design frequency of the pressure system at 3 Hz the pressure spectra appear to be dominated by the waves. The effect on the spectra of the removal of $-p_{\text{avg}}$ from the pressure signal varies dramatically with frequency. In some of the wave spectra a large peak occurs at 0.2 Hz, presumably caused by swell (see p.111). Corresponding excursions of the pressure spectra above their "base level" are almost completely removed by removing $-p_{\text{avg}}$ from the pressure signal. This indicates that the wave-influenced part of the pressure is largely in antiphase with the waves and at most a small part is in quadrature; hence wave generation or damping must be small at these frequencies (some damping is usually observed at low frequencies; this is described in the section on cross-spectra).

It is worth noting at this point that removal of $-p_{\text{avg}}$ has implications important to the assessment of the accuracy of pressure calibrations during field use of the sensor. Since the sensitivity of the sensor has

been known on other occasions to change by as much as a factor of two during field use, every available check on the value and stability of the sensitivity during each run is made. Removal of -0.9% can at most reduce the pressure spectrum to the level which is independent of waves. It has been noted above that the regions of excess energy in the pressure power spectra caused by swell are substantially reduced by removing -0.9% ; it will be pointed out later that the -0.9% removal has the effect of reducing the pressure-waves coherence at the swell frequencies to low values. This is only possible if the sensitivity of the sensor is quite well-determined. The estimates of pressure sensitivity accuracy given in Table 6.3 are based partly on the above considerations.

At frequencies near and above the locally-generated peak in the wave spectrum the situation is different. After the removal of -0.9% a substantial "hump" usually remains in the pressure spectrum, which is often shifted towards higher frequencies. This indicates that a wave-dominated part of the pressure spectra remains which cannot be in anti-phase with the waves; it follows that at these frequencies wave generation is occurring. Further discussion on this large wave-dominated region of the pressure spectrum is postponed, as it can be more fruitfully studied by referral to the pressure-waves cross-spectra.

The spectra at frequencies above 1.5 Hz must be viewed with caution; a number of experimental and analytical difficulties arise at and above 2 Hz, which are discussed in detail in "Data Interpretation", p. 88 ff.

6.5 The Cross-Spectra

Presented in this section are three sets of spectra. First to be presented are the cross-spectra between pressure and wave elevation.

Second, the spectra $\dot{E}(f)$ and $\tau_w(f)$, which are respectively the energy and momentum fluxes from the wind to the waves, are presented. Last to be described are the spectra $\zeta(f)$, the fractional increase of wave energy per radian (see p. 13). The latter three sets of spectra are derived from the pressure-waves cross-spectra.

6.5.1 The Pressure-Waves Cross-Spectra

For each run three spectra are presented: the coherence and phase spectra between pressure p_s and waves η_s , and the phase spectrum between $p_s + \epsilon_{99}\eta$ and η_s . The subscript "s" means that the spectrum concerned is convolved with the spike function. The reasons for presenting the cross spectra between p_s and η_s rather than that between p_s and η have been outlined in Appendix 1. All the spectra presented are corrected for phase errors introduced by the pressure sensor and for the spatial separation of the pressure and wave sensors, according to the methods described in "Data Interpretation", p. 101 ff.

The cross-spectra are presented in Figures 32 through 39. Shown on each figure are the frequencies f_p of the peak of the wave spectrum and f_k , where the phase velocity c equals the wind speed U_k at the height z where $kz = 1$, so $z = \lambda/2\pi = g/4\pi^2 f^2$. U_k is extrapolated from cup anemometer wind speeds assuming a logarithmic profile and a drag coefficient of .0012 in runs 1, 2, 3, and 4, and from sonic anemometer measurements in runs 5 and 6. Where large deviations in the spectra can be attributed directly to noise, breaks are left in the spectral curves (for example near 1.2 Hz in Figure 32). Two horizontal reference lines are drawn on each figure at phase angles of 180° and -90° . In all cases negative phase angles mean the pressure lags the waves.

6.5.1a Coherence

The coherence between p_s and η_s behaves in a general way as expected, being high at frequencies where appreciable wave energy is present and low elsewhere. The statistical significance of the pressure-waves correlation becomes negligible in practice for the lengths of run considered here when the coherence drops below 0.3. In two cases, runs 4b and 5, the generally regular fall in coherence as the frequency increases above f_p is temporarily arrested, rising to a subsidiary "peak" at about 1.6 Hz and returning to low values by 1.8 Hz.

To avoid cluttered graphs the coherence spectra between $p_s + \rho_a g \eta$ and η_s have been omitted. The general effect of removing $-\rho_a g \eta$ from the pressure signal is to lower the coherences between p_s and η_s at all except the highest frequencies. In some runs there is a low-frequency portion of the total wave energy present which is not the result of local wave generation; this can legitimately be called "swell". The swell is best observed in the phase spectra between p_s and η_s ; in regions where it is present the phase is nearly 180° (if the phase is positive, then wave damping is occurring). It is interesting to compare the effect of removing $-\rho_a g \eta$ from p_s on the low-frequency coherence of the runs where swell appears to be present: runs 1, 2a, 3, and 5. Table 6.4 displays the percentage of the p_s, η_s coherence by which the $(p_s + \rho_a g \eta)$ coherence is decreased at the low frequencies where swell is assumed to be present, and at the frequencies f_p of the wave power spectra arising from locally-generated waves.

Also included are U_5 , $\bar{\theta}$ (mean wind direction), c_1 and c_p , the wave phase speeds at the swell and locally generated spectral peaks respectively

and f_n , the frequency above which the coherences of the two pressure spectra with η_s are the same size to within 5%.

A striking feature of the table is the large percentage coherence drop at the swell peak frequency of run 1. This can be understood by recalling the prediction of the pressure at the water surface given by potential flow theory; this is (Equation 13, Appendix 3):

$$p = -\rho g \eta [1 + (1 - U_0/C)^2] \quad 6.2.$$

If U_0 and C have the same sign the pressure will vary between $-2\rho g \eta (U_0 \ll C)$ and $-\rho g \eta (U_0 \approx C)$ for the low frequency waves; if they are opposite in sign the pressure will vary between $-2\rho g \eta (|U_0| \ll C)$ and $-D\rho g \eta (|U_0| \gg C)$ where $D \gg 2$. This means that if the wind and waves were travelling in the same direction and $|p_s|$ and $\rho g |\eta|$ were about the same size, as was the case in run 1, then the $-\rho g \eta$ removal should drop the coherence to low values.

No information is available on the direction of travel of the low-frequency waves in runs other than run 1; some inferences, however, can be made (see Appendix 3). Thus if the swell were travelling with the wind the coherence would be halved if $U_0 \ll C$ and reduced to a small value if $U_0 \approx C$; if on the other hand the swell were moving against the wind the coherence would again be halved if $|U_0| \ll C$, but would only be reduced by 20% if $|U_0| \approx C$. If the swell was running at some other angle to the wind, then the expected drop in coherence would lie between the extremes of 20% and 100%. From the observed drops in coherence at low frequencies, the swell could have been travelling in almost any direction in run 2a, and was probably from the Northwest in runs 3 and 5. The run 5 prediction is the same as was inferred from the

TABLE 6.4

Coherence Changes Caused by Removal of $\rho_{\alpha\beta}$ in
Pressure-Waves Cross Spectra

Run No.	U_5	c_{ps} (cm sec ⁻¹)	c_{pL}		% drop in swell	% drop at local peak	f_n (Hz)
5	150	340	-	SE	40	no peak	1.2
1	220	350	-	W	80	no peak	1.7
2b	310	-	280	ESE	no peak	25	1.2
2a	320	990	280	ESE	50	40	1.4
3	340	900	220	E	40	65	1.7
6	570	-	275	SE	no peak	50	0.9
4b	700	-	320	ESE	no peak	12	1.2
4a	800	800	270	ESE	no peak	10	1.3

velocity-wave phase relation discussed in Appendix 3.

6.5.1b Phase

The behaviour of the phase spectra is best explained in terms of the energy flux ($\overline{p \partial \eta / \partial t}$) from the wind to the waves. This varies as $\sin(-\theta)$, where θ is the phase lead of the pressure ahead of the wave signal. As has been mentioned earlier, $\theta = -180^\circ$ is predicted by potential flow theory and no generation occurs in this case (except an insignificant amount by the Kelvin-Helmholtz mechanism). The most efficient generation occurs when $\theta = -90^\circ$ (pressure lagging the waves by 90°), and damping occurs if $+90^\circ < \theta < 180^\circ$.

So far little has been said about the relative importance of the phase angles between p_s and η_s , and between $p_s + \rho_a g \eta$ and η_s . The wave surface experiences the former, while a sensor fixed in the air would make an Eulerian measurement of the latter. Theoretical predictions such as those of Miles (1960) are made in terms of the phase differences presented here as the $(p_s + \rho_a g \eta)$, η_s spectra; therefore these will be discussed below as "the phase angle between the pressure and the waves".

The phase spectra (Figures 32 - 39) for all the runs show a similar pattern. At frequencies below f_k (where $C = U$ at $z = \lambda/2\pi$) the phase angles are mainly positive, indicating wave damping. At frequencies near or somewhat lower than f_k the phase crosses 180° , indicating the onset of wave growth. The shift with increasing frequency is usually sudden, the phase changing from 180° to anywhere from -160° to -110° over a frequency range of 0.2 to 0.3 Hz. At higher frequencies it changes more slowly, generally continuing to shift toward -90° and reaching it as often as not. At still higher frequencies in most runs there is a

suggestion, (much clearer in the p_s, η_s phases) that the phase may shift back towards 180° ; it can only be called a suggestion, however, since coherences at the higher frequencies (greater than 1.6 Hz) are so low that the phase is not well-defined. Runs 1, 2b, 3, and 6, which had the most spikes in the pressure data, display larger coherences at these higher frequencies than those with few or no spikes, indicating that in those runs much of the phase information at high frequencies is from the spikes themselves and is hence spurious as far as this discussion is concerned.

The erratic behaviour of the $(p_s + \rho_a g \eta)$, η_s phase spectrum at low frequencies in run 1 (Figure 32) is caused by the fact that from 0.05 to 1 Hz the removal of $-\rho_a g \eta$ has reduced the p_s, η_s coherences well below 0.3. A large noise peak at 1.26 Hz appears to have unfortunately coincided with the frequency at which the crossover from damping to wave growth occurred.

The pressure signal in run 2a (Figure 33) is relatively uncontaminated with spikes, and the pressure calibration is considered as known to within $\pm 10\%$. It is the only run where the high-frequency phase does not show a tendency to drop back towards 180° from -90° . The only other runs which are comparatively free from spikes and in which active generation occurs, so that a comparison can be made with run 2a, are runs 4a and 4b (which were hand-digitized); in these the spikes were smoothed out of the pressure signals by hand prior to digitization. This smoothing process should not affect the high frequencies. Subject to the expected errors noted on p. 79, the high frequency phases in these runs can be compared with those of run 2a. They both indicate a trend of the phase

at high frequencies to return toward 180° . Thus it is run 2a which must be treated as the exception. A large 0.2 Hz swell peak is present in the wave spectrum of this run (Figure 15) which is absent in run 2b taken 20 minutes later. The "swell" was thus probably caused by marine traffic. In this run and in run 2b the sharp phase shift occurs at a frequency 0.3 Hz below f_k ; this is a larger $f_k - f_p$ frequency difference than exists in any of the other runs.

Run 2b shows phase shifts of only 60° from 180° , as opposed to the 90° shifts occurring in run 2a. The wind speed had dropped slightly for this run following run 2a; this might account for the less efficient energy transfers. The frequency of the wave peak has risen slightly, from 0.56 Hz in run 2a to 0.58 Hz in run 2b.

The pressure signal in run 3 is also quite "spikey". In this run U_5 was slightly larger than in runs 2a and b and the fetch longer (see Table 6.1). Swell near 0.2 Hz was present, but as noted on p.116 its direction is not clear. The low-frequency phases (Figure 27) show that it was being damped. The phase "peak" at 0.38 Hz is spurious, being associated with a low coherence between $p_s + \rho_a g \eta$ and η_s . The shift from damping to generation in run 3 occurs at a frequency about 0.2 Hz above the peak of the wave spectrum and almost exactly at f_k . The behaviour of the phase between 1.1 and 1.4 Hz is efficiently masked by noise; the phase at higher frequencies, although considered unreliable, shows a tendency to drift back toward 180° from its maximum shift of 90° (180° to -110°) at 0.8 Hz.

The two hand-digitized runs, 4a and 4b, were separated by 10 minutes, 4b being the later of the two. During them the wind speed was higher than

for any of the other runs. In both cases the frequency of the peak of the wave spectrum is well above f_k , indicating that the waves were far from saturated and that therefore during neither run were wave states stationary. The process of hand digitization is believed to introduce phase errors less than 20° below 1.6 Hz; see the discussion in "Data Analysis and Interpretation", p. 79.

The phase difference between p_s, η_s and $(p_s + \rho_{sg}\eta), \eta_s$ are smaller in runs 4a and 4b than in other runs, indicating that the portion of p_s correlated with the waves was much larger than $\rho_{sg}|\eta|$. The sharp phase change associated with the onset of wave growth occurs at a frequency 0.2 Hz above f_k in run 4a and 0.1 Hz above f_k in run 4b.

In run 4a the phase at frequencies above the frequency of the initial sudden change behaves regularly until 1.3 Hz, when it returns from near -90° to near -180° within 0.1 Hz. This sharp change of phase is associated with a very low coherence, indicating that it is not statistically significant. Roughly the same phase behaviour is observed in run 4b except that the return in phase towards 180° is associated with a large peak in the p, η and $(p + \rho_{sg}\eta), \eta$ coherences near 1.6 Hz. This means that the change has some significance, whereas the wild phase fluctuations at frequencies above 1.6 Hz do not, being associated with low coherences.

The reason for the difference in the coherence spectra above 0.8 Hz in runs 4a and 4b, separated as they are by only ten minutes, must for lack of any other explanation be put down to variability in the conditions of the wind and wave fields. The difference only becomes large at frequencies above 0.8 Hz, and as will be seen later contributes little to the energy and momentum fluxes of either run.

Run 5 must be viewed with a knowledge of its time history. The wind was for the most part weak and variable (about 80 cm/sec) only rising to 150 - 200 cm/sec for the last third of the run. The waves in the frequency band from 0.1 - 0.8 Hz were not locally generated, and as has been shown (Appendix 3) they were travelling against what wind there was. The phase remains positive (+150 to 180°) in most of the frequency range for which the coherence exceeds 0.3; hence this "swell" was being damped. The phase variations above 1 Hz are considered to be random and will not be discussed further.

The pressure signal in run 6 is contaminated by a considerable number of spikes. The wave spectrum for the run is very small, presumably because the fetch (1.6 km) was less than for the other runs. As was noted in Table 6.1, a light rain was falling during the run. The sharp low-frequency phase change occurs at a frequency 0.2 Hz lower than f_k and 0.4 Hz below the frequency of the peak of the wave spectrum. The phase between $p_s + \rho g \eta$ and η_s reaches -90° near f_k and then falls gradually back towards 180°, apparently reaching it at 2 Hz before the coherence drops below 0.4. In general if a smooth curve is drawn through the computed phase points of this run, the scatter about this curve is quite small due to the high coherences present over the entire frequency range from 0.2 to 2 Hz.

6.5.2 The Fluxes of Energy and Momentum to the Waves

6.5.2a Summary of Mean Values of \dot{E} and τ_w

Table 6.5 shows, along with U_5 and $\bar{\Theta}$, the integrals under the \dot{E} and τ_w spectra for all runs. These integrals have been truncated at 3.0 Hz, since any pressure and wave signals which occur above 3 Hz are observed to be incoherent (this truncation is particularly important in the τ_w

spectra, since they contain an ω^2 in their numerator--see p.88). In addition the stresses computed in this way ($\overline{\tau}_w$) are compared with those ($\overline{\tau}_s$) measured by the three-component sonic anemometer, when available, and with those computed from

$$\overline{\tau}_c = 0.0012 \rho_a U_5^2 \quad 6.3.$$

Also shown are drag coefficients C_{DW} calculated from

$$C_{DW} = (\tau_w / \rho_a U_5^2) \quad 6.4.$$

A correction must be applied to the τ_w spectra to account for the finite width of the directional distribution of the waves. The wave probe records waves from all directions; since momentum input to the waves only occurs in the wind direction, the momentum withdrawn from the air by a wave travelling at an angle θ with the wind will vary as $\cos \theta$.

A directional distribution for the waves must be assumed so the correction may be calculated; Gilchrist (1965) finds that in East winds at the Spanish Banks site, one which varies as $\cos^2 \theta$ is close to the observed one for waves at frequencies higher than the spectral peak. Therefore the probability of finding a given wave direction at an angle between θ and $d\theta$ to the wind will be given by

$$P(\theta)d\theta = \frac{2 \cos^2 \theta d\theta}{\pi} \quad 6.5.$$

This gives for the corrected momentum flux spectrum

$$\begin{aligned} \tau_{wc}(f) &= \frac{2}{\pi} \int_{-\pi/2}^{\pi/2} \tau_w(f) P(\theta) \cos \theta d\theta \\ &= \frac{2 \tau_w(f)}{\pi} \int_{-\pi/2}^{\pi/2} \cos^3 \theta d\theta \end{aligned}$$

TABLE 6.5

Run No.	U_5 cm sec ⁻¹	$\bar{\theta}$ degrees (true)	\bar{E} erg cm ⁻² sec ⁻¹	σ_E	$\bar{\tau}_W$ dyne cm ⁻²	σ_τ	τ_c dyne cm ⁻²	τ_s dyne cm ⁻²	C_{DW}
5	150	135	-5	7	-.002	.02	.03	-.03	-
1	220	260	13	17	.11	.11	.07	-	.0018
2b	310	115	29	18	.16	.11	.14	-	.0013
2a	320	80	43	18	.24	.10	.15	-	.0019
3	340	115	30	32	.19	.26	.17	-	.0013
6	570	120	60	32	.38	.22	.48	.46	.00095
4b	700	115	90	233	.45	.30	.76	-	.00075
4a	800	115	154	184	.66	.36	.95	-	.00093
	(1)	(2)	(3)	(4)	(5)	(6)	(7)		

Notes: 1. All units are c.g.s.

2. $\bar{\theta}$ is wind direction in degrees (true).

3. σ_E and σ_τ are the standard error of the means of \bar{E} and $\bar{\tau}$ over the total number of data blocks analysed.

4. $\bar{\tau}_W$ is the mean momentum flux from wind to waves, computed from the ρ, η correlation.

5. τ_c is the momentum flux from the air to the sea, computed from $\tau_c = \rho_a C_D U_5^2$; $C_D = .0012$.

6. τ_s is the momentum flux from the air to the sea, as measured by a sonic anemometer.

7. C_{DW} is the dimensionless drag coefficient computed from $C_{DW} = \bar{\tau}_W / \rho_a U_5^2$.

$$= \frac{8 \tau_w(f)}{3} \approx 0.85 \tau_w(f) \quad 6.6;$$

that is, 15% less than the calculated value. The limits of $\pm \pi/2$ are chosen since in a practical situation the probability of finding wind-driven waves travelling against the wind is negligible. Taking more sophisticated and accurate distributions is not worthwhile in view of the size of the correction and the expected accuracy of $\tau_w(f)$. All the τ_w values except run 5 have been corrected for the assumed directional spectrum of the waves (Equation 6.4). The values of \bar{E} and $\bar{\tau}_w$ were computed for each data block analysed (512 or 1024 samples, or time intervals of 10 or 20 seconds), and the σ columns for \bar{E} and $\bar{\tau}_w$ give the standard error of the mean for these populations.

6.5.2b The Spectra of Energy and Momentum Flux

The spectra of Energy and Momentum flux from wind to water are presented in Figures 40 to 47. They are in units of $\text{dyne cm}^{-1} \text{sec}^{-1} \text{Hz}^{-1}$ ($\dot{E}(f)$) and $\text{dyne cm}^{-2} \text{Hz}^{-1}$ ($\tau_w(f)$). Included on each figure is the wave spectrum for the run. Also noted is f_k , the frequency where the wave phase velocity at the peak of the spectrum equals U_k , the wind speed at a distance $1/k = \lambda / 2\pi$ from the mean water surface. It should be noted that, as on all spectra presented in "Results" the lines joining the spectral estimates are meant to be guides to aid the eye in seeing the spectral shapes; they are not meant to imply interpolation between points. Thus $\dot{E}(f)$ and $\tau_w(f)$, since both are computed from exactly the same data, must cross the zero flux line at the same frequency for a given run; the "guide lines" rarely do cross this line at exactly the same frequency.

Run 1, the only one taken in westerly winds, shows low energy transfers. The wind speed was 220 cm sec^{-1} ; the local wave generation is weak

and has a contribution for unknown reasons at frequencies less than f_k . It is considered unlikely that the apparent energy and momentum transfers at frequencies below 1.2 Hz are real.

Run 2a is considered as roughly typical of a fetch limited, easterly wind situation. Although a large wave peak is present at 0.17 Hz, little or no damping is seen to occur. The peak of the wave spectrum is at a frequency lower than f_k ; in the light of results from other similar runs this may indicate the presence of stronger winds upstream of the measurement site. Energy transfer to lower frequencies through nonlinear interactions, such as those proposed by Benjamin and Feir (1966), Phillips (1961), and Hasselman (1963) is another possibility. The peaks in $\dot{E}(f)$ and $\tau_w(f)$ occur in run 2a at frequencies higher than, but less than twice that of the peak of the wave spectrum. At higher frequencies the spectra approach zero, being governed primarily by the rapid decrease of the wave spectrum; the phase between $p_s + \rho g \eta$ and η in this run (see Figure 33) is near -90° at 1.4 Hz, while $\dot{E}(f)$ and $\tau_w(f)$ have dropped to 15-20% of their peak values by this frequency.

The large low-frequency wave spectral peak is less well-defined in run 2b than it is in run 2a. Damping is seen to occur at one frequency, but this cannot be considered as statistically significant. The peaks in $\dot{E}(f)$ and $\tau_w(f)$ are in this part of the run shifted to lower frequencies than in run 2a; they almost coincide with the peak of the wave spectrum. In fact they peak closer to the wave peak in run 2b than in any other. The wind speed being lower in this part of the run, $\dot{E}(f)$ and $\tau_w(f)$ are somewhat lower than in run 2a, the largest differences occurring between 0.7 and 1.2 Hz. The two subsidiary peaks in the

spectra, at 1.04 and 1.62 Hz, are remarkably close to the first and second harmonics of the frequency at the peak of the wave spectrum. Because of the large variability in the individual spectral estimates $\dot{E}(f)$ and $\tau_w(f)$, the two peaks are not considered statistically significant; if they appeared in the spectra of every run they would have to be taken seriously, but they do not.

In run 3, some wave damping is seen to occur at the low-frequency (0.2 Hz) swell peak in the wave spectrum. Not enough information is present, however, to compute the amount of damping. It has negligible effect on \bar{E} and $\bar{\tau}_w$, the mean total energy and momentum fluxes. The wind-generated wave peak occurs at 0.62 Hz, close to f_k , indicating that the spectrum was still growing. The Miles' critical height (Table 6.2) was 9.7 cm for this run and 100 cm for run 2; this and the fact that the frequency of the peak of the wave spectrum is higher than in run 2 also suggest that it is a "younger" spectrum. $\dot{E}(f)$ at its peak is less than in run 2a but greater than in 2b. Presumably because of the presence of many spikes in the pressure record, the spectra converge to zero more slowly at high frequencies than is the case for run 2. It may be this effect which masks any evidence of the harmonic peaks so evident in run 2b. On the other hand, the pressure signal of that run is just as heavily contaminated with spikes as is that of run 3.

Runs 4a and 4b, the two high wind speed runs ($U_5 = 800$ and 700 cm/sec respectively), show the largest energy and momentum transfers (note the larger scales in Figures 44 and 45). Neither show significant damping at low frequencies, in spite of a small swell peak at 0.2 Hz in run 4a. In both runs the peaks of $\dot{E}(f)$ and $\tau_w(f)$ occur at frequencies

above that of the peak of the wave spectra. As in run 2, they appear to occur on the higher-frequency "rear face" of the wave spectrum; they occur well below the frequency of the first harmonics. In both, however, the spectra level off in the region of the frequency of the first harmonics. The high-frequency region of run 4a is marred by going negative; this is not considered to be real, and is associated with the blowup of the phase spectra discussed on p. 121.

The comparative behaviour of $\dot{E}(f)$ and $\mathcal{T}_w(f)$ in runs 4a and 4b shows some similarities with those of runs 2a and 2b. In both run 2 and in run 4 the wind speed dropped between the two sections of the runs, with the result that the spectra show the largest differences at frequencies just above their peaks; in runs 4a and 4b this is from 0.8 to 1.2 Hz. On the other hand the behaviour of the run 4 spectra at frequencies below their peaks is strikingly different from that observed in run 2; this disparity can be put down to the fact that the waves in run 2 were saturated, while in run 4 the wave spectrum was growing rapidly, the peak advancing from 0.6 Hz in run 4a to 0.5 Hz in 4b. $\dot{E}(f)$ and $\mathcal{T}_w(f)$ advance with it, $\dot{E}(f)$ showing the most spectacular change.

Run 5 was taken as a "noise run"; the wind speed was so low that the water surface was unruffled for two thirds of the run, and the intention was to see what $\dot{E}(f)$ and $\mathcal{T}_w(f)$ would be when physical conditions precluded the possibility of wave generation. It is plotted on the same scale as the others (with the exception of runs 4a and 4b) and gives a good qualitative picture of the resolution of the system. For almost the full frequency band where waves existed damping is indicated. The

"tightness" of $\dot{E}(f)$ and $\tau_w(f)$ at high frequencies, although at first surprising having seen the phase spectrum of the run (Figure 38), is explained by noting the relatively small size of the pressure and wave power spectra (Figure 30) compared with those from, for instance, run 6 (Figure 31). The small positive values of $\dot{E}(f)$ and $\tau_w(f)$ occurring above 0.8 Hz are considered to be noise. Note in Table 6.5 that the stress during run 5 from the sonic anemometer agrees closely with that measured by the buoy.

The most striking feature of run 6 is the small size of the wave spectrum. $\dot{E}(f)$ and $\tau_w(f)$, on the other hand, are far from small. The fetch for this run was short, and large energy and momentum fluxes might well be associated with small waves in such a situation. Since the juxtaposition of large \dot{E} and τ_w spectra with small waves is in this case reasonable, additional credence is lent to the accuracy of the calibration of the wave sensing system, which in the case of run 6 has been carefully scrutinised because of the small observed wave spectrum.

The stress computed from the integral under the spectrum shown is, as for runs 4a and b, somewhat lower (35% here) than that computed from Equation 6.1 or in this case from that measured by the sonic anemometer 1.75 m above the mean water level. The stresses computed from the integral under the $\tau_w(f)$ spectrum from runs 1, 2, and 3, on the other hand, exceed those computed from Equation 6.1. These runs differ most prominently from runs 4 and 6 in the relation of the wave phase velocity c_p at the peak of the spectrum to the mean wind speed U_5 ; $U_5 - c_p$ is near zero for runs 1, 2, and 3 and is much greater than zero for runs 4 and 6.

This evidence suggests that as the wind speed relative to the waves

increases an increasing proportion of the momentum input to the water goes not to the waves but to some other momentum sink, such as currents. Certainly from Table 6.5 the buoy measurements indicate that a dominant fraction of the total wind stress over water goes initially directly into waves. The last paragraph indicates that the fraction decreases as $(U - c)$ increases.

6.5.3 The Spectra of ζ

Miles (1957) defines ζ as the negative damping ratio, or the fractional growth rate in mean wave energy per radian:

$$\zeta = \frac{1}{\omega E} \frac{\partial E}{\partial t} \quad 6.7.$$

Since the wave spectra and \dot{E} spectra are available, spectra of ζ are computed from

$$\zeta(f) = \frac{Q_{\eta\eta}(f)}{\rho_w g \Phi_{\eta}(f)} \quad 6.8$$

where use has been made of Equations 5.3 (p. 82) and 5.9 (p. 87). Two points must be made: first, the presence of spikes and of large drifts in the pressure signal all introduce low-frequency noise in the p_s quadrature spectrum, but there is no corresponding noise in $\Phi_{\eta}(f)$, the power spectrum of the wave signal. This causes large fluctuations in the low-frequency ζ spectra; these are not considered real. Second, as for the other spectra, the ζ spectra above 2 Hz ($\omega > 13$ rad/sec) are almost entirely composed of noise, and are not shown.

Also included on the graphs are ζ spectra calculated from the formula

$$\zeta_{sc} = \frac{\rho_a}{\rho_w} (U_{\lambda}/c - 1) \quad 6.9,$$

where c is the wave phase velocity and U_λ is the mean wind speed at a height one wavelength above the water surface, extrapolated from a logarithmic profile assuming $C_D = .0012$. This formula is an empirical one proposed by Snyder and Cox (1967) which fits their wave growth data and those of Barnett and Wilkerson (1967) moderately well.

The spectra are presented, except for run 5, in Figures 48 to 55. The first thing to note is the similarity of the present results with Snyder and Cox's empirical curves in the frequency range from the onset of active wave generation to $\omega = 10$ rad/sec. The curves, except near where they cross the line of zero energy transfer, are always within a factor of two. They begin to diverge at higher frequencies, the present results falling below those computed from the Snyder and Cox relation. A similar tendency, although not nearly so marked, shows up in the equivalent regions of the spectra shown by Snyder and Cox and Barnett and Wilkerson. In the case of the present data, the falloff is probably explained as the effect on the pressure-waves coherence of interference by the buoy with both signals.

In runs 3 and 4, the data fall below Snyder and Cox's prediction at all frequencies. These runs, from their small critical heights (all < 10 cm), were taken while the wave spectra were still growing; the generation process was not stationary or homogeneous. The fact that the data fall below those of Snyder and Cox, which were taken in a more or less saturated wave field, indicates the possibility that the generation process becomes increasingly efficient (higher \dot{E} for a given \bar{E}) as the wave field approaches saturation.

Run 6 is a special case; it has a low critical height (1.2 cm), but

ζ falls well above ζ_{sc} . In this case the fetch was much less (1.6 km as compared with 6.7 and 2.5 km; see Figure 2) than for the other runs. Also, water depths in the direction from which the wind was blowing shoal as the shore is approached and some fairly steep wooded cliffs 30 meters high shelter the shore, further reducing the effective fetch. Thus, although \dot{E} is large since $U - c$ is large, \bar{E} is relatively small, leading to the high ζ values.

The other runs (1, 2) generally show values of ζ in the region of active generation which exceed ζ_{sc} . This can be expected. Since in these runs the wave spectrum is saturated or even oversaturated ($U_5 < c_p$), they are more closely related to those taken by Snyder and Cox and Barnett and Wilkerson. These investigators measured not energy input at one point as in the present experiment, but wave growth with increasing fetch; their spectra therefore do not include that portion of the energy input which passes from the waves to all other sources via breaking, etc. while the spectrum is being formed.

SECTION 7: DISCUSSION OF RESULTS

7.1	Introduction	133
7.2	Recent Attempts to Explain Wave Generation	133
	7.2.1 Miles (1967)	133
	7.2.2 Stewart (1967)	135
7.3	The Power Spectra	139
7.4	The Phase Spectra	141
7.5	The Energy and Momentum Flux Spectra	144
	7.5.1 The Mean Energy Flux	145
	7.5.2 The Wave-Supported Wind Stress	146
	7.5.3. The Energy and Momentum Flux Spectra	149
	7.5.3a Observed and Predicted Transitions Fetches	150
	7.5.3b Energy Transfer in the Wave Spectrum .	152
7.6	The ζ Spectra	155
	7.6.1 Mean Values of ζ	155
	7.6.2. The Spectra of ζ	156
	7.6.3 A Dimensionless Relation between $\zeta(f)$ and Wind Speed	159

SECTION 7: DISCUSSION OF RESULTS

7.1 Introduction

The results presented in the last section are in very sparse company. In fact they are the only (two-dimensionally) Eulerian pressure measurements made on the surface of naturally generated sea waves; the only comparable measurements are those of Shendim and Hsu (1967), over mechanically generated waves in a wind tunnel (described in "Observations", p. 33 ff.). Whereas the wind tunnel work may in some ways (i.e. in the use of the single sinusoid for a wave) more closely approximate the conditions set out as simplifications in particular idealized models, the present results relate directly to reality, and thus it is hoped, will enable theorists to apply the necessary simplifications to their models to better effect.

7.2 Recent Attempts to Explain Wave Generation

After the works of Snyder and Cox (1966) and Barnett and Wilkerson (1967) appeared and strong doubts in the efficacy of Miles' inviscid model were aroused, alternative mechanisms were considered for getting energy into the waves. For the sake of completeness, those which appear to be relevant to the present results will be discussed in the following paragraphs.

7.2.1 Miles (1967)

Miles (1967) reviews the evidence for and against his inviscid model, and is forced to reconsider the effects on the momentum transfer of wave-induced perturbations of the turbulent Reynolds stress $-\rho_a \overline{u'w'}$.

He suggests that the role of the Reynolds stresses may increase in importance as the time scale of the turbulence increases relative to the time scale of a given spectral component in the wave field. He therefore suggests the use of a dimensionless time-scale parameter

$$\begin{aligned}\Lambda &= \left\{ 1 / \left(\frac{\partial U}{\partial z} \right)_{z_c} \right\} \div 1/kc \\ &= kc / \left(\frac{\partial U}{\partial z} \right)_{z_c} = kKz_c(c/u_*)\end{aligned}\quad 7.1,$$

where the slope of the mean velocity profile is evaluated at the critical height z_c for waves of wavenumber k , $K(\approx 0.4)$ is von Karman's constant, and a logarithmic wind profile is assumed.

Miles then goes on to elucidate the role played by these effects of the turbulence. He reverts to his original (1957) formulation of the equation for the momentum flux from air to waves, this time retaining the terms containing the turbulent Reynolds stresses. All variables are averaged in the crosswind direction. He obtains in this way two terms in the momentum equations; the first consists of the vertical integral of the covariance between the vertical velocity and the vorticity along a flow streamline (corresponding to momentum transfer via the inviscid laminar mechanism), and the second represents the wave-induced perturbations of the Reynolds stress at the sea surface (Phillips, 1966; Equation 4.3.23, is shown by Miles to be equivalent to his formulation of the momentum equations, which is the one under discussion here). The first of these two terms in the momentum equations is linked to the second by an equation for the advection of the vorticity by the perturbation Reynolds stresses. Miles remarks that the finding of

Phillips (1966) that the second term can be neglected is questionable, and suggests that further theoretical progress is barred until more experimental information becomes available on the Reynolds stress distribution at the surface of the water.

7.2.2 Stewart (1967)

Stewart (1967), in a review paper, discusses several nonlinear mechanisms which had not up to that time been mentioned in the literature. The first considers the effects of the turbulence on the momentum transfer via Miles' inviscid laminar mechanism. The amount of momentum transfer by this mechanism is proportional both to the ratio of the curvature to the slope of the wind profile, and to the rms vertical velocity, all evaluated at the critical height z_c where the mean wind speed equals the wave speed. Since both the ratio and the vertical velocity are very nonlinear functions of z_c the turbulence, by causing local variations in z_c , can cause the increases in momentum transfer during wind gusts to greatly exceed the decreases associated with lulls, thus greatly increasing the mean momentum transfer over that which would be computed by assuming a mean z_c which is averaged over many wavelengths.

He proposed that there may be different regimes of generation, depending on the size of the ratio L of the critical height to the rms wave height. This idea is connected with his arguments that the exponential falloff of streamline amplitude with height used by Miles as his model of the airflow is probably unrealistic in the light of observed spectra of turbulent velocities above sea waves, which show no obvious

wave peaks. This leads him to propose that in fact the streamline configuration over the waves may not be as shown in Lighthill (1962) or Phillips (1966; p. 91) but instead, in the coordinate system moving with the phase speed of the waves, the "cats-eye" associated with flow around the critical height may be situated in the troughs instead of over the crests. This configuration requires the presence not only of pressure gradients, but also of shear stress gradients along the wave surface. The stresses must be arranged to produce the given streamline pattern, and are thus low in the troughs and high on the crests. This in turn leads to a distribution of low pressures to leeward and high pressures to windward of the wave crests, which is exactly the distribution which generates waves. If this mechanism is indeed operative, it would not be separable from Miles' inviscid mechanism by measurement of normal pressures alone; the shear stress distribution would have to be measured as well, in regions very close to the water surface. In view of the great difficulties involved in making such measurements, it appears that the existence of this mechanism would be hard to detect.

The distribution of the shearing stress along the wave suggests another mechanism to Stewart. The effects of the stress distribution will be felt by a thin surface layer in the water. If the momentum balance in this layer is considered, it is found that the divergence of the flow in it caused by the stress distribution induces variations in its thickness Δ along the wave profile. These variations in Δ act on the wave as if they were variations $\rho g \Delta$ in the pressure on the wave. With the stress distribution described above this extra pressure lags the waves by 90° , and thus represents generation. Stewart calculates

that the value for the momentum transport associated with the latter mechanism is $ka\tau_0$, where k is wave number, a is wave amplitude, and τ_0 is the amplitude of the shearing stress; it has since been pointed out by Longuet-Higgins (1969a) that this should be $ka\tau_0/2$. This represents a fraction $ka/4$ (≈ 0.05 for typical sea waves) of the total momentum transfer from air to sea; for short wavelength waves with large slopes, this fraction might become considerably larger than the above-mentioned figure of 5%, which is taken as that likely for normally observed slopes in a wind-driven sea.

Stewart then goes on to suggest a final possibility. Momentum can be added selectively to the crests of long waves via the breaking there of steep short-wavelength waves, which would presumably pass their momentum directly to the orbital velocities of the long waves. He notes further that neither this mechanism nor the preceding one depends for its action on normal pressures, and hence neither would be observed by measurements of these pressures.

Observations on wave growth which are considered to have been taken in a regime in some sense similar to that obtaining in the present set of measurements have been reviewed earlier ("Observations", p. 17 ff). As was pointed out, they give conflicting evidence; the field measurements generally show larger discrepancies from Miles' inviscid theory than those in wind tunnels. Miles, as mentioned earlier (p. 134), has suggested that this may be due to the increased effects in the field measurements of the turbulent Reynolds stresses on the momentum transfer, as represented by the largeness of the parameter Λ given by Equation 7.1. (Stewart (1967) has suggested in turn that the type of

momentum transfer regime operating in a given situation may be governed by the size of

$$L = z_c (\overline{\eta^2})^{-\frac{1}{2}} \quad 7.2.$$

Phillips (1966) describes the regimes of wave generation in terms of the ratio c/u_* , wave phase velocity over friction velocity. He concludes that three separate mechanisms are operative for different values of c/u_* ; for $c/u_* < 5$ (although he does not specifically say so) the mechanism must become controlled by viscosity (Miles' viscous laminar model); for $10 < c/u_* < 20$ the inviscid laminar model is operative, while for $c/u_* > 20$ the interaction of the turbulent Reynolds stresses with the air flow over the waves is assumed to be dominant. All of the ratios: Λ , L , and c/u_* , are displayed for the present runs in Table 7.1. All values are taken at the locally-generated peak of the relevant wave spectrum.

From the table, it is clear that Λ and L are dominated by z_c ; they are with the exception of run 6 nearly the same in size. They show moreover that the present measurements cover a large range of values, and thus should provide information on more than one wave generation regime. The range of values of c/u_* suggest that all three regimes: viscous laminar, inviscid laminar, and Reynolds stress-dominated, are likely to be present in the runs. It is interesting that although the range of variation of c_p/u_* (where c_p is the wave phase velocity at the peak of the wave spectrum) is very much less than for Λ and L , the three parameters, which are all derived from wave characteristics at the spectral peak, are all arranged in the same order.

TABLE 7.1

Run No.	U_5	u_* cm/sec	c_p	c_p/u_*	ω_p rad/ sec	z_c cm	$(\overline{\eta^2})^{1/2}$ cm	Λ	L
Notes:		(1)	(2)	(2)	(2)			(3)	(4)
(5) 5	150	5.2	332	(64)	2.95	10^4	3.4	$(\geq 10^3)$	$(\geq 10^3)$
1	220	7.6	370	49	2.65	10^4	4.2	$\geq 10^3$	$\geq 10^3$
2b	310	10.7	275	26	3.57	145	3.8	19	38
2a	320	11.0	270	25	3.63	83	4.3	11	19
3	340	11.7	225	19	4.36	9.7	5.0	1.5	1.9
6	570	19.6	270	13.8	3.63	1.2	2.4	9×10^{-2}	5×10^{-1}
4b	700	24.1	305	12.6	3.21	0.7	4.6	3.7×10^{-2}	1.5×10^{-1}
4a	800	27.6	265	9.6	3.70	0.2	4.8	1.1×10^{-2}	4.2×10^{-2}

Notes: 1. $u_* = (C_D U^2)^{1/2}$ is calculated as $U_5/29$ (i.e. $C_D = .0012$).

2. Subscript "p" means 'evaluated at the peak of the wave spectrum'.

3. $\Lambda = 0.4 \omega_p z_c / u_*$.

4. $L = z_c / (\overline{\eta^2})^{1/2}$.

5. In run 5, the values for c/u_* , Λ , and L may not be realistic, since swell comprises the major part of the wave energy present.

7.3 The Power Spectra

The pressure power spectra are best characterised as rising monotonically with decreasing frequency, with the principal part of the 0.1 - 5 Hz range having a wave-induced "hump". This hump is superimposed on what will be called the "basic" pressure spectrum: that found over sand at Boundary Bay; see Figures 81 and 82. The Boundary Bay spectra were found to scale as well as could be expected (see pp.199 ff) to the best available field results (those of Priestley 1965) and to the wind tunnel results of Willmarth and Wooldridge (1962). The principal uncertainty in the scaling is always the thickness of the atmospheric turbulent boundary layer; while that of the wind tunnel boundary layers is accurately known, there seems to be little satisfactory data besides those obtained from inferences on the thickness of the corresponding atmospheric layer.

The monotonic rise of the pressure spectra as the frequency decreases is in accord with results from many other investigations; it shows up very well, for instance, in the pressure spectra given by Gossard (1960). This fact makes it hard to specify a value for $\overline{p^2}$, the mean square pressure fluctuations, as has been done in the past by Phillips (1957), Longuet-Higgins et al (1963), and Kolesnikov and Efimov (1962).

The power spectra measured using the buoy are very noisy at low frequencies. At these frequencies they are high by factors of 2 - 10 when scaled to the results of Priestley or Willmarth and Wooldridge. For this reason the discussion of this portion of the pressure spectra is not carried beyond the above simple scaling. It is felt that the Boundary Bay results (see Appendix 2), although taken in a different boundary layer, are better representations of the likely form of the

pressure spectrum at frequencies less than about 0.2 Hz.

At higher frequencies, the power spectra are dominated by the effects of the waves, in the sense that it is the wave-induced part of the spectrum which determines their slope. Whereas the Boundary Bay spectra show a more or less continuous slope, the present spectra display a "hump"; it is very tempting to try to integrate under it, assuming the base spectrum to have the slope of a straight line joining the low-frequency portion of the spectrum to the asymptote to the high-frequency "tail". The seemingly high spectral estimates at low frequencies, and the contamination of the pressure signal with spikes at high frequencies (described in Appendix 1) indicate that any such attempt would not prove fruitful.

The principal finding pointed out by the $p + \rho_a g \eta$ spectra is the large part of this pressure which is coherent with the waves. This is to be contrasted with the observations discussed by Stewart (1967), that even at relatively small values of kz (where k is the wave number of the waves and z the anemometer height) spectra of turbulent velocity fluctuations show little or no evidence of the effect of the waves. This might be expected to be the case; the rms velocity fluctuations associated with the wave motion observed by a probe even at relatively small values of kz are of order $ka\sqrt{Uu}$, compared with $\sqrt{u^2}$ for the turbulent fluctuations, the two being about equal in typical conditions. However the pressure fluctuations due to the waves at the same value of kz should be of order $\rho_a ka \overline{(Uu)^2}$ whereas those due to the turbulence are of order $\rho_a u_*^2$, which is at least an order of magnitude smaller. Thus even if the turbulent velocity fluctuations effectively mask those caused by the waves, the wave-induced pressure fluctuations could still exceed those caused

by turbulence.

One further fact should be mentioned. As far as can be determined from the spectra (which with the important exception of run 2a are contaminated by the effects of spikes beyond 2 Hz), they are modified by the effects of the wave generation process at all frequencies above the peak of the locally-generated wave spectrum. In the case of run 2a, for which the influence of spikes can be ignored, the influence of the wave generation process appears to extend to 2 Hz, which is the limit beyond which pressure measurements probably are grossly contaminated with dynamic pressures (see p. 91 ff).

7.4 The Phase Spectra

There are two phase spectra presented: that of pressure versus wave elevation, and that of pressure plus static head $p + \rho g \eta$ versus wave elevation. For comparison with theory the obvious choice is the former, since it is much less prone to error (see the Results section); at the same time the results of Shemdin and Hsu are presented in terms of $p + \rho g \eta$. For this reason both are discussed, bearing in mind the larger errors implicit in the $p + \rho g \eta$ phase results. Table 7.2 displays the comparison, for 0.6 Hz waves for all runs, between measured phases and those predicted from Miles' inviscid laminar model with appropriate assumptions for the wind profile. The p, η phases are computed from Equation 4.1, which is identical with that used by Longuet-Higgins et al (1963), and the $(p + \rho g \eta), \eta$ phases from $\theta_t = \tan^{-1} \beta/\alpha$; α and β are from Miles (1959a, Figures 4 and 5). It is immediately seen that the runs divide themselves into three groups. For the first group

TABLE 7.2

Comparison of Observed Phase Angle of Pressure Relative to
Waves at 0.6 Hz, with That Calculated from
Miles' Inviscid Laminar Model

Run No.	U_5 cm sec ⁻¹	c/u_*	Ω	θ_t degrees p, η	θ_m degrees $(p + \rho g \eta), \eta$	θ_t degrees $(p + \rho g \eta), \eta$	θ_m degrees $(p + \rho g \eta), \eta$
Notes:	(1)	(2)	(3)	(4)	(3)	(4)	(4)
1	220	34	10^{-2}	-180	-172	-179.7	-
2b	310	24	5×10^{-3}	-179.8	-164	-165	-152
2a	320	23	5×10^{-3}	-179.5	-157	-149	-113
3	340	22	4×10^{-3}	-179.3	-174	-145	-152
6	570	13.3	1.5×10^{-3}	-174.5	-131	-156	-111
4b	700	10.8	10^{-3}	-173.5	-156	-163	-146
4a	800	9.4	7.5×10^{-4}	-172.5	-152	-166	-142

Notes: 1. $c = 260 \text{ cm sec}^{-1}$, the phase velocity of a 0.6 Hz wave.

2. $\Omega = gZ_0/U_1^2 = 0.565/U_*^2$, where a logarithmic profile is assumed, $U_1 = 2.5 U_*$, and $Z_0 = 3.6 \times 10^{-3} \text{ cm}$ (equivalent to assuming $C_D = .0012$).

3. θ_t is the phase lead of p relative to η computed from

$$\theta_t = \tan^{-1} \left[\frac{-\beta (U_1/c)^2}{1 - \alpha (U_1/c)^2} \right];$$

see Longuet-Higgins et al (1963), Equation 53.

α and β are obtained from Miles (1959a), Figures 4, 5.

For the phase of $(p - \rho g \eta)$ relative to η , $\theta_t = \tan^{-1} \beta/\alpha$.

4. θ_m is the corrected measured phase angle, and is accurate to $\pm 2^\circ$ for the p, η correlation (see "Data Analysis and Interpretation", p. 104).

$c/u_* > 30$ (in run 1); for the second, $c/u_* \approx 20 - 30$, and for the third, $c/u_* \approx 10$. Run 1 is of particular interest in comparing the present results with those of Longuet-Higgins et al (1963). They show in their Table 4 a comparison of measured versus theoretical phase differences for various values of ω . The peak of their wave spectrum is at $\omega = 0.6$ rad/sec, giving a c/u_* for a 960 cm/sec wind of 50.4. At a frequency of about 0.9 rad/sec, c/u_* for their data is about equal to that of run 1 of the present data at $\omega = 3.8$ rad/sec ($f \approx 0.6$ Hz). For run 1 at this frequency the measured phase is about -172° , and lies within the expected error ($\pm 10^\circ$) of their reported value of 182° . The phase shift predicted by Miles' theory is less than 1° . The highest value of c/u_* at which the present results can be considered reliable is 10; the phase in run 1 at the frequency (2 Hz) where $c/u_* \approx 10$ is -126° , a shift from -180° of $+54^\circ$. At the corresponding frequency at which $c/u_* \approx 10$ in their data, which is 3 rad/sec, their phase shifts are still essentially zero. Thus the two results are not inconsistent at low frequencies ($c/u_* > 20$, say) but differ markedly for the higher frequencies. The differences must be put down to differences in measurement technique or unaccounted-for errors. The presence of dynamic pressures in antiphase with the waves in the pressure signal from their buoy may account for a major part of the difference.

For $20 < c/u_* < 30$ (runs 2 and 3 in Table 7.2) it appears that the inviscid laminar model predicts phase shifts in p which are too small by angles of 5 to 20° . Phillips (1966) proposes that for $c/u_* > 20$ the generation process must be dominated by the interaction of the wavy air flow with the turbulent Reynolds stresses, since at these values of c/u_* the

critical height is high, and so is in a region where the curvature of the mean wind profile is small. The additional phase shifts may be caused either by the turbulent Reynolds stresses or by some other mechanism such as that proposed by Stewart (1967), whereby the momentum transfer to the waves is caused by the balance over a wavelength between horizontal turbulent shear stresses and gradients of normal pressure.

The runs for which $10 < c/u_* < 20$ (4a, 4b, 6) are those in which Miles' inviscid mechanism should dominate. In these runs, the observed phase shifts are about 20 to 40 degrees larger than predicted. Taking into account the phase accuracy of the measurements it is clear that the inviscid laminar model is not the only mechanism generating waves for this range of c/u_* either. It will be seen later (p.159) that observed rates of wave growth exceed those predicted from the theory by factors of five to eight.

Included in Table 7.2 is a comparison between the observed phases of $p_s + \rho_a g \eta$ with respect to η , and the corresponding phases predicted from Miles' inviscid laminar model. This comparison is inserted so that the results from the present experiment may be compared with those of Shemdin and Hsu (1966). (The earlier manuscript report of Shemdin and Hsu is used for this comparison since some results presented in it but not readily available elsewhere have since been referred to in the literature.) Shemdin and Hsu make a comparison of $c/u_1 = 0.4 c/u_*$ versus measured $(p + \rho_a g \eta), \eta$ phase and that computed from Miles' (1957) theory. The values of c/u_* for their study range from 3.0 to 13.5. For $c/u_* \simeq 10$ their measured phase shifts exceed the theoretically predicted ones by $10 - 20^\circ$ in their "best" run (the results from which

are shown in Shemdin and Hsu (1967) in their Table 2) and by 30° in the only other run presented. The phase discrepancies from runs 4a, 4b, and 6 range from 17° to 45° , and are thus not inconsistent with those observed by Shemdin and Hsu in their wind-wave tunnel.

The wind-wave tunnel results for lower values of c/u_* can be compared with the present data at higher wave frequencies. At 1.5 Hz c/u_* ranges from 3.8 to 5.3 in runs 4a, 4b, and 6. The discrepancies between observed and theoretical phase shifts are 8° , 23° , and 17° for the three runs (see Figures 36, 37, and 39); Shemdin and Hsu find discrepancies ranging from 7° in their "best" run to 47° in the other run at $c/u_* = 4.5$.

Because of the large scatter in the present phases and the apparently even larger scatter in those of Shemdin and Hsu, it is not worthwhile pursuing the comparison further. It is evident that in spite of the great differences in the conditions of measurement of the wind-wave tunnel work and the present field work, the measured phases are not inconsistent, both exhibiting significantly larger shifts from -180° (they average 20° in Table 7.2) than those predicted by Miles' (1957, 1959a) theory.

7.5 The Energy and Momentum Flux Spectra

These spectra, shown in Figures 40 to 47, represent one of the major contributions of this thesis. In the following section they will be discussed and compared where possible with other measurements. First to be discussed will be the integrals under the spectra; this will be followed by a consideration of the spectra themselves.

7.5.1 Mean Energy Flux

The values of \bar{E} and $\sigma_{\bar{E}}$, respectively the integrated energy flux to the waves and its standard error of the mean over the run, are shown as functions of mean wind speed in Table 7.3. Also inserted are values obtained by Kolesnikov and Efimov (1962) from their free-floating buoy in conditions of active wave generation. These are marked with a KE in the "Run Number" column. It has already been pointed out (p. 22) that these results are suspect; however they are to the writer's knowledge the only energy flux measurements comparable with those presented here, and so they are included because of their uniqueness.

From the table it can be seen that both sets of results show considerable scatter when compared with wind speed alone. Nonetheless those of Kolesnikov and Efimov are within an order of magnitude of those found in this experiment. Lack of reported wave data in the Russian publication precludes any more objective comparison.

The standard errors of the mean ($\sigma_{\bar{E}}$) for each run are also given in Table 7.3; they represent the expected variability over a given run of the values of \bar{E} obtained for each data block in the run, and are computed from Equation 5.5. It will be immediately seen that the values of $\sigma_{\bar{E}}$ are large; in run 4b $\sigma_{\bar{E}}$ is more than double the value of \bar{E} , while in general it ranges from one-half to about one times \bar{E} .

It should be noted that two runs (4 and 5, for which the ratios $\sigma_{\bar{E}}/\bar{E}$ are largest) showed positive evidence of a lack of stationarity (in the sense that all runs are fetch-limited they all can be considered as spatially inhomogeneous, with the possible exception of run 1). Run 4

was taken in two sections and all spectra for the two runs are significantly different, indicating a development of the wave and wind fields with time. The large scatter from block to block in the energy and momentum flux spectra appears to hide any trends within runs 4a and 4b. Run 5 definitely shows such a trend; the wind speed was observed to increase from start to finish, and to change direction by 20 to 30° in the course of the run.

The distributions of the \dot{E} values about their means have been plotted for each run, and compared using the Chi-squared test against normal distributions with the same means and standard deviations; no statistically significant deviations from the normal distributions were found. No attempt was made to compute higher-order moments, although a visual inspection of the \dot{E} distributions showed no obvious skewness or kurtosis in any of them.

The above findings are taken to mean that the wave generation process, although it causes on the average a positive energy input to the waves, is basically a random process with large scatter. Further, there appears from this data to be no evidence of strong "intermittency" in the sense that all of the energy input occurs at relatively infrequent intervals during which large transfers take place; the generation process should rather be considered as one which is active all the time but which at a given time is either enhanced or diminished by random variations in the relative phase between the pressure and the waves.

7.5.2 The Wave-Supported Wind Stress

One of the most important questions which must be answered about

TABLE 7.3

Comparison of Observed Values of \bar{E} with Those Obtained by
Kolesnikov and Efimov (1962)

Run No.	U_5 cm sec ⁻¹	\bar{E} erg cm ⁻² sec ⁻¹	$\sigma_{\bar{E}}$	$\bar{\tau}_w$ dyne cm ⁻²	$\sigma_{\bar{\tau}}$
Notes:	(1)	(2)	(2)	(2)	(2)
5	150	-5	7	-.002	.02
1	220	13	17	.11	.11
2b	310	29	18	.16	.11
2a	320	43	18	.24	.10
3	340	30	32	.19	.26
KE	500	10			
KE	510	50			
KE	540	60			
6	570	60	32	.38	.22
4b	700	90	233	.45	.30
KE	710	90			
KE	790	130			
4a	800	154	184	.66	.36
KE	1050	350			
KE	1060	310			

- Note: 1. Values of U_5 for Kolesnikov and Efimov (KE in "Run No.") are extrapolated assuming a logarithmic profile with $C_D = .0012$ from given speeds at 2.5 m.
2. \bar{E} and $\bar{\tau}_w$ are the mean integrals under the $\dot{E}(f)$ and $\dot{\tau}_w(f)$ spectra for each run; $\sigma_{\bar{E}}$ and $\sigma_{\bar{\tau}}$ are standard errors of the mean over the number of data blocks done (always > 20).

the wave generation process is, "What fraction of the Reynolds stress $-\rho_a \overline{uw}$ exerted by the wind on the water surface goes directly into waves?". Stewart (1961) considered this question, and by examining wave data measured at known fetches and wind speeds came to the conclusion that a lower limit to the fraction $\overline{\tau_w}/\overline{\tau}$, where $\overline{\tau_w}$ is the mean wave-supported stress and $\overline{\tau} = -\rho_a \overline{uw}$, is about 0.2. He considered this to be a lower limit because the parameter he estimated in determining $\overline{\tau_w}$ was wave momentum present at a given fetch, which because of wave dissipation mechanisms is in fact only a part of the total momentum flux to the waves. His conclusion was that it would be possible for $\overline{\tau_w}/\overline{\tau}$ to be nearly one.

Phillips (1966) estimated $\overline{\tau_w}/\overline{\tau}$ for the waves for which $c > 5u_*$ by computing $\overline{\tau_w}$ from his version of the Miles-Phillips theory (which includes the effects of the interaction of the turbulent Reynolds stresses in the air with the flow over the waves) and by comparing this computed value with $\rho_a u_*^2$. He found that for these longer waves $\overline{\tau_w}/\overline{\tau} \lesssim 0.1$. Since the waves considered by Stewart in his analysis were all such that $c > 5u_*$, Phillips' theoretical finding contradicts Stewart's, which was based on observations. In view of the observations by Snyder and Cox (1966) and Barnett and Wilkerson (1967) which show that observed wave growth rates exceed those predicted by the Miles-Phillips theory by about one order of magnitude, Phillips' result, which was calculated from the predictions of this theory, must be regarded as doubtful.

The average momentum input to the waves has been computed for all the runs. These values for $\overline{\tau_w}$ are shown in Table 6.5; they are redisplayed in Table 7.4 as fractions of $\rho_a C_D U_5^2$, where $C_D = .0012$. Also

shown are values of cp/u_* , and a "wave-drag coefficient" $C_{DW} = \bar{\tau}_w / \rho_a U_5^2$. The mean C_{DW} for the runs is .0014, and all values shown fall within the combined standard deviations of the mean values of C_D quoted by Smith (1967): $.0010 \pm .0003$, and Weiler and Burling (1967): $.0015 \pm .0004$, which were obtained from direct measurements of $-\rho_a \overline{uw}$ at the same site. Thus, although the observed scatter in C_D appears large at first sight, it is not large when compared with other observations. In runs 5 and 6 $-\rho_a \overline{uw}$ was measured with a sonic anemometer, and the observed agreement (see Table 6.5) of the stress measured by the buoy with the sonic anemometer measurements is particularly heartening. It indicates that the values for the stress given by the buoy measurements give as accurate a measure of $\bar{\tau}$ as does the formula $\bar{\tau}_c = .0012 \rho_a U_5^2$. This means that the most direct evidence from which the value of $\bar{\tau}_w / \bar{\tau}$ can be inferred is that of run 6, which indicates that the ratio is about 0.8. The large experimental uncertainties in the buoy measurements, particularly in the pressure sensor calibration, indicate an expected error of $\pm 20\%$ in this figure.

It thus becomes fairly certain that Stewart's estimate that a large fraction of the wind stress over water is supported directly by the waves is substantially correct; the value indicated for the fraction is 0.8. Since this finding disagrees with that of Phillips, it strongly suggests that his theoretical estimate for $\bar{\tau}_w$ is too low by about one order of magnitude, in agreement with the findings of the wave growth measurements of Snyder and Cox, and Barnett and Wilkerson.

The result obtained here for $\bar{\tau}_w / \bar{\tau}$, 0.8, is larger than that (0.1 - 0.4) observed in a recent study by Wu (1968). His measurements

TABLE 7.4

Fraction of the Wind Stress Supported by the Waves

Run No.	c_p/U_5	c_p/u_*	$\bar{\tau}_w/\bar{\tau}_c$	C_{DW}
Notes:	(1)	(2)	(3)	(4)
1	1.7	49	1.6	.0018
2b	0.9	26	1.1	.0013
2a	0.9	25	1.6	.0019
3	0.7	19	1.1	.0013
6	0.5	13.8	0.8	.00095
4b	0.4	12.6	0.6	.00075
4a	0.3	9.6	0.7	.00083
<u>Mean Values</u>			1.1	.0014
<u>Standard Error of Means</u>			0.4	.0005

- Notes: 1. c_p is the wave phase velocity at the locally-generated peak of the wave spectrum.
2. $u_* \approx U_5/29$ ($C_D = .0012$); U_5 is mean air speed at a height of 5 meters.
3. $\bar{\tau}_w$ is the mean stress measured by the buoy system; $\bar{\tau}_c$ is calculated from $\bar{\tau}_c = \rho_a C_D U_5^2$, except in run 6, where $\bar{\tau}_c$ is replaced with the stress $\bar{\tau}_s$ measured by the sonic anemometer.
4. $C_{DW} = \bar{\tau}_w / \rho_a U_5^2$.

were made in a wind-water tunnel over naturally-generated waves, and c_p/u_* in his tunnel never exceeded 7.5, a value somewhat less than the lowest c_p/u_* observed in the present study. Thus it can be assumed that his results apply to a different generation regime. His measured values of $\bar{\tau}_w$ were obtained in two ways, neither of which can give results strictly comparable with those presented here. He first took the difference between drag coefficients measured over waves and over solid surfaces with the same measured roughness length; he also observed the increase in wave momentum with fetch. The latter observation was then used to confirm the validity of the former.

Since the present results are in terms of momentum flux to the waves and not observed momentum increase, and since the c/u_* values are so different, the discrepancy between the two experimental values of $\bar{\tau}_w/\bar{\tau}$ is not considered to be an important one.

It is interesting to note the apparent decrease of $\bar{\tau}_w/\bar{\tau}_c$ with c_p/U_5 in Table 7.4. If this were real it would indicate that the wave generation was becoming more efficient at absorbing the wind stress with increasing c_p/U_5 ; $\bar{\tau}_c$, however, is computed from C_D , which is not known with sufficient accuracy; it may indeed be that variations in C_D cause all of the observed variation in $\bar{\tau}_w/\bar{\tau}_c$!

7.5.3 The Energy and Momentum Flux Spectra

Three frequencies associated with the energy flux spectra will be singled out for comment. These are the frequencies f_p , of the locally-generated maxima in wave spectra; f_E , at the maxima of energy flux spectra; and f_k , the frequency at which the wind speed at a height $1/k$

$= \lambda/2\pi$ equals the wave phase speed. The choice of $\lambda/2\pi$ for the height used to determine f_k is purely arbitrary; it is generally small enough in these measurements so that it is within the height range over which anemometer wind speed measurements are available but not so small that the curvature of the profile is large. In this way inaccuracies in the extrapolation of the wind profile by assuming it to be logarithmic are minimized.

The value of $f_k = \omega_k/2\pi$ is related to u_* if a logarithmic wind profile is assumed (f_k is defined as the frequency at which the phase speed of the wave equals the mean wind speed U_k at a height $1/k = \lambda/2\pi$):

$$U_a - U_k = U_a - g/\omega_k = \frac{u_* \ln \left(\frac{z_a}{z_k} \right)}{K} = \frac{u_*}{K} \ln \left(\frac{z_a \omega_k}{g} \right)^2,$$

where K is Von Karman's constant and the subscript a denotes "at anemometer height", in this case 5 meters. This can be put in the transcendental form

$$f_k^2 \exp(gK/2\pi f_k u_*) = (g/4\pi^2 z_a) \exp(K/\sqrt{C_D}) = \text{constant} \quad 7.3,$$

where $C_D = u_*^2/U_5^2$ is the dimensionless drag coefficient, assumed to be 0.0012. If u_* can as a first approximation be taken as constant for the full fetch over which wave generation is occurring, then f_k will be constant. Since f_p can be expected to decrease with increasing fetch, the ratio f_k/f_p can be expected to increase with fetch. It should also be noted that f_k/f_p is related directly to c_p/u_* through the dispersion relation for the waves and Equation 7.3 above.

7.5.3a Observed and Predicted Transition Fetches

The question of the value of the fetch at which the growth with

time of a given wave component shifts from a linear to an exponential rate of increase is still not satisfactorily answered. There are now many measurements of the frequency of the steep front face of the wave spectrum for given fetches and wind conditions (see, for instance, Barnett and Wilkerson, 1967); these show a great deal of scatter. Almost invariably, however, the observed "transition" fetches are less than those predicted by Miles' inviscid laminar model. Phillips (1966, Figure 4.6) gives a plot of N_T , the theoretically predicted number of wave periods to transition, versus c/u_* ; if N_T is related to the transition fetch through $F_T = c_g N_T / f_f$, where c_g is the group velocity of the waves and f_f the frequency of the front face of the wave spectrum, then the fetches at which the observed spectra have reached transition can be compared with theoretically predicted fetches; this comparison is shown in Table 7.5. The observed transition fetches are less than predicted except in two cases: run 1 and run 3.

Run 1 has a long fetch (40 km), and was taken in light winds. Since no information on conditions upwind of the sensors is available it is not known how homogeneous the wind field really was; for this reason the result is not interpreted as showing significant disagreement with theory.

Run 3, in which the wind direction was 80° (True), has a much larger fetch than runs 2 or 4 in which the wind was from 115° . A large change in fetch with azimuth occurs at about 105° ; see Figure 2. This fact alone makes the comparison with theory difficult; unaccounted-for errors of $\pm 10^\circ$ in wind direction or unnoticed shifts just before the run began could bring the observed and predicted transition fetches into good

TABLE 7.5

Observed and Predicted Transition Fetches

Run No.	f_f Hz	C_f cm/sec	u_* cm/sec	C_f/u_*	N_T	F_T (km)	F_O (km)
Notes:	(1)				(2)	(3)	(4)
1	.3	520	7.6	68.5	6×10^2	5.2	40.
2b	.49	329	10.7	30.8	1×10^3	3.2	2.4
2a	.48	325	11.	29.6	1×10^3	3.4	2.4
3	.6	260	11.7	22.2	2×10^3	4.6	6.7
6	.50	312	19.6	15.9	3×10^3	9.4	1.6
4b	.44	354	24.1	14.7	2×10^3	8.9	2.4
4a	.48	325	27.6	11.8	1×10^3	3.4	2.4

- Notes: 1. The subscript f means "evaluated at the low-frequency face of the locally-generated wave spectrum".
2. N_T is the number of wave periods to transition. It is obtained from Phillips (1966, Figure 4.6).
3. F_T is the theoretically predicted transition fetch, and is given by $F_T = \frac{(N_T c_g)}{f_f}$, where c_g is the group velocity of the waves at the low-frequency face of the wave spectrum.
4. F_O is the observed fetch for the given wind direction; see Table 6.1.

agreement or throw them into greater disagreement. Furthermore all wind-driven wave fields have a fairly broad directional distribution, so that the wave spectra from runs 2 and 4 may be partly made up of energy from waves travelling in directions as much as 30° off that of the wind, and hence over fetches as large as 7 km. These waves may produce a large fraction of the total energy at low frequencies, near the locally-generated spectral peak. This means that the downwind fetch may not be the effective one, and in the present circumstances may be too small in runs 2 and 4. This error would increase the observed transition fetches in runs 2 and 4, bringing them into closer agreement with theory; its effect is, however, at least partially offset by larger theoretical N_T 's in this case. By the same token the predicted transition fetch for run 3 may be too small if the waves at frequencies near the spectral peak were travelling at an angle to the wind. It is considered that the results from run 3 indicate approximate agreement between predicted and observed fetches, while results from run 2 are equivocal, and those from run 4 show significant disagreement.

7.5.3b Energy Transfer in the Wave Spectrum

A glance at the $\dot{E}(f)$ spectra (Figures 40 to 47) shows that in all cases the frequency f_p of the peak of the wind-generated wave spectrum occurs at or substantially below f_E and f_z , the frequency of the peaks of the energy and momentum flux spectra respectively. Two factors besides that of growth via normal pressures can contribute to this. First, if wind speeds had recently dropped or if swell from another source had entered the region, damping of swell at frequencies just below the wave

peak could cause a shift of f_E and f_r to higher frequencies; this effect is thought to be small, since the swell peaks in the wave spectra are generally at frequencies less than $f_p/2$.

The second factor is the presence of some mechanism whereby energy can be transferred to the waves at the peak of the spectrum other than by normal pressures. A number of such mechanisms are available. The first and most obvious is energy transfer from higher frequencies via nonlinear interactions among wave components. One such transfer process, which is probably the most important wave-wave interaction near the peak of the spectrum of a wind-generated wave field, is that of sideband feeding (Benjamin and Feir, 1967), whereby a "classical Stokes wave", being unstable, generates sidebands at lower and higher frequencies. The low-frequency sidebands generate sidebands of their own at still lower frequencies, and thus move the front face of the spectrum to lower frequencies; this process is completely independent of the wind.

As has been pointed out by Stewart (1967), it is also possible for the wind to generate waves without the aid of normal pressures. He suggests two such mechanisms (see pp. 136, 7); both of these have been further considered and enlarged upon recently by Longuet-Higgins (1969a, 1969b). The first mechanism, which is caused by a variation along the wave propagation direction of the Reynolds stress on the water surface, has already been discussed on p. 136. The second is outlined in Longuet-Higgins (1969b). In essence it involves the "sweeping up" by long waves of momentum from shorter waves; because the action of the mechanism is similar to that of a maser, Longuet-Higgins refers to it as a "maser mechanism". The short waves are presumed to grow via normal wind pressures;

these become steep and may break at the convergences on the front faces of the longer waves. Whether they break or not momentum is transferred to the longer waves, but the mechanism is most effective if the short waves actually do break; presumably most energy is transferred to frequencies near the peak of the wave spectrum.

An energy flux spectrum measured by correlating normal pressure with wave vertical velocity would not show this energy transfer at the peak of the wave spectrum, but would have a maximum at a higher frequency. Therefore the integrated energy flux measured in this way would include the energy transfer associated with the "maser" mechanism, provided that the maximum in the energy flux spectrum was not at such a high frequency that it was outside the frequency range of the sensors.

In order for the maser mechanism to be effective, the energy loss of the short waves to the long ones via breaking must exceed their energy gain through the working of the Reynolds stresses of the long waves. For this to occur, Longuet-Higgins shows that the velocity ratio c_s/c_e must be much less than 1, where c_s and c_e are the phase velocities of the short and long waves. Since $c = g/\omega$, their frequency ratio equals c_e/c_s and so must be large.

The observed ratio f_E/f_p is always one or greater, but never exceeds two. In fact the present measurements cease to be accurate above about $4f_p$, and so it might be expected that the energy input in the maser process is from waves with frequencies higher than any measured by this experiment. Two possibilities are open; either the present measurements are a gross underestimate of the energy flux because they cannot measure fluxes to high-frequency waves, or the maser mechanism

is relatively inefficient, and accounts for only a small fraction of the energy flux to the waves. The latter possibility seems more likely, in view of the efficiency of the normal pressures exhibited by the observed large phase shifts of the pressure from -180° towards -90° near f_p , and the fact that the energy and momentum flux spectra do fall to low values at 3-4 times f_E .

7.6 The ζ Spectra

A discussion of the spectra of ζ , the fractional increase in wave energy per radian, will be put off in order to begin the section with a comparison of the mean values of ζ with those predicted by theory. This comparison is given in Table 7.6.

7.6.1 Mean Values of ζ

$\bar{\zeta}_m$, the measured mean values of ζ , are given as $\bar{E}/\omega \bar{E}$; in the present case since the measured \bar{E} and $\bar{E} = \rho_w g \bar{\eta}^2$ are integrated values for the energy flux and wave spectra for a given run, the radian frequency ω_p of the peak of the locally-generated wave spectrum is chosen for ω . The theoretical predictions $\bar{\zeta}_t$ corresponding to $\bar{\zeta}_m$ are computed from Miles (1957, Equation 2.10):

$$\bar{\zeta}_t = \frac{\rho_a}{\rho_w} \left(\frac{U_1}{c_p} \right)^2 \beta_t \quad 7.4;$$

the values of β_t are obtained from Miles (1959a, his Figure 4). Thus whereas \bar{E} and $\bar{\eta}^2$ are integrations under the corresponding spectra, the theoretical predictions are for a single sinusoid at the observed frequency of the peak of the wave spectrum. The comparison may therefore

TABLE 7.6

Comparison of Observed and Predicted Values of

$$\bar{\zeta} = \bar{E} / \omega \bar{E}$$

Run No.	ω_p rad sec ⁻¹	C_p/U_1	Ω	β_t	$\bar{\eta}^2$ cm ²	\bar{E} Erg cm ⁻² sec ⁻¹	$\bar{\zeta}_m$	$\bar{\zeta}_t$
Notes:				(1), (2)			(3)	(3)
1	2.6	19.6	1×10^{-2}	$< 10^{-2}$	18	13	2.8×10^{-4}	2.5×10^{-8}
2b	3.6	10.4	5×10^{-3}	0.25	14	229	5.9×10^{-4}	2.8×10^{-6}
2a	3.6	10.0	5×10^{-3}	0.3	18	43	6.8×10^{-4}	3.0×10^{-6}
3	4.4	7.6	4×10^{-3}	1.9	25	30	2.8×10^{-4}	4.1×10^{-5}
6	3.6	5.5	1.5×10^{-3}	3.2	6	60	2.8×10^{-3}	1.3×10^{-4}
4b	3.2	5.0	1×10^{-3}	3.5	21	90	1.4×10^{-3}	1.7×10^{-4}
4a	3.7	3.8	7.5×10^{-4}	3.6	23	154	1.8×10^{-3}	3.1×10^{-4}

Notes: 1. The subscript "t" refers to values calculated from Miles' inviscid laminar theory; the subscript "m" refers to measured values.

2. β_t is obtained from Miles (1959a, Figure 4).

3. $\bar{\zeta}_m = \bar{E} / e_w g \omega_p \bar{\eta}^2$; $\bar{\zeta}_t = e_a / e_w \left(\frac{U_1}{C_p} \right)^2 \beta_t$.

be unfair; it is made principally because the \dot{E} spectra are sharply peaked quite near ω_p (the choice of ω_p instead of $\omega_E = 2\pi f_E$ is arbitrary; the value of $\bar{\zeta}_t$ is not changed significantly by using one instead of the other); they can in some sense be thought of as representing the spectra from a single sinusoid.

The values of $\bar{\zeta}_m$ and $\bar{\zeta}_t$ and of c_p/U_1 , given for all the runs in Table 7.6, show that the measured integrated values $\bar{\zeta}_m$ exceed the theoretical ones for single sinusoids by factors of 8 - 200 (the average ratio is about 100) except for run 1, for which the factor is 10^4 and which must be considered an exception. The large value of c_p/U_1 for run 1 and the fact that wind conditions were unknown over the long (40 km) fetch indicate first, that any local generation was definitely not caused by Miles' inviscid mechanism and second, that it is probable that the waves present were generated by stronger winds upstream from the measurement site. This second indication is considered highly probable.

Two facts shown by Table 7.6 indicate the presence of a mechanism different from the inviscid laminar model. The first is the large discrepancies between measured and predicted values of $\bar{\zeta}$, and the second is the much smaller range and percentage variation between runs in the measured values as compared with the theoretical ones. The latter phenomenon is as striking as the former; whereas $\bar{\zeta}_t$ varies over the runs by a factor of 100, $\bar{\zeta}_m$ varies by only a factor of 5. There are not enough values to judge the form of the variation of $\bar{\zeta}_m$ with c/U_1 ; it does not appear to be similar to that of $\bar{\zeta}_t$ with c/U_1 .

7.6.2 The ζ Spectra

The ζ spectra themselves, shown in Figures 48-55, display a remark-

able resemblance to curves drawn according to Equation 6.9 (p. 130). This is an empirical relation suggested by Snyder and Cox (SC), which fits their data and those of Barnett and Wilkerson (BW) quite well. The frequency where the SC curve crosses the $\xi = 0$ axis is that at which the wave phase velocity equals the wind velocity at a height of one wavelength; it appears not to be as good an approximation to the "cross-over frequency" of the observed ξ curve as is ω_k , although neither is particularly good. The only part of the observed ξ curves which differs from the SC relation is the high-frequency region, where the observed values fall below the SC predictions. As was mentioned in "Results", there is some evidence of similar high frequency behaviour in the SC and BW data. The falloff in the present data, however, occurs at values of c/u_* always less than 10, while the lowest c/u_* in the SC and BW data is greater than 10. Since their measurements are of wave growth, it could be expected that the high-frequency wave components in their spectra were approaching equilibrium and had therefore ceased to grow; this would explain the falloff of their results at high frequencies. The present measurements, on the other hand, are of energy flux. This means that what should be observed (by an instrument with sufficient resolution at short wavelengths) is the total energy input to the system due to normal pressures; this input will presumably come from different sources in different frequency bands (different ranges of c/u_*); if it is assumed to vary inversely as c/u_* it should increase with frequency up to 13.4 Hz, the frequency at which the waves reach their minimum phase velocity.

If the high-frequency falloff in ξ is to be believed it must be interpreted in some other way. Stewart (personal communication) suggests

that the behaviour of ζ at high frequencies can be explained in terms of a "sheltering" of short-wavelength waves by the longer ones near the peak of the wave spectrum, so that over most of a long wave cycle little energy can be added to the short waves by the wind. The term "sheltering" immediately brings Jeffreys' theory (1925) to mind; the "sheltering" being considered here is not, however, of the type considered by Jeffreys. It is concerned instead with flow reversal in the coordinate system moving with the wave phase velocity c at the critical height where $U = c$. This reversal can be considered as a type of separation, and if the "separation bubble" formed by the flow in this coordinate system lies in the trough of the waves as suggested by Stewart (1967) rather than near the crest as suggested by Phillips (1966; his Figure 4.3), then the short-wavelength waves in the troughs would be in an "eddy" which keeps pace with the long waves for most of the time, and thus could indeed spend a large proportion of their time in regions of the air flow where little energy could be added to them.

Another piece of inferential evidence exists which suggests that the falloff in the observed ζ spectra at high frequencies is real and not an artifact of the measurement system. From the discussion on p. 148, it is clear that the momentum transfer to the waves measured by the buoy is a large fraction of the total wind stress on the water surface. Since the momentum transfer to the waves is calculated from the same information as is ζ , then if the observed falloff in ζ were not real the computed momentum transfers to the waves would be much larger than those given in Table 7.4, and the values of C_{DW} computed from these large momentum transfers would become much greater than those observed by

Smith (1967) and Weiler and Burling (1967). Since these workers measured the total transfer from the air to the sea, it would be difficult to see how the measured momentum input to the waves via normal pressure could be larger.

Since the observed ζ spectra fall below the empirical curve suggested by Snyder and Cox at high frequencies, it may be that their empirical curve overestimates the energy (and momentum) transfer at high frequencies. Snyder and Cox integrated under their curve to compute the momentum transfer to the waves in their experiment; it may therefore be that their anomalously high wave drag coefficient ($C_{DW} \approx .007$) is accounted for by this overestimation of the energy flux.

The ζ spectra predicted by Miles' (1957) inviscid laminar model are also shown in Figures 48-55. They clearly lie far below the observed ζ spectra and those calculated from Snyder and Cox's empirical formula, except at the higher frequencies ($\omega \approx 10$ rad/sec or $f \approx 1.6$ Hz); at the lower frequencies the observed values of ζ exceed those predicted from Miles' inviscid laminar mechanism by factors of 5 to 8. The conclusion to be reached is that at all values of c/u_* (at the peak of the relevant wave spectra the c_p/u_* range covered by the data is $10 < c_p/u_* < 50$) the inviscid laminar model of Miles (1957) is insufficient to account for the observed fluxes of energy and momentum to the waves.

7.6.3 A Dimensionless Relation between $\zeta(f)$ and Wind Speed

At the suggestion of Dr. A. E. Gill a dimensionless plot of $\zeta(f)$ versus U_5/c has been prepared, and is shown in Figure 55. It can immediately be seen that the spectra are fairly well-grouped in the

region $0.5 < U_5/c < 5$; the line drawn through the points is a visual estimate of the "best fit" which has been forced to pass through the value of ρ_a/ρ_w , the density ratio of air to water, at $U_5/c = 0$. It passes through zero at $U_5/c \approx 1.1$, and if a logarithmic profile with a drag coefficient of .0012 is assumed, it is found that $U_5/U_z \approx 1.0$ at a height $z \approx 2$ meters. This suggests that a reasonable formula for computing $\zeta(f)$ might be

$$\zeta(f) \approx \rho_a / \rho_w (U_2/c - 1) \quad 0.5 < U_5/c < 6^* \quad 7.5,$$

where U_2 is the mean wind speed at a height of 2 meters. The equation is not applicable above $U_5/c = 6$; $\zeta(f)$ should probably be set to zero at higher values of U_5/c to avoid the possibility of computing excessive energy and momentum transfers at high frequencies.

It will be noticed that this empirical relation is similar to that of Snyder and Cox (1966). In order to compare the two relations, the calculated Snyder and Cox curves for the runs were put on the dimensionless plot with the measured values of $\zeta(f)$; in general it was found that the Snyder and Cox curves fitted the data as well as relation 7.5 did; differences were small. In fact the only advantage claimed for Equation 7.5 over the Snyder and Cox formula is that it is slightly simpler, since within its range of validity $\zeta(f)$ can be calculated from it without the need of matching a logarithmic profile to a computed wavelength.

The range $0.5 < U_5/c < 6$ translates to $50 < c/u_ < 6$ if a drag coefficient of .0012 is assumed.

SECTION 8: CONCLUSIONS

8.1	Introduction	161
8.2	The Power Spectra	162
8.3	The Cross-Spectra	162
8.4	The Energy and Momentum Flux Spectra	163
8.5	Mean Flux of Energy to the Waves	163
8.6	Mean Flux of Momentum to the Waves	163
8.7	ζ , the Fractional Energy Increase of the Waves per Radian	164
8.8	The Boundary Bay Experiment	165
8.9	Air Flow over Waves Moving into the Wind	166

SECTION 8: CONCLUSIONS

8.1 Introduction

A measurement system consisting of a wave sensor and a buoy in which was mounted a pressure sensor has been designed, built, thoroughly tested, and used to obtain simultaneous recordings of wave height and normal pressure at the water surface in the presence of wind-driven sea waves. Special analysis techniques have been developed for dealing with large spurious spikes in the pressure signal, and it has been shown that these spikes do not materially affect the results in the frequency range of interest, which is between 0.1 and 2 Hz.

The recordings obtained with the measurement system are the first simultaneous field measurements of pressure and waves in which the sensors have been constrained to move only vertically (quasi-Eulerian measurement), and they are the most comprehensive of all the existing measurements. They should thus provide the necessary basis for future predictions of the magnitude and phase (relative to the waves) of the normal pressures which appear to be the principal source of the energy transfer from the wind to the waves.

Power spectra of the pressure and wave height signals and the cross-spectra between them have been presented for six separate runs, which cover a wide range of wind and wave speeds. Energy and momentum flux spectra and the integrals \bar{E} and $\bar{\tau}_w$ under these spectra have been computed and are presented for all the runs. The frequency distributions of ζ , the fractional increase in wave energy per radian, and a dimension-

less plot of $\zeta(f)$ versus U_5/c have been calculated and are also presented.

8.2 The Power Spectra

The wave power spectra behave as expected for the site, exhibiting high-frequency slopes between -4.5 and -5. In some runs a considerable amount of long-wavelength swell was present which was presumably generated by marine traffic in the area.

The pressure power spectra appear to be made up of two parts, consisting of a "basic" spectrum similar to those observed over land, on which is superimposed a wave-induced "hump". Addition of $\rho g \eta$ to the pressure signal has the effect of removing the superimposed hump at low frequencies whereas it has little effect at high frequencies, indicating that at high frequencies most of the pressure signal which is coherent with the waves is in quadrature with them.

8.3 The Cross-Spectra

The phase between the pressure and the waves has been compared with the phase predicted by Miles' (1957) "inviscid laminar" model of wave generation. At frequencies near the locally-generated peaks in the wave spectra, observed phases are shifted from -180° (that is, pressure high over wave troughs) by an amount which exceeds predicted values by 20° ; the estimated error in this measurement is less than $\pm 5^\circ$. This discrepancy occurs over a range $9.5 \leq c_p/u_* \leq 35$, where c_p is the wave phase velocity at the peak of the wave spectrum and u_* is the friction velocity.

8.4 The Energy and Momentum Flux Spectra

Spectra of the fluxes of energy and momentum from the wind to the waves are presented here for the first time. They both are peaked sharply at a frequency at or (usually) slightly higher than f_p , the frequency of the peak of the wave spectrum. The sharply-peaked $\tau_w(f)$ spectrum is contrasted with the rather broad - $\rho_a u w$ spectrum measured at relatively short distances above the waves (Smith, 1967; Weiler and Burling, 1967).

The fact that the peaks of the $\dot{E}(f)$ and $\tau_w(f)$ spectra are at frequencies higher than f_p suggests either that wave-generation mechanisms are active which transfer energy by means other than normal pressures, or that energy is being transferred from higher to lower frequencies in the wave field itself.

8.5 Mean Flux of Energy to the Waves

The integrals under the $\dot{E}(f)$ spectra have been determined at 20-second intervals throughout each run; the \bar{E} values presented are the means of these averages. The individual integrals under the $\dot{E}(f)$ spectra are found with a Chi-squared test to be approximately normally distributed about their means, and are found to have large standard deviations; these facts indicate that the wave generation process is random in nature and varies considerably in time (or space).

8.6 The Mean Flux of Momentum to the Waves

The mean values of τ_w , the wave-supported momentum flux, have been computed for each run and found NOT to be significantly different from the mean fluxes computed from $\rho_a C_D U_5^2$, where C_D , the drag coefficient,

is taken to be .0012. A "wave-drag coefficient" C_{DW} has been computed from the $\bar{\tau}_w$, and is .0014 with standard error .0005. In one measurement the total momentum input to the air-sea boundary $\bar{\tau} = -\rho_a \bar{u}w$ was measured; the ratio $\bar{\tau}_w/\bar{\tau}$ for this case was 0.8. On the basis of these results, it is felt that the assertion made by Phillips (1966) that $\bar{\tau}_w/\bar{\tau} < 0.1$ is probably incorrect.

8.7 ζ , the Fractional Energy Increase of the Waves per Radian

Frequency distributions of measured values of ζ have been prepared and compared with the predictions of Miles' inviscid laminar model and with an empirical curve suggested by Snyder and Cox (1966). The measured values of ζ are greater than those predicted by Miles' theory by factors of between 5 and 8, and are about the same size as those predicted by Snyder and Cox's empirical relation, over most of the frequency range of interest. Thus the present data support the finding of Snyder and Cox that Miles' (1957) inviscid laminar mechanism is inadequate to explain observed rates of wave growth.

At high frequencies the measured values of ζ fall below the Snyder and Cox curve. This indicates that the slow-moving short-wavelength waves in this frequency range are not generated as efficiently as those nearer the peak of the wave spectrum; the possibility therefore exists that shorter waves may be "sheltered" for a large portion of the time by the long waves at the peak of the spectrum. This could happen if, as suggested by Stewart (1967), the flow distribution over the waves is such that the "cats-eye" flow distribution (in the coordinate system moving with the wave phase speed) which was first described by Lighthill

(1962) is situated in the wave trough.

A dimensionless plot of $\zeta(f)$ versus U_5/c_p has been presented; the observed values of $\zeta(f)$, although somewhat scattered for $U_5/c > 4$, are approximated quite well by

$$\zeta(f) = \rho_a / \rho_w (U_2/c - 1),$$

where U_2 is the wind speed at a height of two meters. This simple relation fits the data as well as the Snyder and Cox curve does over the range $0.5 < U_5/c < 6$; for $U_5/c > 6$ it does not apply, since at these values of U_5/c the measured values of $\zeta(f)$ may fall rapidly towards zero. The falloff in $\zeta(f)$ at high frequencies, if it is real, must be taken into account in any computation of integrated fluxes of energy or momentum to the waves.

8.8 The Boundary Bay Experiment

This experiment was first conceived as a field test of the buoy sensor and a sensor developed by J. A. Elliott of the Institute, against a standard sensor. The test, which was made on a gently-sloping sand flat, indicated that all three instruments produced results which were essentially indistinguishable over the frequency range of interest in the pressure-waves experiment (0.1 to 2 Hz).

Besides this result the experiment provided some interesting information on the structure of the pressure field in the turbulent atmospheric boundary layer. These results are listed below.

1. The pressure power spectra obtained show reasonably good agreement with other measurements, both in the field (Priestley, 1965) and

in a wind tunnel (Willmarth and Wooldridge, 1962).

2. The pressure power spectra have been found to group well when non-dimensionalized with $(\rho_a u_*^2)^2$ for radian wave-numbers greater than 10^{-2} cm^{-1} ; this indicates the existence of a relationship between the pressure and the Reynolds stress $\tau = \rho_a u_*^2$ in the boundary layer.

3. The vertical "scale size" of the pressure-generating eddies is about one-half, and the crosswind scale size is about one-tenth, of their downwind scale size. The latter result agrees roughly with the more detailed findings of Priestley (1965).

4. The broadband advection velocity of the pressure-generating eddies is about $0.6 U_\infty$, where U_∞ is taken to be $30 u_*$.

5. At high frequencies (2-5 Hz) the pressure in the air shows a large phase lead (90 to 180°) over the downwind air speed at the same elevation.

6. There is some evidence that low-frequency (0.05 - 2 Hz) vertical accelerations exist in the shear flow near the ground; this is based on the apparent presence of a vertical gradient of the part of the pressure coherent with the downwind air speed.

8.9 Air Flow over Waves Moving into the Wind

A fairly detailed study has been made of the phase relations between wave elevation, surface pressure, and downwind and vertical air velocity over a group of waves of four-second period which were traveling against a light wind. The air flow over the wave group was found to be approximately given by potential flow theory; the observed differ-

ences, although small, are important. The phase of the pressure was $+165^\circ$ relative to the waves instead of 180° , and the phase of the wind velocity along the waves was $+12^\circ$ instead of 0° ; the phase of the vertical velocity was 90° , as predicted. The energy flux from the waves to the wind was computed and found to be $20 \text{ erg cm}^{-2} \text{ sec}^{-1}$, which represents a Q for the waves of about 4000. The momentum flux from waves to wind has also been computed and found to be $0.04 \text{ dyne cm}^{-2}$; the total momentum flux from water to air was simultaneously measured at a height of 1.75 meters with a sonic anemometer, and was $0.002 \text{ dyne cm}^{-2}$. This may indicate the presence of a vertical stress gradient of magnitude $-2 \times 10^{-4} \text{ dyne cm}^{-2}/\text{cm}$. The observed perturbations from potential flow are much smaller than those which would be extrapolated from the predictions of Phillips (1966); however it is considered that the flow regime over the waves in this case was quite different from the case considered by Phillips.

APPENDIX 1: SPIKE REMOVAL

A1.1	Introduction	168
A1.2	The Spike Removal Process	169
A1.3	Definitions	171
A1.4	The Effects of a Regular Spike Window	175
A1.5	The Effect of the Spikes on the Power Spectra	177
A1.6	The Effect of the Spikes on the Phase Spectra	178
A1.7	The Effect of the Spikes on the Energy Flux Spectra	180
A1.8	Conclusions	182

APPENDIX 1: SPIKE REMOVAL

A1.1 Introduction

This appendix deals with the analysis problems introduced by the presence in the pressure signal of large, spurious "spikes". These spikes occur in the data whenever water washes over the pressure-sensing diaphragm at the surface of the buoy. They are characterised by generally large amplitudes and a rise-time much faster than that of the normal turbulent pressure fluctuations; their amplitude is often large enough to saturate the recording system. Their effects on the signal last for periods of 0.1 - 2 seconds. Their occurrence in time cannot be said to be fully random, since they are caused by the motion of the buoy on the waves; they occur most often at or near the crests of the large waves and also on some of the small, steep waves.

Thus the pressure signal which is analysed must be a modified one; in the actual analysis its mean value is set to zero, so wherever a spike occurs in the original pressure signal and is removed, the digitized data values are replaced with zeros for the duration of the spike. This modified pressure signal is written

$$p_s(t) = p(t) \cdot S(t) \quad \text{A1.1,}$$

where $p_s(t)$ is the observed pressure signal from which the spikes have been removed, $p(t)$ is the signal which would be observed in the absence of spikes, and $S(t)$ is a "Spike function" defined by

$$\begin{aligned} S(t) &= 0 && \text{during a spike} \\ &= 1 && \text{at all other times} \end{aligned} \quad \text{A1.2.}$$

Equation A1.1 cannot be inverted to recover $p(t)$; that is to say the pressure information lost during a spike is irretrievable. This represents a fundamental limitation in the interpretation of the pressure data. This section therefore will be devoted to exploring the effects of the spikes, in the hope of gaining an understanding of the spike-induced distortions of the observed pressure spectra.

The first section of this appendix will deal with a fairly detailed account of the inner workings of the spike removal process. This will be followed by a section giving some definitions and derivations. Three different analyses follow; the first is a cross-spectral analysis of computer-generated sine waves in which artificial spikes have been inserted. The next is a comparison of the power spectra of wave signals obtained in the field with power spectra of the same signals in which holes have been inserted at times when spikes occur in the pressure signals which were measured at the same time. Lastly, phase and quadrature spectra between modified pressure and modified wave signals from complete runs made in the field are compared with phase and quadrature spectra between unmodified pressure and unmodified wave signals from scattered data blocks in the same runs, in which no pressure spikes occurred.

A1.2 The Spike Removal Process

A brief outline of the functions of the spike removal subroutine SPKSKP has been given in "Data Analysis and Interpretation", p. 86. This outline will be enlarged upon in the following paragraphs.

The detection of spurious data by the routine is on the basis of

slope; if the absolute magnitude of the pressure difference between successive data points is larger than a threshold value (DIFMAX) which must be determined separately for each run, then SPKSKP will automatically zero a preset number (NSKIP) of the data points succeeding the point at which the spike is first detected. Before these points are zeroed they are checked against the maximum pressure value (VALMAX) which is likely to occur; at the same time the difference between each point to be zeroed and its succeeding point is checked against DIFMAX. If either limit is exceeded, SPKSKP restarts the zeroing procedure and skips a further NSKIP points beyond the newly detected spike. If NSKIP successive points beyond a "spike" pass both criteria they are all zeroed; the $(NSKIP + 1)^{st}$ and following points pass unmodified unless a new spike is detected. The checking continues until the end of a given data block is reached. SPKSKP is called once for every data block analysed, and accepts two data arrays: $p_o(t)$, the observed pressure data, and $S(t)$, an array in which all data values are set initially to one. It sets both $p_o(t)$ and $S(t)$ to zero for at least $(NSKIP + 1)$ successive values during spikes. SPKSKP returns $p_o(t)$, the pressure with spikes removed, and $S(t)$, the "Spike" function" of Equation A1.2.

The computer program (FORTRAN IV) for SPKSKP is reproduced in Appendix 1a. In the Fortran program there is included an option not mentioned here because it is not used in the final analysis whereby the spikes, instead of being replaced by zeroes, can be replaced by a straight line interpolated between their beginning and end data points.

SPKSKP returns to the main program via one of two routes. If during the zeroing procedure the number of data points zeroed in one block

exceeds a preset number of points (JFRAC; usually set to one-half the number of data points in the block), the main program is instructed to ignore the block being analysed and start on the next one. During the normal return process SPKSKP prints out the total number of data points skipped and then delivers $p_s(t)$ and $S(t)$ to the digital preconditioning program FIDDLE. There the pressure signal has any residual mean (over each block) removed from it and is returned to the main program for Fourier analysis.

A1.3 Definitions

In order to make the following accounts clearer some basic definitions are given first. It is hoped that their inclusion will eliminate uncertainties as to the location of factors of π , 2, etc.

We wish to perform a spectral analysis on a signal $v(t)$, which begins at time $t = 0$ and extends to $t = T$. This signal is sampled at fixed intervals of time

$$t_j = j\Delta t, \quad j = 0, 1, 2, \dots, T/\Delta t \quad \text{A1.3,}$$

where Δt is the sampling interval, and is the reciprocal of the sampling frequency f_s ($v(t)$ is arranged to contain no significant energy at frequencies exceeding $f_s/2$). The resulting collection of data points $v(t_j)$ is then divided into equal time intervals τ , where

$$N \Delta t = \tau \ll T \quad \text{A1.4.}$$

These sets of $N \Delta t$ data points are hereafter called "blocks".

The spectral analysis technique used in the present work is one developed by Cooley and Tukey (1965), and commonly referred to as the

"Fast Fourier Transform" (the name of the actual computer program is PKFORT). This program is used to produce for each block of data points the set of coefficients of the discrete Fourier series which exactly describes the sampled (discrete) signal within that block. These coefficients are complex, and occur at frequencies separated by intervals

$$\Delta f = 1/\tau \quad \text{A1.5}$$

and extending from $f = 0$ to $f_s/2$, the folding or Nyquist frequency. The real part of the Fourier coefficient at $f = 0$ is the mean value of the data points in the block. From these Fourier coefficients power or cross-spectral estimates at each frequency are determined. This analysis is repeated for each complete block of data points in the run; the final power or cross-spectral estimates for a complete run are the averages over the number of blocks in the run.

The Fast Fourier Transform program thus accepts an array $v(t_j)$ of data points and replaces them with an array of complex Fourier coefficients $A(f_k)$ where $f_k = k\Delta f$ is the frequency of the k^{th} harmonic of the signal within the block.

$$A(f_k) = \frac{1}{N} \sum_{j=0}^{N-1} v(t_j) \exp(-2\pi i j k / N) \quad \text{A1.6;}$$

where N is the number of data points in the block and $i = \sqrt{-1}$. Putting $f_k = \omega_k / 2\pi = k/N \Delta t$ and using A1.3 and A1.4,

$$A(f_k) = \frac{1}{\tau} \sum_{j=0}^{N-1} v(t_j) e^{-i \omega_k t_j \Delta t} \quad \text{A1.7.}$$

$$A(f_k) = B(f_k) + i C(f_k) \quad \text{A1.8}$$

is complex; it contains amplitude and phase information on the Fourier harmonic at the frequency f_k .

In the spectral analysis program SCOR (see "Data Analysis and Interpretation", p. 82) estimates of (power) spectral densities

$$\Phi_e(f_k) = \frac{|A(f_k)|^2}{2 \Delta f} = \frac{\tau}{2} \left[B(f_k)^2 + C(f_k)^2 \right] \quad A1.9$$

are computed at each frequency for each block. The final estimate of the power spectrum for a run consists of a single set of $\Phi_e(f_k)$, in which the estimate at each frequency is averaged over the total number of complete blocks in the run.

Since the block and run durations are finite the $\Phi_e(f_k)$ are estimates of some kind of "ensemble" averages $\Phi(f_k)$. The $\Phi(f_k)$ would arise from the average over several realizations of $v(t)$ which derive from the same set of physical conditions; that is to say if the $v(t)$ measurement were begun on several occasions at identical time intervals following the onset of the (identical) causal processes, then certain parameters such as the variance of $v(t)$, its estimated power spectrum $\Phi_e(f_k)$ (and $v(t)$ itself) should each be statistically distributed in the same fashion for each realization of $v(t)$. We seek to find "good estimates" of these parameters or of their distributions.

The analysis of $v(t_j)$ in a series of blocks is equivalent to multiplying $v(t)$ by the "data window"

$$\begin{aligned} D(t) &= 1 & 0 \leq t \leq \tau \\ &= 0 & \text{otherwise} \end{aligned} \quad A1.10$$

This is equivalent to convolving $\Phi_e(f)$ with the "spectral window"

$$\Phi_{D(f)} = \tau \frac{\sin^2(2\pi f\tau/2)}{(2\pi f\tau/2)^2} \quad A1.11;$$

this is exactly the "rectangular lag window" discussed in Blackman and Tukey (1959; pp. 68-70).

The modified (spike-contaminated) pressure signal $p_s(t) = p(t)S(t)$ is the only one available with which to form a cross-spectrum with the wave signal $\eta(t)$. The question arises: should it be $\eta(t)$ or $\eta_s(t) = \eta(t)S(t)$ which is used to obtain the cross-spectrum?

The Fourier transforms $FT_{p_s}(f)$ and $FT_{\eta_s}(f)$ of $p_s(t)$ and $\eta_s(t)$ are convolutions:

$$\begin{aligned} FT_{p_s}(f) &= FT_p(f) * FT_S(f) \text{ and} \\ FT_{\eta_s}(f) &= FT_{\eta}(f) * FT_S(f) \end{aligned} \quad A1.12,$$

where $FT_S(f)$ is the "Fourier transform window" of $S(f)$. At a given frequency, the phase spectrum $\theta_{p_s \eta_s}(f)$ is given by the difference of the arc tangents of the ratios of imaginary to real parts of $FT_{p_s}(f)$ and $FT_{\eta_s}(f)$. Because $FT_p(f)$ (which is in practice not available) and $FT_{\eta}(f)$ have both been convolved with the same transform window, the ratios of imaginary to real parts of $FT_p(f)$ and $FT_{\eta}(f)$ are both modified in the same way by the convolution and therefore $\theta_{p_s \eta_s}(f)$ is to a first approximation the same as $\theta_{p \eta}(f)$. If, on the other hand, $p_s(t)$ is correlated with $\eta(t)$, the ratio of the imaginary to the real part of the $p_s(t)$ Fourier transform is modified by convolution with the spike window while the $\eta(t)$ transform ratio is not. For this reason the $\overline{p_s(t) \eta_s(t)}$ cross-spectra are used exclusively for the presentation of the results.

A1.4 Effects of a Regular Spike Window

In order to assess the influence of "holes" in the pressure signal resulting from the removal of spikes, hypothetical pressure and wave signals have been generated on the computer and analysed with the same procedures used on the field data. Both signals consist of a single sinusoid with zero mean; they have the same amplitude and frequency but differ in phase by 30° . Their frequency is arranged so a data block does not contain an integral number of cycles. If desired, either signal may be zeroed for a fixed length of time once every L cycles, L being any positive integer; both L and the duration of the "holes" produced by the zeroing procedure can be preset for a given run.

These hypothetical pressure and wave signals have been analysed exactly as the field signals are analysed; power and cross spectra of the pressure and wave "signals" are obtained. A number of different combinations of sine waves, hole durations, and values of L have been analysed. For the sake of brevity the cross-spectra from only one combination is presented, for which the "pressure" and "wave" signals both consist of a single sinusoid, and the spike function repeats once per cycle of this sinusoid. This combination was chosen because it clearly shows the spectral distortions introduced by the repetitive spike function used and because the contamination introduced by removing data from every cycle of the signal is more severe than the contamination which occurred in any of the runs analysed.

The particular "signals" used were

$$p'(t) = 5.0 \sin (2\pi N f_0 / f_s) \text{ dyne cm}^{-2},$$

$$\begin{aligned}
 \eta'(t) &= 5.0 \sin(2\pi N f_o / f_s + \pi/6) \text{ cm, and} \\
 S'(t) &= 0 \quad (M f_s / f_o + 30) \leq N \leq (M f_s / f_o + 50) \\
 &= 1 \quad \text{otherwise.}
 \end{aligned}
 \tag{A1.13}$$

In Equation A1.13 N is the sample number and f_s the sampling frequency (chosen here to be 50 Hz), f_o is chosen to be 0.4 Hz, and $M = 0, 1, 2, \dots$ is the cycle number. Thus from Equation A1.13 the period of the sinusoids was 125 samples, and a "hole" occurred once per cycle at the phase $2\pi(M + 30/125)$ and ended 20 samples, or $(2\pi \times 20/125)$ radians, later.

Ten blocks of 1024 samples each were analysed for two cross-spectra: $p'(t)S'(t)$ versus $\eta'(t)$, and $p'(t)S'(t)$ versus $\eta'(t)S'(t)$. The results of these analyses are displayed in Figures 56 to 63.

Figures 56 and 59 show respectively the power spectra of $p'(t)S'(t) = p'_s(t)$ and $\eta'(t)$; Figure 59 clearly shows the envelope of the block spectral window given by Equation A1.11. The vertical bars on the power spectral estimates are standard errors about the mean over the 10 blocks for each spectral estimate; the horizontal bars give the bandwidth. The pressure power spectrum in Figure 56 shows that the effect of multiplying the pressure signal with the "Spike function" (which repeats once per cycle starting at $2\pi(1.24)$ and ending at $2\pi(1.4)$ radians) is the generation of harmonics of the fundamental; replicas of the block spectral window appear at 0.8, 1.2, and 1.6 Hz. The coherence spectrum is shown in Figure 57 and the phase spectrum in Figure 58. It will be remembered from Equations A1.13 that the phase of the pressure signals lags the wave signal by 30° . Although the phase spectrum is

almost constant with frequency near 0.4 Hz the measured phase lag at 0.4 Hz is 38° .

Turning now to Figures 60 to 63, which display cross-spectra between $p'_s(t)$ and $\eta'_s(t)$, the phase at 0.4 Hz in Figure 62 is seen to be within 0.1 of 30° , lending credence to the arguments made on p. 174 that the $\overline{p_s \eta_s}$ correlation should be used for finding the phase spectrum rather than the $\overline{p_s \eta}$ correlation. Note the large coherences at harmonics of 0.4 Hz in Figure 61 as compared with the rather small coherences at the harmonics in Figure 57; the high-frequency coherences of the $\overline{p_s \eta_s}$ correlations from the field data are also found to be larger than those of the $\overline{p_s \eta}$ correlations. This indicates that at high frequencies in the $\overline{p_s \eta_s}$ spectra from the field data the observed phases are probably entirely determined by the influence of the spikes.

A1.5 The Effect of the Spikes on the Power Spectra

Because the information from the regions of the pressure signal in which spikes are present is irretrievably lost, only a qualitative estimate can be made of the effect of the spikes on the pressure power spectra. This estimate has been made by multiplying an observed wave signal $\eta(t)$ by the spike function $S(t)$ derived from the simultaneously observed pressure signal, and observing the effect of the spike window on the wave power spectrum.

The spectra of $\eta(t)$ and of $\eta(t)S(t) = \eta_s(t)$ are shown for the field runs in which appreciable spike contamination occurred (runs 1, 2b, 3, and 6) in Figures 64 to 67. The general effect of the spike contamination is seen to be a smearing out of the uncontaminated spectra, with

energy being removed from the peak and added at the high frequencies; energy is also added at frequencies below the wind-generated spectral peak in runs 1 and 6, while it is removed from these regions in runs 2a and 3. It appears that in the four runs shown energy is added to the frequencies below the wind-generated peak if no swell peak appears in the spectrum and removed if the swell peak is present. This apparent correlation between the action of the spikes on the spectra and the presence of the swell peak may be related to the total number of spike occurrences, assuming that the presence of swell in the wave field would increase the likelihood of large numbers of spikes.

The action of the spikes on the wave spectra at high frequencies is to decrease their falloff rate. The contaminated spectra cross the uncontaminated spectra near 1.5 Hz, the contaminated spectra being larger at higher frequencies. Above 2.5 Hz the spectra diverge rapidly; since neither the pressure nor the waves are well-measured at these frequencies, these large discrepancies are not discussed further.

A1.6 The Effect of the Spikes on the Phase Spectra

The recorded pressure signal consisted generally of clear signal interspersed with regions of spike activity. As a check on the effect the spikes have on the phase spectra, the spike detection and removal program SPKSKP was altered slightly so that the detection of a spike anywhere in a data block caused the entire block to be ignored.

This alteration in SPKSKP allowed the analysis of blocks of clear

data; these were, however, scattered at random time intervals throughout the run. In practice, to get a sufficient number of blocks for good statistics the block length had to be shortened from 20 seconds for the "spikey" data to 5 seconds for the clear data. Therefore the lowest frequency which could be resolved was raised from 0.05 Hz in the case of the "spikey" data to 0.2 Hz for the clear data.

Phase spectra between pressure and waves for runs 1, 2b, 3, and 6 (see "Results" for detailed descriptions of these runs) are shown in Figures 68 to 71. In each figure two curves are drawn corresponding to two ways of preconditioning the data; the full curve shows the phases between p_s and η_s from all blocks in each run for data subjected to the spike removal process, the dotted curve shows the phases between p and η from the blocks during which no detectable spikes occurred. The dotted and full vertical lines at high and low frequencies are the frequency limits beyond which the relevant phases become unreliable; that is, the frequencies where the coherence falls below about 0.3 (see the discussion of this coherence limit in "Results", p. 115).

The phase spectra computed in the two different ways show substantial agreement. The largest discrepancies are about 20° , but in most cases the phases are within 10° of each other at a given frequency.

This comparison of clean and spike-contaminated data provides

direct evidence that the effect of the spikes on the phase spectra is quite small.

A1.7 The Effect of the Spikes on the Energy Flux Spectra

The possibility still exists that significant spike-induced distortions can occur in the quadrature spectrum $Qu_{p\eta}(f)$, in spite of the generally small distortions in the phase spectra; for this reason the energy flux spectra $\dot{E}(f)$ (which are derived from the $Qu_{p\eta}(f)$ through relation 5.9) computed from the "clear" and "spikey" pressure data are also compared, in Figures 72 to 75:

It will be seen that although the two $\dot{E}(f)$ spectra agree quite closely in runs 2b and 6, there occur what appear to be large discrepancies between the two spectra in the other two runs (1 and 3).

The significance of these discrepancies cannot be assessed statistically since the scatter over the data blocks analysed is invariably large--so large in fact that all of the "large" discrepancies noted between the two $\dot{E}(f)$ spectra in runs 1 and 3 lie within one standard error of each other. The possible physical significance of this large scatter in the $\dot{E}(f)$ spectra is taken up in "Discussion of Results" on p. 146.

The observed discrepancies in runs 1 and 3 between the $\dot{E}(f)$ spectra are hence within the observed scatter in the results. The discrepancy in run 1 occurs at one frequency only, 0.37 Hz; this is the frequency of the peak of the wave spectrum. It will be noted that the analysis of the "clean" data indicates stronger wave generation (has a larger negative $\dot{E}(f)$ spectrum) at this frequency than does the "spikey" data analysis. Since the wind speed for this run was lower (see Table 6.1) than the wave speed at 0.37 Hz there is little likelihood that generation was actually occurring; therefore the result from the "spikey" data is probably closer to being realistic. It is interesting that in spite of discrepancies in the $\dot{E}(f)$ spectra from the two sets of data the integrals under these spectra are almost identical; the "spikey" data gives $\bar{\dot{E}} = 16.6 \text{ erg cm}^{-2} \text{ sec}^{-1}$ and the "clean" data gives $\bar{\dot{E}} = 16.3 \text{ erg cm}^{-2} \text{ sec}^{-1}$. This agreement is the result of the weighting of the higher-frequency spectral estimates (they have larger bandwidths) in the integration process, which minimizes low-frequency discrepancies. The good agreement between the two values of $\bar{\dot{E}}$ makes it unnecessary to pursue further the reasons for the differences in the two $\dot{E}(f)$ spectra.

Run 3 (Figure 74) is somewhat different. The discrepancy noted at the higher frequencies (1.1 to 2 Hz) in the phase spectra for the run (Figure 70) indicates that the average phase angles of the "clear" data are different from those of the spikey data. The integrated energy flux $\bar{\dot{E}}$ from the clear data is $62 \text{ erg cm}^{-2} \text{ sec}^{-1}$, while the value determined the spikey data is $30 \text{ erg cm}^{-2} \text{ sec}^{-1}$, 50% lower. Both of the $\dot{E}(f)$ spectra from run 3 indicate wave damping at 0.2 Hz, at which frequency a large amount of swell energy was present in the wave power spectrum. Therefore there is in this case no objective criterion by which to judge which of

the two analyses is more nearly correct. The "spikey" data might be expected to underestimate $\dot{E}(f)$ since it has had energy removed from it via the spike removal process; on the other hand if it is assumed that energy input was largest to the largest-amplitude waves, then since the largest waves caused spikes more often, the clear data would miss this energy transfer and hence might be expected to underestimate $\dot{E}(f)$. The only choice remaining is to assume that \dot{E} for run 3 is not known to better than $\pm 50\%$.

A1.8 Conclusions

The object of this appendix has been to study the effects of the removal of spikes from the pressure signal on the power and cross spectra of pressure and wave signals which form the most important results of this thesis. The conclusions resulting from this study are listed below.

1. By computing the power and cross spectra of computer-generated sine waves of the same frequency but different phase, one or both of which was modified to be replaced by zeros once every cycle for a duration of one-sixth of a cycle (a "hole"), two conclusions have been reached. The first is that the power spectrum of the "hole-contaminated" sine wave is distorted so that energy is removed from the spectral peak at the fundamental frequency and inserted at the harmonics of the signal. The second conclusion is that the phase difference between the two sine waves compared is accurately reproduced by the cross-spectral analysis only if the cross spectrum between two signals contaminated in the same way by the presence of holes is used to determine the phase.

2. The effect of the spike removal on the power spectra of the field data is a redistribution of energy, as in conclusion (1). There

is however no evidence that the excess energy is shifted into harmonics of the frequency of the peak of the wind-generated wave spectrum.

3. A comparison has been made between phase spectra between pressure and waves for two different methods of treatment of the pressure data. In one case the data were analysed normally in the sense that when a spike occurred it was replaced with zeroes; in the other case only data blocks in which no spikes appeared were analysed. The comparison shows fairly good agreement, suggesting that the phase spectra are affected little by the energy redistribution noted in conclusion (2).

4. A comparison has also been made of energy flux spectra between pressure and waves for the aforementioned two methods of treating the pressure data. Of the four runs with appreciable numbers of spikes, the agreement between the energy flux spectra computed from the data analysed in the two ways was very good in two cases (runs 2b and 6); agreement in the other two cases (run 1 and 3) was poor. The integrated energy fluxes \overline{E} were computed for the two runs where agreement was poor; the \overline{E} values computed from the clean and spikey data agreed closely for run 1, while the \overline{E} computed from spikey data underestimated that computed from clean data by 50% in run 3. As a result the run 1 discrepancies are considered to be unimportant while those in run 3 indicate that serious spike contamination is present in this run and that the accuracy of the computed results for the run are suspect.

```

C IF SPIKE DETECTED , START L COUNTING, START CORRECTION ROUTINE
C --( OR, IF IFSKP IS 1, RETURN TO CALLING PROGRAM WITH IERSP = 2- )
49 IF( IFSKP.GE.1 ) GO TO 410
50 L=1
IF( M.GT.JFRAC ) GO TO 310
C CORRECTION ROUTINE ALSO CHECKS AHEAD IF ANOTHER SPIKE OCCURS DURING NSKIF
C THE DO WILL CORRECT ALL POINTS TO NSKIP BEYOND IT.K TOTALIZES CORRECTED
C --POINTS.
NSTART = I + K
NEND = I+K+NSKIP - 1
DO 200 J= NSTART, NEND
C CHECK FOR END OF ARR(NPTS)
IF ( J.GE.NPTS) GO TO 300
C TEST FOR SATURATION OF A TO D
IF(ABS(ARR(J)).GE.VALMAX) GO TO 250
C CHECK AHEAD FOR NEXT + GOING SPIKE
DIFJ = ARR(J+1) -ARR(J)
IF ( DIFJ.GT.DIFMAX ) GO TO 250
ARR(J) =0.
SARR(J) =-0.
K=K+1
M = M + 1
200 CONTINUE
GO TO 300
250 ARR(J) =0.
SARR(J) =-0.
K=K+1
M = M + 1
GO TO 50
300 CONTINUE
GO TO 320
310 NSTOP= I + K
WRITE( 6,315 ) JFRAC, NSTOP
315 FORMAT( 1H0,2X,29HDATA QUESTIONABLE MORE THAN ,14,42H VALUES SKIP
1PED. SPIKE REMOVAL STOPPED AT , 14, 9H1H VALUE. )
C IERSP IS RETURNED AS 2 IF FRAC*IBL IS EXCEEDED
IERSP = 2
GO TO 330
410 WRITE( 6,415 ) I
415 FORMAT(2H ,32HSPIKE ENCOUNTERED AT SAMPLE NO. ,14,17H . BLOCK 1GN
10REM )
IERSP = 2
RETURN
320-- IFLINE = IFLIN + 1
WRITE(6,325) AIFLIN( IFLINE) , M
325 FORMAT( 1H ,2X,54HSPIKE REMOVAL COMPLETED. SKIPPED VALUES REPLACED.
1 WITH ,A8,1H.,1X,15,21H DATA VALUES SKIPPED. )
C IERSP = 0 MEANS NORMAL RETURN
IERSP = 0
330 RETURN
END

```

SUBROUTINE SPKSKP(ARR,SARR,NPOW,IERSP,IFLIN)

C SPIKE REMOVAL SUBROUTINE. REMOVES SPIKES FROM PRESSURE DATA, AND ALSO
C FROM A TEST ARRAY WHICH IS INITIALLY ALL 1.

NPTS = 2**NPOW

PTS = NPTS

DIMENSION ARR(1), SARR(1), AIFLIN(2)

C READ IN REQUIRED DATA. NSKIP IS BASIC NUMBER OF DATA POINTS CORRECTED
C AFTER A SPIKE. DIFMAX IS MAXIMUM ALLOWED DIFFERENCE BETWEEN SUCCESSIVE
C POINTS. VALMAX IS MAXIMUM ALLOWED VALUE OF DATA POINTS.

C FRAC IS MULTIPLIER TO SET MAX. ALLOWED NO. OF POINTS TO BE SKIPPED.

C IFSKP SETS MODE OF OPERATION IF 0, SPKSKP SKIPS SPIKES ON ENCOUNTER

C IF 1, SPKSKP SKIPS WHOLE BLOCKS ON ENCOUNTERING A SPIKE.

DATA AIFLIN(1), AIFLIN(2)/ 6H ZEROS, 6H LINES/

IF (IERSP.NE.0) GO TO 20

READ (5,16) FRAC, DIFMAX, VALMAX, NSKIP, IFLIN, IFSKP

16 FORMAT (4X, F6.5, 2(4X, F6.1), 7X, I3, 2(9X, I1))

JFRAC = PTS*FRAC

WRITE(6,17) JFRAC, DIFMAX, VALMAX, NSKIP

17 FORMAT (1H0, 2X, 44HMAXIMUM ALLOWED NUMBER OF SKIPPED VALUES IS ,

1 14, 1H. / 3X, 8HDIFMAX =, F7.3, 2X, 8HVALMAX =, F8.3, 2X, 7HNSKIP =, I3)

C SPIKE REMOVAL ROUTINE. INITIALIZE COUNTERS.

20 K = 0

L = 0

M = 0

NEND = 0

C START-CHECKING DATA BY-LOOKING-FOR DIFFERENCES BETWEEN SUCCESSIVE DATA POINTS

C GREATER THAN MAXDIF. PROGRAM CORRECTS DATA POINTS BY SETTING THEM TO ZERO OR

C BY REPLACING THEM WITH A STRAIGHT LINE FROM START TO END OF SPIKE. IT

C CORRECTS NSKIP POINTS AFTER A SPIKE, AND WILL, IF A NEW SPIKE OCCURS IN THE

C RANGE OF NSKIP, CORRECT NSKIP POINTS BEYOND THE NEW SPIKE. K COUNTS

C TOTAL POINTS CORRECTED, L IS USED TO SHORT OUT THE SPIKE TEST ROUTINE WHILE

C I IS BEING INCREMENTED TO THE END OF THE SERIES OF CORRECTED POINTS.

DO 300 I=2, NPTS

IF(L.EQ.0) GO TO 25

L=L+1

IF(IFLIN.EQ.0) GO TO 24

IF(L.NE.2) GO TO 22

INIT = NEND - K

JEND = NEND + 1

RK = K + 1

ADD = (ARR(JEND) - ARR(INIT)) / RK

22 ARR(I - 1) = ARR(I - 2) + ADD

C TEST COUNTER TO SEE IF LAST CORRECTED POINT REACHED

24 IF -(L.GT.(K + 1)) GO TO 25

GO TO 300

C CHECK FOR SPIKES

25 DIF = ARR(I) - ARR(I-1)

C RESET K, M AFTER MULTIPLE SPIKE REMOVAL COMPLETE

K=0

C TEST FOR PRESENCE OF INITIAL SPIKE (+OR- GOING)

IF(ABS(DIF).GT.DIFMAX) GO TO 49

C IF DATA OK, RESET L, RETURN TO DATA CHECKING LOOP

L=0

GO TO 300

APPENDIX 1a:

FORTRAN IV PROGRAM FOR SPKSKP

APPENDIX 2: THE BOUNDARY BAY EXPERIMENT

A2.1	Introduction	184
A2.2	Description of Site	185
A2.3	Equipment	186
A2.3.1	The Buoy Sensor	186
A2.3.2	The Reference Barocel	187
A2.3.3	The Elliott Probe	188
A2.3.4	Auxiliary Equipment	188
A2.4	Calibration	190
A2.5	Data Analysis	191
A2.6	Results	192
A2.6.1	Summary of Relevant Information	192
A2.6.2	The Hot-Wire Data	192
A2.6.3	The Pressure Power Spectra	195
A2.6.4	Non-Dimensional Pressure Spectra	198
A2.6.5	Comparison of Power Spectra with Other Measurements	199
A2.6.6	The Pressure Cross-Spectra	202
A2.6.7	Pressure-Velocity Correlations	208
A2.6.7a	Comparison with Favre <u>et al</u> (1957)	210
A2.7	Conclusions	215
A2.7.1	Sensor Tests	215
A2.7.2	The Structure of the Pressure Field	216

APPENDIX 2: THE BOUNDARY BAY EXPERIMENT

A2.1 Introduction

In the summer of 1968 the opportunity arose of comparing the pressure sensor used in the buoy with others being developed and used by Mr. J. A. Elliott, a fellow student at the Institute of Oceanography.

Two sensors were used in the comparison with the buoy sensor. One was an unmodified "Barocel" transducer, a commercial device made by Datametrics Inc. of Waltham, Mass., U.S.A., which was used to measure pressure fluctuations on a fairly level sand surface. The other was a probe developed by Elliott which used a Barocel as its transducer and with which pressure measurements were made in the body of the turbulent air flow above the sand surface.

The principal objectives of the experiment were to obtain pressure measurements with each of the three sensors, to compare the resulting spectra, and thus to establish whether or not the buoy sensor and the Elliott probe were measuring true pressures. The possibility existed that pressures measured by the two might be contaminated by dynamic pressures originating from the disturbance to the flow caused by their shapes. The unmodified Barocel was taken as the standard for the tests, its pressure-sensing port being arranged in a standard manner for surface measurements.

A secondary objective was to make some preliminary investigations of the pressure field in the air, at various heights and at various down-

stream and cross-stream separations.

A2.2 Description of Site

A suitable, easily accessible land site was at hand, thanks to the efforts of another Institute student, Mr. N. E. J. Boston, who was conducting measurements of small-scale temperature structure in the atmospheric boundary layer over a sand flat at Boundary Bay, about ten miles by road from the Institute.

Figure 76 shows a map of the immediate area of the experiment. The sand flat, completely covered at high tide, is bare for about 2.5 km seaward of the dike at low tide. Its surface of fine sand is nearly level on the average with a seaward slope of less than 1 : 2,500. There are some shallow pools of residual water (averaging 1 - 10 m in diameter) at low tide. Growing on the sand are numerous clumps of a low-lying plant; these clumps are about 60 cm in diameter and about 10 cm high. Thus the sand, although smooth on the average, has roughness elements present which have horizontal scales of 10 - 100 cm.

The high tide shoreline (about 10 meters from the base of the dike) is strewn with logs, some as much as 20 m long and 1.5 m in diameter. The dike is about 3 m high and 10 m in width. There is a drainage ditch on the shoreward side; beyond it flat farmlands (part of the delta of the Fraser River) stretch inland for 5 - 10 km.

The three hunting shacks on the shoreline all have electric power (115 VAC, 60 Hz); Mr. H. R. Hipwell, the owner of one, kindly consented to allow us the use of it. Cables were constructed (Boston) which allowed the experiment to be set up about 100 m from the shoreline.

A2.3 Equipment

The three pressure sensors and the ways they were deployed in the experiment will be described first.

A2.3.1 The Buoy Sensor

The transducer, electronics, and buoy have been described earlier (see "Experiment"). During the Boundary Bay experiment the apparatus was arranged in two ways. At first "case 1" the buoy was not used. The microphone and its oscillator were firmly clamped into a thermally insulated (5 cm thickness of styrofoam) wooden box along with the reference sensor. The aluminum backup volume used in the buoy was replaced with a glass jar of twice the usual volume which was itself insulated with 3 cm of styrofoam. The microphone was connected to a 0.8 mm diameter pressure port which was flush with the top of the box and which was a carefully drilled and polished hole in a brass plug (3 cm in diameter). The pressure connection to the sensor was made with a 16 cm length of 2 mm I.D. steel tubing. Long-term (periods of 100 seconds or more) pressure variations were filtered out by a pneumatic high-pass filter consisting of the built-in leak around the diaphragm of the microphone and the backup volume. To make measurements with this arrangement the entire box was buried flush with the sand. Some care was taken to insure that roughness elements within 2 m upstream of the pressure tap were kept small (scale sizes less than 1 cm).

For the second set of measurements ("case 2") the buoy microphone and oscillator were placed in a separate box, and the buoy was fixed to the top of the box. The buoy surface was made as nearly as possible

identical with that used during tests on waves, the only difference being that the rubber diaphragm used in the sea experiments was replaced by a carefully drilled 0.8 mm diameter pressure tap in the perspex sheet which normally covered the electronics package (see Experiment, Figure 5). The electronics, microphone, and backup volume were in the thermally insulated box below. The tap was connected to the microphone by 20 cm of 2 mm I.D. steel tubing. The experiments were conducted with the buoy and the box below it buried in sand to the depth at which it would normally float in calm water. No attempts were made to see the effect of varying its angle of tilt with respect to the sand surface.

A2.3.2 The Reference Barocel

The Datametrix "Barocel" transducer is of the capacitance type. It has a resolution of less than 0.1 dyne cm^{-2} differential pressure on its most sensitive range and a frequency response in the arrangement used that was flat from 0 to 10 Hz (with some phase error above 7 Hz; see Figure 78). Stated accuracy and linearity are 0.25% of full scale. It has 9 pressure ranges covering pressures from 0 - 13 millibars ($1 \text{ mb} = 10^3 \text{ dyne cm}^{-2} = 10^{-3} \text{ atmos.}$).

For the first series of experiments the reference Barocel was placed in the same box as the buoy sensor; it measured pressure at a pressure tap identical with that used for the buoy sensor and situated 5 cm crosswind from it. One side of the transducer was connected to the tap with 13.5 cm of the same (2 mm I.D.) tubing as that used for the buoy sensor; the other side was connected to a small vacuum flask which served as a backup volume. Long-term pressure changes were equalized

with a 4 cm length of 0.15 mm I.D. hypodermic needle, which was connected between the two pressure ports of the transducer and acted as a pneumatic high-pass filter. This arrangement and the thermal box was designed and built by Elliott.

For the second set of measurements the reference Barocel pressure tap was in the box, which was buried as for case 1; the buoy and its box were buried at different times, crosswind and downwind from the reference Barocel.

A2.3.3 The Elliott Probe

The details of this probe will be discussed in a forthcoming publication. It is mounted on the end of a 50 cm "sting" along which pressures sensed by the probe are transmitted by tubes to a Barocel transducer with a backup volume arrangement similar to that used for the reference sensor. The transducer and backup volume are contained in a 12.5 cm O.D., 35 cm long aluminum cylinder with a conical nose; cables carry the transducer output to the signal conditioning electronics which can be located as far as 80 m from the probe (the same is true for the reference Barocel).

A2.3.4 Auxiliary Equipment

Wind speed was measured with two "Casella" cup anemometers; these returned electrical pulses to counters at the recording area which counted once per cup revolution; total counts were recorded every five minutes with a one-minute break to write the numbers down. Wind speed was obtained from calibration curves provided by the manufacturer. Wind

speed was obtained from calibration curves provided by the manufacturer. Wind direction was measured with a small vane which turned the wiper of a potentiometer, and readout on a meter calibrated at five-degree intervals.

Downwind fluctuations of turbulent wind speed were measured for all of the runs with a "Disa" constant temperature hot-wire anemometer; the wire was placed vertically in the air flow at various heights above the sand.

The hot-wire signal, the three pressure signals, and a voice log were recorded at $7\frac{1}{2}$ ips tape speed on a 14-channel "Ampex FR-1300" portable instrumentation tape recorder in the FM mode (voltages are converted to frequency-modulated audio signals and recorded; they are demodulated on playback. Frequency response is flat from 0 - 2 kHz.) For some runs a mercury thermometer was used to measure air temperature and sand temperature.

Figure 77 shows a typical setup. A portable mast 4.5 meters high is erected on the sand at low tide about 150 meters down from the high tide line. Signal cables are laid from the sensors on and near the mast back to the panel truck 40 meters distant which contains the tape recorder and all signal conditioning equipment. Power is obtained from two cables laid from the hunting shack on shore to the truck.

On the mast are three cup anemometers at heights of 4.5, 2.0, and 0.5 meters (the middle anemometer did not function reliably and results from it were not used). Also on the mast, at a height of 4 meters for the particular setup shown, is the probe of the hot-wire anemometer. The

three pressure instruments are buried within 2 meters of the base of the mast and oriented into the wind. The rocket-like object on the sand is the cylinder containing the electronics for the Elliott probe. The wind direction vane is located halfway between the truck and the mast (the experiments did not depend for their validity on an accurate measurement of wind direction).

A2.4 Calibration

All three pressure sensors were calibrated in the laboratory with the equipment described in the "Experiment" section (p. 58 ff). They were in every case calibrated with the same pressure tubing configurations used in the field. The amplitude and phase calibration for the buoy sensor at frequencies from 0.05 to 10 Hz are displayed in Figure 78. These were obtained by sinusoidally varying the pressure in the calibration drum at various frequencies. The buoy sensor signal was compared with that from a Barocel which had one port at drum pressure and the other at atmospheric pressure.

The amplitude and phase of the Barocel signal began to differ a measurable amount from the buoy sensor at frequencies above 7 Hz; this is assumed to be caused by the Barocel and not the buoy, since a resonance is known to occur in the drum at 45 Hz and there was no reason to suspect a rolloff in the buoy sensor below 100 Hz (the resonant frequency of its forevolume is 300 Hz). No calibrations were made above 7 Hz. Assuming the buoy sensor to be correct at high frequencies and the Barocel to be correct at low frequencies, the frequency response of the drum-driver system is shown in Figure 79.

A2.5 Data Analysis

The data was analysed using the same general methods described in "Data Analysis and Interpretation". The analog tapes were first played back into a six-channel chart recorder; sections suitable for analysis were chosen using as criteria the length of time during which all signals functioned simultaneously and the general steadiness of the "eyeballed" variance of the signals (as an indication of stationarity). Promising sections were marked.

These sections were then played back at eight times real speed, filtered with carefully phase-matched low-pass filters (to prevent aliasing), and digitized at a sampling rate of 500 samples per second on the Institute A/D converter (62.5 Hz "real-time" data sampling rate).

The resulting digital tapes were checked for parity errors and other likely digital failures. If they proved suitable they were then analysed with the Fast Fourier Transform package developed at the Institute. The computer output from this package gave power spectra and cross spectra including Co, Qu, Phase and Coherence for all signals analysed (see "Data Analysis and Interpretation"). The data was Fourier transformed in blocks of 2048 points each (32.7 seconds of real time). The final spectral estimates were averages over the total number of data blocks in a given run. Also printed out were standard error of the mean and average trend for each spectral estimate and cross-spectral estimate at each frequency. For this analysis spectral densities at individual frequencies were averaged over roughly logarithmic (approximately $\frac{1}{2}$ octave) bandwidths.

A2.6 Results

A2.6.1 Summary of Relevant Information

A summary of information relevant to the field runs is presented in Table A2.1. The results from the data of these runs will be presented in three sections. In the first the determination of the "friction velocity" u_* from the hot-wire data is described; this permits normalization of pressure spectra into a form suitable for comparison with other observations. In the second section power spectra of the signals from the three pressure sensors are compared. These power spectra are also compared with those obtained by other investigators. In the third section the cross-spectra of the buoy sensor data with the data from the two pressure sensors and from the hot-wire anemometer are presented.

A2.6.2 The Hot-Wire Data

For all of the runs simultaneous hot-wire anemometer data were available. Power spectra were computed for the data taken, and in some cases cross spectra with the pressure data were also computed. The power spectra are discussed first.

In Figure 80 $\log \Phi_{uu}(k)$, the log of the spectrum of turbulent downwind speed fluctuations u , is plotted versus $\log(kz)$, where z is a hot-wire height, for one of the runs analysed. It is considered to be typical of all the velocity spectra obtained. The line fitted to the points is of slope $-5/3$; as for all the velocity spectra this line fits the points very well over one decade of frequency.

These spectra have been used to obtain a value for u_* , the "friction

TABLE A2.1

Information Summary for Boundary Bay Runs: September, 1968

Run	Date (Sept. 1968)	Time of day	Wind Speed at 4m (cm sec ⁻¹)	Wind Direct- ion	Sensor	Height (cm)	Horizontal Separation (cm)	Cloud Cover (tenths)
Notes:			(1)		(2)		(3)	
1a	4	1530	390	NW	p _a	30	0	0.0
					p _b (ground)	0	5 cw	
					u'	400	200 cw	
5a	27	1430	310	NW	p _a	30	60 cw	0.2
					p _b (buoy)	2	60 cw	
					u'	30	50 cw	
5b	27	1500	340	NW	p _a	30	60 cw	0.2
					p _b (buoy)	2	60 cw	
					u'	30	50 cw	
5c	27	1600	400	NW	p _a	30	60 dw	0.2
					p _b (buoy)	2	60 dw	
					u'	30	60 dw, 10 cw	
5d	27	1700	420	NW	p _a	30	60 dw	0.2
					p _b (buoy)	2	60 dw	
					u'	30	60 dw, 10 cw	
5e	27	1730	450	NW	p _a	100	60 dw	0.2
					p _b (buoy)	2	60 dw	
					u'	100	60 dw, 10 cw	

- Notes: 1. Mean wind speed measured with cup anemometers at heights of 50 and 400 cm.
2. p_a = Elliott air pressure sensor; p_b = buoy pressure sensor (on ground or in buoy on ground); u' = hot-wire anemometer.
3. cw = crosswind from reference pressure sensor; dw = downwind from reference pressure sensor.

velocity" (see, for instance, Lumley and Panofsky (1964)) from the value of $\Phi_{uu}(k)$, in the $k^{-5/3}$ region of the spectrum. It was shown by Taylor in 1960 (see, for example, Weiler and Burling (1967)) that

$$\begin{aligned} u_*^2 &= \left(\frac{2\pi Kz}{U} \right)^{2/3} \cdot \frac{k^{5/3} \Phi_{uu}(k)}{K^1}, \\ &= 1.13 \left(\frac{2\pi z}{U} \right)^{2/3} f^{5/3} \Phi_{uu}(f), \end{aligned}$$

where $K \simeq 0.4$ is Von Karman's constant, z is the height of the anemometer and U is the mean wind speed at that height; $K^1 = 0.48$ is Kolmogorov's universal constant for air in the Universal Inertial Subrange of turbulence scales (the value of K^1 is that given in Pond, Stewart, and Burling (1963));

$$k = \frac{2\pi}{\lambda} = \frac{2\pi f}{U}$$

is the wavenumber and λ the scale size of the turbulent eddies. The last statement is the "Frozen Turbulence" assumption, or Taylor's hypothesis.

In the arguments leading to the expression for u_*^2 is included the assumption that in the Inertial Subrange under discussion the rate of production of mechanical energy is equal to the rate of energy dissipation. For the Boundary Bay runs no record of the mean temperature profile or of the mean humidity profile was kept. Both of these quantities affect the buoyancy of the air and hence the rate of production of energy by convection. The above assumption excludes convective energy; therefore the calculated value u_* may be in error. From the sparse temperature measurements taken it was concluded that buoyancy effects were small

(see Lumley and Panofsky (1964), p. 104) compared with other errors, for instance those due to drifts in the hot-wire calibration. The hot-wire wind speed calibration for these experiments is poor; it is probably only known to within $\pm 30\%$ of its assumed value for the determination of $\Phi_{uu}(f)$.

The results of the analysis just described are presented in Table A2.2. They have been used in the non-dimensional spectra of pressure versus wave number discussed below. (p.198 ff).

A2.6.3 The Pressure Power Spectra

Pressure spectra for runs 1a and 5a (see Table A2.1), are presented in Figures 81 and 82. On each figure are superimposed a set of three pressure spectra, one for each of the three sensors being compared. The first set is typical of spectra found with the buoy sensor in the "case 1" configuration (pressure tap flush with sand); the second is typical for the "case 2" configuration (pressure tap on buoy, "floating" on the sand).

The two figures show the comparison of the three sensors on the two separate days on which runs were taken which are used in this Appendix. The spectra in Figure 81 are from the earlier of the two days, for which all gains and calibrations were well-known. The buoy sensor spectrum in Figure 82 is the first of five spectra taken on the second of the two days; for all of these five runs the particular gain setting of one amplifier was not noted correctly. Upon analysis the buoy sensor spectral densities for all five runs were found to be higher by a factor of two than those of the other two sensors. For this reason the buoy

TABLE A2.2

Summary of Results of u_* Analysis on Hot-Wire
Anemometer Spectra

Run	Time of day	Wind Speed at hot- wire height (cm sec ⁻¹)	Wind Direct- ion	Hot-wire height (cm)	$\Phi_{uu}(f)$ ($\frac{\text{cm}^2 \text{sec}^{-2}}{\text{Hz}}$)	u_* (cm sec ⁻¹)	z_o (cm)	C_D (x 10 ⁻³)
Notes:							(1)	(2)
1a	1530	375	NW	400	9.5	30.5	2.4	6.1
5a	1430	255	NW	30	8.1	18.0	0.1	4.9
5b	1500	280	NW	30	8.1	17.8	0.05	4.0
5c	1600	340	NW	30	13.8	22.3	0.07	4.3
5d	1700	350	NW	30	18.	23.9	0.09	4.7
5e	1730	370	NW	100	8.9	25.2	0.07	4.7

Notes: 1. $z_o = z \exp \left(\frac{-KU}{u_*} \right)$ is the "roughness length", and

2. $C_D = \frac{2}{U^2} u_*^2$ is the "drag coefficient" for the boundary layer.

sensor spectral densities for all five runs taken on the second day have been halved to bring them into accord with those of the other sensors.

The curves, after the above-mentioned adjustments have been made to the buoy sensor spectrum in Figure 82, fall within the limits of calibration errors (see Figure 78) with the exception in the "case 2" configuration of the estimates at frequencies above 2 Hz for the buoy sensor. Typically the buoy sensor showed higher spectral values at frequencies less than 0.05 Hz in all runs.

The cause of the former discrepancy is not understood. The possibility exists that the extra energy may be associated with a low- q eddy shedding from the sides of the buoy. If the buoy were assumed to be a vertical cylinder of infinite height, then an eddy-shedding frequency can be calculated from $f = \frac{SU}{D}$, where S , the Strouhal number, is about 0.2 for such a cylinder, D is the cylinder diameter and U the wind speed. If the log profile for run 5a is extrapolated to obtain a wind speed at 5 cm and D is taken as the buoy diameter (23 cm), then

$$f \approx 0.2 \times 100 / 23$$

$$\approx 1 \text{ Hz.}$$

Another possibility is that the buoy signal is contaminated with some fraction of the dynamic pressures associated with the air flow over the buoy. This would occur if the provisions made for rejecting the dynamic pressures were not correctly set up. Their effect would be "broadband"; that is they would be largest where u was largest, and would push the slope of the buoy sensor power spectrum compared with the

spectra from the other sensors towards $-5/3$, which is expected for the velocity spectrum. This is not observed; therefore dynamic pressures do not appear to be the cause of the high-frequency "hump" being discussed. They may be the cause of some other discrepancies, which will be mentioned in the discussion of the buoy sensor - hot wire correlations (p.209).

The "extra" energy at low frequencies is directly attributable to superior thermal insulation of the backup volume of the Elliott-designed reference sensor (the thermal noise of the Elliott air probe also appears to be somewhat higher than that of the reference sensor). The noise is almost certainly caused by temperature-induced pressure fluctuations in the backup volume of the buoy sensor; such temperature sensitivity had been observed before and during the experiment. Its principal effect is drift, which because of the "block" spectral window (see Appendix 1) is spread over the low frequencies. Neither of these two discrepancies is likely to have caused significant errors in the results obtained with the buoy over the water, since they are in parts of the spectrum where relatively little energy was present in any of the wave spectra. The low-frequency "noise" would be incoherent with the waves, and would be kept low by the much smaller temperature variations encountered by the buoy on water. Perhaps the most significant error will be in the observed values of $\overline{p^2}$, which will be high if the "thermal noise" is high (this amounts to a factor of about 1.5 over the reference sensor in the Boundary Bay runs).

A2.6.4 Non-Dimensional Pressure Spectra

As was mentioned in the section on velocity spectra (p. 192), they

were used to obtain estimates of the friction velocity u_* which in turn were used to produce non-dimensional plots of the pressure spectra. Because of uncertainties in the hot-wire calibrations, this was done only for runs 5a - 5e, which were all taken on the same day. The assumption therefore is that the calibration of the hot-wire did not change during the three-hour period over which the runs were taken.

A plot of $k \Phi_{pp}(k) / \rho_a^2 u_*^4$ versus $\log(k)$ is presented in Figure 83; the spectra shown are all from the buoy sensor.

It should be noted that the "frozen turbulence" hypothesis is invoked in determining k , and that the velocity at 50 cm height has been used in this determination as a scaling factor. Since the "frozen turbulence" hypothesis is probably not correct for any scale, a better non-dimensional plot is probably not worth seeking unless the "advection" velocity U_{ad} of the pressure fluctuations at each frequency is known, so that a "k" may be calculated for each "f" from

$$k = 2\pi f / U_{ad}$$

to put into the non-dimensional formula.

A2.6.5 Comparison of Power Spectra with Other Measurements

Gossard (1960) reports spectra of pressure fluctuations in the frequency range 10^{-6} - 10 Hz. He reports a -2 slope (on a log-log plot) in the frequency range from 0.5 - 5 Hz. The slopes in this range in the Boundary Bay results are roughly $-4/3$ and are thus at variance with Gossard's results. His high-frequency spectra, as far as can be inferred from his paper, were obtained with a microbarograph in the shape of a cylinder one foot in diameter, located in a well-exposed location on a

tower. With this configuration it is hard to see how the instrument was not measuring a large percentage of the total head fluctuations $\frac{1}{2} \rho_a U u'$ (see p. 42), which would lead one to expect a slope of $-5/3$ for his results. This is not too far from his reported $-6/3$ slope over one decade.

Priestley (1965) collected many pressure spectra on the ground beneath the atmospheric boundary layer. He also measured longitudinal and lateral space-time correlations in the pressure field. His power spectra were in most cases quite linear on a log-log plot, with slopes varying from -1.6 to -2.4 at frequencies above 0.06 Hz. The slopes appeared to be weakly related to solar heating. Below these frequencies, the curves sloped less steeply than the slopes just quoted. Priestley shifted all his spectra vertically, matching them in the frequency range $.03 - .35$ Hz; he then used the amount of vertical shift as an "absolute power density scaling factor", by which each spectrum must be multiplied to give the actual value of $\overline{p^2}$. These scaling factors are plotted by Snyder and Cox (1966) against wind speed at some fixed height, and are found to follow a U^4 power law fairly closely. The same technique was applied to the present data, fitted to Priestley's matched spectra. The resulting scaling factors followed a U^4 line as well, but the scaling factors were larger than Priestley's by a factor of about 1.5 . This difference might be explained by the fact that Priestley's mean U was measured at a height of 10 meters while U was measured at 4 meters at Boundary Bay.

The pressure spectra observed in wind tunnel boundary layers are not easily compared with the present data. Willmarth and Wooldridge

(1962), for instance, provide dimensionless pressure power spectra for which the scaling parameters are δ^* , the displacement thickness of the boundary layer, U_∞ , the free-stream velocity, and $q^2 = \frac{1}{2} \rho_a U_\infty^2$, the free-stream dynamic pressure. None of these is known for the atmospheric boundary layer under study. If guesses for them are made, the shape of the spectra could be compared. Reasonable values for Boundary Bay might be

$$\begin{aligned}\delta^* &\simeq 0.1 \delta \simeq 0.1 \times 2 \times 10^4 \text{ cm} = 2 \times 10^3 \text{ cm}, \\ U_\infty &\simeq 30u_* \simeq 900 \text{ cm/sec}, \\ \text{and } q^2 &= \frac{1}{2} \rho_a U_\infty^2 \simeq 0.5 \times 1.23 \times 10^{-3} \times 81 \times 10^4 \\ &= 500 \text{ dyne cm}^{-2}\end{aligned}$$

Here δ , the thickness of the atmospheric boundary layer, is taken to be 200 m. If the Boundary Bay runs are normalized in this way, and if Corcos' (1963) corrections are applied to the Willmarth and Wooldridge spectra, their slope is found to be -1, as compared with the $-4/3$ slope commonly occurring in the present data.

Some recent results published by Gorshkov (1967) are difficult to fit into any pattern. When scaled to Priestley's curves the resulting scaling factors do not have a -4 slope when plotted against wind speed (on a log-log plot). The spectra in some cases are straight lines (slopes varying from -1.8 to -2.3); in other cases they consist of two lines, the higher-frequency part having the higher negative slope; and in other rarer cases they contain "jogs" similar to those seen in some of the Boundary Bay spectra (see Figure 82 at 0.1 Hz). Gorshkov's spectra are consistently higher at low frequencies than any other results. The best that can be said is that a few of the spectra roughly agree with

some of the Boundary Bay spectra.

A2.6.6 The Pressure Cross-Spectra

Information will be presented from three sets of cross-spectra: between buoy sensor pressure and Elliott air sensor pressure, between buoy sensor pressure and reference sensor pressure; and between buoy sensor pressure and hot-wire velocity. The results will be given in terms of coherence and phase.

Coherences for all runs from the cross-spectrum between the buoy sensor and the air sensor are shown in Figure 84. In all cases the air sensor was directly above the buoy sensor; it was at a height of 30 cm in all runs except 5e, when it was at 100 cm.

The generally lower coherences for run 5 are possibly due to the presence of larger signal drifts than those encountered in run 1a, which in the case of run 5 prevented the full use being made of the dynamic range of the tape recorder; however, the feature might be associated with the greater drag coefficient and roughness apparently prevailing during run 1a (see Table A2.2). This would be particularly likely if conditions were more unstable during this run.

The effect on the coherence of the larger height of the air sensor in run 5e is shown in striking fashion. This falloff in coherence is related to the lowest scale size of the turbulent eddies near one height which generate pressures at the ground. By making some rather broad assumptions a vertical scale size of these eddies can be calculated.

The calculation will involve finding the frequency ($f_{\frac{1}{2}}$) at which

the coherence in Figure 84 drops to one-half of its low-frequency value for each of the two heights, 30 and 100 cm, and relating this to a scale size ($\lambda_{\frac{1}{2}}$) through the "frozen turbulence" hypothesis. This is a rather dubious calculation at best; however it is expected to yield reasonable qualitative answers. Scale sizes found this way can be compared with those found by assuming that at the "half-coherence" frequency the height of the air sensor is one-half the wavelength ($\lambda_m = 2z_A$) of the pressure-generating eddy above the ground sensor.

When this is done the results are shown in Table A2.3. It seems that the vertical scale size of the pressure-generating eddies is between one-half and one times as large as that predicted from the frozen turbulence hypothesis and the assumption concerning the "half-coherence" wavelength.

The phase relation between the buoy sensor and the air sensor (directly above it) is presented in Figure 85 for all runs. The phase agreement is considered good, the small discrepancies at frequencies above 2 Hz probably being associated with inaccuracies in the calibration system (see Figure 78) and the generally low coherences at these frequencies (Figure 84).

The coherences between the buoy sensor and the reference sensor are shown in Figure 86; the relative positions of the sensors for these runs are given in Table A2.1. The coherences show a definite tendency to fall off at low frequencies. This would be expected because of the greater low-frequency "thermal noise" of the buoy sensor. The high coherences for run 1a are partly due to the closer proximity of the

TABLE A2.3

Advection Velocity of Pressure-Generating Eddies

Run	Z_A	U_4	u_*	U_{HA}	$f_{\frac{1}{2}}$	U_{ad}	λ_m	$\lambda_{\frac{1}{2}} = U_{HA}/f_{\frac{1}{2}}$
Notes:	(1)	(2)	(3)	(4)	(5)	(6)	(7)	(8)
1a	30	390	30	200	3.5	-	60	55
5a	30	310	18	190	1.8	-	60	100
5c	30	400	22	260	2.6	310	60	100
5e	100	450	25	360	1.2	340	200	400

- Notes:
1. Z_A = height of air sensor (cm).
 2. U_4 = mean wind speed at 4 m (cm sec^{-1}).
 3. u_* = friction velocity.
 4. U_{HA} = mean wind speed at air sensor (cm sec^{-1} ; extrapolated from log profile).
 5. $f_{\frac{1}{2}}$ = frequency at which coherence drops to $\frac{1}{2}$ its low frequency value.
 6. U_{ad} = measured advection velocity (see p. 207).
 7. $\lambda_m = 2Z_A$; see text.
 8. $\lambda_{\frac{1}{2}}$ = wavelength obtained from "frozen turbulence" hypothesis at $f_{\frac{1}{2}}$.

of the sensors in run 1a than in run 5, and partly due to the much larger drifts encountered in run 5.

The effect of separating the sensors by various amounts in the crosswind and downwind directions is shown dramatically. The principal inference to be made from this is that the lateral spatial correlation coefficient falls off more rapidly than does the longitudinal one. This has been observed previously both in wind tunnels (Willmarth and Wooldridge, 1962) and in field studies (Priestley, 1965). Priestley (compare his Figure 8) finds that if C and D are respectively crosswind and downwind scale sizes, then $C \approx 0.8 D^{0.7}$. For a frequency of 0.5 Hz the "frozen turbulence" hypothesis gives a downwind scale size of 700 cm; the above formula then gives 80 cm for the crosswind "scale size" (scatter in Priestley's data could make this as low as 55 cm, however). In Figure 11B coherences for 60 cm crosswind separations have dropped to about one-half of the coherences for 5 cm crosswind separations at 0.5 Hz; this indicates that the crosswind scale size is about 60 cm. The results, then, are in rough agreement with Priestley's conclusions on this point.

The corrected phase lead of the buoy sensor over the reference sensor is shown in Figure 87. At low frequencies the buoy is seen to lag the reference sensor by an amount which decreases with increasing frequency. The phase of the air sensor (not shown) shows the same tendency. This cannot be explained by the hypothesis that the instruments were misaligned with respect to the wind, since in this case the phase lag would increase with frequency.

The only possibilities that remain are either (a) that the high-pass pneumatic filter in the reference sensor (see p. 188) changed its characteristics after calibration, or (b) that the calibrations were inaccurate. Calibrations of the reference sensor were performed both before the experiment and after its completion, and the phase characteristic of the reference sensor filter was in fact observed to have changed between the two calibrations. The corrections introduced by the second calibration were such that they brought the phase between the buoy sensor and the air sensor into closer agreement, but caused larger discrepancies in the buoy sensor-reference sensor phase. Thus case (a) is not thought to be the likely cause of the discrepancy.

The likelihood of case (b) is best seen by examining the standard errors in the phases from calibrations and comparing these with the scatter in the results. The standard error in the determination of phase by the calibration is $\pm 10^\circ$; this includes instrumental errors as well as observed scatter of the points about the calibration curve. The standard deviation of the spectral densities about the mean phase curve in Figure 12B is $\pm 10^\circ$. Thus measurements from the buoy and reference sensors lie within each others' standard errors except at the three lowest frequencies.

The high-frequency phase behaviour of the two instruments is interesting. The phase differences remain around zero for those runs where the instruments were crosswind from each other, but in the runs where the buoy sensor was downwind from the reference sensor buoy pressures lag the reference sensor pressures by increasing amounts as the frequency increases. The differences between the three curves for downwind separa-

tions is not statistically significant, but the consistency of the curves suggests that the phase is smaller at high wind speeds than at low speeds. For the low wind-speed case (run 5c), the phase changes nearly linearly at a mean rate of about -70° per Hz. For a downwind separation of 60 cm this gives a broadband "advection velocity" ($U_{ad} \approx 360^\circ \cdot (\Delta x) / (\partial \theta / \partial f)$, where Δx is downwind separation and $\partial \theta / \partial f$ is the rate of change of phase with frequency) of the pressure fluctuations of $\frac{360 \times 60}{70} \approx 310$ cm sec $^{-1}$; the high wind speed case gives 63° per Hz, or an advection velocity of $\frac{360 \times 60}{63} \approx 340$ cm sec $^{-1}$ (run 5e). To see if these values are consistent with those quoted by Willmarth and Wooldridge (1962; p. 206) it is necessary to scale the present measurements, since they quote their results as applying over ranges of the dimensionless frequency $\omega \delta^* / U_\infty$, where δ^* and U_∞ are defined as before (p.201). For these cases,

$$\delta^* \approx 2 \times 10^3 \text{ cm (as before), and}$$

$$U_\infty \approx 700 \text{ cm sec}^{-1} \text{ from the logarithmic profile;}$$

the angular frequency ω ranges from 2.5 to 12.5. This gives, for the present conditions, $7 \leq \omega \delta^* / U_\infty \leq 36$. For dimensionless frequencies between 0.4 and 0.95 Willmarth and Wooldridge obtain $0.83 U_\infty$ for an advection velocity; they get $0.69 U_\infty$ for $4.0 \leq \omega \delta^* / U \leq 7.0$. For the present two runs ($U_\infty \approx 700$ and 740 cm sec $^{-1}$ for runs 5c and 5e respectively), the ratios are 0.45 and 0.46. Considering the large expected error in the phase measurements, the broad assumptions made, and the fact that the dimensionless frequencies here are higher than those of Willmarth and Wooldridge, who obtain a value of 0.69 for the ratio, the agreement is good; certainly the comparison with the wind tunnel work

should not be taken as any more than qualitative. Unfortunately, the results presented here are not directly comparable with those of Priestley (1965); his advection velocities are related to measured wavelengths (his wind speed measurements were minimal), while those presented here are broadband and are related to mean wind speed.

A2.6.7 Pressure - Velocity Correlations

The coherence and phase of the buoy sensor signal with that from the hot-wire located either 30 or 100 cm above it are shown in Figures 88 and 89. These results show marked differences from the coherence and phase (shown in Figures 90 and 91) between the air sensor and the hot-wire (these were both the same distance, 30 or 100 cm, above the buoy sensor; the hot-wire was 10 cm crosswind from the air sensor). The coherence between the reference sensor (on the ground, 60 cm upwind of the buoy sensor) and the wind is shown in Figure 92.

At frequencies below 1 Hz the buoy sensor shows coherences higher on the average than those of the air sensor. This difference increases with decreasing frequency, possibly to a maximum of 0.2 at 0.05 Hz; however the low points at the lowest frequency may be affected by "thermal noise" in the buoy sensor. At low frequencies the phase between the two pressure instruments is zero (Figure 85) but whereas the phase of the buoy sensor remains at 0° relative to the wind fluctuations until 1 Hz, the phase lead of the air sensor relative to the (nearby) wind sensor rises to 90° at 1 Hz. At frequencies above 2 Hz the phases of both pressure instruments relative to the wind are roughly the same, but both are scattered and the coherence is small.

Because of the physical separation of the three sensors (buoy pressure, air pressure, hot-wire), it is only possible to make inferences about the differences between these correlations of each pressure sensor with the wind at low frequencies--say less than 0.5 Hz.

The most striking difference is that the low-frequency coherence between the air sensor and the nearby wind sensor is 0.1 - 0.3, while that of the buoy sensor with the wind sensor is 0.35 - 0.6. This would seem to indicate that 50 - 100% of the latter coherence arises through dynamic pressures (i.e. noise) at the buoy. Since the signals from both sensors are in phase with the hot-wire at low frequencies any such "noise" must have been in phase with the hot-wire. For the Boundary Bay runs, a dummy wave probe was inadvertently not placed in the buoy as it was for the wind tunnel tests of the design and calibration of the buoy; it is known that its absence would cause a disturbance at the pressure port of -1.5% of the stagnation pressure at the bow of the buoy if potential flow is assumed. This would cause the phase of the resultant signal observed by the buoy to migrate towards 180° , but this is not observed in Figure 89. Therefore another cause must be sought for this phenomenon. It was also found that the pressure tap was mispositioned on the buoy surface, being about 2.5 mm too close to the ring (see Figure 13). If it is assumed that a 3 mm error was made this would cause a contamination of about +3%, this time in phase with the wind speed. The resultant maximum expected dynamic pressure contamination is $1.5 \approx 2\%$. The next step is to make an estimate of the ratio of dynamic to static pressures in the flow over the buoy. At 0.06 Hz in run 5e, the rms static pressure amplitude measured by the reference sensor (over

a 0.03 Hz bandwidth) was about 1.2 dyne cm^{-2} ; the corresponding rms turbulent velocity amplitude was 20 cm sec^{-1} . Therefore the maximum expected dynamic pressure was $\frac{1}{2} \rho_a U \sqrt{\overline{u'^2}} \approx 5 \text{ dyne cm}^{-2}$ (\bar{U} at 4 meters height was 450 cm sec^{-1}); this is five times the static pressures observed. Thus a 2% contaminating dynamic pressure is equivalent to a "noise" which is roughly 10% of the measured static pressures. This is lower by at least a factor of 5 than that required to produce the observed excess coherence between the buoy pressure and the wind 60 cm above it.

Further evidence of the reality of the "high" coherences between the buoy pressure and the wind is provided in Figure 92, which shows the coherences between the reference sensor (on the ground) and the wind; these coherences are also higher than the coherences between the air sensor and the wind (although they are somewhat lower than the coherences of the buoy sensor pressure with the wind).

A2.6.7a Comparison with Favre et al (1957)

It is therefore necessary to consider the possibility that a vertical pressure gradient exists, which may be related to vertical accelerations in the flow between the sensors. Such vertical accelerations appear to have been observed in boundary layer flows in a wind tunnel by Favre et al (1957). In their experiment they inserted two hot-wire anemometers into a boundary layer which was grown from natural transition on a flat glass plate, and measured correlations between the downwind velocity fluctuations at various vertical, longitudinal, and lateral spacings. They found that for a given downstream separation Δx and given time delay Δt there is

one vertical separation Δz for which the correlation is a maximum; by varying both Δt and Δz there is one combination of Δt and Δz for each Δx at which the correlation is a greatest maximum. Δz for this greatest maximum was then plotted against the corresponding Δx ; the resulting "curve of maximum correlation" was convex to the boundary, reaching its lowest height at the location of the fixed sensor close to the boundary and curving upwards in the up-and-downstream directions. This curvature may indicate that in the mean, vertical accelerations existed in their flow which caused downward-moving eddies to be decelerated and upward-moving ones to be accelerated. This argument is of course an oversimplification; their results are broadband, since the accelerations involved larger and larger scales as the sensor separations increased. Nevertheless an attempt has been made by the present writer to estimate the size of these accelerations. The boundary layers in the wind tunnel and at Boundary Bay were scaled by choosing results for the same range of the dimensionless frequency $\omega \delta / U_\infty$, which in Favre et al ranges from 0 to 400. For the Boundary Bay experiment δ was taken to be 2×10^4 cm; U_∞ was 740 cm sec^{-1} (run 5e). These values of δ and U_∞ correspond to a frequency range of 0 to 2 Hz in the Boundary Bay spectra. The curvature of the "curve of maximum correlation" in Favre et al was measured from their Figure 7 and a mean vertical acceleration estimated from this; when scaled to the case of run 5e (air sensor 100 cm directly above the buoy sensor on the ground, hot-wire at the same height and 10 cm crosswind) the vertical acceleration amounted to -3 cm sec^{-2} . The acceleration had to be extrapolated from the results in Favre et al, since the lowest height at which they measured (that of their Figure 7) scaled to a 600

cm height at Boundary Bay.

In order to compare the Boundary Bay results with the accelerations estimated from Favre et al the vector differences between the pressure, wind speed cross-spectra at the two levels were determined. The amplitudes $\sqrt{C_o^2 + Q_u^2}$ of the cross-spectra between pressure and wind were drawn on a phasor diagram at angles to the real axis given by their phase ($\theta = \tan^{-1} (Q_u/C_o)$), and the vector difference taken between them at each frequency. Then the rms downwind velocity fluctuations (\underline{u}) from the hot-wire spectra were divided into the magnitudes $\Delta(\overline{pu})$ of the resulting differences to give Δp as a function of frequency; these were then summed from 0 - 2 Hz. The results of these calculations are given in Table A2.4.

The sum of the pressure differences is 1.7 dyne cm^{-2} . Over a height difference of 100 cm this gives a vertical pressure gradient of $1.7 \times 10^{-2} \text{ dyne cm}^{-2} \text{ cm}^{-1}$, which would produce a "typical" vertical acceleration

$$\frac{\partial w}{\partial t} = - \frac{1}{\rho} \frac{\partial p}{\partial z} \simeq -14 \text{ cm sec}^{-2} \quad \text{A2.1.}$$

This figure, although larger than the -3 cm sec^{-2} result extrapolated from the wind tunnel work, is not an order of magnitude larger. It seems possible therefore that the observed difference between the pressure, wind speed cross-spectra at the two heights is real, and is not associated with incorrect sensing by one of the instruments.

It is interesting to observe that the phase angles (Table A2.4) between the parts of the pressures coherent with \underline{u} at the two heights are neither at 180° or 90° , but are almost all confined to the region

between these two values. This fairly tight grouping is rather remarkable in view of the already small pressure, velocity coherences; if it is real, then the phase resolution of the instruments is better than might be gathered from the scatter in the direct phase comparisons (see Figure 85).

Another method of comparing observed with expected results is to estimate the vertical component of the wind speed w from

$$\sqrt{\overline{w^2}} / u_* = \text{constant}$$

where the expression is constant only if the air is neutrally stable. Assuming for the sake of argument that neutral stability existed for run 5e allows $\overline{w^2}$ to be estimated. Panofsky et al (1967) quote a value of 1.2 - 1.3 for the constant for measurements over land; measurements made at this Institute (Miyake et al, 1969) indicate that the constant is 1.4 for measurements over the sea. For run 5e u_* is 25 cm/sec; using 1.25 for the constant gives $\sqrt{\overline{w^2}} \approx 30 \text{ cm sec}^{-1}$. The "observed" vertical acceleration of 14 cm sec^{-2} would reduce this to zero in roughly 2.1 seconds; in this time an "eddy" at 100 cm height would travel horizontally about 10 meters. All of these values are appropriate for the flow.

Both of these discussions indicate that vertical accelerations near the ground can account for the observed differences in \overline{pu} coherence at the two levels. The main finding of this portion of the investigation is therefore that there probably exists a vertical pressure gradient near the ground in the atmospheric boundary layer, which exists in response to natural vertical accelerations in the flow. The exact size of the gradient and its variation with scale size are unknown, and

TABLE A2.4

Calculated Pressure Differences Between Air
and Ground Sensors for Run 5e

Frequency (Hz)	Bandwidth (Hz)	$\Delta \overline{pu}$	θ (degrees)	$\Phi_{uu}(f)$ (cm ² sec ⁻² Hz ⁻¹)	Δp (dyne cm ⁻²)
Notes:		(1)	(2)		(3)
0.0264	0.0305	216	156	1.93×10^4	-0.25
0.0591	0.0305	186	137	1.56×10^4	-0.25
0.0903	0.0305	135	147	7.75×10^3	-0.25
0.121	0.0305	91	112	7.6×10^3	-0.19
0.165	0.0610	35	116	4.4×10^3	-0.14
0.227	0.0610	5	94	2.4×10^3	-0.03
0.302	0.0916	12	71	1.8×10^3	-0.08
0.407	0.122	6	118	1.1×10^3	-0.06
0.543	0.153	4	58	8.9×10^2	-0.05
0.723	0.214	5	204	5.2×10^2	-0.09
0.965	0.275	5	145	3.8×10^2	-0.13
1.28	0.366	2	148	2.4×10^2	-0.08
1.71	0.488	0.5	74	1.5×10^2	-0.03
Total					-1.7

- Notes: 1. Units of $\Delta \overline{pu}$, the vector difference between the air and ground p,u cross spectra, are (dyne cm⁻²) · (cm sec⁻¹) Hz⁻¹.
2. θ is the phase of $\Delta \overline{pu}$.
3. $\Delta p = (\Delta \overline{pu} / \sqrt{\Phi_{uu}}) \times \sqrt{\text{Bandwidth}}$.

deserve further investigation.

A2.7 Conclusions

The general conclusions reached are related to the objectives of the experiment, which were first, to test the two sensors for dynamic pressure "noise" and second, to make investigations of the turbulent pressure field with a view to designing future experiments.

A2.7.1 Sensor Tests

The first objective has been met, with reservations. The two instruments produce power spectra which over the mid-frequency range (0.1 - 1 Hz) are identical within expected error. The higher spectral estimates in the low-frequency pressure power spectra of the buoy sensor are satisfactorily explained as greater "thermal noise" in that sensor; this phenomenon should introduce little or no error into the pressure-wave correlation experiments. The high-frequency "hump" in the buoy sensor is not well-understood, but is at too high a frequency to have much effect on the pressure-wave correlations.

The cross-correlations between pressure sensors behave very well. The only cause for concern lies in the low-frequency phase differences between the buoy and air sensors and the reference sensor (both lag it by about 20°); it is considered that the differences are barely significant at the lowest frequencies (≤ 0.1 Hz) only, and therefore need not be taken seriously for work over waves.

The principal cause for concern about whether the buoy sensor signal is contaminated by dynamic pressures is in the correlations with the hot-

wire velocity signal. The coherences with velocity are higher by a factor of two for the buoy sensor (30 cm below and 10 cm crosswind from the hot-wire) than they are for the air sensor (at the same height as, and 10 cm crosswind from, the hot-wire). It is found that the observed coherence differences can be explained if it is assumed that a vertical pressure gradient exists in the flow between the pressure sensors; there is some experimental evidence (Favre et al 1957) that a pressure gradient does exist and that its magnitude is approximately that required to explain the observations.

A2.7.2 The Structure of the Pressure Field

The second objective of the experiment was to investigate the structure of the pressure field and thus lay the groundwork for a more definitive future experiment. Priestley (1965), in a series of well-controlled experiments, has looked at the crosswind and downwind structure of the pressure field in the atmosphere. The present results substantially agree with his, and the wind tunnel work of Willmarth and Wooldridge (1962), although in the latter case the comparison is difficult because the scaling parameters used in the wind tunnel are not known for the field work. The vertical structure of the pressure field has never before been studied. It should be noted here that the results quoted concerning vertical structure are from Elliott's instrument, and are thus his work. They are presented here with his permission for completeness only, and the interpretations are those of the writer.

The conclusions reached were:

1. The power spectra of five runs, all taken on the same day at

various wind speeds, are grouped fairly well when plotted in nondimensional form if ρu_*^2 , the ground shear stress, is used as the parameter. This indicates its importance in determining the pressure field above the ground.

2. From the variation in coherence between air and ground sensors with vertical separation, it is inferred that the vertical scale of the pressure-generating eddies is slightly compressed (by a factor of two) with respect to the horizontal scales.

3. From the differences in coherence between sensors on the ground depending on whether they are crosswind or downwind from each other, the ratio D/C of downwind to crosswind scales is found to be about ten, which is in fairly good agreement with Priestley (1965), who found the two scales to be related by $C \approx 0.8D^{0.7}$.

4. From the phase relation between sensors on the ground placed downwind from each other, two broadband advection velocities for the pressure eddies were inferred. They were in the ratios of 0.5 and 0.6 to an estimate of U_∞ , the "free-stream velocity" in the boundary layer over the ground, and showed rough agreement with the wind tunnel work (Corcos 1963).

5. Where the ground sensor and air sensor agreed, they showed large phase differences from the hot-wire signal at high frequencies; these amounted to about 180° at 5 Hz. Since, however, coherences in both cases were less than 0.1 at high frequencies and hence not statistically significant, no inferences were attempted.

6. Coherences of the horizontal component of the turbulent wind

speed u with two pressure signals, one from a sensor on the ground and one from a sensor in the air 100 cm vertically above the ground sensors, showed significant differences. These can be explained as being caused by vertical accelerations in the flow near the ground. The phase relations among p , u , and w show some order in the results presented; it is felt that an experiment carefully designed to map out these phase relations is required before the structure of the vertical acceleration and pressure fields can be fully understood.

APPENDIX 3:

THE INTERACTION OF SWELL WITH AN OPPOSING WIND

A3.1	Introduction	219
A3.2	Theory	220
A3.3	The Direction of Travel of the Waves	222
	A3.3.1 Phase Information	223
A3.4	Phase Corrections	224
A3.5	Comparison of Observed Amplitudes with Potential Theory .	225
A3.6	The "Wave Driven Wind"	228
A3.7	Wave Damping	228
A3.8	Momentum Flux	231
A3.9	Conclusions	232

APPENDIX 3:

THE INTERACTION OF SWELL WITH AN OPPOSING WIND

A3.1 Introduction

One of the data runs analysed was taken with very low wind speeds (November 17, 1967: see "Results", Table 6.1). The wind speed was so low (100-200 cm/sec) that the water surface was not ruffled. The buoy pressure sensor, the wave probe, and the sonic anemometer were operated throughout the run, giving simultaneous data on surface pressure and elevation and the three components of the total wind vector. The only water motions present were those caused by swell. In the course of the run, a well-defined group of waves which has an average period of four seconds passed through the measurement site. They were presumably the wake from some large, fairly fast freighter. They were noted in the log of the run, but their direction of travel was unfortunately not mentioned and so this information was lost.

When the run was played back later on a chart recorder the effects of this group of waves were clearly visible, not only on the pressure and vertical velocity but also on the horizontal velocity traces.

The object of this Appendix will be to interpret these traces, and to see how well they agree with first-order potential flow theory (with a brief excursion into second-order theory, to calculate transport velocities in the air). Energy and momentum inputs to the waves will be calculated and from these the wave damping by the wind is determined. It

is hoped too that excitement may be stirred in the heart of a future student, who may then decide to investigate this fascinating (to me) sidelight more thoroughly.

A3.2 Theory

The potential theory for gravity waves on a density discontinuity between two fluids when there is a uniform mean velocity U_0 in the upper fluid is worked out in many texts; the present brief development is from Lamb (1932, § 232). The flow in both fluids is considered to be irrotational, incompressible, and inviscid. The velocity potential ϕ is introduced so that

$$u = - \partial \phi / \partial x, \quad w = - \partial \phi / \partial z \quad \text{A3.1}$$

where u , x , w , and z are horizontal and vertical air velocities and distances respectively, positive to the right and upwards. η is displacement from the mean water surface; $k = 2\pi/\lambda$ is wave number and wavelength, c is wave phase speed, and $\omega = 2\pi f$ the radian frequency.

The condition that the vertical velocity of the surface be given by the total time derivative of η gives, to first order in η ,

$$\left[\partial \eta / \partial t + U_0 \partial \eta / \partial x = - \partial \phi / \partial z \right]_{z=0} \quad \text{A3.2}$$

as the required surface boundary condition. The governing equation is Laplace's equation:

$$\partial^2 \phi / \partial x^2 + \partial^2 \phi / \partial y^2 = 0 \quad (\text{see Lamb, § 227}) \quad \text{A3.3.}$$

If surface elevation is taken to be a wave of amplitude $a \ll \lambda$, periodic in x and t and travelling in the plus x direction

$$\eta = ae^{ik(ct-x)}, \quad A3.4$$

then the velocity potential for the air becomes to first order

$$\phi = -U_0 x + Be^{-kz}e^{ik(ct-x)}. \quad A3.5$$

Substitution of A3.4 and A3.5 into A3.2 to obtain B gives

$$= -U_0 x = ia (U_0 - c) e^{-kz}e^{ik(ct-x)}. \quad A3.6$$

The air pressure is obtained from Bernoulli's equation for irrotational motion;

$$\frac{p}{\rho} = \frac{\partial \phi}{\partial t} - gz - \frac{1}{2} \left\{ \left(\frac{\partial \phi}{\partial x} \right)^2 + \left(\frac{\partial \phi}{\partial z} \right)^2 \right\} + \text{constant}, \quad A3.7$$

where ρ is the density of the air and g the acceleration due to gravity.

Substitution from A3.6 gives

$$p = -\rho \left\{ gz + kae^{ik(ct-x)}e^{-kz} (U_0 - c)^2 \right\} + \text{constant} \quad A3.8$$

where $-\frac{1}{2} \rho U_0^2$ has been absorbed in the constant.

At the water surface $z = \eta$,

$$p = -\rho \left\{ g\eta + k\eta (U_0 - c)^2 \right\} + \text{constant} \quad A3.9$$

where $\eta e^{-k\eta}$ is replaced by η to this approximation. If one subtracts the mean from A3.9 it can be put in the form

$$p - \bar{p} = -\rho g\eta \left\{ 1 + \left(1 - \frac{U_0}{c}\right)^2 \right\}; \quad A3.10$$

this is the fluctuating pressure which would be present at a buoy floating on the water surface in the presence of a steady, vertically uniform

wind U_0 . It is interesting to note that if U_0 is zero A3.10 becomes

$$(p - \bar{p})U_0 = 0 = -2 \rho g \eta \quad \text{A3.11.}$$

Returning to examine A3.10, it can be seen that if $\frac{U_0}{c}$ is negative (waves travelling against the wind) pressure fluctuations of many times $\rho g \eta$ could be observed. Taking the real part of A3.4, A3.1, and A3.10, where A3.6 is used, gives as the first-order approximation for a sinusoidal wave observed at $x = 0$,

$$\eta = a \cos kct \quad \text{A3.12}$$

$$u = U_0 + ka (U_0 - c) e^{-kz} \cos kct \quad \text{A3.13}$$

$$w = ka (U_0 - c) e^{-kz} \sin kct \quad \text{A3.14}$$

$$p - \bar{p} = -\rho g a \cos kct \left\{ 1 + \left(1 - \frac{U_0}{c} \right)^2 \right\} \quad \text{A3.15}$$

It should be noted in A3.13, 14 and 15 that the quantity $(U_0 - c)$ becomes $(U_0 \cos \theta - c)$ for U_0 travelling at an angle θ to \underline{c} .

A3.3 The Direction of Travel of the Waves

The chart recordings showing the signals as recorded on tape (amplified and inverted where necessary to preserve the phase relations among the original signals) are shown in Figure 93. The group of four-second waves in the time interval from 420 to 500 seconds stand out clearly against the background of 1 - 1.5 second waves and turbulent fluctuations. The three bottom traces are from the sonic anemometer, being the two horizontal wind components along the sonic paths A and B (shown in Figure 94) and the vertical velocity w in that order. The orientation of the anemometer, wave probe, and pressure sensor as they

were during the run are shown in Figure 94; the sonic anemometer was at a height of 1.75 meters above the mean water level. It is seen that the effect of the waves on the wind was much greater along path B than along path A; therefore the waves must have been travelling in a direction roughly normal to A. The sense, however, is indeterminate.

The digital analysis produces for each data block, as well as spectra, the mean values of the modulus and direction of the wind speed vector recorded by the sonic anemometer (see "Data Analysis and Interpretation", p. 86). These were plotted and are shown in Figure 95, in the hope that they could be used to determine the direction of the waves on the assumption that there would be a "wave-driven wind" which would cause a clearly recognizable departure from "ambient" conditions. This was not found; random fluctuations among block means were large enough to completely hide any such effect (which is only several cm/sec; see p. 228.

A3.3.1 Phase Information

In order to determine the phase of the pressure and the vertical and horizontal velocities with respect to η , the wave signal, cross-spectra of all the signals (pressure, sonic A, sonic B, and sonic w) with η were computed. Cross-spectra were computed on only the short (the 4-second group lasted about 30 seconds) section of the total run in which the wave group occurred (see Figures 93, 95). Coherences between η and other signals are shown in Figure 96 and phases in Figure 97. They show a large peak in coherence near 0.25 Hz and that p leads η by 165° , sonic A and B lead η by 18° and sonic w leads η by 98° . Note that the

coherence at 0.25 Hz between the sonic A signal and η is somewhat less than that between sonic B and η .

All of these phases are in rough agreement with the predictions of potential theory (Equations A3.12 to A3.15) if it is assumed that the waves were travelling roughly against the wind.

A3.4 Phase Corrections

If the waves were in fact travelling into the wind, and for lack of evidence to the contrary this assumption will be taken as the basis for future calculations, then the problem of phase corrections to the sonic signals because of the 1.2 meter horizontal separation of the anemometer from the wave probe and pressure sensor must be considered. It will be assumed that the wave direction was perpendicular to the sonic A direction (see Figure 94). Then from the distances involved the center of measurement of the sonic anemometer was about 30 cm towards the source of the waves from the wave probe. To calculate the correction to the phase of the cross-spectra the wavelength of the waves must be known. The period of the waves was four seconds. The water depth during the run was 3 m. The wavelength in water of depth h can be calculated from

$$c^2 = f^2 \lambda^2 = \frac{g}{k} \tanh kh = \frac{\lambda g}{2} \tanh \frac{2\pi h}{\lambda}; \quad \text{A3.16}$$

the result of solving this transcendental equation for $f = 0.25$ Hz gives a value for λ of 19 meters; this when put into Equation A3.16 gives a value for c of 480 cm/sec.

Knowing the wavelength, the phase angle correction to the sonic anemometer signals can now be calculated. It is

$$\delta\theta = \frac{30}{1900} \times 360 = 5.7 \approx 6^\circ,$$

and the sonic signals will lead the wave and pressure signals by this amount. The corrected phase angles between the wave signal and the other variables are displayed in Table A3.1.

TABLE A3.1

Variables	Observed* Phases	Expected* Phases
η, P	-165°	-180°
η, B	-12°	0°
η, w	-92°	-90°

*Negative phase angles indicate that η lags the variable concerned.

Also shown are the phases from Equations A3.12 to Ae.15 expected from potential flow theory. The agreement of phases with potential theory, though not exact, is seen to be quite good.

A3.5 Comparison of Observed Amplitudes with Potential Theory

The part p_s of the fluctuations in air pressure p which is associated with the waves can be estimated from the observed cross-spectra using the relation (see "Data Analysis and Interpretation", Equations 5.2 and 5.3)

$$\left(\overline{p_s^2}\right)^{\frac{1}{2}} = \sum_{f_i} \left\{ Co^2 p_{\eta}(f_i) + Qu^2 p_{\eta}(f_i) \right\}^{\frac{1}{2}} \sqrt{(\Delta f)_i} / (\Phi_{\eta}(f_i))^{\frac{1}{2}} \text{ dyne cm}^{-2}$$

A3.17

where the sum is taken over the three frequencies $f_i = 0.195, 0.292$, and

0.390 Hz. These are the three frequencies which are nearest 0.25 Hz, the observed frequency of the 4-second group; $(\Delta f)_i$ is the bandwidth associated with the i^{th} frequency. Similar calculations can be done to obtain from their spectra the vertical and horizontal wind velocities $\left(\overline{w_s^2}\right)^{\frac{1}{2}}$ and $\left(\overline{u_s^2}\right)^{\frac{1}{2}}$ associated with the air flow over the waves. All of these quantities are compared in Table A3.2 with predictions from potential theory computed from Equation A3.12 to A3.15 (subscript "t") and visual estimates of amplitudes (subscript "v") obtained from chart recordings.

The functions seen by the various sensors if potential flow exists are given by Equations A3.12 to A3.15. The height of the anemometer was $z = 175$ cm; the mean wind speed $U_0 \simeq 200$ cm/sec. The waves have wave-number $k = \frac{2\pi}{1900} \simeq 3.3 \times 10^{-3} \text{ cm}^{-1}$, and speed $c = -480$ cm/sec; if the direction of U_0 is taken (from the sonic analysis) to be 125° (True), and of c to be 285° (True) perpendicular to A, then this gives

$$(U_0 \cos(160^\circ) - c) \simeq 670 \text{ cm/sec.}$$

This when substituted in Equations A3.12 to A3.15 gives the fluctuations

$$\begin{aligned} u &\simeq 1.2 a \cos kct = 1.2 \eta \text{ cm/sec} \\ w &\simeq 1.2 a \sin kct = -1.2 \eta^* \text{ cm/sec} \\ (p - \bar{p}) &\simeq -3 \rho g \eta \text{ dynes/cm}^2 \end{aligned} \tag{A3.18}$$

for the requisite predictions from potential theory (the asterisk denotes a complex conjugate).

The visual, spectral, and theoretical values presented in Table A3.2 are seen to agree to well within one order of magnitude, indicating that

TABLE A3.2

Comparison of Theoretical and Observed Pressure and Velocity
Amplitudes over Swell Moving Against the Wind

η_v	$(\overline{\eta_s^2})^{\frac{1}{2}}$	u_v	$(\overline{u_s^2})^{\frac{1}{2}}$	u_t	w_v	$(\overline{w_s^2})^{\frac{1}{2}}$	w_t	p_v	$(\overline{p_s^2})^{\frac{1}{2}}$	p_t
cm			cm/sec			cm/sec			dyne/cm ²	
10	8	6	12	10	6	9	10	30	34	24

Subscripts:

"v" : visual estimates from chart recordings

"s" : estimates from spectra using relations analagous to A3.17.

"t" : theoretical predictions from Equations A3.12 to A3.15, where
 $(\overline{\eta_s^2})^{\frac{1}{2}}$ is substituted for a ; see p. 226.

to first order potential flow theory is successful in predicting the observed results. The differences between spectra and predicted amplitudes are small enough to be within the expected errors in the calculations, which are admittedly "quick and dirty".

A3.6 The "Wave Driven Wind"

Harris (1966) has measured mean velocities above waves which appear to be associated with them, in a wind-water tunnel. He compares their magnitudes with the Stokes' drift velocity in the air, given by

$$\bar{U}_{\text{stokes}} = a^2 c k^2 e^{-2kz} \quad \text{A3.19.}$$

Since this "mean drift" cannot be observed by an anemometer at a fixed height and horizontal position (it sees only sinusoidal motion), it is not clear what association it has with the "wave driven wind" observed by Harris; since he does, however, and since the velocities he observes are about 100 times those calculated from A3.19, the calculation will be repeated here for the present conditions. Using the values of c , k , and z from p.224 and $a = 10$ cm for the wave amplitude gives

$$\begin{aligned} \bar{U}_{\text{stokes}} &\approx 0.2 \text{ cm/sec, and} \\ 100 \bar{U}_{\text{stokes}} &= 20 \text{ cm/sec.} \end{aligned}$$

Thus it is expected that the mean winds observed by Harris would be too small to be observed in this experiment, since ambient fluctuations in wind speed (and direction) were large (see Figure 95).

A3.7 Wave Damping

The phase of the pressure relative to the waves (p leads η by 165° ,

a 15° discrepancy from the potential flow prediction) indicates that wave damping was occurring. The analysis system (see "Data Analysis and Interpretation", p. 87) calculates \bar{E} , the rate of change of wave energy per unit area per unit time, for each block of data analysed; \bar{E} for the blocks in which the four-second wave group appeared was negative, and averaged about $-20 \text{ erg cm}^{-2}\text{sec}^{-1}$. Since the total wave energy is given by

$$\bar{E} = \frac{1}{2} \rho_w g a^2 \quad (\text{Lamb, } \S \text{ 230}) \quad \text{A3.20;}$$

where ρ_w is the density of water, then for an amplitude of 10 cm $\bar{E} \approx 5 \times 10^4 \text{ erg cm}^{-2}$, and the damping coefficient \bar{E}/\bar{E} for the wave group is $4 \times 10^{-4} \text{ sec}^{-1}$, giving the waves a time of about 40 minutes to reach $1/e$ of their initial amplitude, or a Q of 3900. Miles (1957) puts his results in terms of

$$\frac{1}{Q} = \zeta = \frac{\bar{E}}{\omega \bar{E}}, \quad \text{A3.21}$$

the "fractional increase in wave energy per radian"; here ζ works out to about -2.5×10^{-4} . This negative value is slightly less than positive values obtained in situations of active wave generation; see "Results", Table 6.6 (it is realized, of course, that Miles' (1957) mechanism is inapplicable here; the comparison is made with measured values, not theoretically predicted ones).

Phillips (1966) makes an estimate of the "attenuation coefficient" of waves in an adverse wind on the assumption that the attenuation is caused by the interaction of the turbulent Reynolds stresses with the wave-induced undulations in the flow. The attenuation caused by this

mechanism is exponential; he writes it as

$$E(t) = E(0)e^{-2\gamma_w t} \quad \text{A3.21,}$$

giving for ζ , from Equation A3.21,

$$\zeta = -\frac{2\gamma_w}{\omega} \quad \text{A3.22.}$$

Phillips plots $-\gamma_w/\omega$ against c/u_* in his Figure 4.1.19 for the range $5 \leq c/u_* \leq 50$. u_* for the period of time while the wave group was passing the sensors was measured with the sonic anemometer, giving

$$\begin{aligned} u_* &= (\overline{uw})^{\frac{1}{2}} \\ &= (\tau_{\text{sonic}}/\rho_a)^{\frac{1}{2}} \\ &\approx 1.3 \text{ cm/sec;} \end{aligned}$$

this, with a c for the waves of 480 cm/sec gives a value for c/u_* of 375, far outside of Phillips' range. The ζ calculated from Phillips' figure for $c/u_* \approx 50$ is about -6.5×10^{-4} ; it increases throughout the range with increasing c/u_* . Since at $c/u_* = 50$ it is already more than double the observed ζ , the extrapolation of Phillips' results to higher values of c/u_* is unreasonable. The damping regime discussed by Phillips involves interaction of turbulent Reynolds stresses with the waves; the small value of u_* measured in this experiment indicates that these stresses were very small and suggests that the mechanism which was damping the waves was of a different sort; the fact that the theoretical predictions are higher than the observed values of ζ (whereas in the case of wave generation the predictions of this same theory underestimate observed rates of wave growth) strongly suggests that Phillips' theoretical curves

for $-\tau_w/\omega$ will reach a maximum and decrease at values of c/u_* higher than the range plotted.

A3.8 Momentum Flux

The relative phases of the pressure and sonic B signals show the greatest deviations from potential theory; p leads η by 165° , 15° less than the predicted 180° , while sonic B leads η by 12° , 12° more than the predicted 0° . This fact observed alone seems contradictory; the phase of the pressure signal indicates that the non-potential flow process shifted the streamlines of the mean flow so they lagged the waves; the sonic B signal indicates the opposite. At the same time the sonic w signal has no significant phase shift from 90° . This means that sonic w leads sonic B by 80° ; this difference from quadrature indicates the presence of momentum transfer. Further, the 10° shift is in the direction of a positive \overline{uw} covariance or a negative wind stress $\tau = - \rho_a \overline{uw}$, indicating that momentum transfer from waves to wind was occurring. If the stress is calculated from the co-spectrum between sonic B and w in the frequency range of the waves,

$$\tau_{\text{sonic}} = - \rho_a \overline{uw} = - 0.002 \text{ dyne cm}^{-2}.$$

This, then, is to be compared with that calculated from the pressure-waves correlation (for the frequency range of the four-second group)

$$\tau_w = \frac{\overline{E}}{C} = - 0.04 \cos 20^\circ \approx - 0.04 \text{ dyne cm}^{-2}.$$

The stresses calculated from the two methods have the same sign but differ in magnitude by a factor of 20.

The fact that the stresses are of the same sign indicates self-consistency in the measurements; if energy was being transferred from waves to wind the momentum transfer would be expected to be in the same direction.

The difference in stress measured at the two levels is outside the limits of expected experimental error. Even quite unreasonable shifts in the angle of the incoming waves with respect to the wind would not bring the two into agreement. Therefore it appears that a stress gradient may have existed over the waves. If this were so, then its approximate size would be

$$\frac{\Delta \tau}{\Delta z} \simeq -2 \times 10^{-4} \text{ dyne cm}^{-2}/\text{cm}.$$

This gradient would create a horizontal acceleration

$$\frac{\partial u}{\partial t} = -\frac{1}{\rho} \frac{\partial \tau}{\partial z} \simeq 0.17 \text{ cm sec}^{-2}.$$

If Δt is taken as 30 seconds (the time for the group to pass by), then the maximum change in horizontal velocity caused by the gradient would be 5 cm/sec, which is a fairly small value. Therefore although the stress gradient appears to have existed, its effect on the flow was probably not large. Because stress gradients have not often been observed, it would be interesting in any future work to make attempts to define them in detail.

A3.9 Conclusions

A section of record of about 30 seconds duration, containing simultaneous information on static pressure and the three components of the fluctuating wind speed over a group of about seven waves of 4 second

period which were running against the mean wind, has been analysed in detail.

The results of the analysis show that to first order the flow over the waves is predicted by simple potential theory. They show further that deviations from potential flow, although small, are of crucial importance to the time history of the waves.

Three phenomena were investigated. The first, the "wave-driven wind" observed by Harris (1966) proved to be hidden in ambient mean wind speed and direction fluctuations, and was not investigated further.

The second was energy transfer. The particular wave group studied was in a regime of damping caused by adverse winds. The damping coefficient calculated from the pressure, waves correlation gives a Q for the wave group of 3900. This represents a rate of damping slightly smaller than rates of growth observed in situations of weak but active wave generation. The rate of damping is also much smaller than that predicted from theoretical considerations by Phillips (1966); it is thought that the flow regime in the experiment was quite different from that assumed by Phillips.

The third phenomenon investigated was momentum transfer. It was found to be negative (from waves to wind) both by correlations of pressure with wave elevations at the sea surface and by sonic B - sonic w correlations measured at 1.75 m above the surface. The stress at 1.75 m proved to be less than that at the surface, indicating a weak vertical stress gradient of about 2×10^{-4} dyne cm^{-2}/cm .

While the phase of the pressure signal relative to that of the waves

was shifted from 180° to $+165^\circ$, the phase of the sonic B signal with respect to the waves was shifted from 0° to $+12^\circ$, both by the wave damping mechanism. The sonic w signal remained at about 90° with respect to the waves. These facts indicate (and again it must be stressed that the conclusions are highly speculative) that whereas the pressure phase indicates that the streamlines close to the water surface are shifted so they lag the waves, at only 0.1 wavelength above the surface the streamlines appear to be arranged so that w remains in quadrature with the waves while u leads them.

The question of the mechanism of energy and momentum transfer from waves travelling against the wind remains an open one. Miles' (1957) theory of shear flow instability is obviously inapplicable, since in this case there is no "critical height" at which wave speed equals wind speed; this does not of course rule out the possibility that other shear flow instability mechanism may be operative.

If the damping has anything to do with mean shear flow instability, then it will be necessary to know what the structure of the mean flow is like over such waves, perhaps very close to the water surface. If the mechanism involves turbulence, then the structure of the turbulence must also be known and separated from the "undulance" discussed here.

It seems to the author that a more detailed study is required of wave damping under light wind and adverse wind conditions; the present results generate more problems than they solve. Because the problem, like that of wave generation, is of practical importance in wave and swell forecasting, the results of such a study would be rewarding and of more than academic interest.

BIBLIOGRAPHY

- Auerbach, J. and P. D. Richardson (1967) Development of wind-driven waves in a cylindrical vessel. *Phys. Fluids* 10 (6), 1342-4.
- Barnett, T. P. and J. C. Wilkerson (1967) On the generation of ocean wind waves as inferred from airborne radar measurements of fetch-limited spectra. *J. Mar. Res.* 25(3), 292-321.
- Benjamin, T. B. (1959) Shearing flow over a wavy boundary. *J. Fluid Mech.* 6, 161-205.
- _____ and J. E. Feir (1967) The disintegration of wave trains on deep water. *J. Fluid Mech.* 27 (3), 417-30.
- Bingham, C., M. D. Godfrey and J. W. Tukey (1967) Modern techniques of power spectrum estimation. *IEEE Transactions on Audio and Electroacoustics*, Vol. AU-15 (2), 56-66.
- Blackman, R. B. and J. W. Tukey (1959) "The Measurement of Power Spectra." Dover Publications, Inc., New York. 190 pp.
- Bole, J. B. and E. Y. Hsu (1969) Response of gravity water waves to wind excitation. *J. Fluid Mech.* 35 (4), 657-75.
- Bryant, P. J. (1966) Wind generation of water waves. Ph.D. dissertation, University of Cambridge.
- Burling, R. W. (1955) Wind generation of waves on water. Ph.D. dissertation, Imperial College, University of London.
- Cohen, L. S. and T. J. Hanratty (1965) Generation of waves in the concurrent flow of air and a liquid. *A.I. Ch. E.J.* 11, 138-44.
- Cooley, J. W. and J. W. Tukey (1965) An algorithm for the machine calculation of complex Fourier series. *Math. of Comput.* 19, 297-301.
- _____ (1966) "PKFORT: Finite complex Fourier transform." IBM SHARE Program Library, No. SDA3465.
- Conte, S. D. and J. W. Miles (1959) On the numerical integration of the Orr-Sommerfeld equation. *J. Soc. Indust. Appl. Math.* 7, 361-66.
- Corcos, G. M. (1963) The structure of the turbulent pressure field in boundary-layer flows. *J. Fluid Mech.* 18, 353-78.
- Cornish, V. (1934) "Ocean Waves and Kindred Geophysical Phenomena." London: Cambridge University Press, 164 pp.
- Cox, C. S. (1958) Measurements of slopes of high-frequency wind waves. *J. Mar. Res.* 16, 199-225.

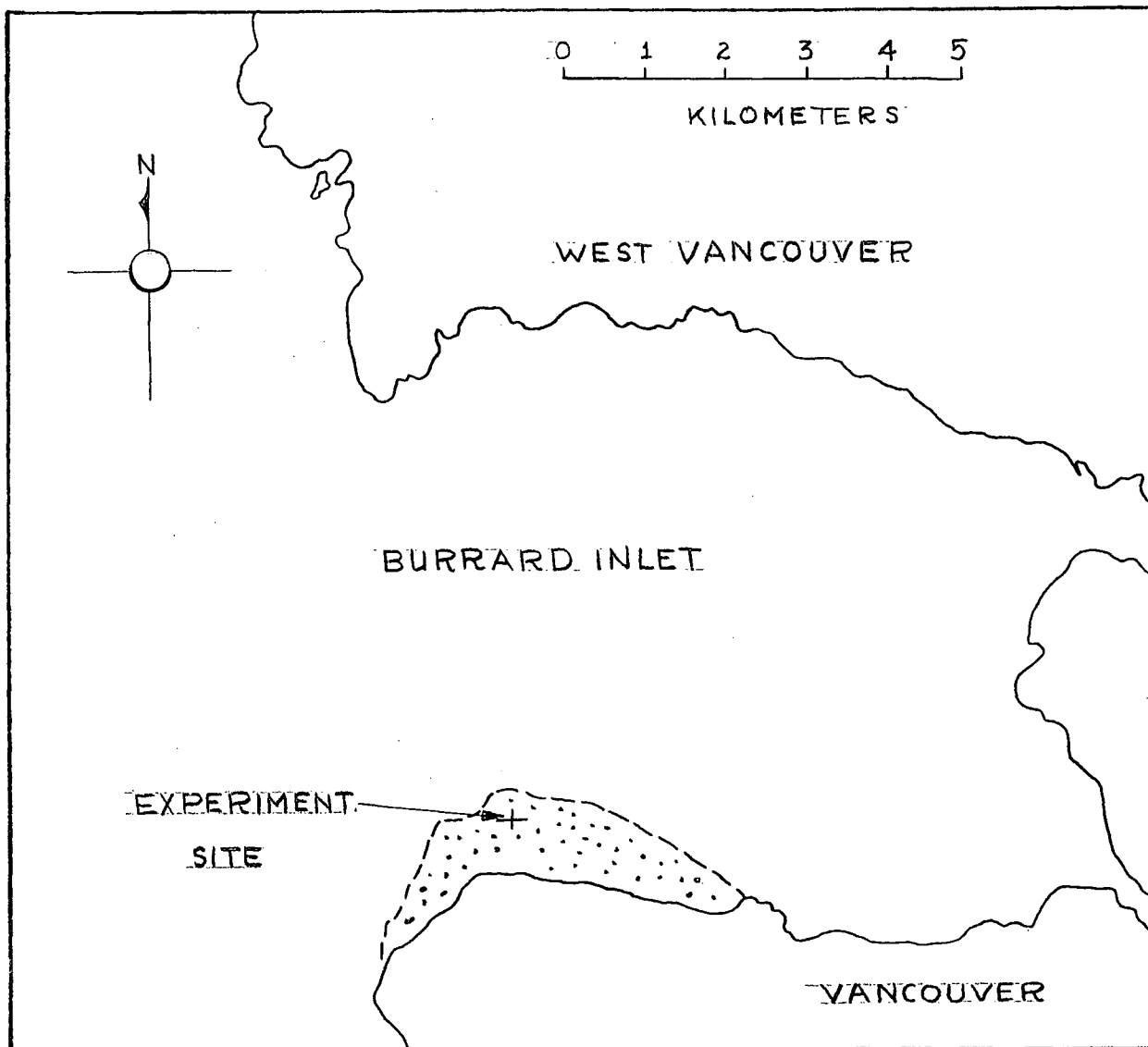
- _____ and W. H. Munk (1954a) Statistics of the sea surface derived from sun glitter. *J. Mar. Res.* 13, 198-227.
- _____ (1954b) Measurements of the roughness of the sea surface from photographs of the sun's glitter. *J. Optical Soc. Amer.* 44, 838-50.
- Eckart, C. (1953) The generation of wind waves over a water surface. *J. Appl. Phys.* 24, 1485-94.
- Ellison, T. H. (1965) Atmospheric turbulence. "Surveys in Mechanics" (ed.) G. K. Batchelor). Cambridge University Press, pp. 400-30.
- Favre, A. J., J. J. Gaviglio and R. Dumas (1957) Space-time double correlations in a turbulent boundary layer. *J. Fluid Mech.* 3, 313.
- Gilchrist, A. W. R. (1965) On the directional spectrum of ocean waves. Ph.D. dissertation, University of B. C. 166 pp.
- Gorshkov, N. F. (1967) Measurements of the spectrum of pressure micro-pulsations in the near-earth layer of the atmosphere. *Izv., Atmospheric and Oceanic Physics* 3 (4) 447-51.
- Gossard, E. E. (1960) Spectra of atmospheric scalors. *J. Geophys. Res.* 65 (10), 3339-51.
- Hamada, T. (1963) An experimental study of development of wind waves. Port and Harbour Res. Inst. (Japan) Report No. 2. Kanagawa.
- Hanratty T. J. and P. E. Woodmansee (1965) Stability of the interface for a horizontal air-liquid flow. "Proceedings of Symposium on Two-Phase Flow," Volume 1. Devon: University of Exeter.
- Harris, D. L. (1966) The wave driven wind. *J. Atmos. Sci* 23 (6), 688-93.
- Hasselmann, K. (1960) Grundgleichungen der seegangs voraussage. *Shiffstechnik* 7, 191-5.
- _____ (1963) On the non-linear energy transfer in a gravity wave spectrum. Part 2. *J. Fluid Mech.* 15, 273-81. Part 3. *Ibid.* 15, 385-98.
- Havelock, T. H. (1940) The pressure of water waves upon a fixed obstacle. *Proc. Roy. Soc. A* 175, 409-29.
- Helmholtz, H. (1868) Über discontinuierliche flüssigkeitsbewegungen. *Mber. preuss. Akad. Wiss.*, pp. 215-28.
- Hidy, G. M. and E. J. Plate (1965) On the frequency spectrum of wind generated waves. *Phys. Fluids* 8, 1387.
- _____ (1966) Wind action on water standing in a laboratory channel. *J. Fluid Mech.* 26, 651-88.

- Hires, R. I. (1968) An experimental study of wind-wave interactions. Chesapeake Bay Inst., Johns Hopkins University Tech. Rep. No. 37, 169 pp.
- Holmes, P. (1963) Wave generation by wind. Ph.D. dissertation, University of Wales (Swansea).
- Jeffreys, Sir H. (1925) On the formation of water waves by wind. Proc. Roy. Soc. A 110, 341-7.
- Kinsman, B. (1960) Surface waves at short fetches and low wind speeds --a field study. Chesapeake Bay Inst., Johns Hopkins University Tech. Rep. No. 19 (Vol. 1), 175 pp.
- Kolesnikov, A. G. and G. E. Kononkova (1961) Instrumental determination of energy transmitted by normal wind pressure to the surface of sea waves. Izvestia, Geophys. Ser., pp. 1551-1559.
- _____ and V. V. Efimov (1962) Apparatus for the measurement of the energy transmitted to ocean waves by the normal pressure of the wind. Okeanologia, Akademii Nauk SSR 4 (3), 505-12.
- Krümmel, O. (1911) "Handbuch der Ozeanographie," Volume 2. Stuttgart. 764 pp.
- Lamb, Sir H. (1932) "Hydrodynamics" (6th edition). Cambridge University Press (New York: Reprinted by Dover Publications, Inc., 1945). 738 pp.
- Lighthill, M. J. (1962) Physical interpretation of the mathematical theory of wave generation by wind. J. Fluid Mech. 14, 385-98.
- Lin, C. C. (1955) "The Theory of Hydrodynamic Stability." Cambridge University Press. 155 pp.
- Lock, R. C. (1954) Hydrodynamic stability of the flow in the laminar boundary layer between parallel streams. Proc. Camb. Phil. Soc. 50, 105-24.
- Longuet-Higgins, M. S. (1969a) On the action of a variable stress at the surface of water waves. Phys. Fluids (in the press).
- _____ (1969b) A nonlinear mechanism for the generation of sea waves. Proc. Roy. Soc. A (in the press).
- _____, D. E. Cartwright and N. D. Smith (1963) Observations of the directional spectrum of sea waves using the motions of a floating buoy. "Ocean Wave Spectra." Englewood Cliffs, N. J.: Prentice-Hall, pp. 111-32.
- Lumley, J. L. and H. A. Panofsky "The Structure of Atmospheric Turbulence." New York: Interscience. 239 pp.

- Miles, J. W. (1957) On the generation of surface waves by shear flows. J. Fluid Mech. 3, 185-204.
- _____ (1959a) On the generation of surface waves by shear flows. Part 2. J. Fluid Mech. 6, 568-82.
- _____ (1959b) On the generation of surface waves by shear flows. Part 3. J. Fluid Mech. 6, 583-98.
- _____ (1960) On the generation of surface waves by turbulent shear flows. J. Fluid Mech. 7, 469-78.
- _____ (1962) On the generation of surface waves by shear flows. Part 4. J. Fluid Mech. 13, 433-48.
- _____ (1965) A note on the interaction between surface waves and wind profiles. J. Fluid Mech. 22, 823-7.
- _____ (1967) On the generation of surface waves by shear flows. Part 5. J. Fluid Mech. 30, 163-75.
- Mitsuta, Y., M. Miyake and Y. Kobori (1967) Three dimensional sonic anemometer-thermometer for atmospheric turbulence measurement. Kyoto University Internal Report; 10 pp.
- Miyake, M. M. et al (1969) Intercomparison of turbulent fluxes over water determined by aerodynamic and eddy correlation techniques. Quart. Jour. Roy. Met. Soc. (in the press).
- Motzfeld, H. (1937) Die turbulente strömung an welligen wänden. Z. angew Math. Mech. 17, 193-212.
- Munk, W. H. (1955) High frequency spectrum of ocean waves. J. Mar. Res. 14, 302-14.
- Neumann, G. (1953) On ocean wave spectra and a new method of forecasting wind-generated sea. Beach Erosion Board, U. S. Army Corps of Engineers, Tech. Mem. No. 43, 42 pp.
- Panofsky, H. A., N. Busch, B. Prasad, S. Hanna, E. Peterson and E. Mares (1967) Properties of wind and temperature at Round Hill, South Dartmouth, Mass. Res. and Dev. Tech. Rep. ECOM-0035-F, U. S. Army Electronics Command, Fort Huachuca, Arizona.
- Patton, R. S. and H. A. Marmer (1932) The waves of the sea. "Physics of the earth," Volume 5, Oceanography Nat. Res. Council. pp. 207-28.
- Phillips, O. M. (1957) On the generation of waves by turbulent wind. J. Fluid Mech. 2, 417-45.
- _____ (1966) "The Dynamics of the Upper Ocean." Cambridge University Press.

- _____ (1967) The maintenance of Reynolds stress in turbulent shear flow. *J. Fluid Mech.* 27, 131-44.
- _____ (1961) On the dynamics of unsteady gravity waves of finite amplitude. Part 2. *J. Fluid Mech.* 11, 143-155.
- Plate, E. J. and G. M. Hidy (1967) Laboratory study of air flowing over a smooth surface onto small water waves. *J. Geophys. Res.* 72 (18), 4627-41.
- _____, P. C. Chang and G. M. Hidy (1969) Experiments on the generation of small water waves by wind. *J. Fluid Mech.* 35 (4), 625-56.
- Pond, S., R. W. Stewart and R. W. Burling (1963) Turbulence spectra in the wind over waves. *J. Atmos. Sci.* 20 (4), 319-24.
- Priestley, J. T. (1965) Correlation studies of pressure fluctuations on the ground beneath a turbulent boundary layer. U. S. Nat. Bur. Stand. Rep. 8942; 92 pp.
- Shemdin, O. H. (1968) Wind Generated Waves: recent and future developments. Fifth Space Congress, Oceanography Session, Cocoa Beach, Fla.
- _____ and E. Y. Hsu (1966) The dynamics of wind in the vicinity of progressive water waves. Stanford Univ., Dept. of Civil Eng. Tech. Rep. No. 66.
- _____ (1967) The dynamics of wind in the vicinity of progressive water waves. *J. Fluid Mech.* 30, 403-16.
- Smith, S. D. (1967) Thrust anemometer measurements of wind-velocity spectra and of Reynolds stress over a tidal inlet. *J. Mar. Res.* 25 (3), 239-62.
- Snyder, R. L. and C. S. Cox (1966) A field study of the wind generation of ocean waves. *J. Mar. Res.* 24 (2), 141-78.
- Stanton, Sir T. E., D. Marshall, and R. Houghton (1932) The growth of waves on water due to the action of the wind. *Proc. Roy. Soc. A* 137, 283-93.
- Stewart, R. W. (1961) The wave drag of wind over water. *J. Fluid Mech.* 10, 189-94.
- _____ (1967) Mechanics of the air-sea interface. *Phys. Fluids*, Supplement: Boundary Layers and Turbulence, S47-S55.
- Sverdrup, H. U., and W. H. Munk (1947) Wind, Sea, and Swell: Theory of Relations for Forecasting. U. S. Hydrogr. Office, Wash., Pub. No. 601. 44 pp.

- Taylor, R. J. (1960) A new approach to the measurement of turbulent fluxes in the lower atmosphere. J. Fluid Mech. 10, 449-58.
- Thijssen, J. T. (1951) Growth of wind-generated waves and energy transfer. "Gravity Waves." Nat. Bur. Stand. Washington circular No. 521, 281-7.
- Thomson, Sir W. (1871) Hydrokinetic solutions and observations. Phil. Mag. (4) 42, 368-72.
- Ursell, F. (1956) Wave generation by wind. "Surveys in Mechanics" (ed. G. K. Batchelor). Cambridge University Press. Pp. 216-249.
- Weiler, H. S. and R. W. Burling (1967) Direct measurements of stress and spectra of turbulence in the boundary layer over the sea. J. Atmos. Sci. 24 (6), 653-64.
- Wiegel, R. L. and R. H. Cross (1966) Generation of wind waves. J. Waterways and Harbors Div., ASCE 92, 1-26.
- Willmarth, W. W. and C. E. Wooldridge (1962) Measurements of the fluctuating pressure at the wall beneath a thick turbulent boundary layer. J. Fluid Mech. 14, 187-210.
- Wu, Jin (1968) Laboratory studies of wind-wave interactions. J. Fluid Mech. 34 (1), 91-111.
- Wuest, W. (1949) Beitrag zur entstehung von wasserwellen durch wind. Z. angew. Math. Mech. 29, 239-52.



FROM CANADIAN HYDROGRAPHIC SERVICE CHART No. 3586

FIGURE 1
MAP AT SITE OF EXPERIMENT

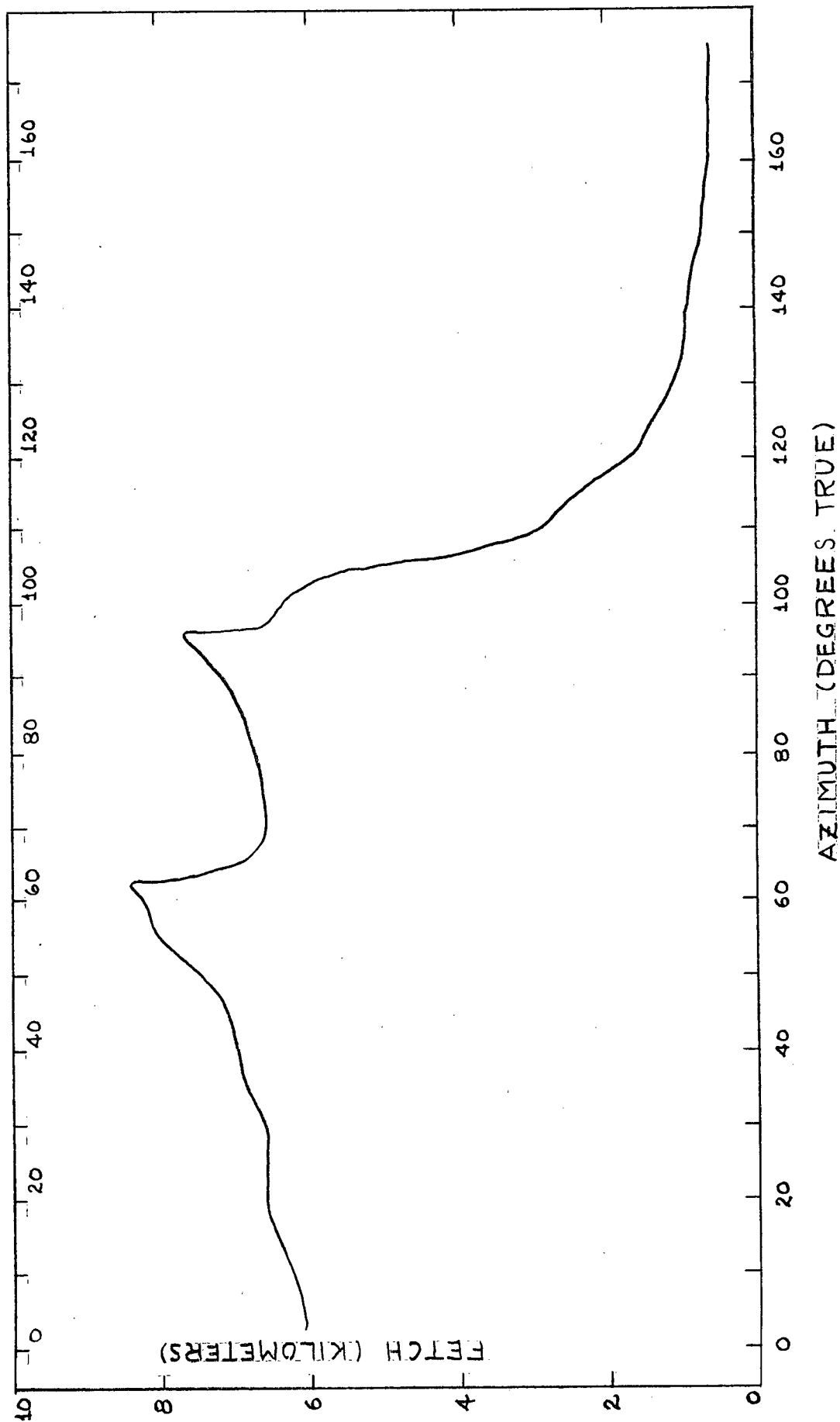
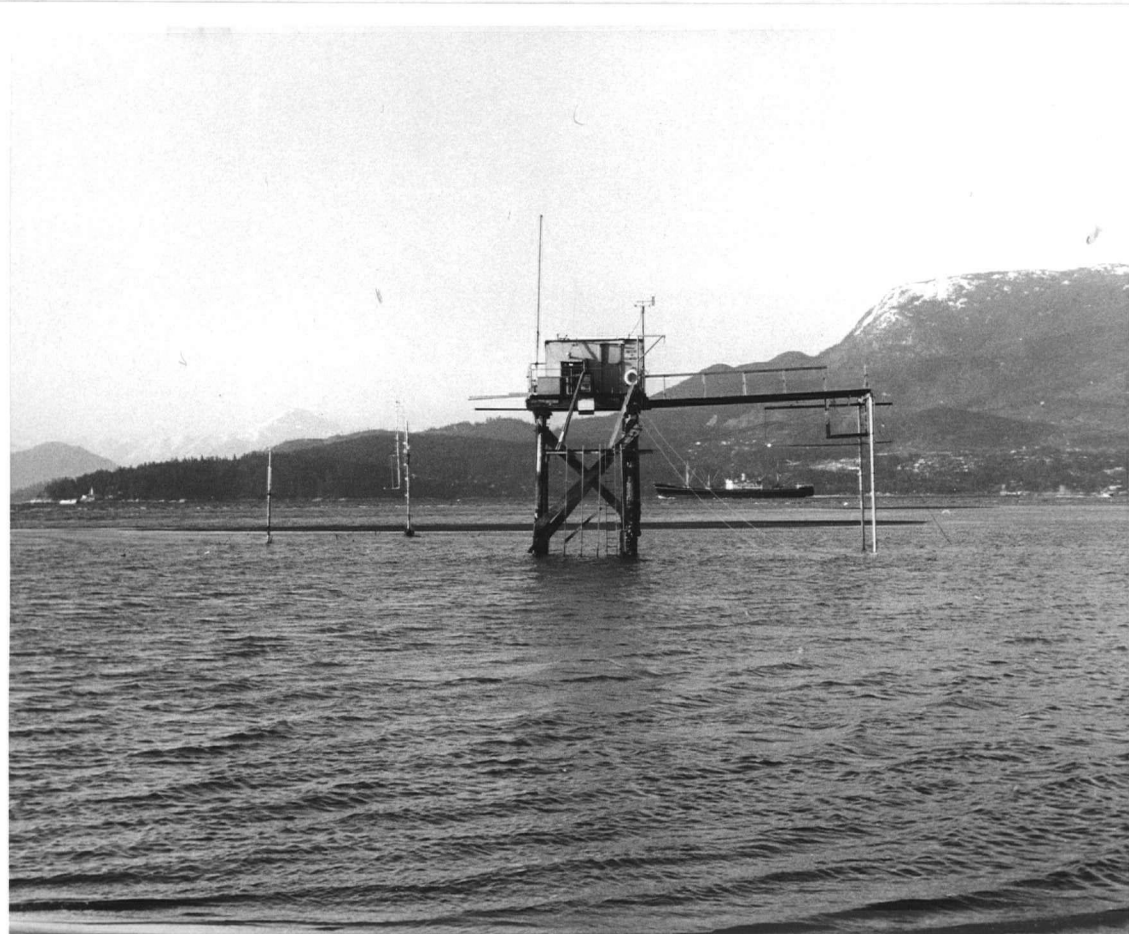


FIGURE 2. AVAILABLE FETCH AT SITE



↑ ↑
INSTRUMENT
MASTS

↑
RECORDING
PLATFORM

→
SOUTHEAST

FIGURE 3.

PHOTOGRAPH OF RECORDING PLATFORM AND INSTRUMENT
MASTS (LOOKING NORTHEAST)



↑↑
HUNTING SHACKS

↑
PRESSURE
SENSORS

↑
ANEMOMETER
MAST

FIGURE 77.

PHOTOGRAPH OF EQUIPMENT DEPLOYMENT PRIOR TO A RUN AT BOUNDARY BAY

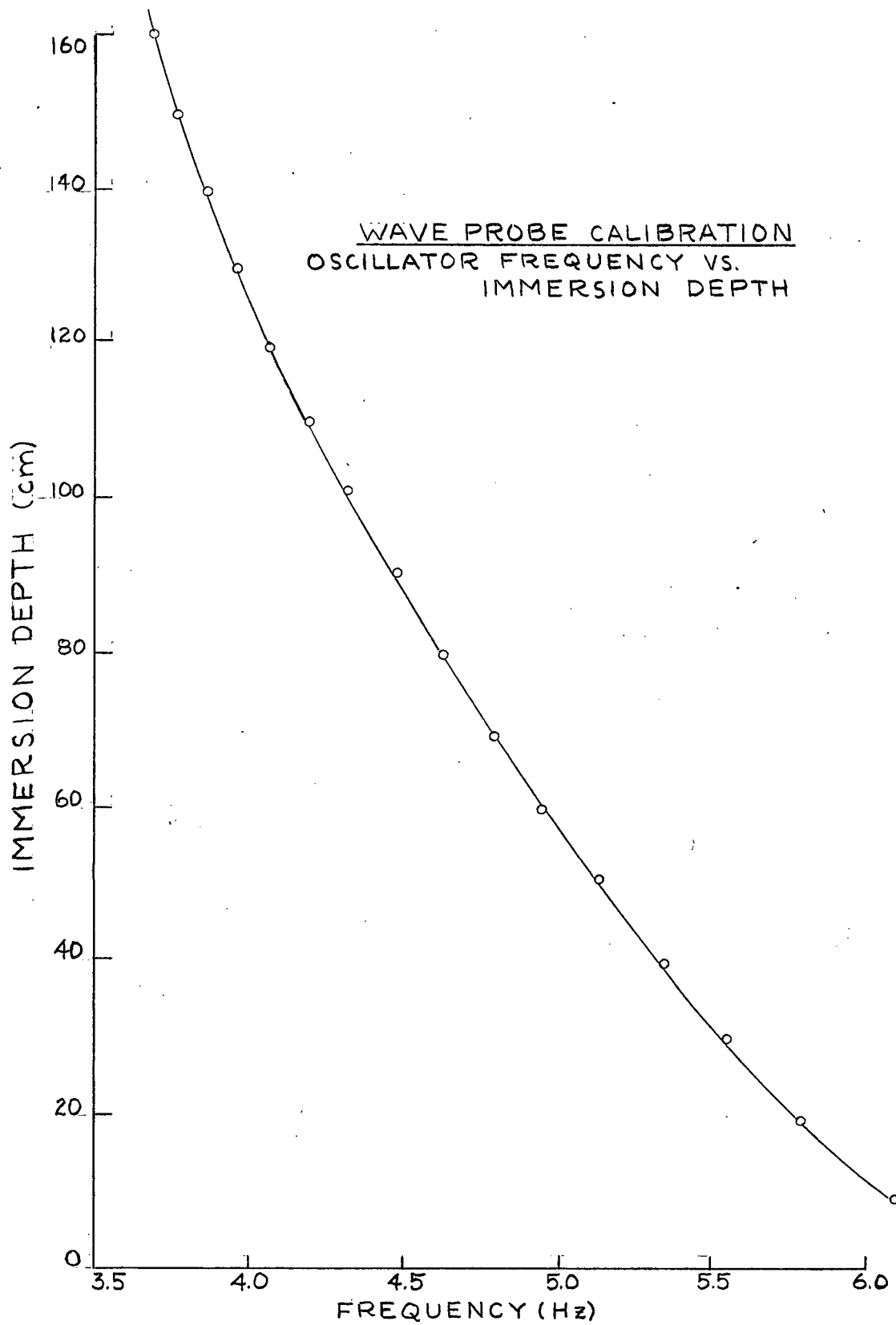
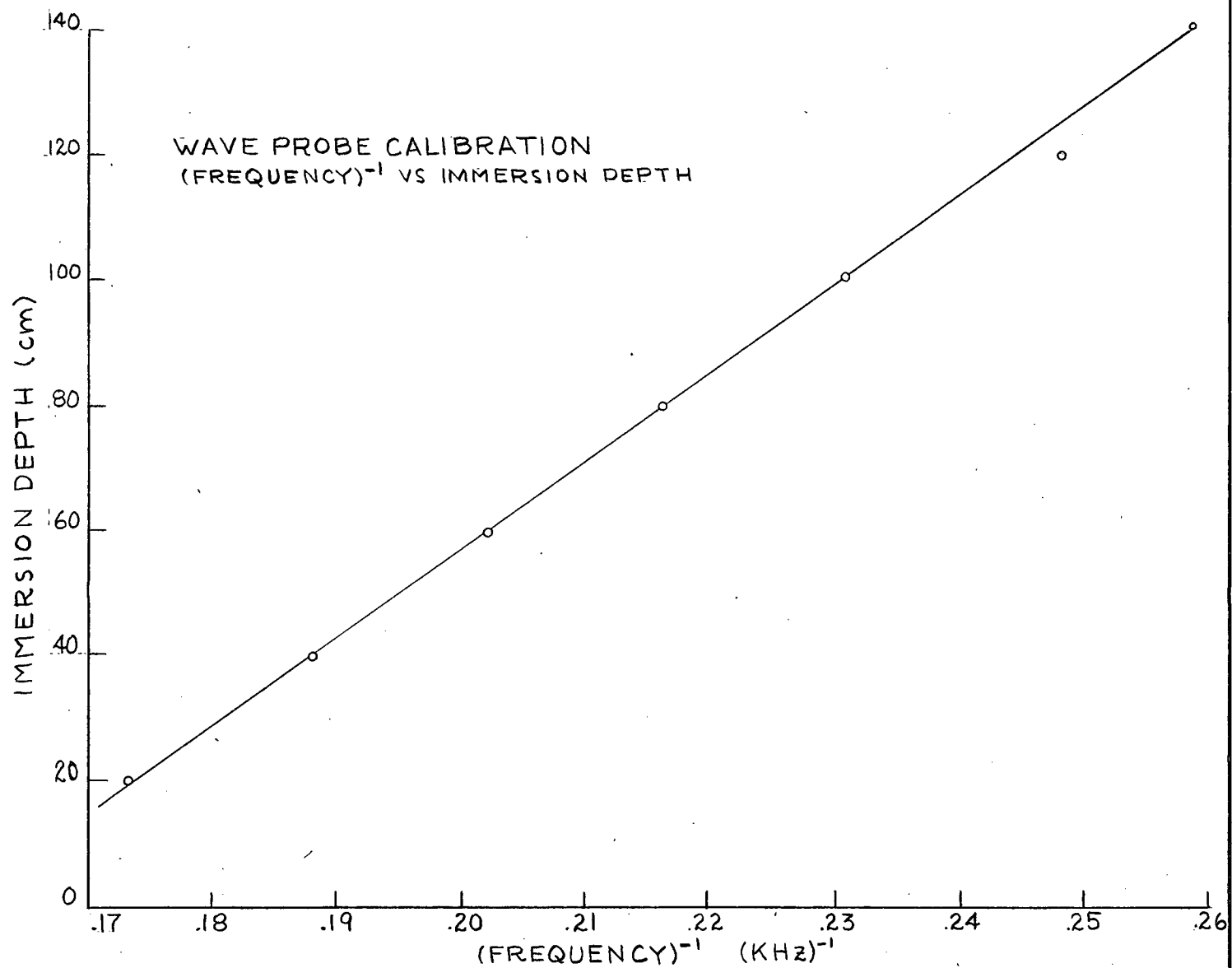


FIGURE 4.

WAVE PROBE CALIBRATION: OSCILLATOR (FREQUENCY)⁻¹
VS. IMMERSION DEPTH

FIGURE 5.



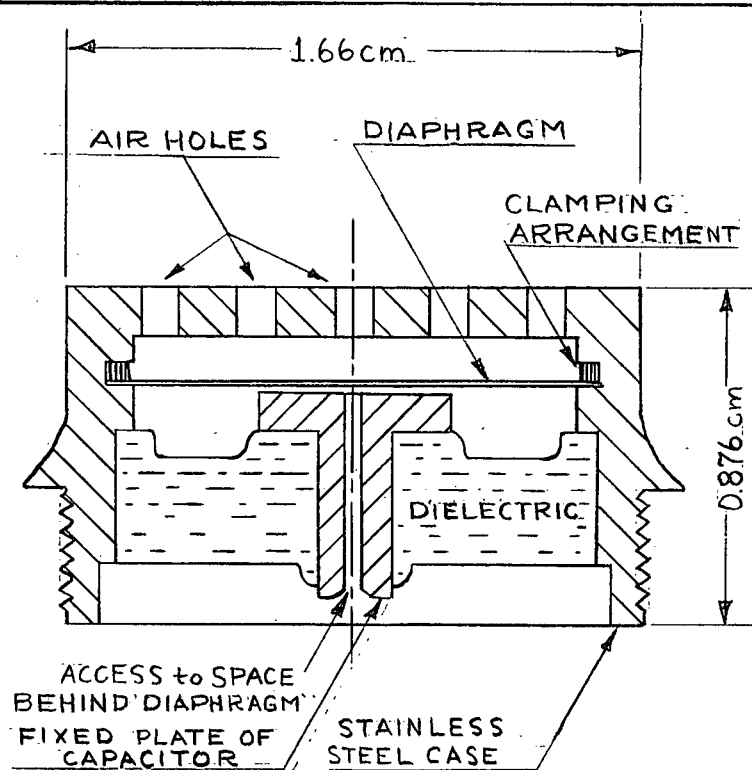


FIGURE 6. SCHEMATIC CROSS-SECTION OF MICROPHONE

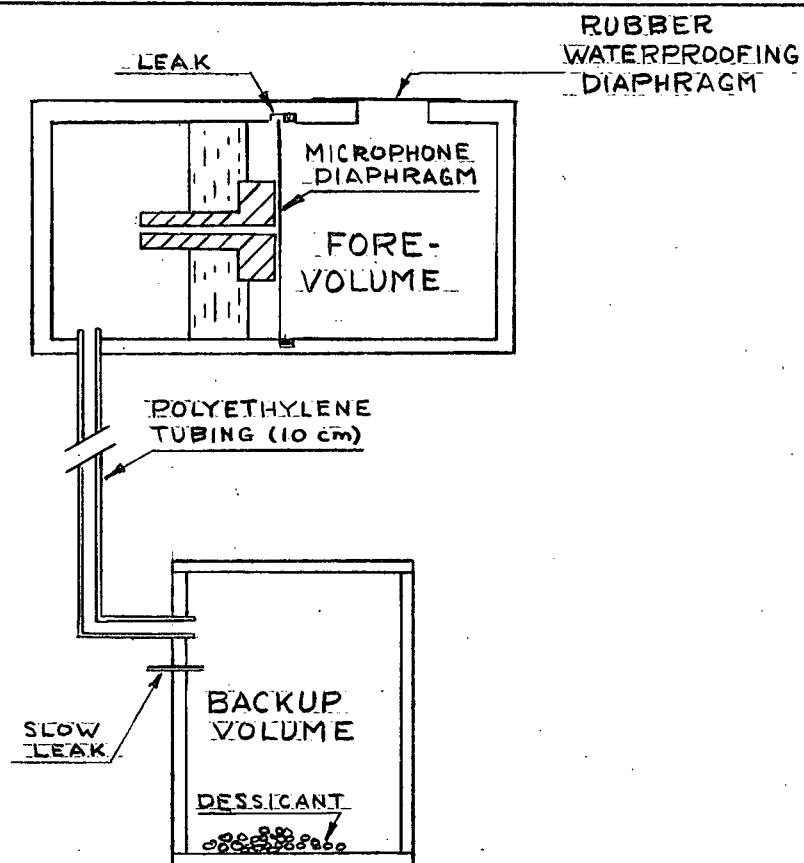


FIGURE 7. SCHEMATIC DIAGRAM OF PRESSURE MEASUREMENT SYSTEM

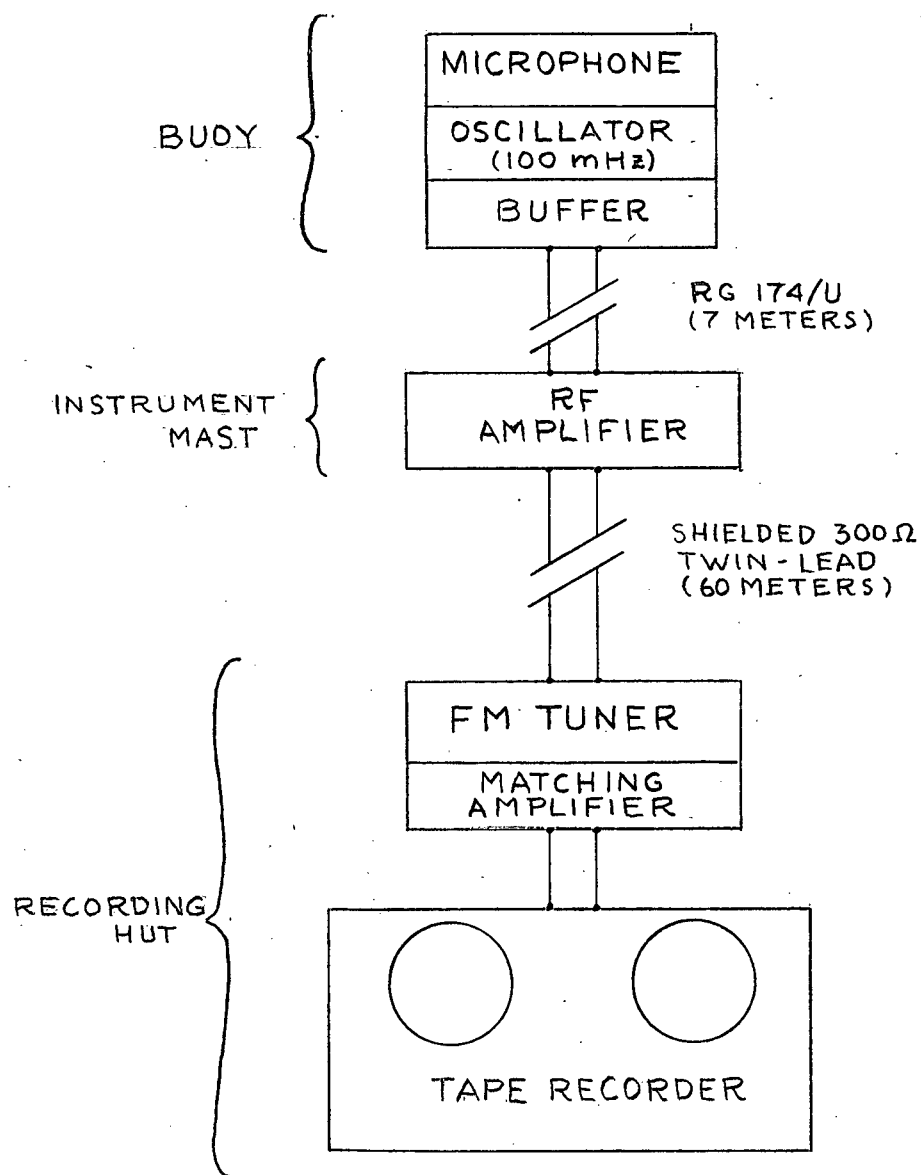
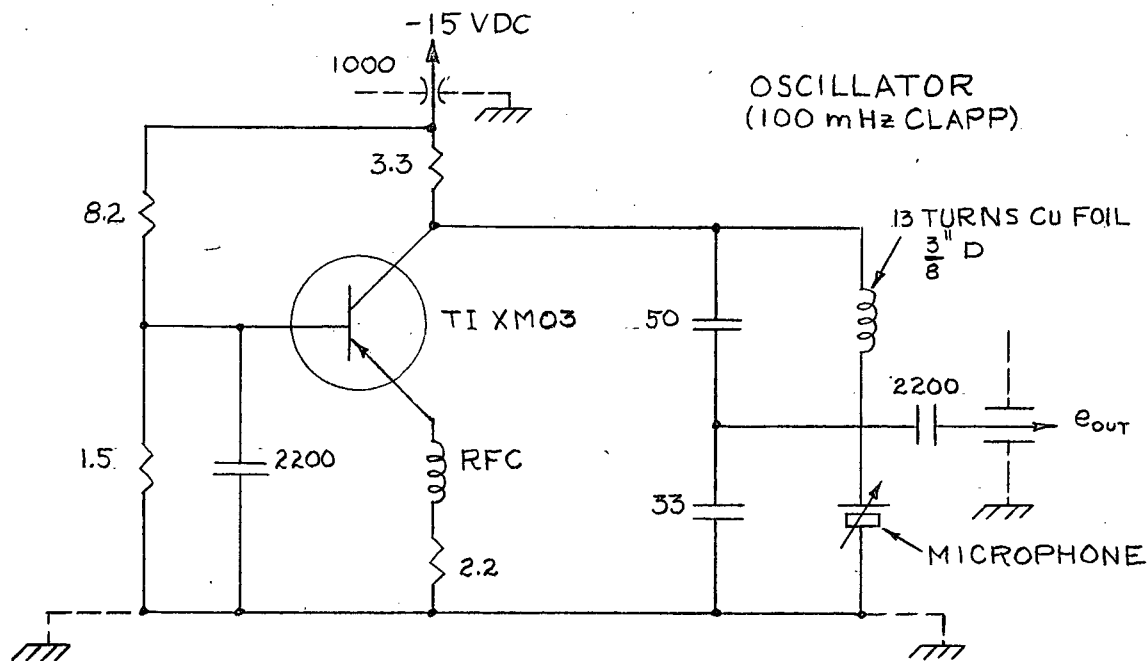


FIGURE 8.

PRESSURE RECORDING ELECTRONICS: BLOCK DIAGRAM



1. RESISTANCES IN K Ω .
2. CAPACITANCES IN PF.
3. e_{out} - e_{in} FEEDTHROUGH < 10 PF.
4. ALL GROUNDS TO AL. CASE.

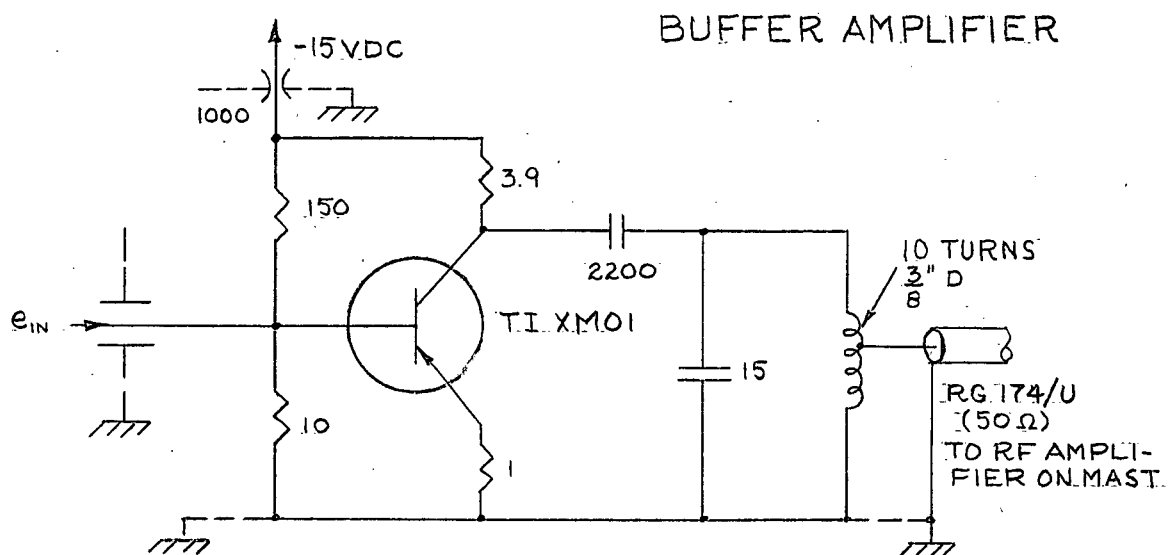


FIGURE 9.

WIRING DIAGRAMS OF BUOY OSCILLATOR AND AMPLIFIER

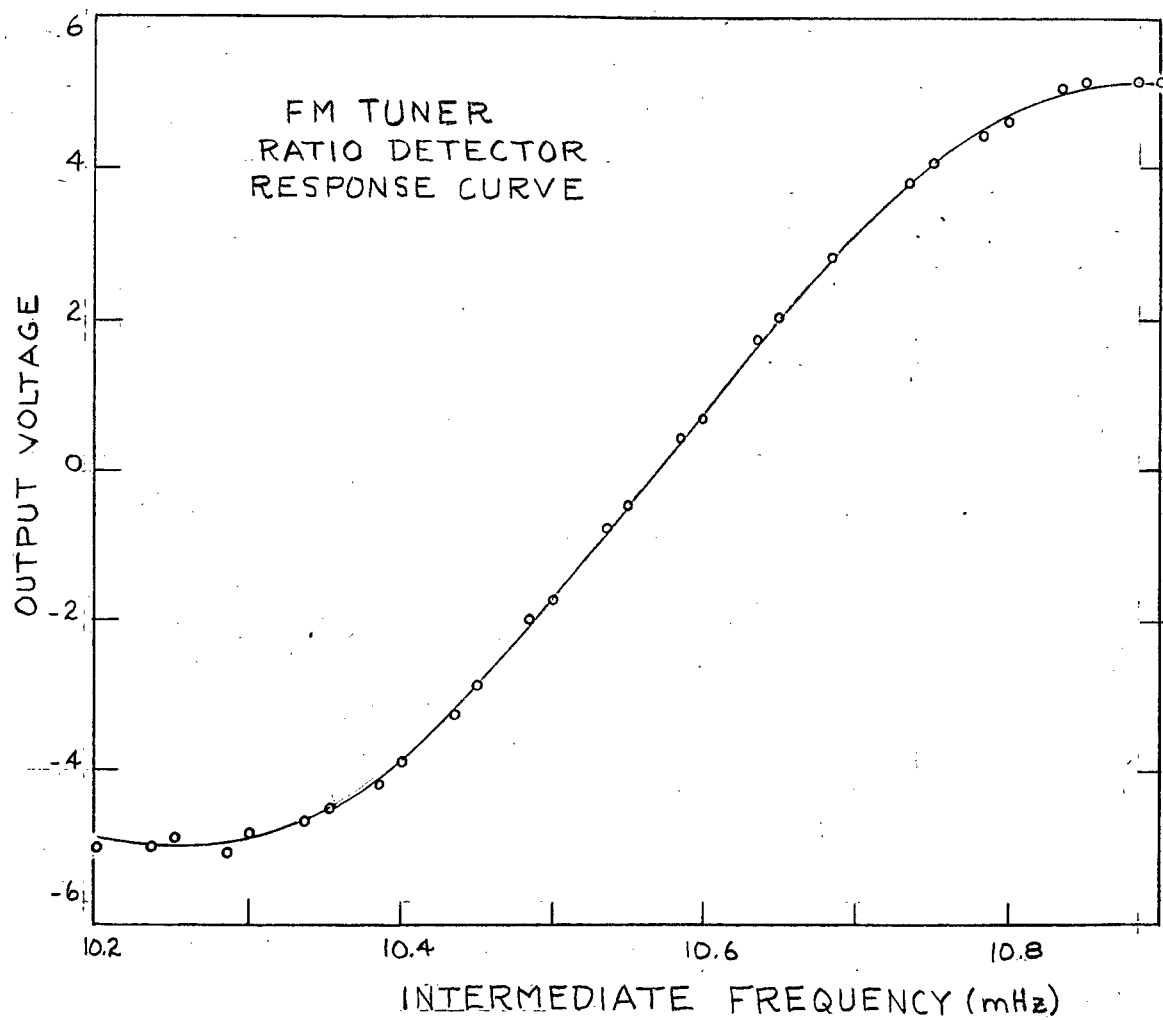


FIGURE 10.

FM TUNER RATIO DETECTOR RESPONSE CURVE

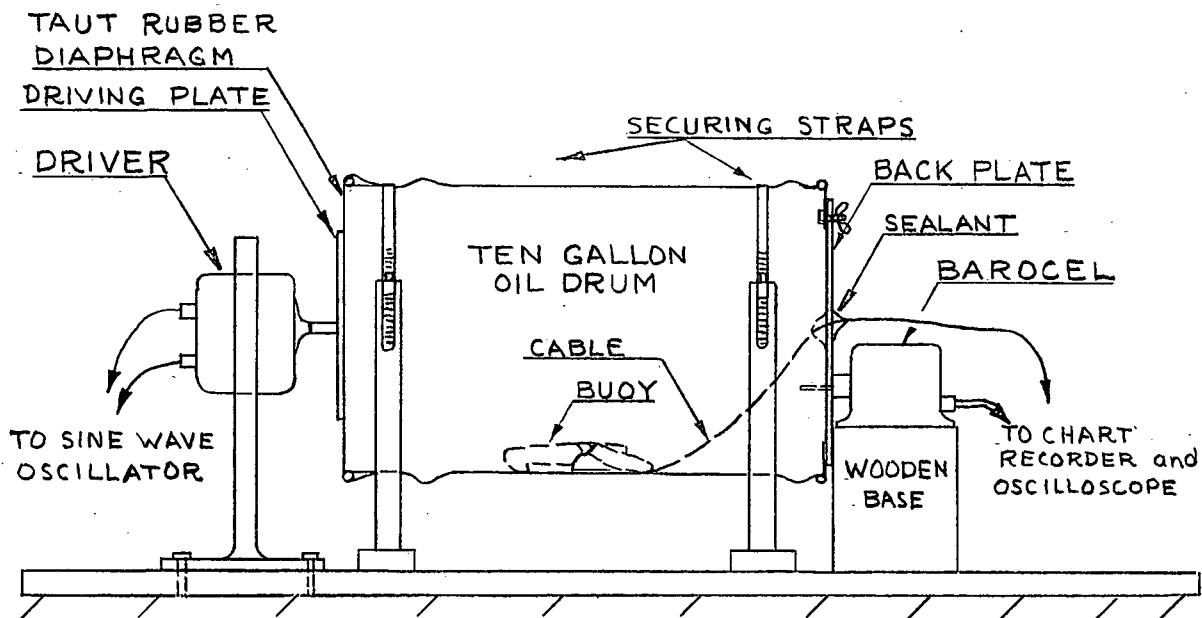


FIGURE 11.

PRESSURE SENSOR CALIBRATION SETUP

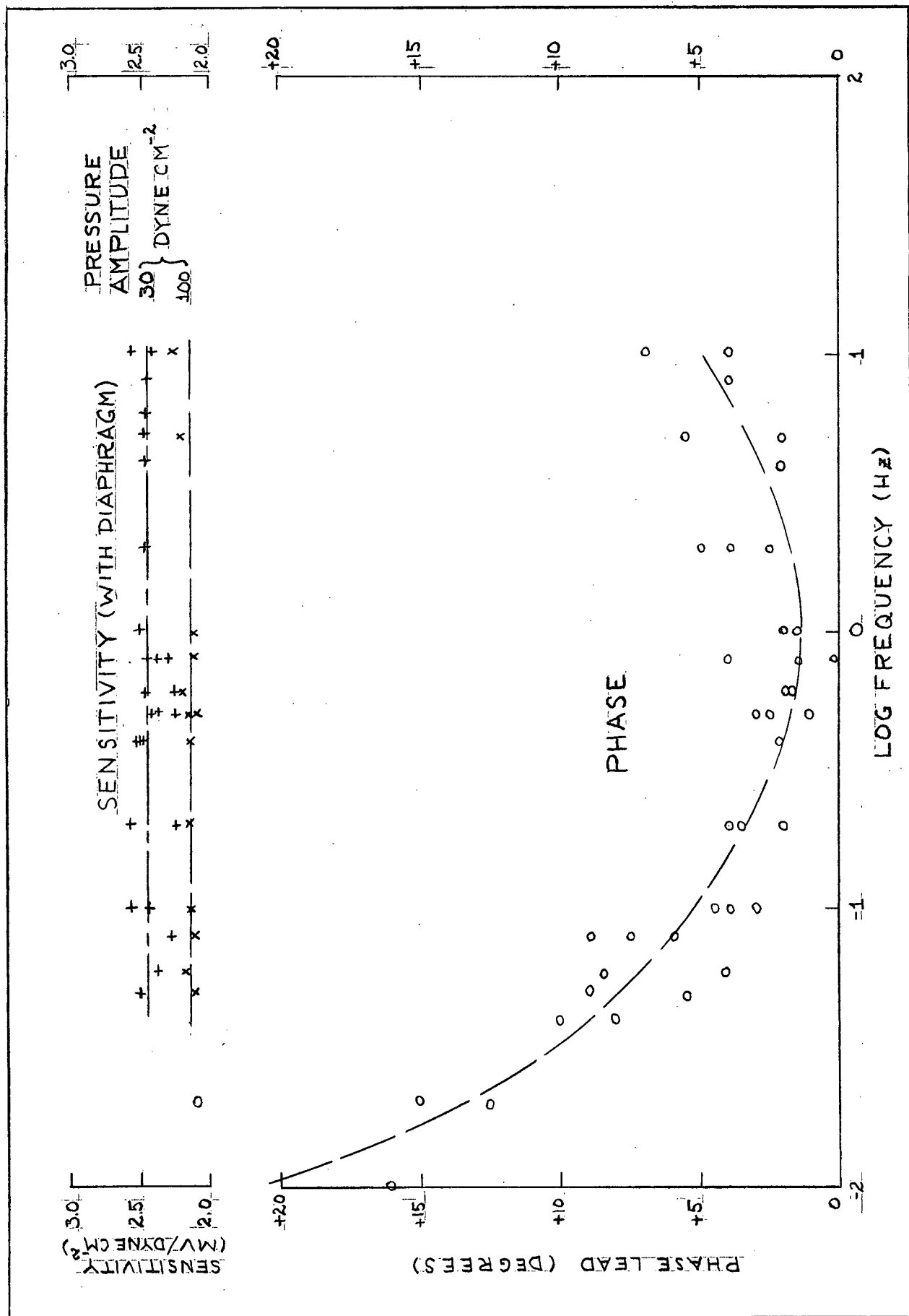


FIGURE 12. LABORATORY CALIBRATION OF THE BUOY PRESSURE SENSOR

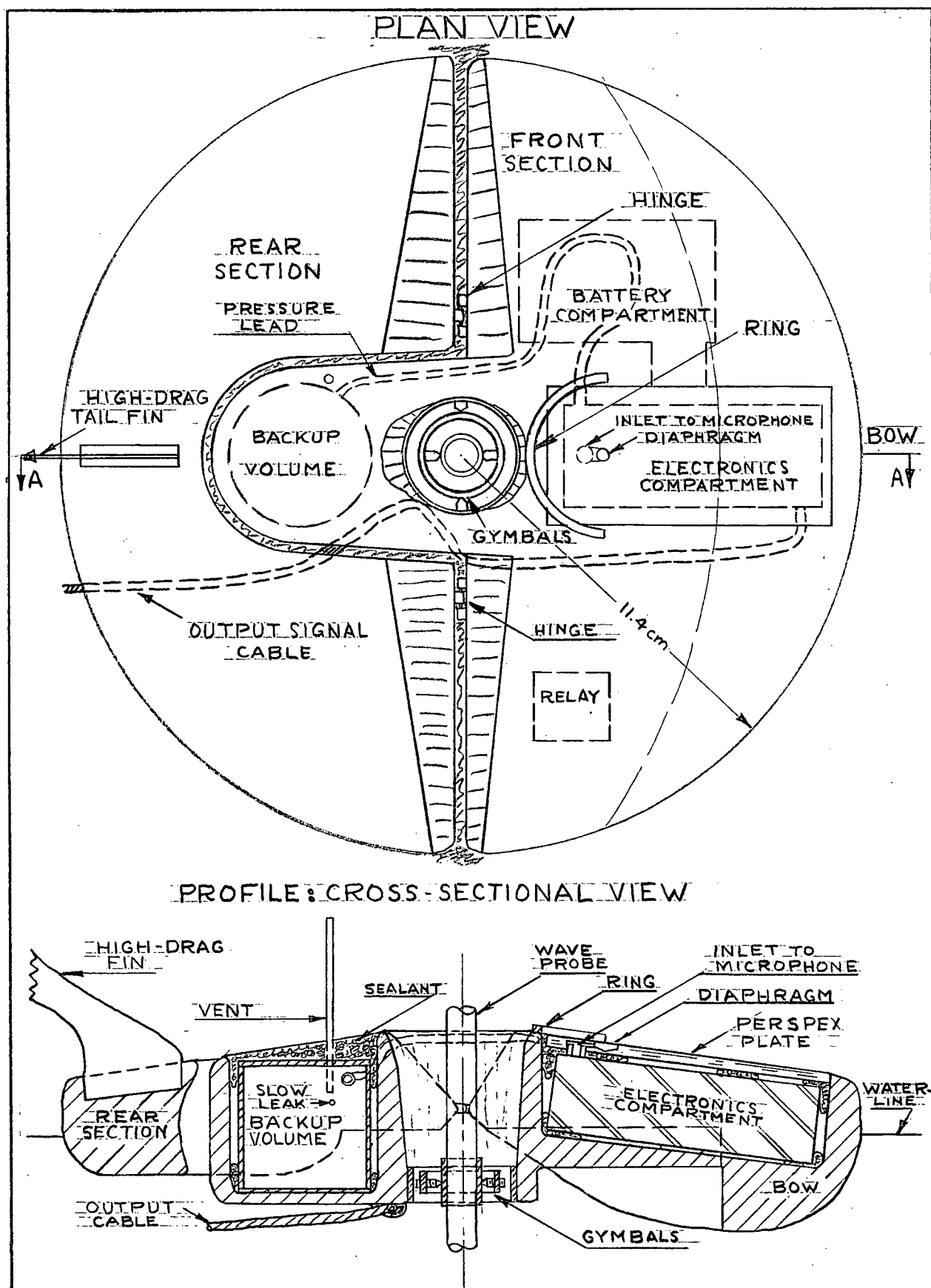


FIGURE 13. DIAGRAM OF THE BUOY

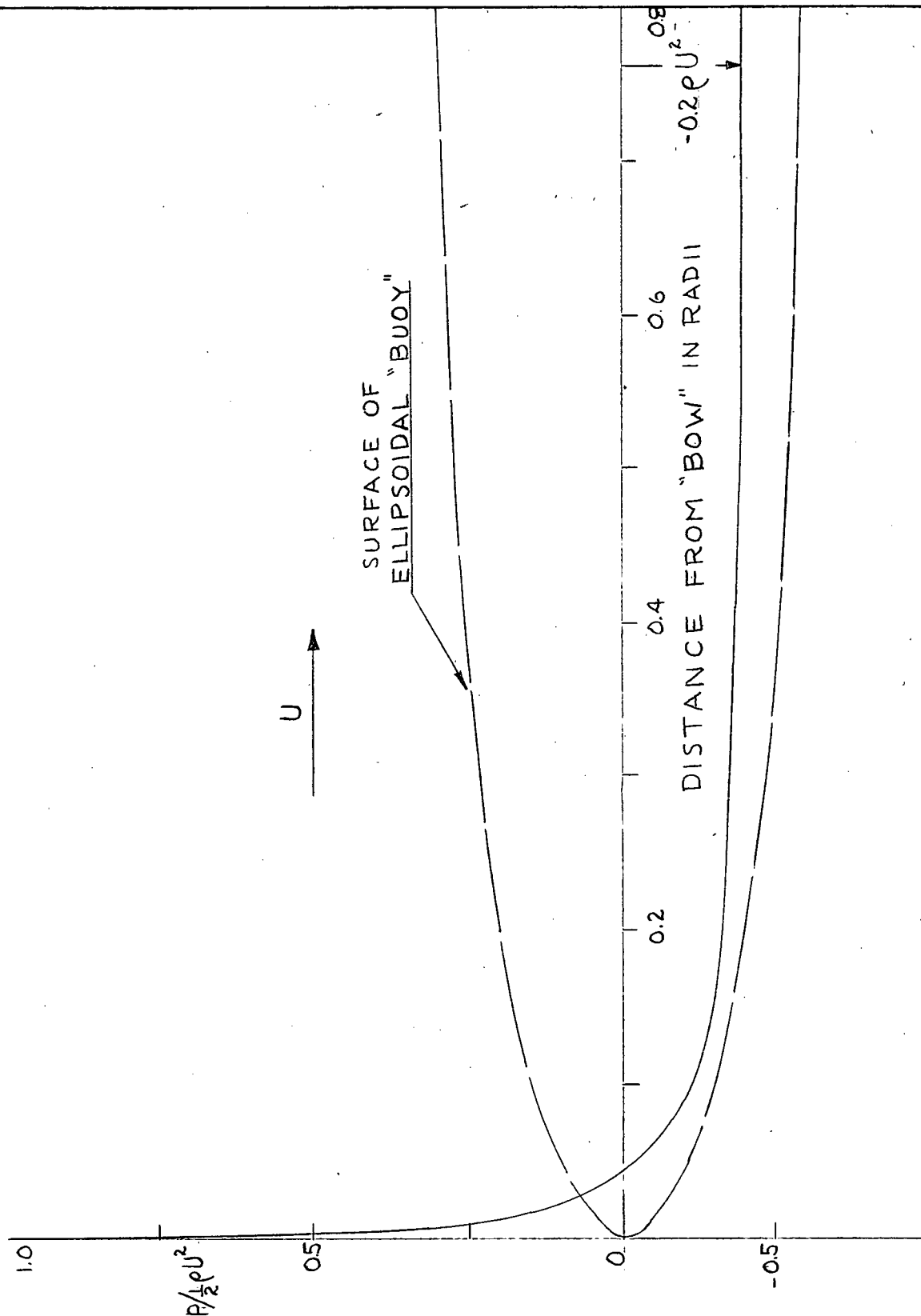
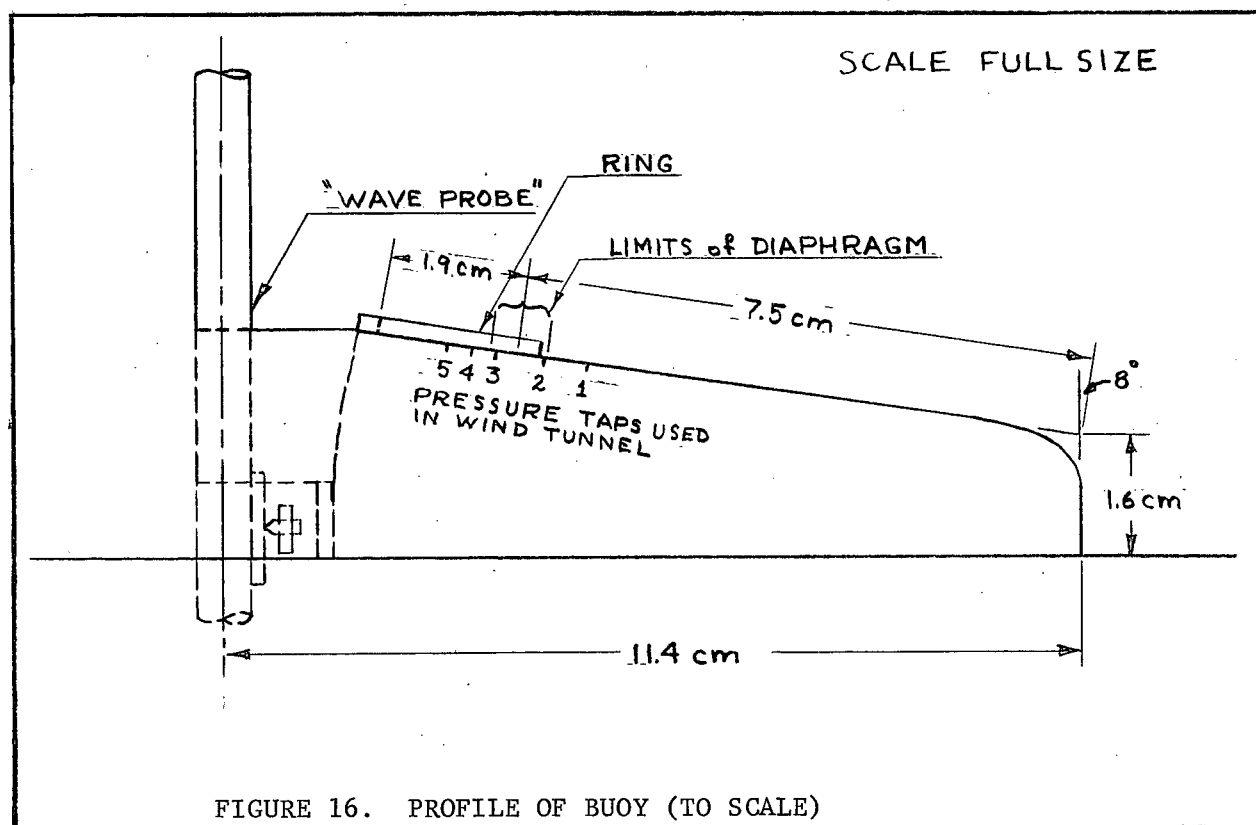
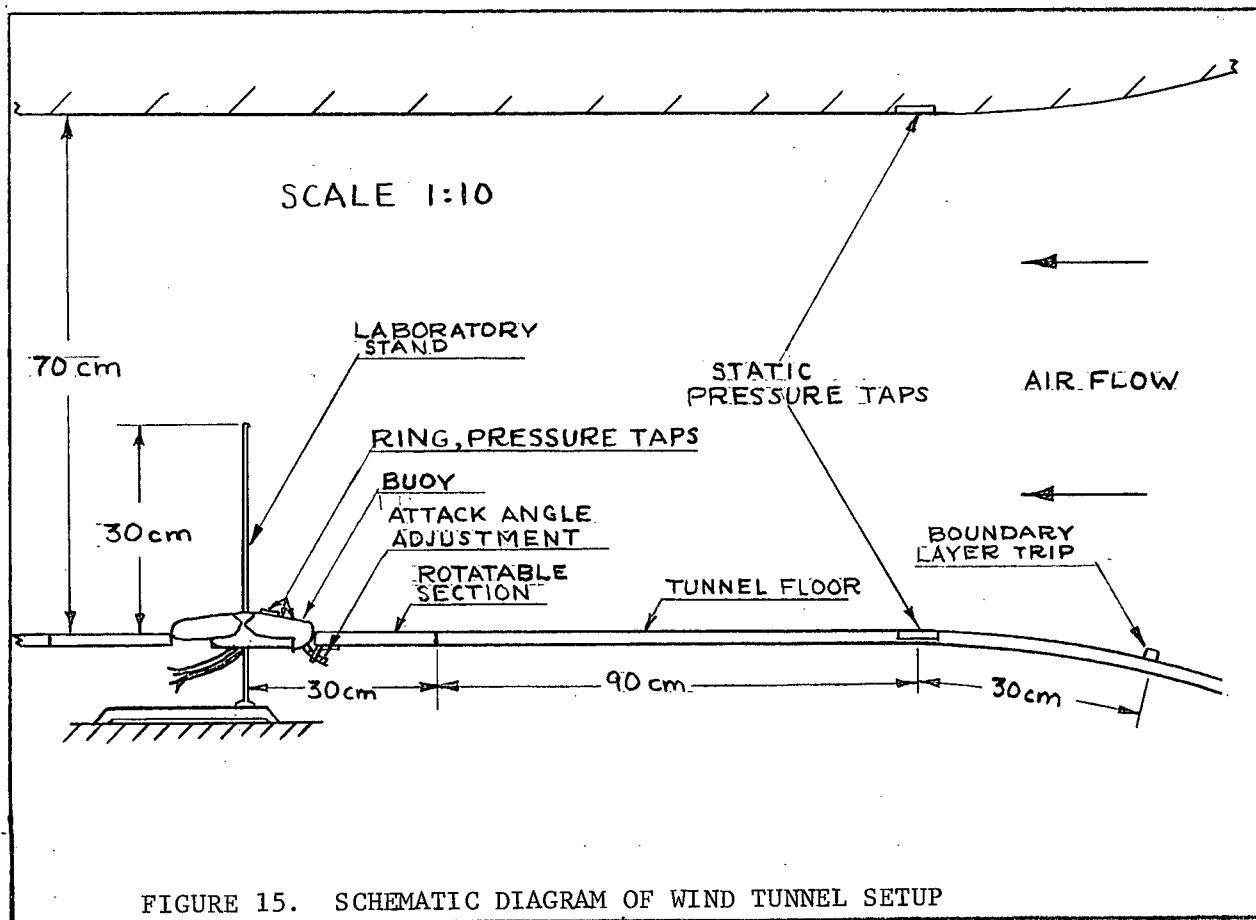


FIGURE 14.
PRESSURE DISTRIBUTION OVER A PLANETARY ELLIPSOID SIMILAR TO
BUOY IN SHAPE



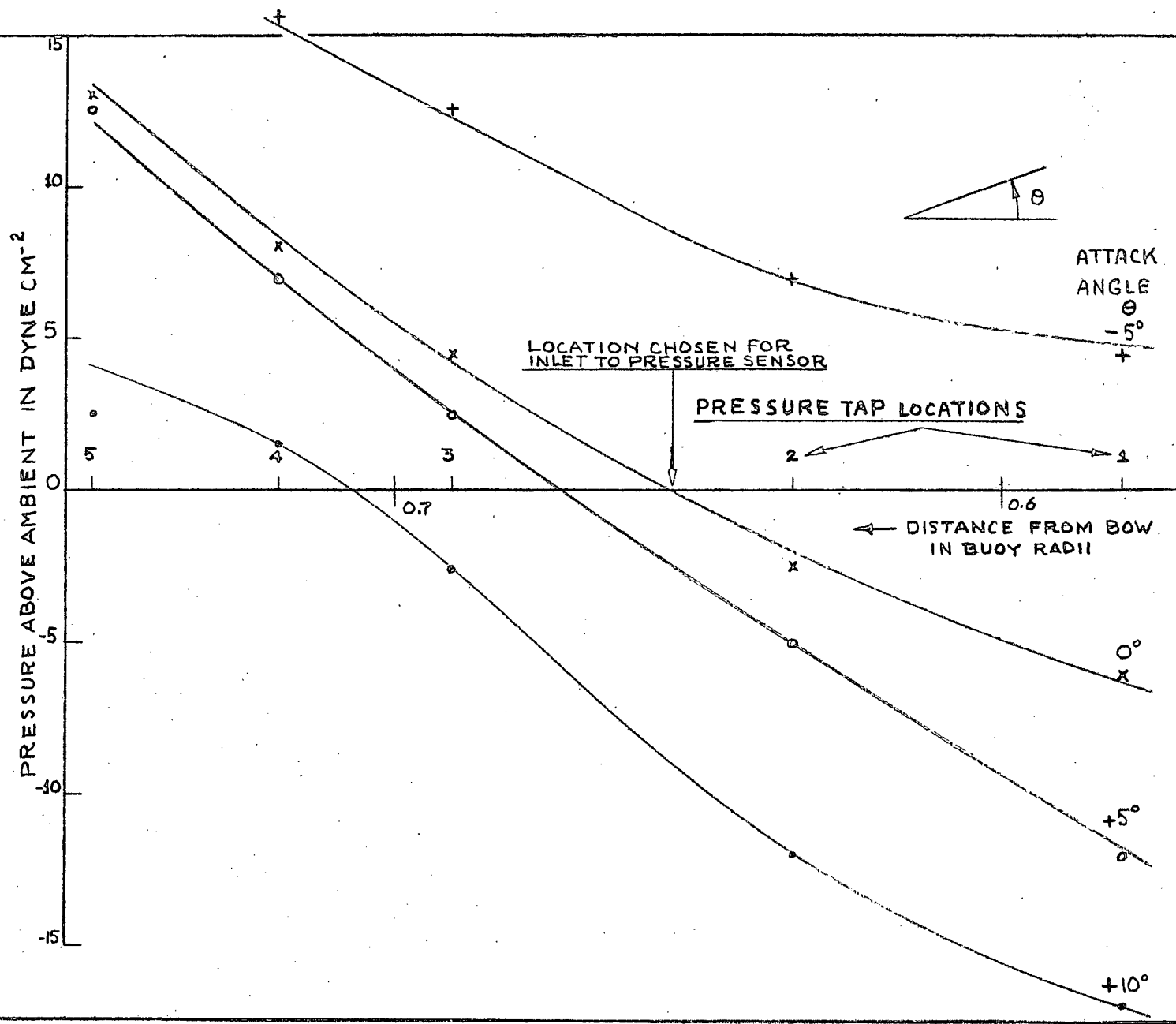


FIGURE 17.

AERODYNAMIC CALIBRATION OF BUOY: PRESSURE VS. DISTANCE
FROM BOW FOR VARIOUS ATTACK ANGLES

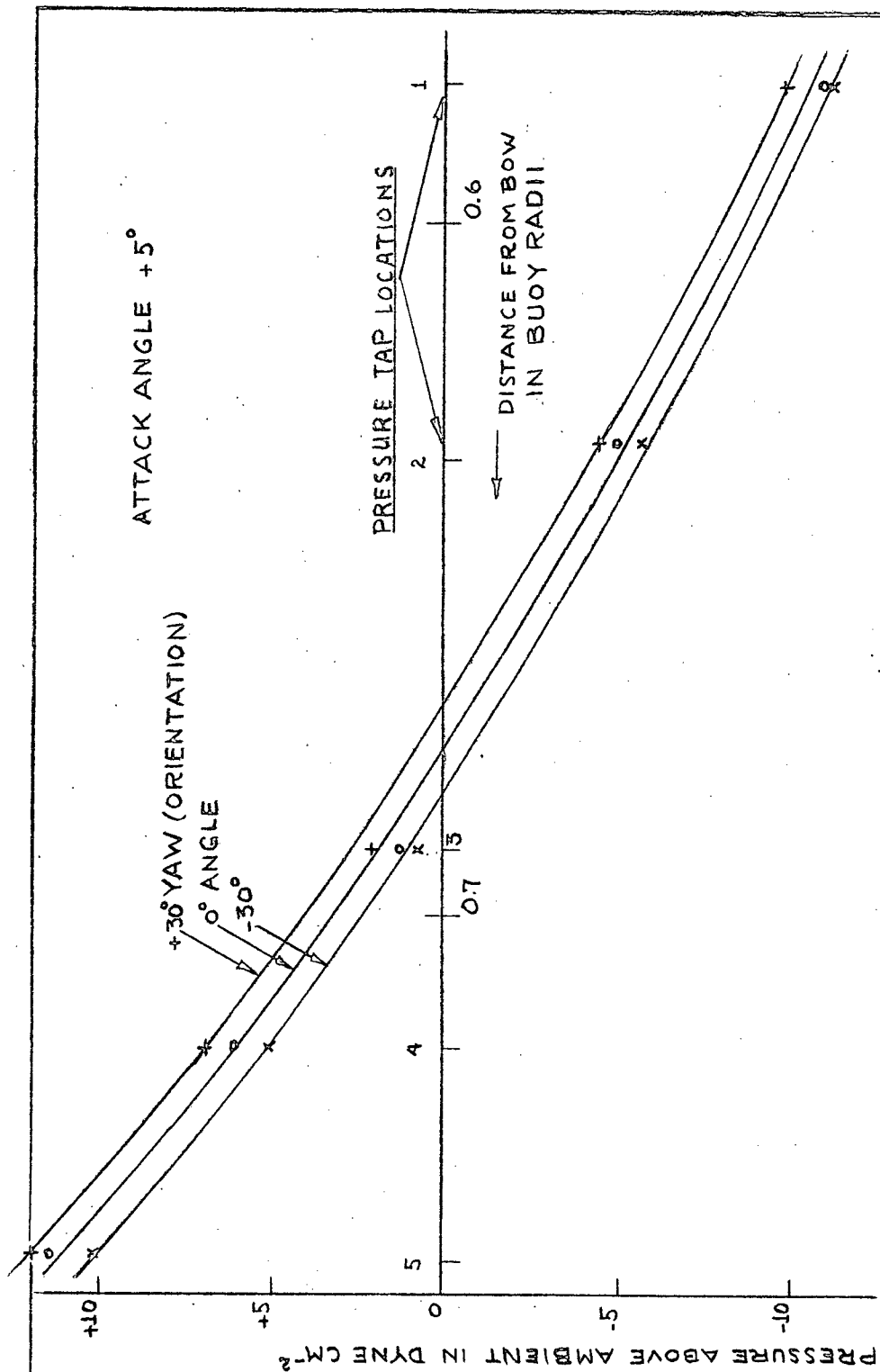


FIGURE 18.

AERODYNAMIC CALIBRATION OF THE BUOY: PRESSURE VS. DISTANCE FROM BOW FOR $+30^\circ$ YAW ANGLES

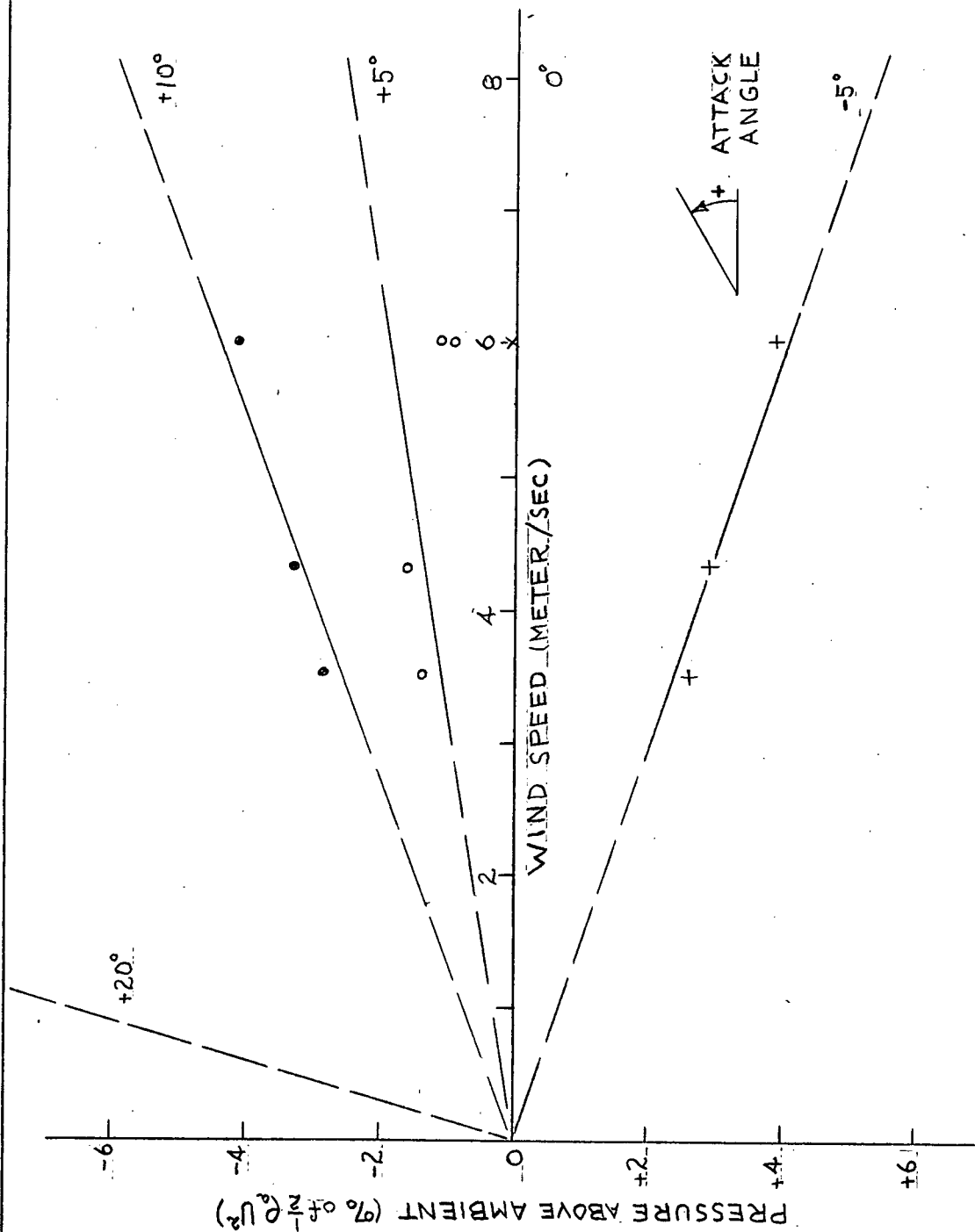


FIGURE 19.

AERODYNAMIC CALIBRATION OF THE BUOY: FRACTION OF STAGNATION HEAD AT PRESSURE PORT VS. WIND SPEED

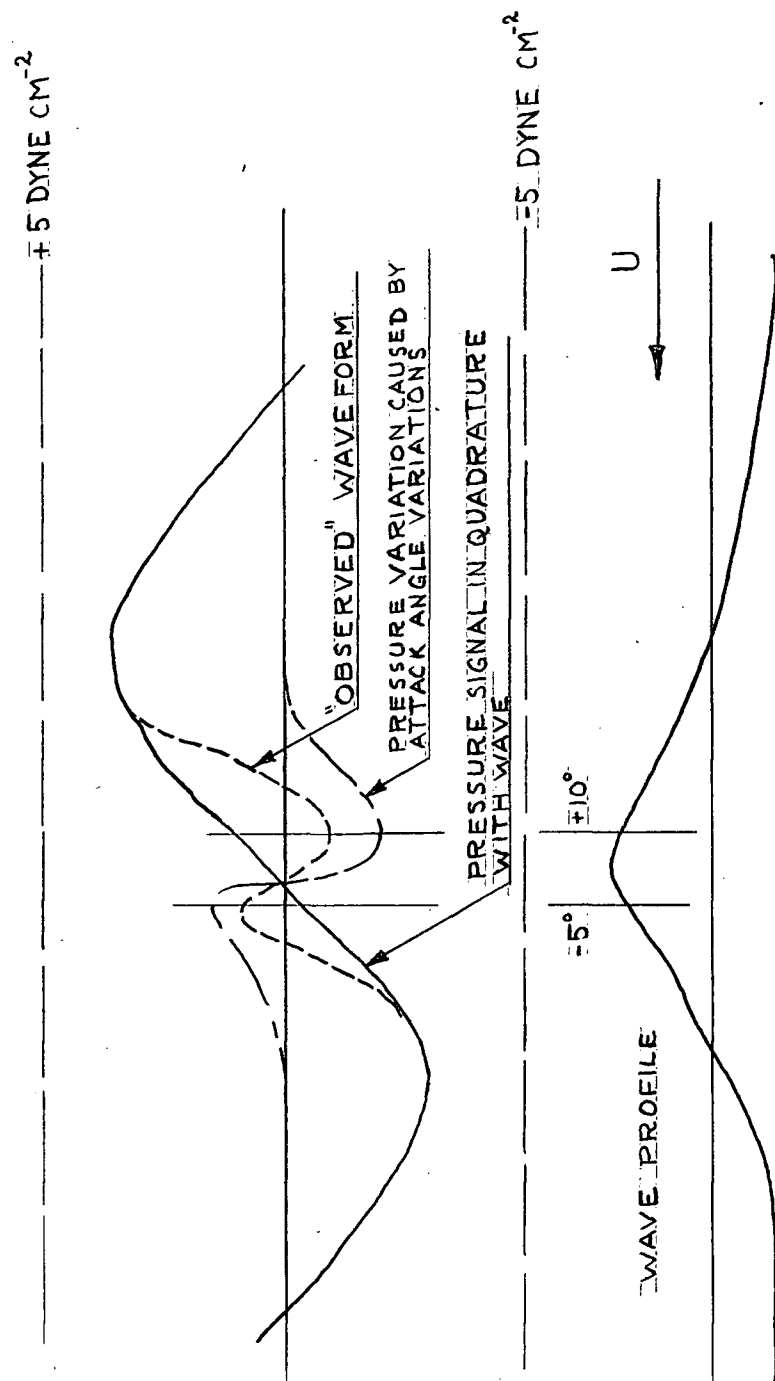


FIGURE 20.

SCHEMATIC REPRESENTATION OF THE EFFECT OF ATTACK
ANGLE ON THE PRESSURE MEASURED
BY THE BUOY

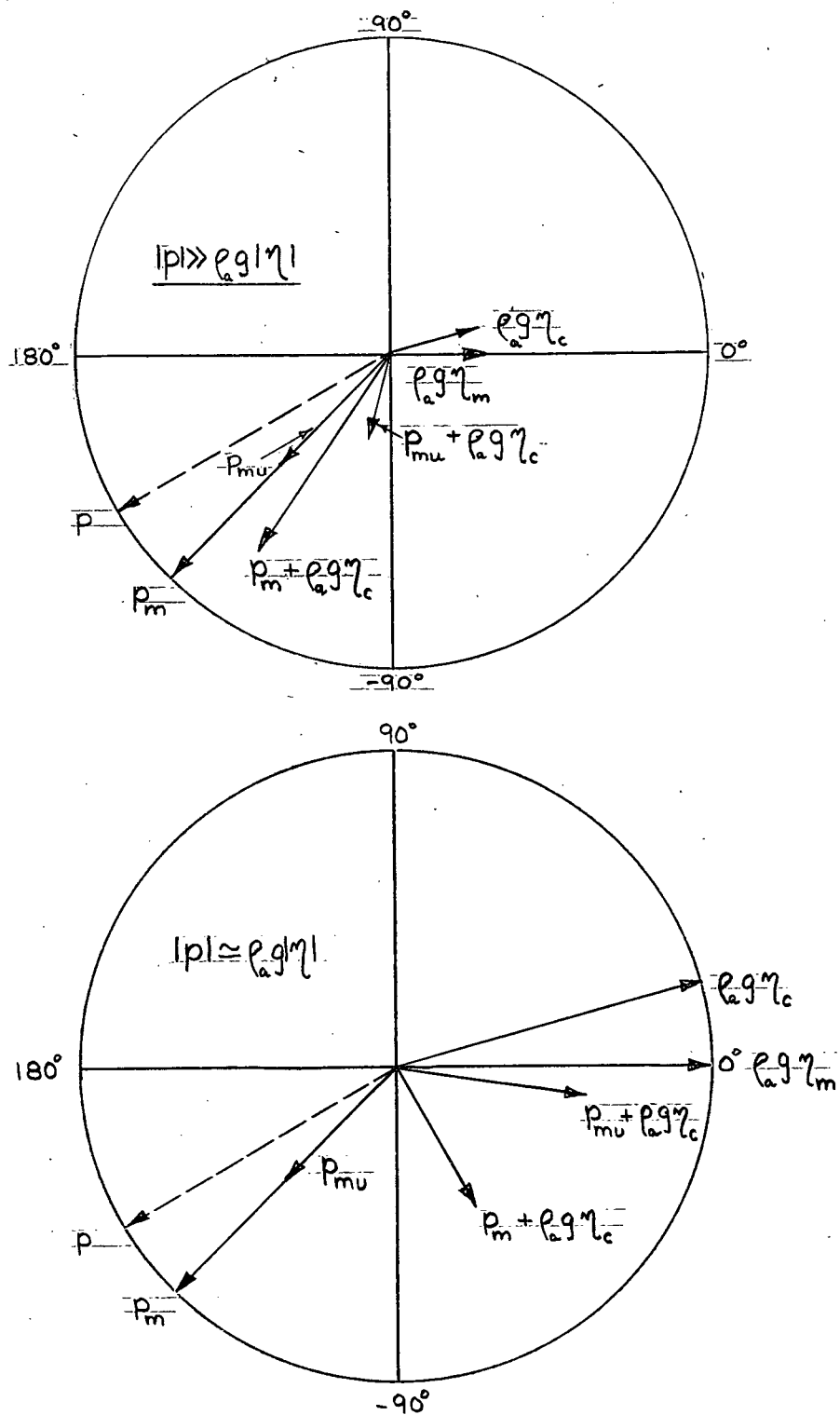


FIGURE 21.

EFFECTS ON $p + e g \eta$ PHASOR OF 50% ERROR
IN PRESSURE CALIBRATION

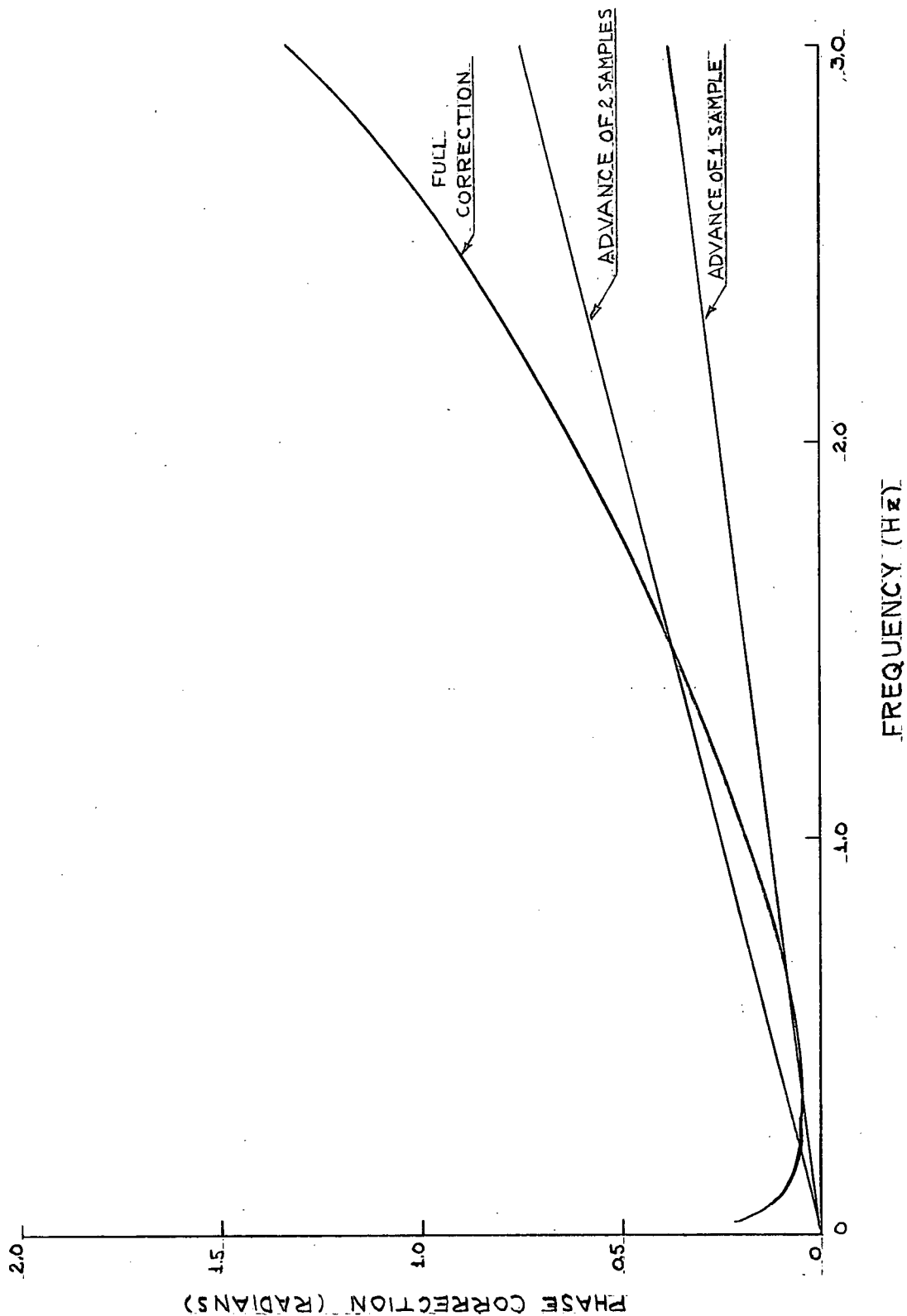


FIGURE 22.

PHASE CORRECTIONS FOR TIME SHIFT OF η SIGNAL COMPARED
WITH FULL CORRECTION CURVE

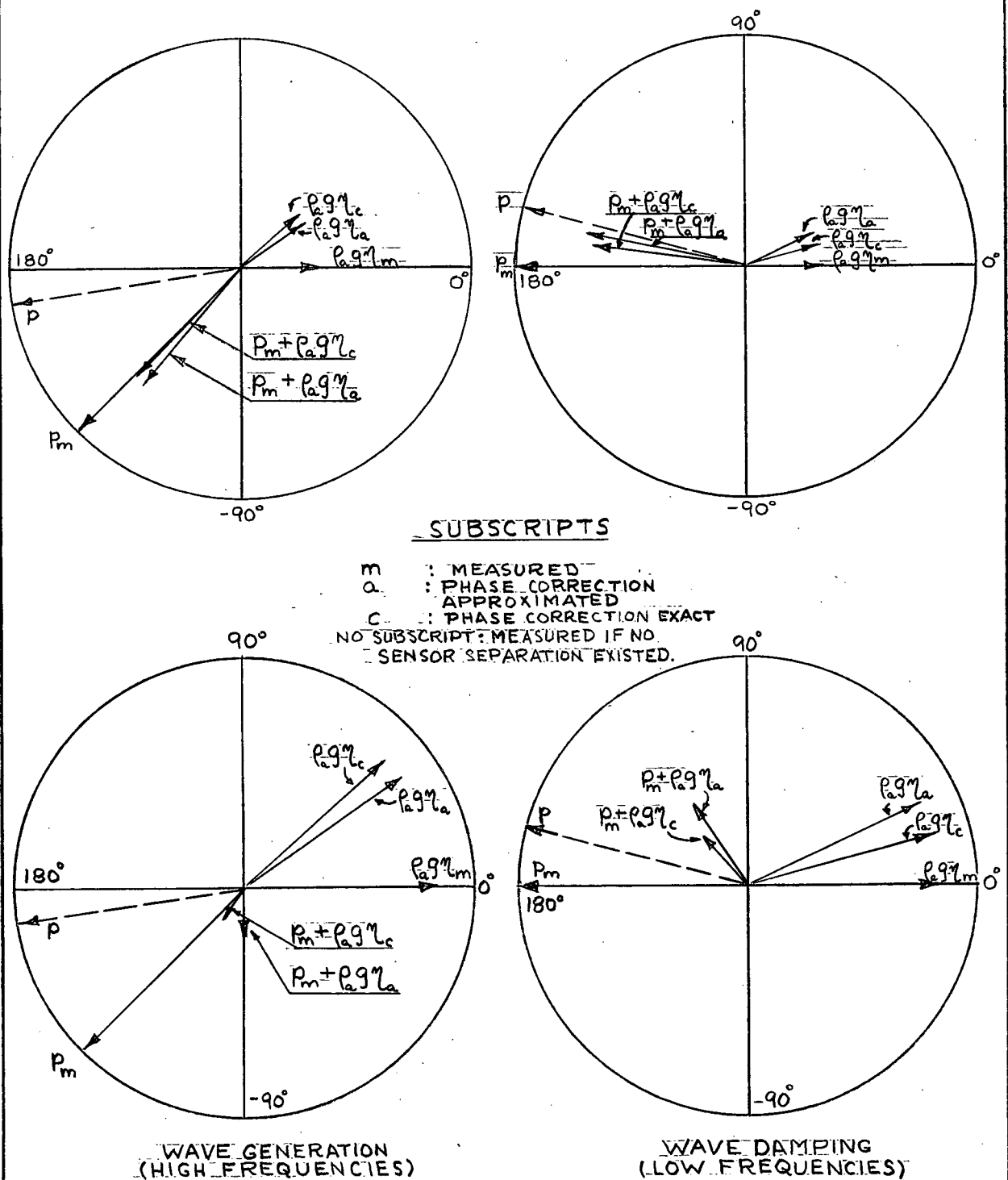
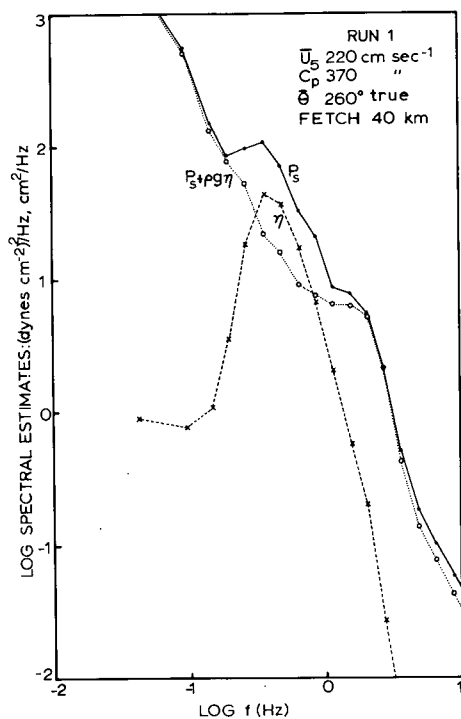
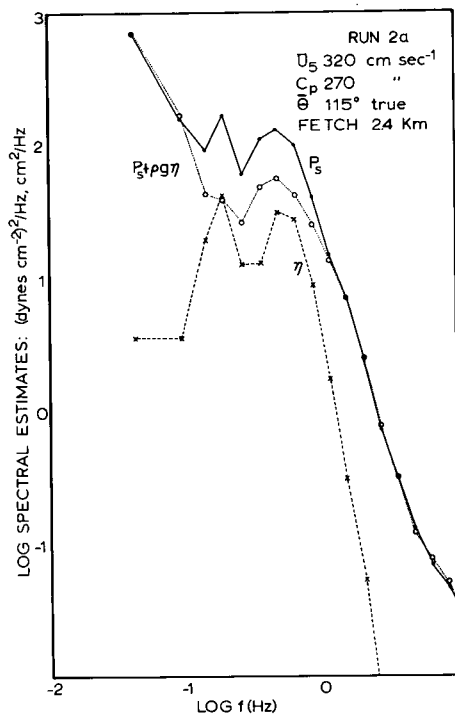


FIGURE 23.

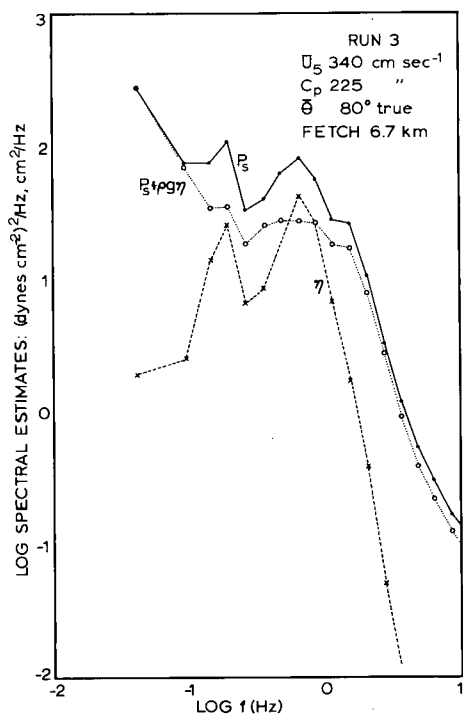
EFFECTS ON $p + e.g.\gamma$ PHASORS OF LOW AND HIGH-FREQUENCY APPROXIMATIONS TO FULL PHASE CORRECTION CURVE



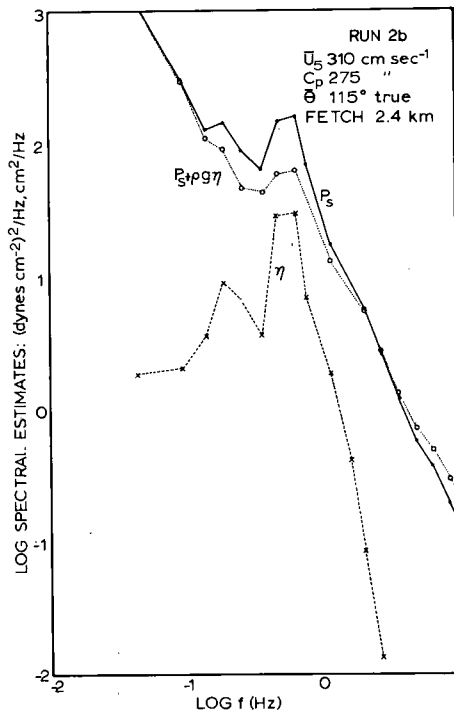
24



25



27

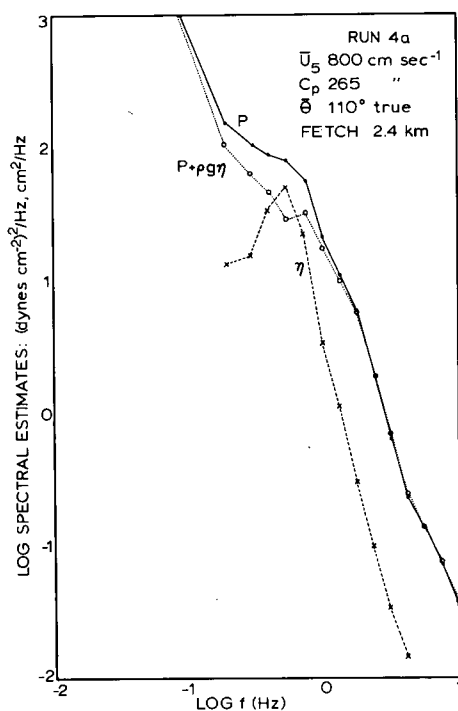


26

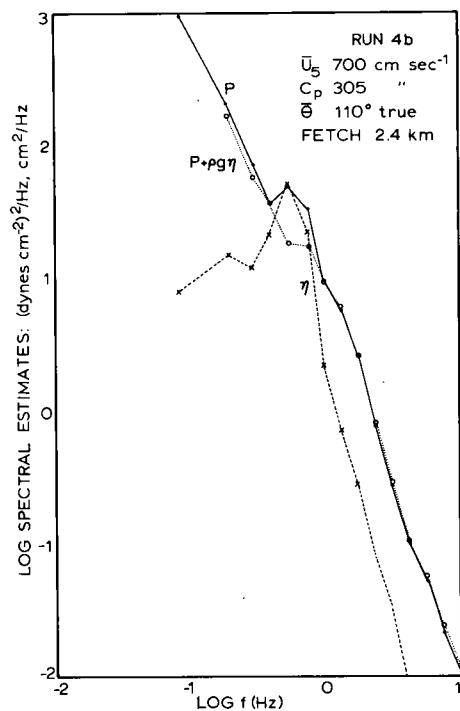
FIGURES 24-27.

POWER SPECTRA OF p_s , $p_s + p_{97}$, η

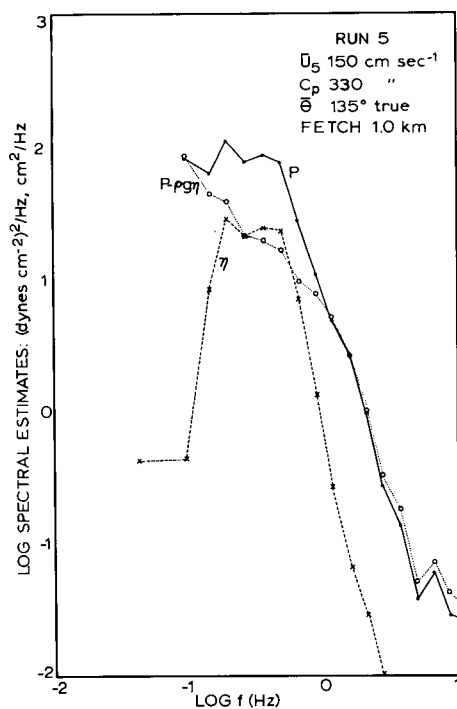
FOR RUNS 1, 2, 2a, and 3



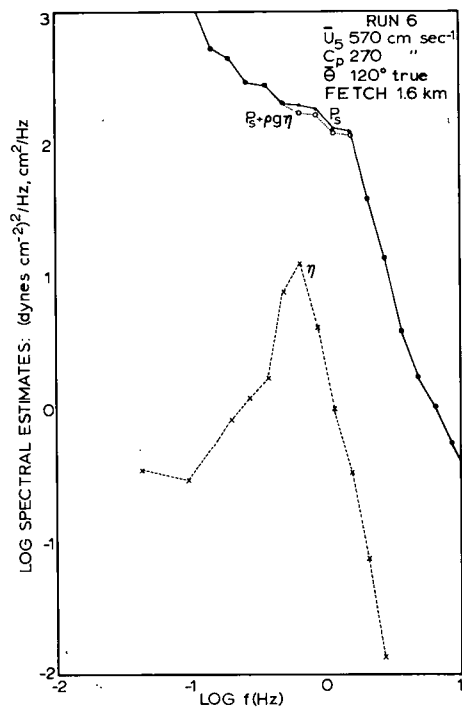
28



29



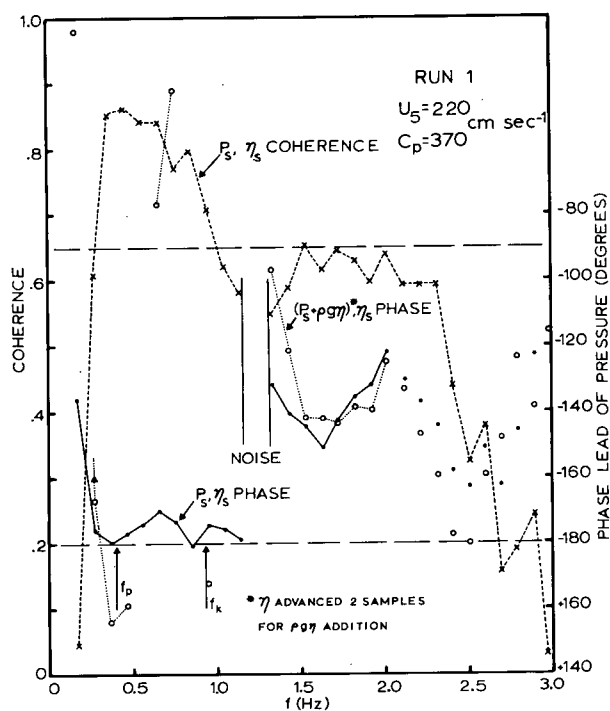
30



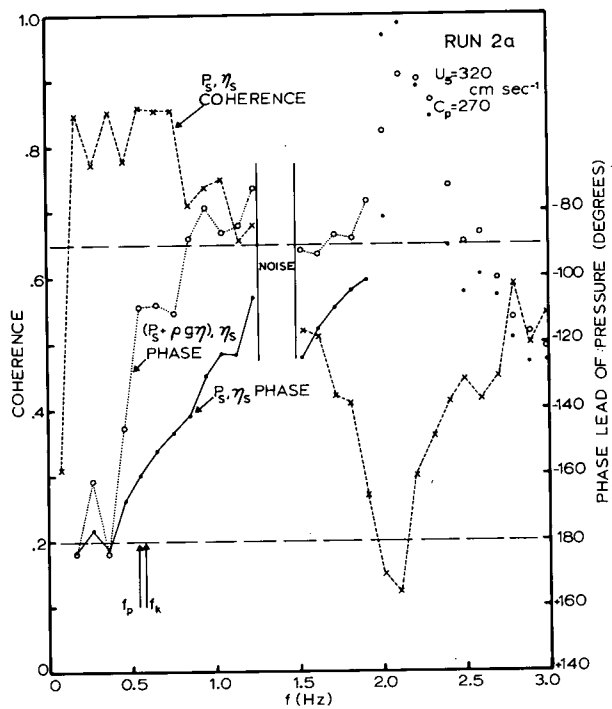
31

FIGURES 28-31.

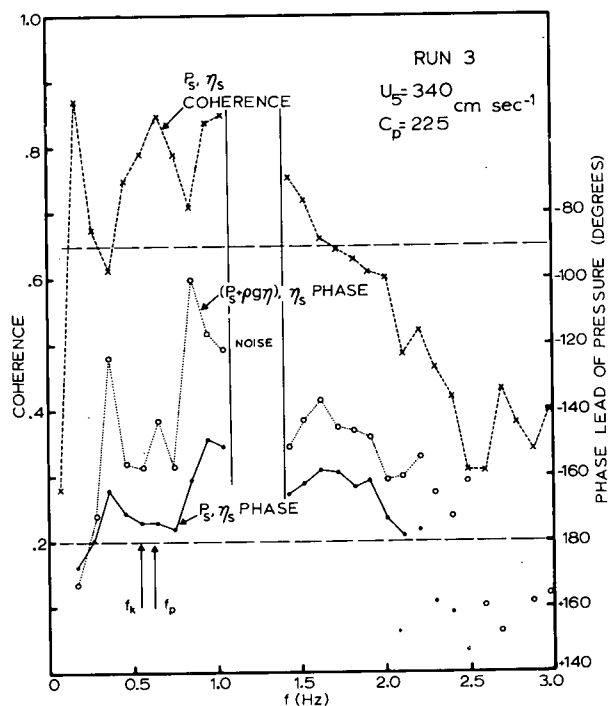
POWER SPECTRA OF p , $p + e_{pg\eta}$ and p_s , $p_s + e_{pg\eta}$
 FOR RUNS 4a, 4b, 5 and 6



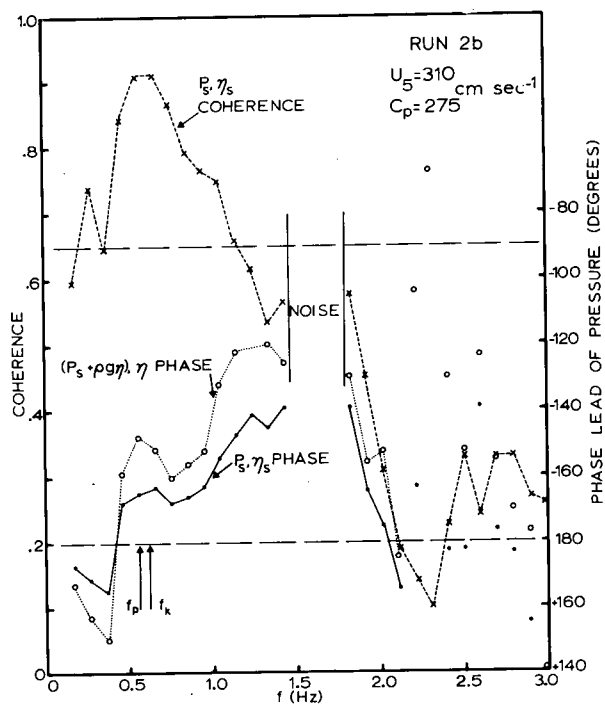
32



33



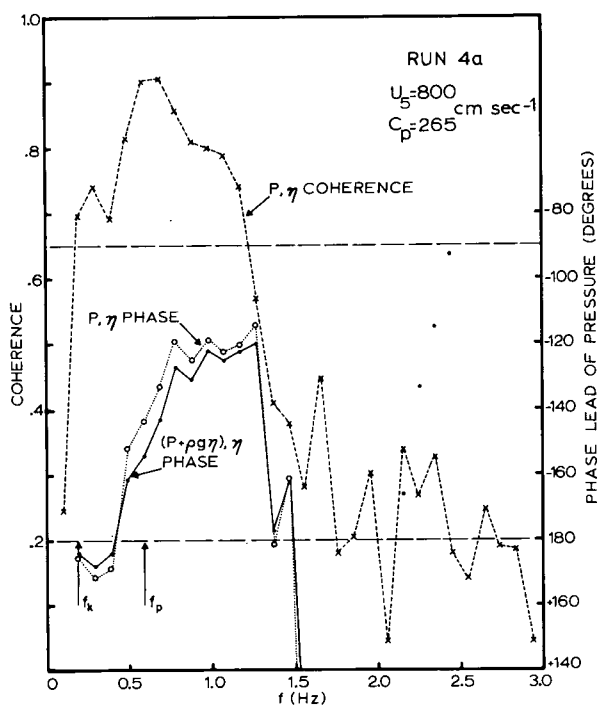
35



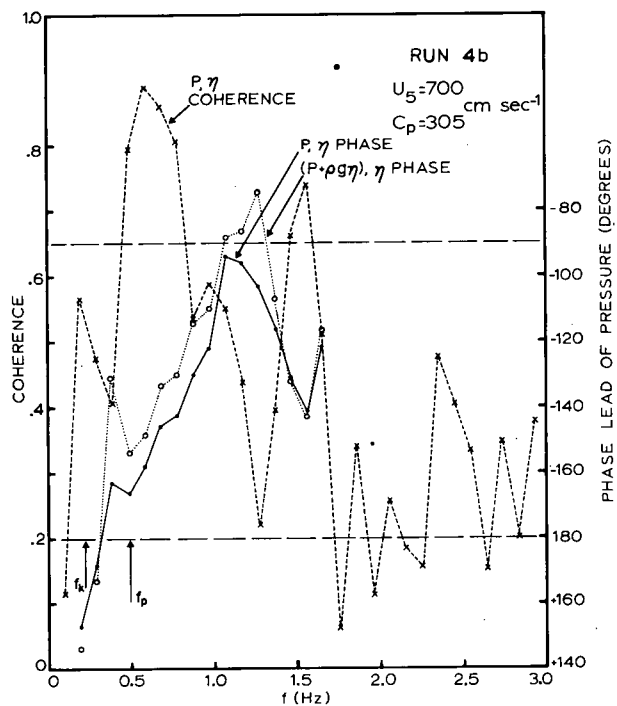
34

FIGURES 32-35.

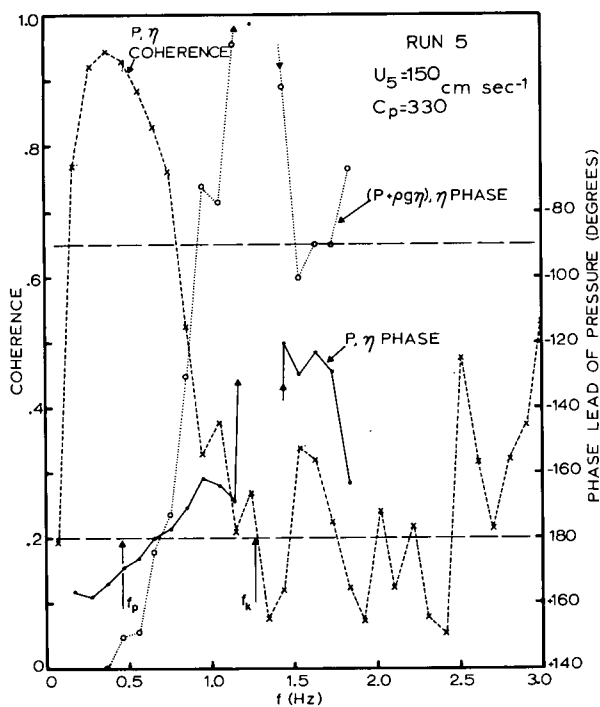
COHERENCE SPECTRA BETWEEN p_s, η_s ; PHASE SPECTRA
 BETWEEN p_s, η_s AND $(p_s + \rho g \eta), \eta_s$
 FOR RUNS 1, 2a, 2b, and 3



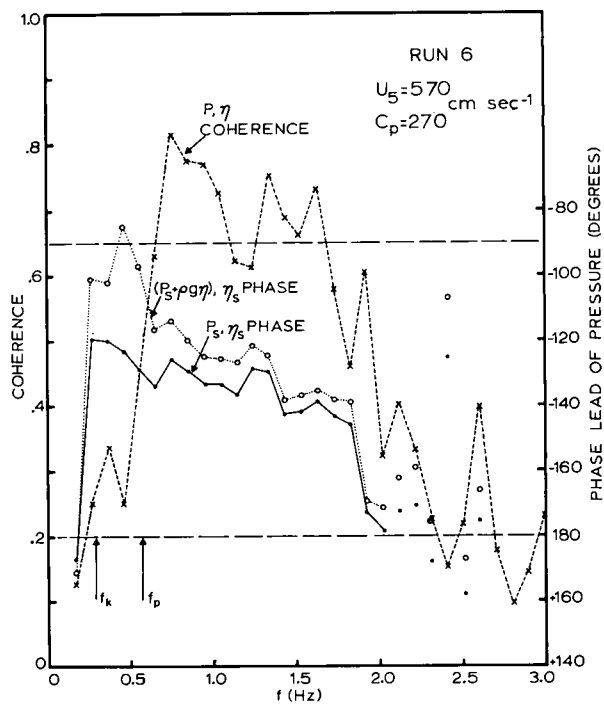
36



37



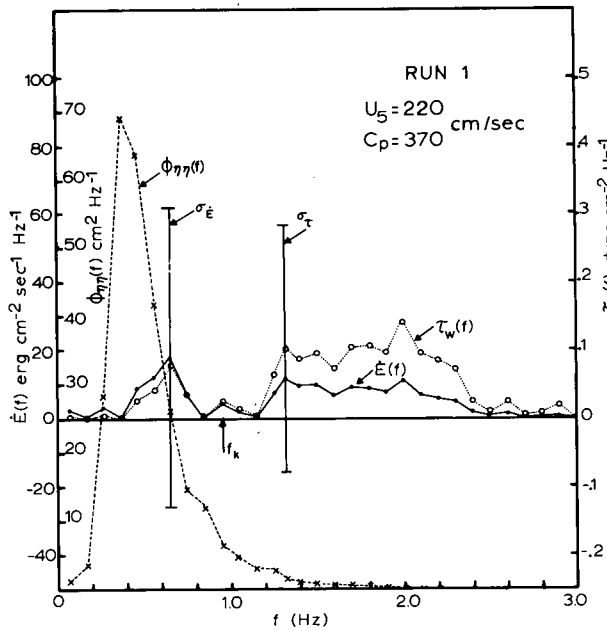
38



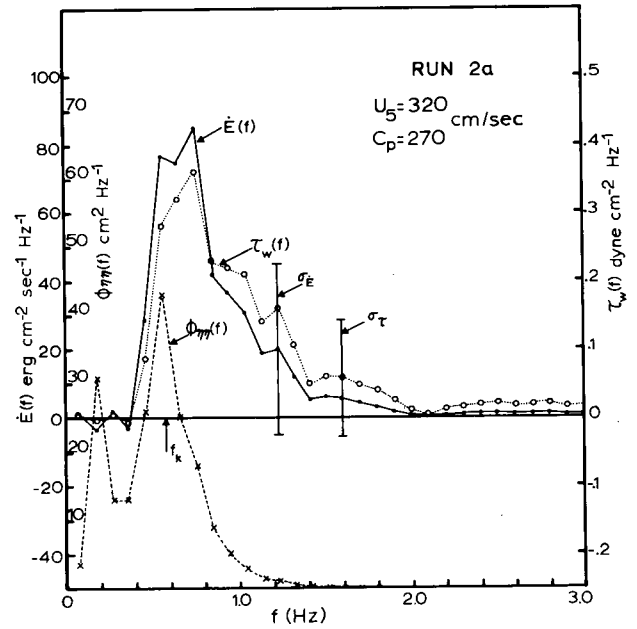
39

FIGURES 36-39.

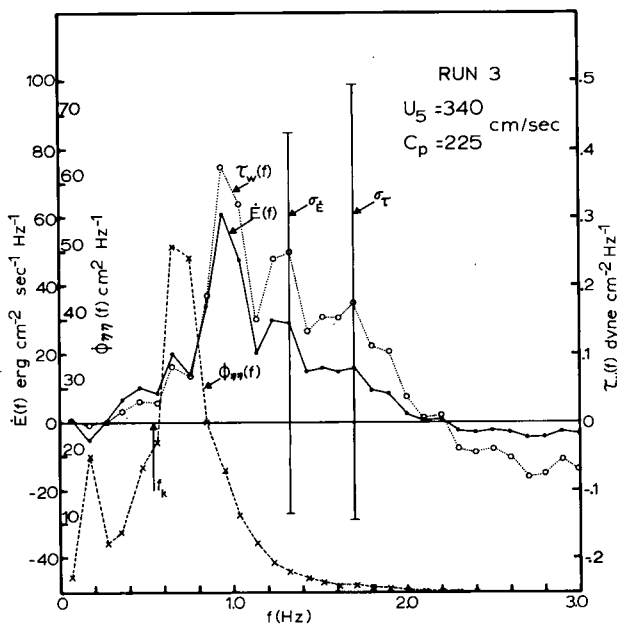
COHERENCE SPECTRA BETWEEN p_s , η_s ; PHASE SPECTRA
BETWEEN p_s , η_s and $(p_s + \rho g \eta)$, η_s
FOR RUNS 4a, 4b, 5, and 6



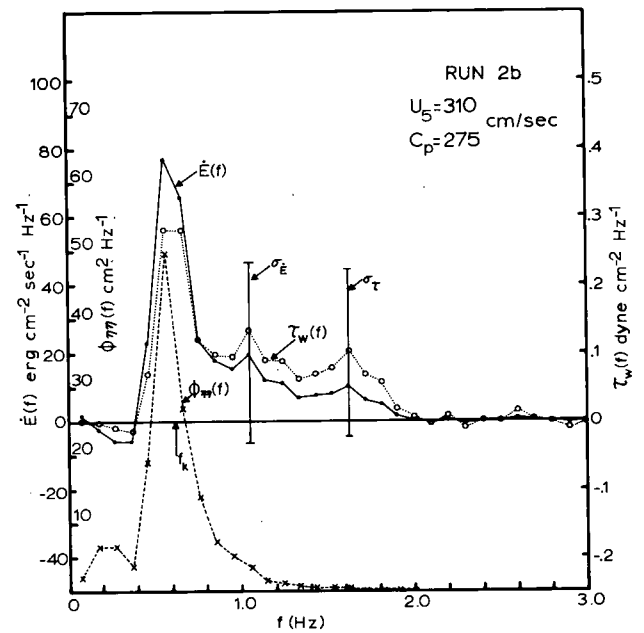
40



41



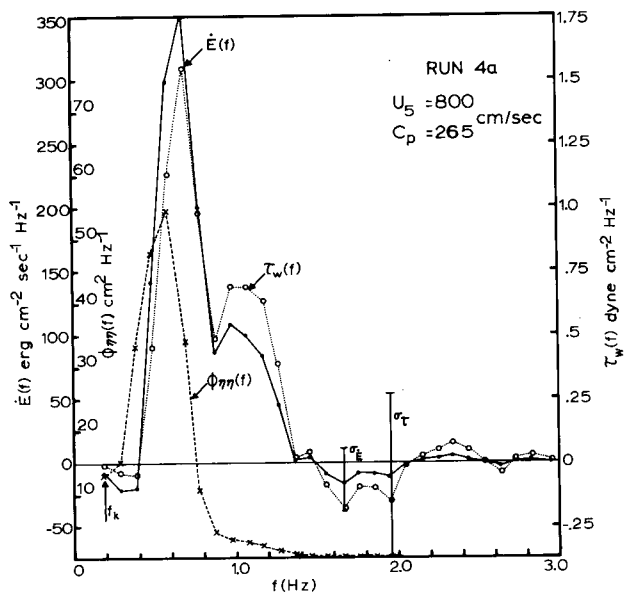
43



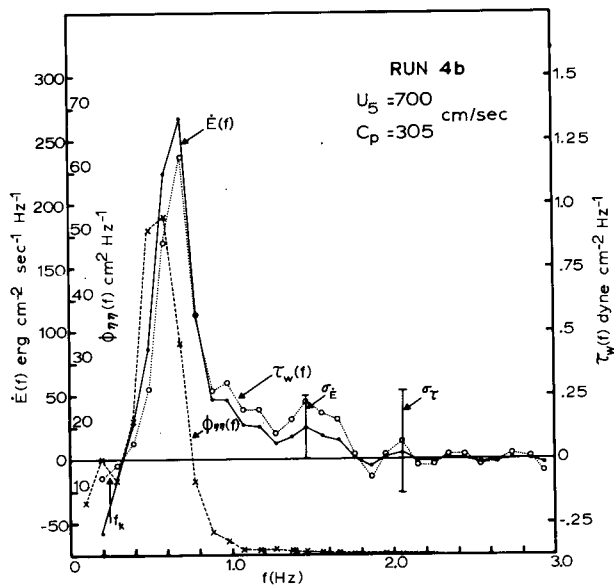
42

FIGURES 40-43.

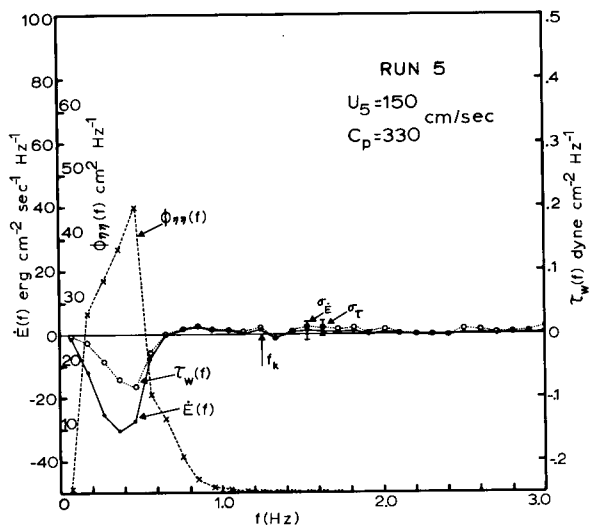
ENERGY AND MOMENTUM FLUX SPECTRA AND WAVE POWER
SPECTRUM FOR RUNS 1, 2a, 2b, and 3



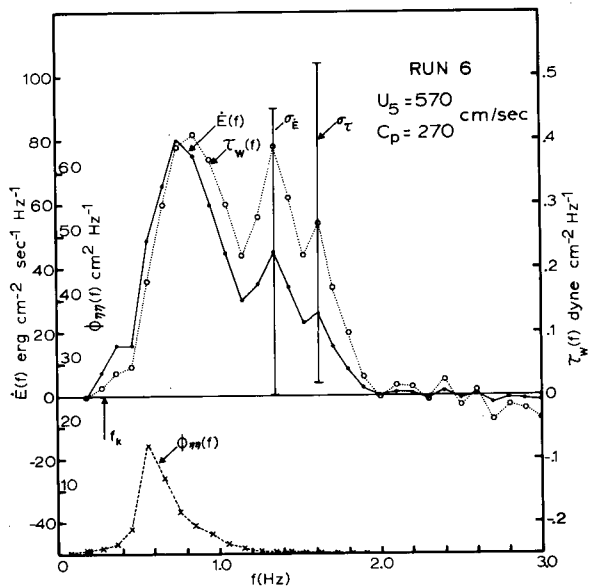
44



45



46

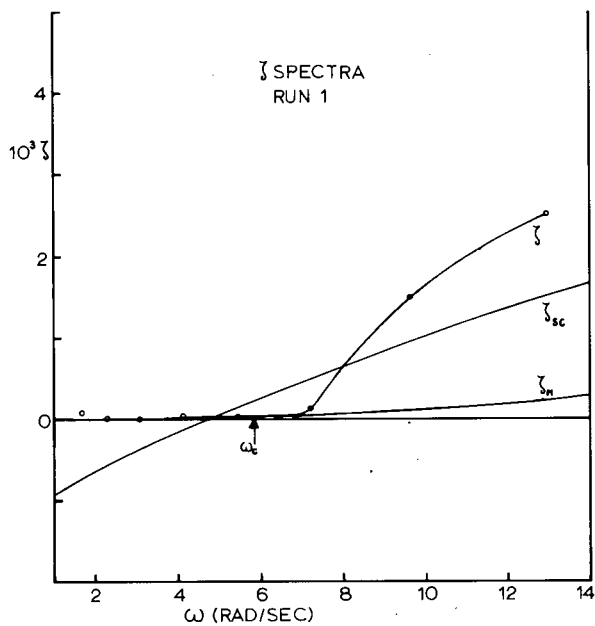


47

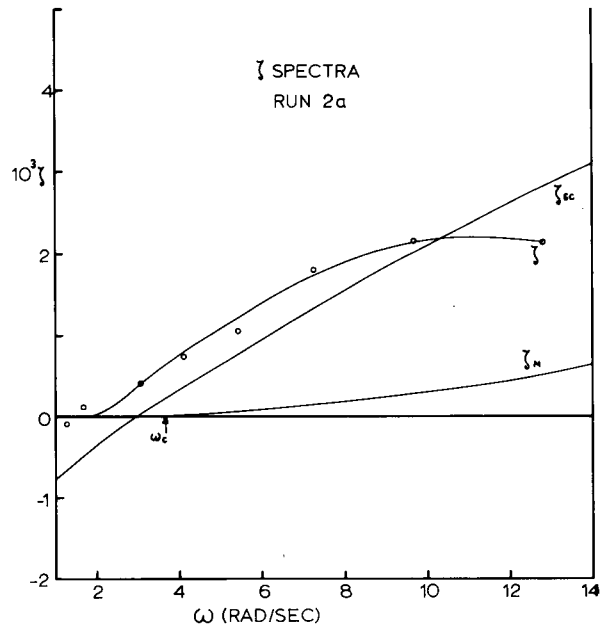
FIGURES 44-47.

ENERGY AND MOMENTUM FLUX SPECTRA AND WAVE POWER

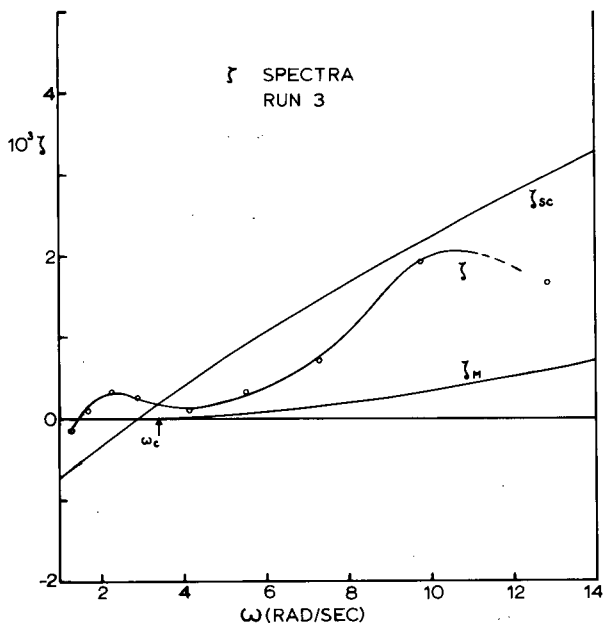
SPECTRUM FOR RUNS 4a, 4b, 5, and 6



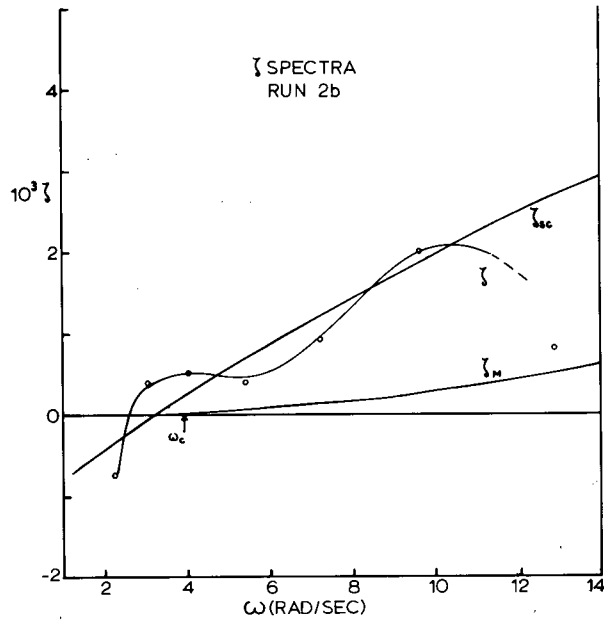
48



49



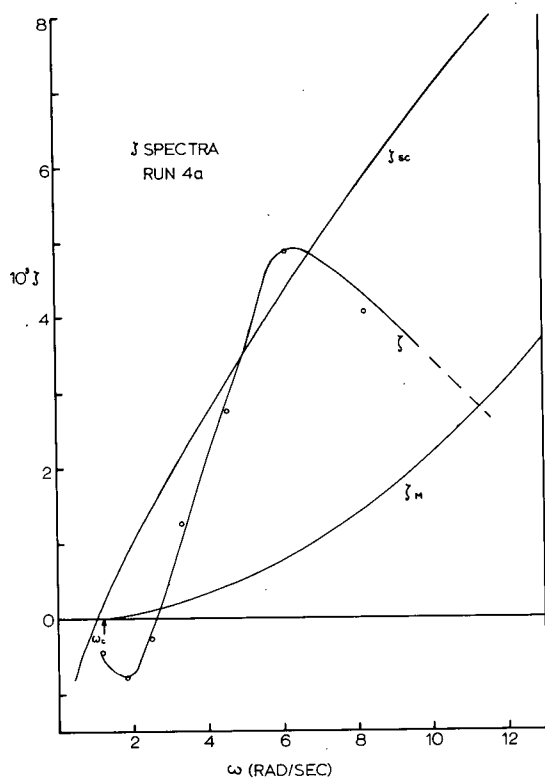
50



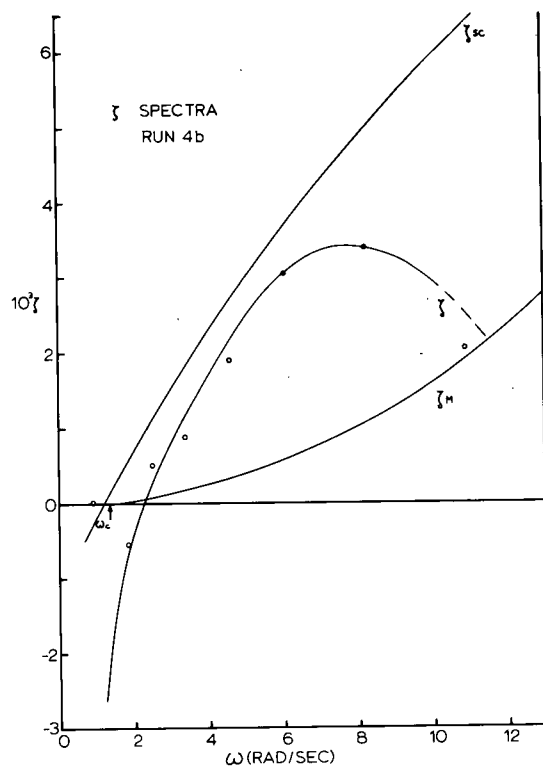
51

FIGURES 48-51.

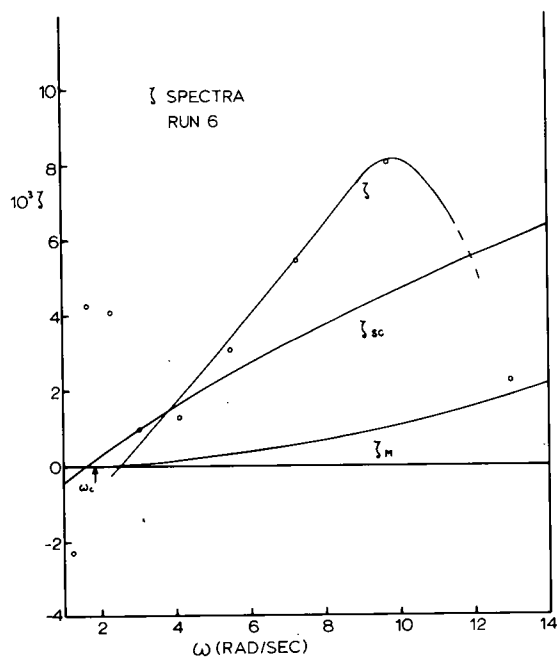
SPECTRA OF ζ : COMPARISONS WITH SNYDER AND COX,
MILES FOR RUNS 1, 2a, 2b, and 3.



52



53



54

FIGURES 52-54.

SPECTRA OF ζ : COMPARISONS WITH SNYDER AND COX, MILES
FOR RUNS 4a, 4b, and 6.

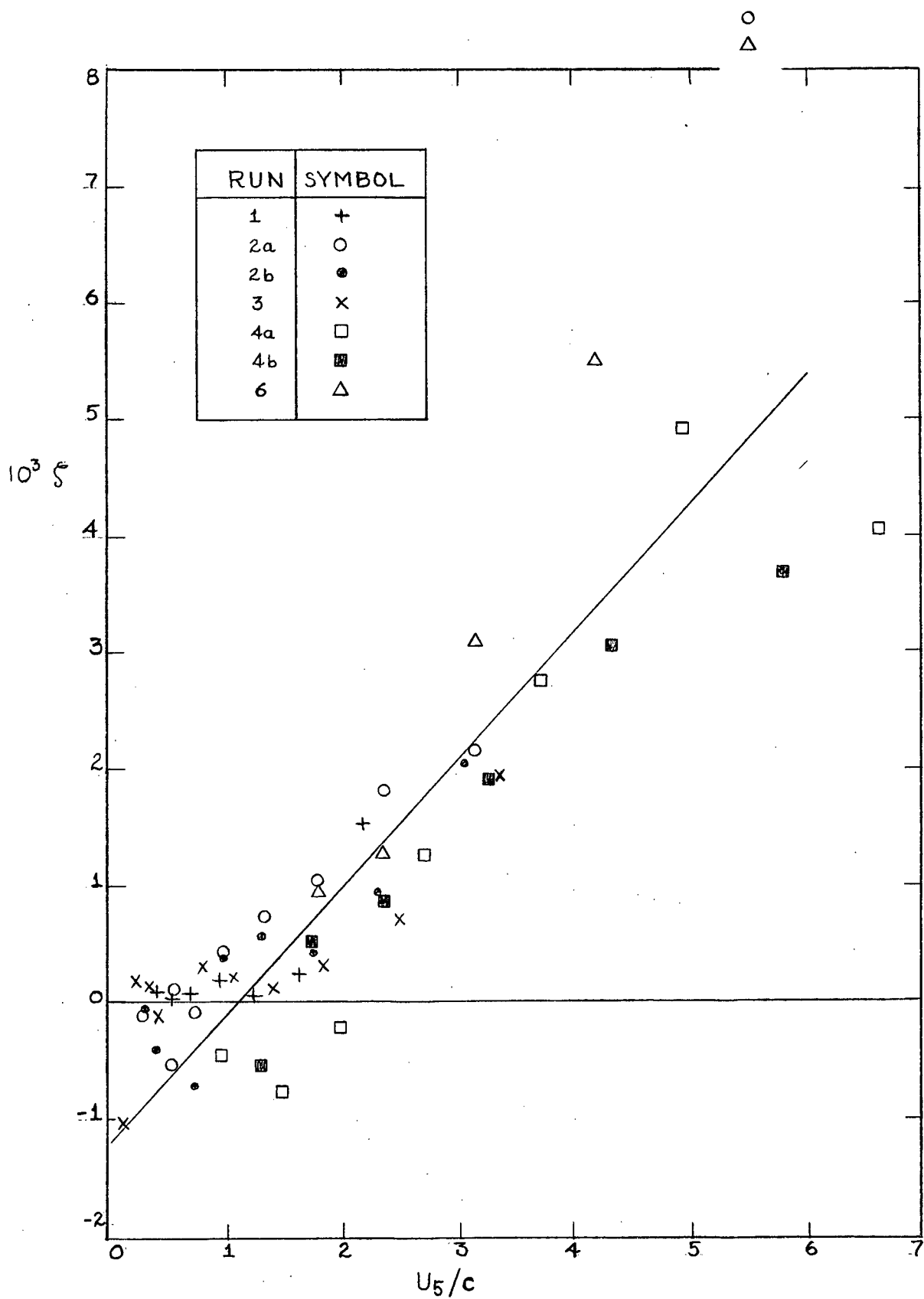


FIGURE 55.
 DIMENSIONLESS PLOT OF ζ VERSUS U_5/c

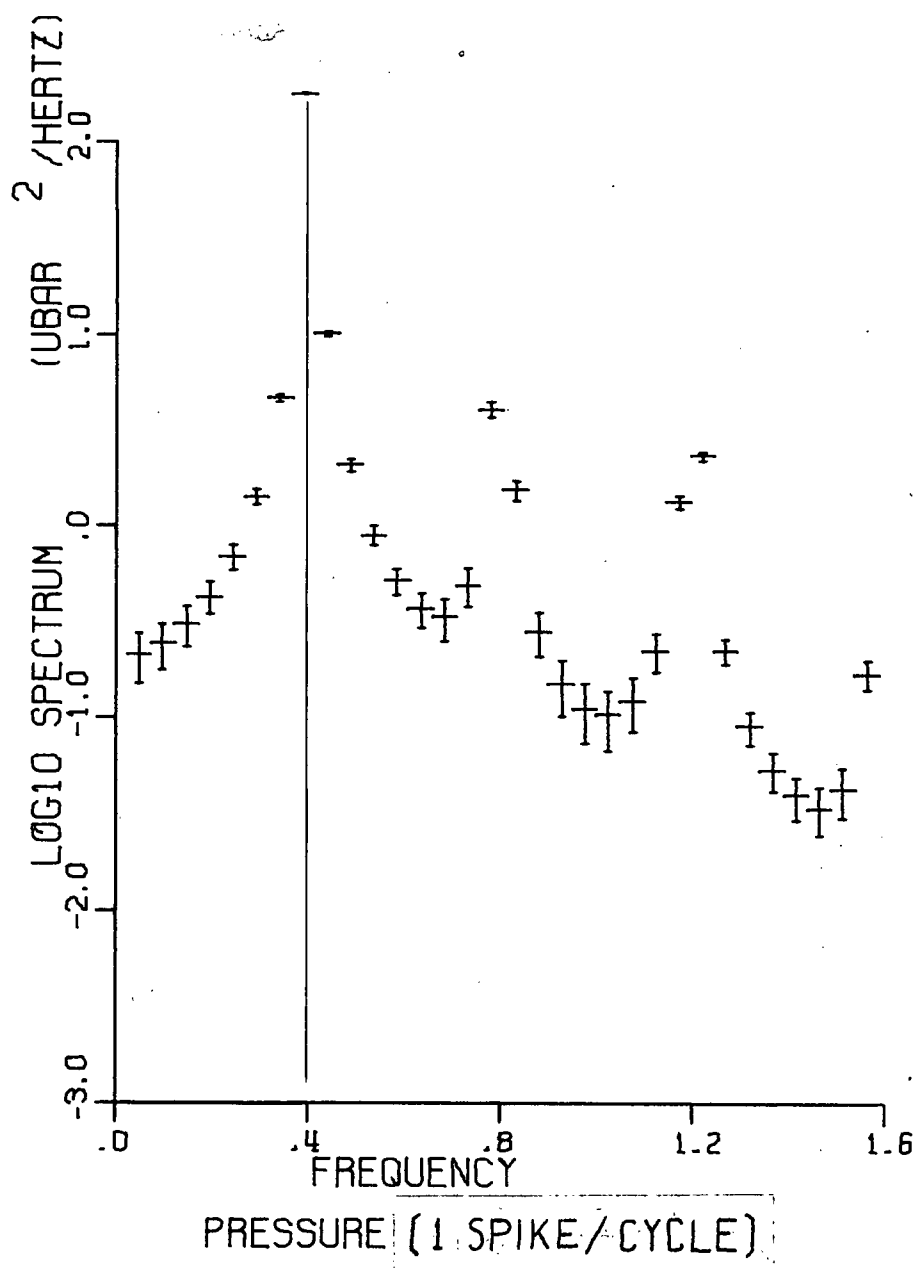
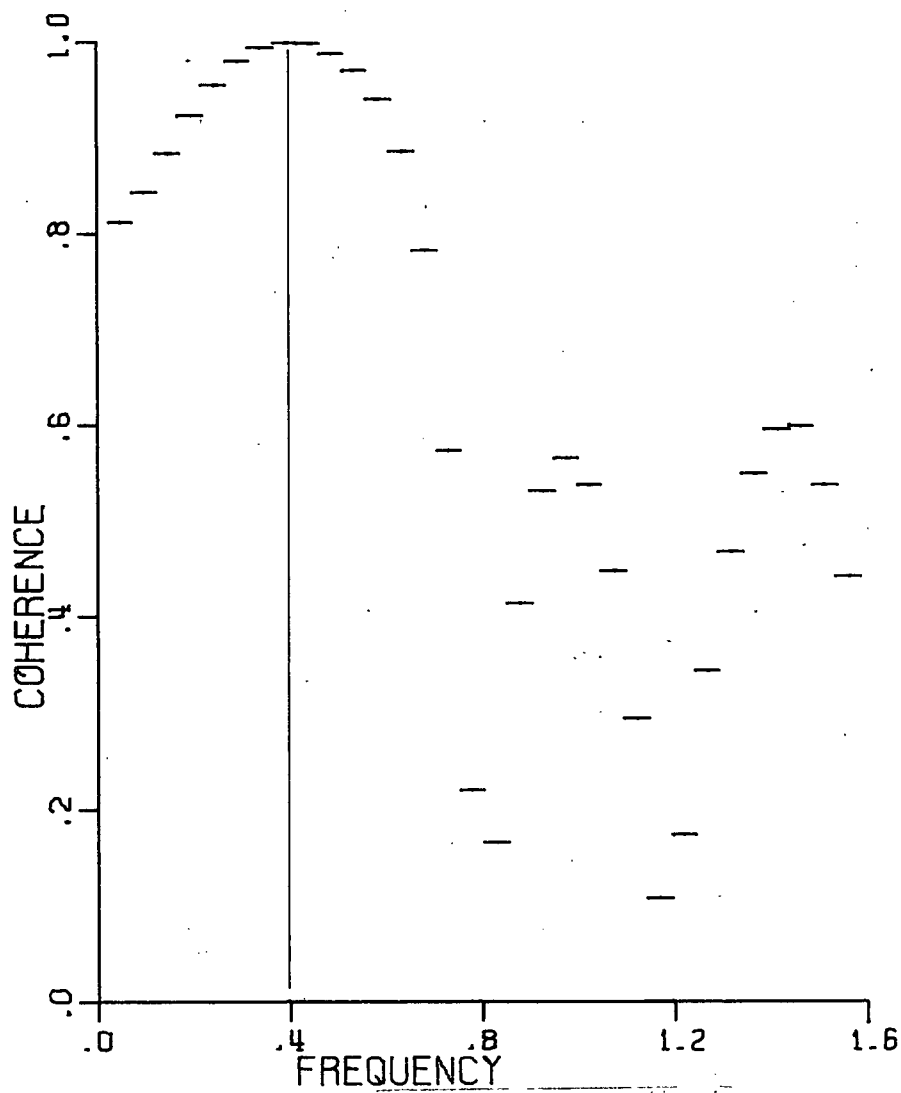


FIGURE 56.

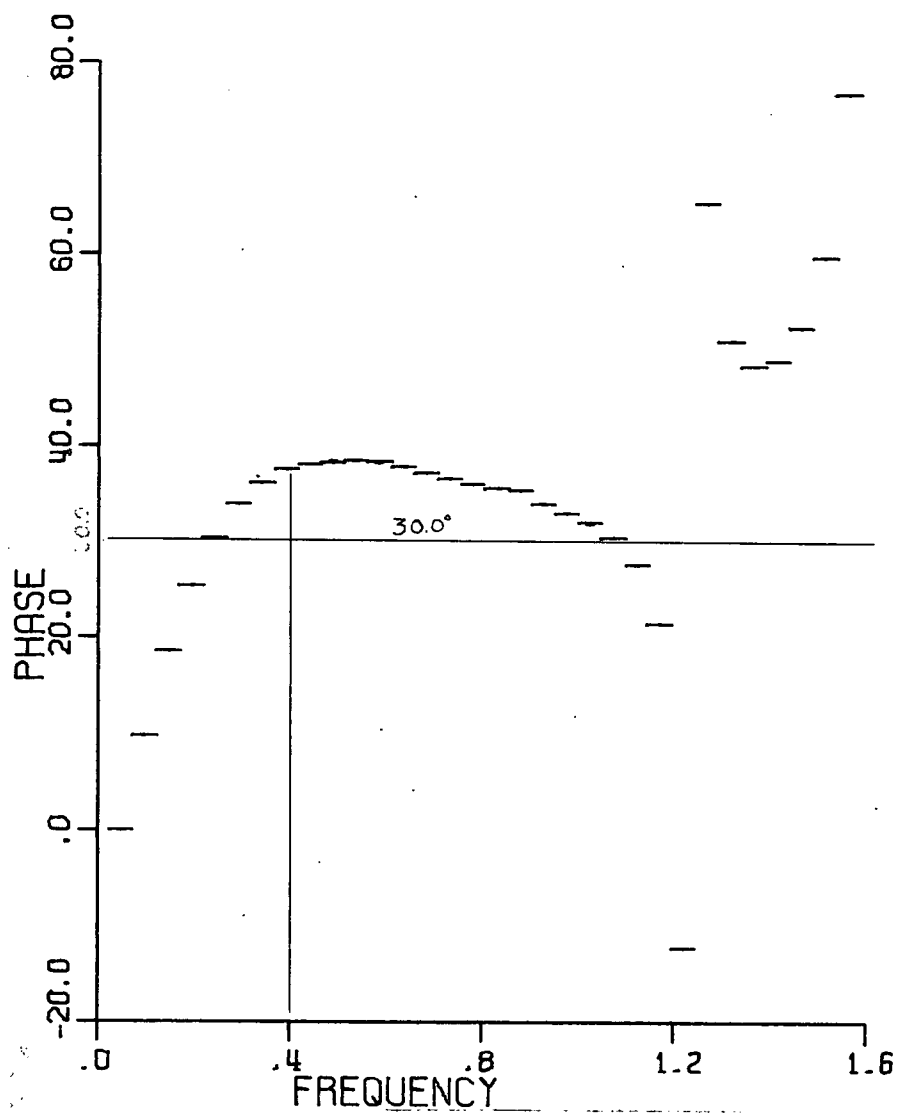
POWER SPECTRUM OF $p_s(t)$



PRESSURE (1 SPIKE/CYCLE)
WAVES (NO SPIKES)

FIGURE 57.

COHERENCE BETWEEN $p_s(t)$ and $\eta(t)$



PRESSURE (1 SPIKE/CYCLE)
WAVES (NO SPIKES)

FIGURE 58.

PHASE ANGLE BETWEEN $p_s(t)$ and $\eta(t)$

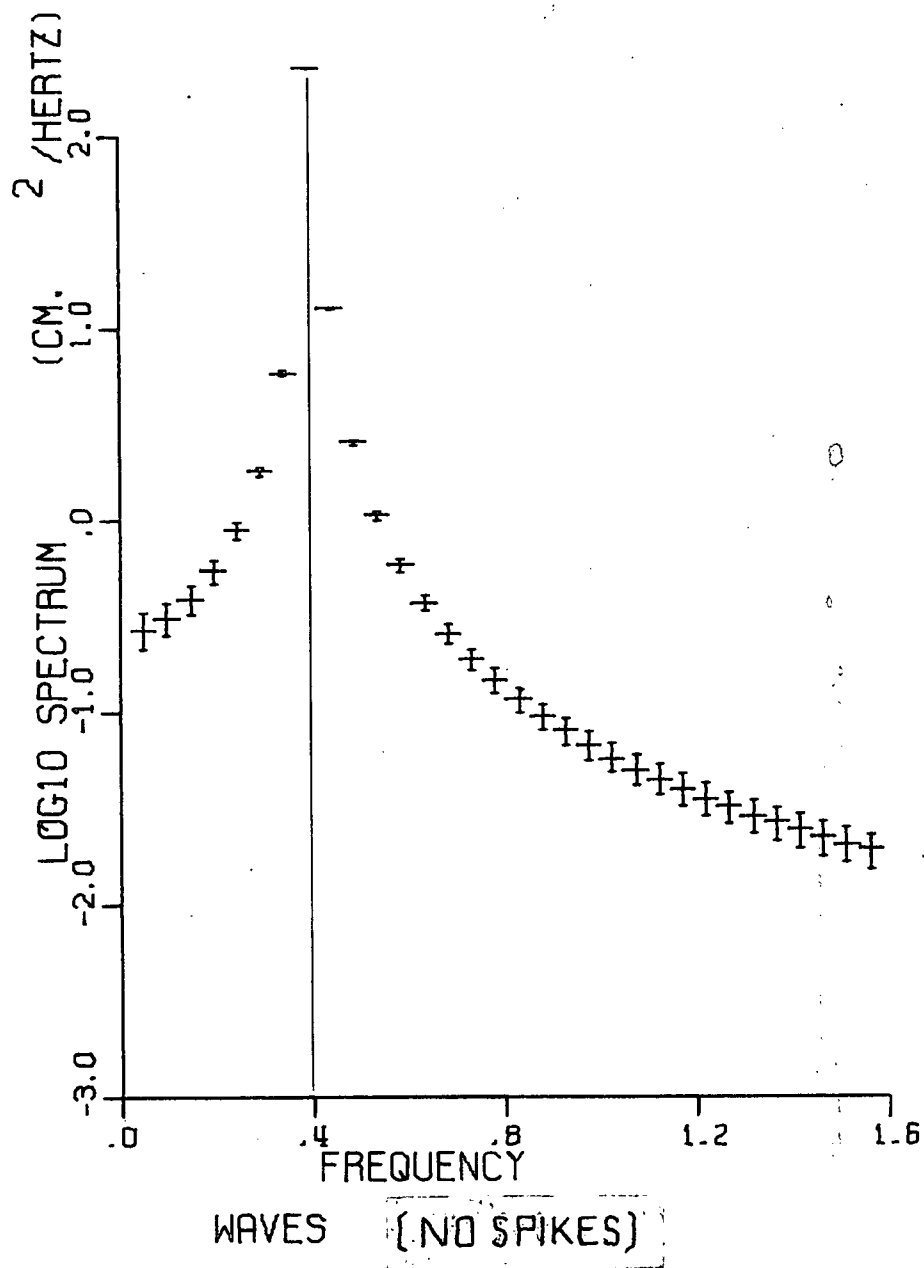


FIGURE 59.

POWER SPECTRUM OF $\eta(t)$

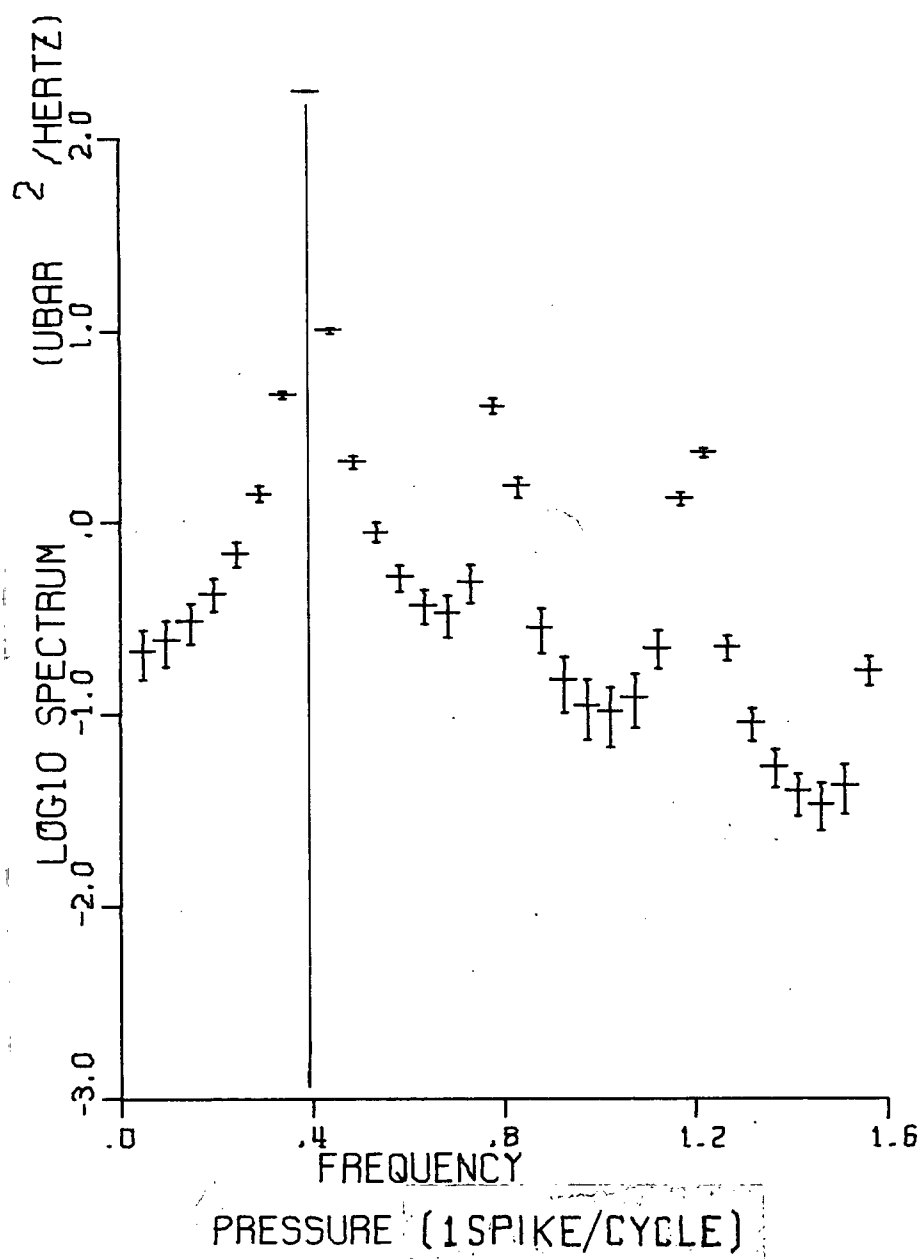
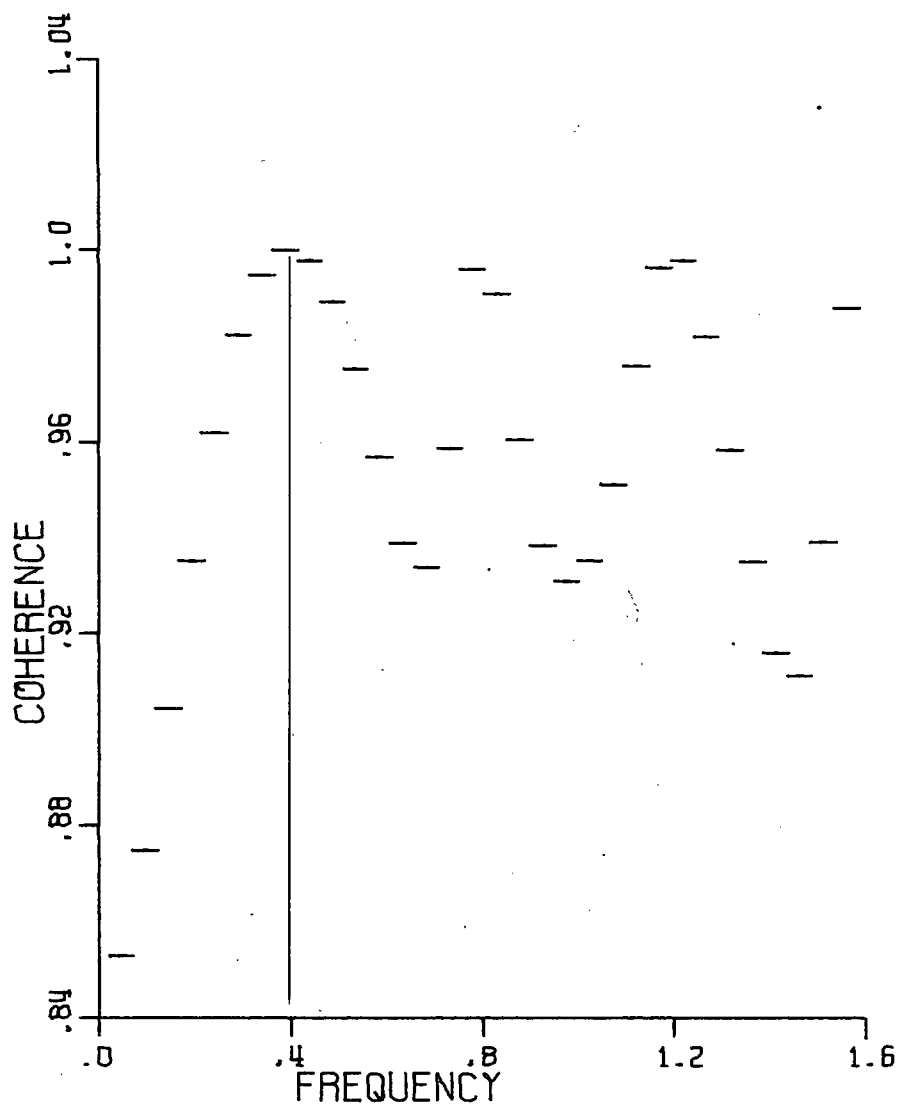


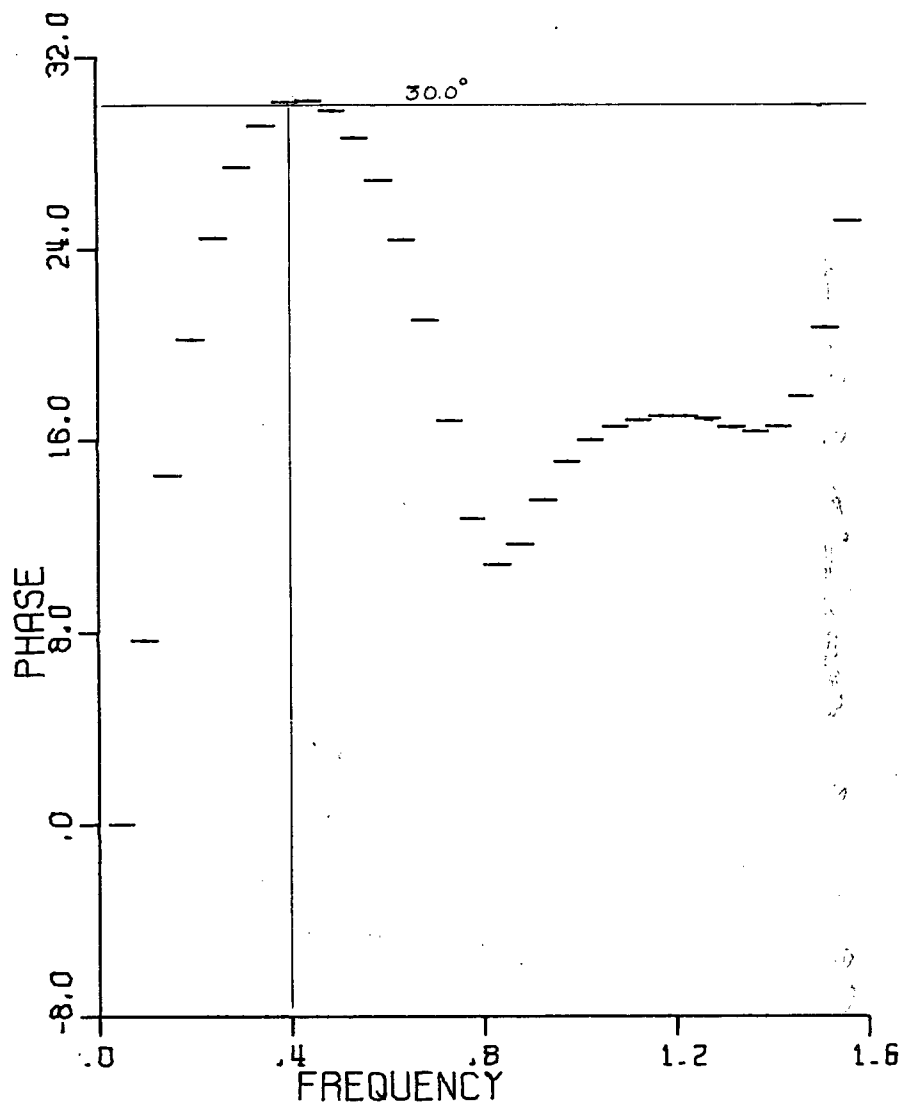
FIGURE 60.
POWER SPECTRUM OF $p_s(t)$



PRESSURE WAVES [1 SPIKE/CYCLE]

FIGURE 61.

COHERENCE BETWEEN $p_s(t)$ and $\eta_s(t)$



PRESSURE
WAVES

(1 SPIKE/CYCLE)

FIGURE 62.

PHASE ANGLE BETWEEN $p_s(t)$ and $\eta_s(t)$

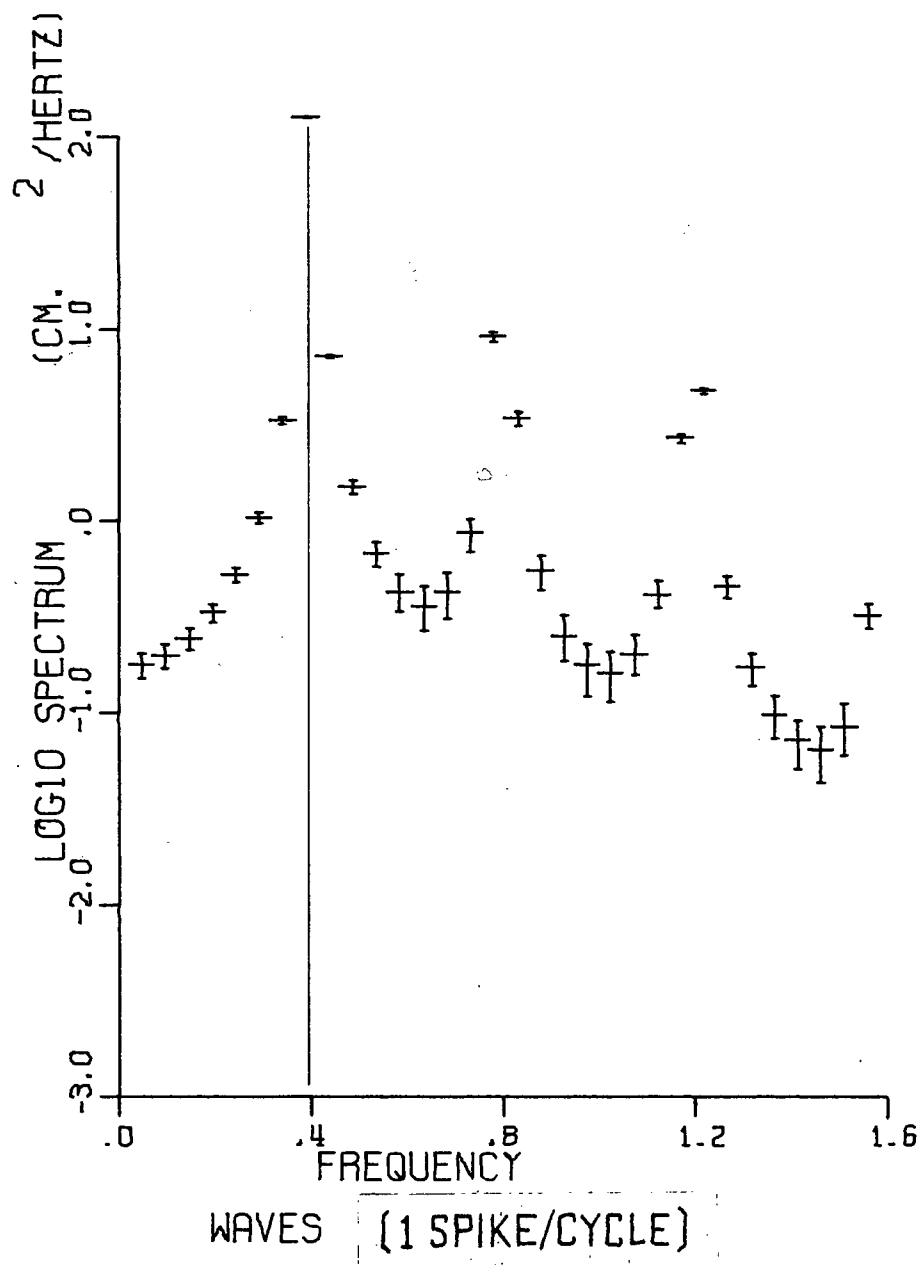
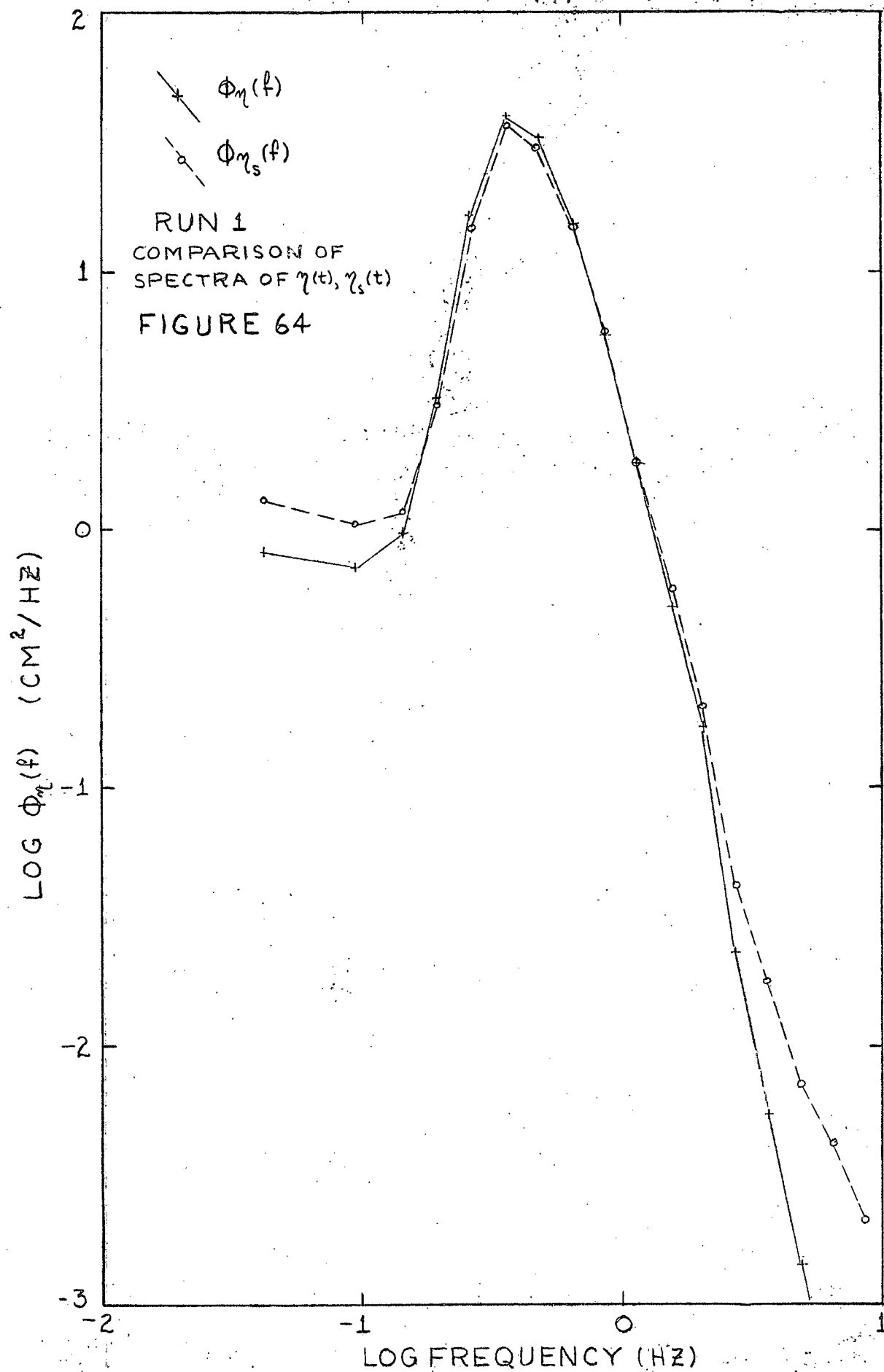
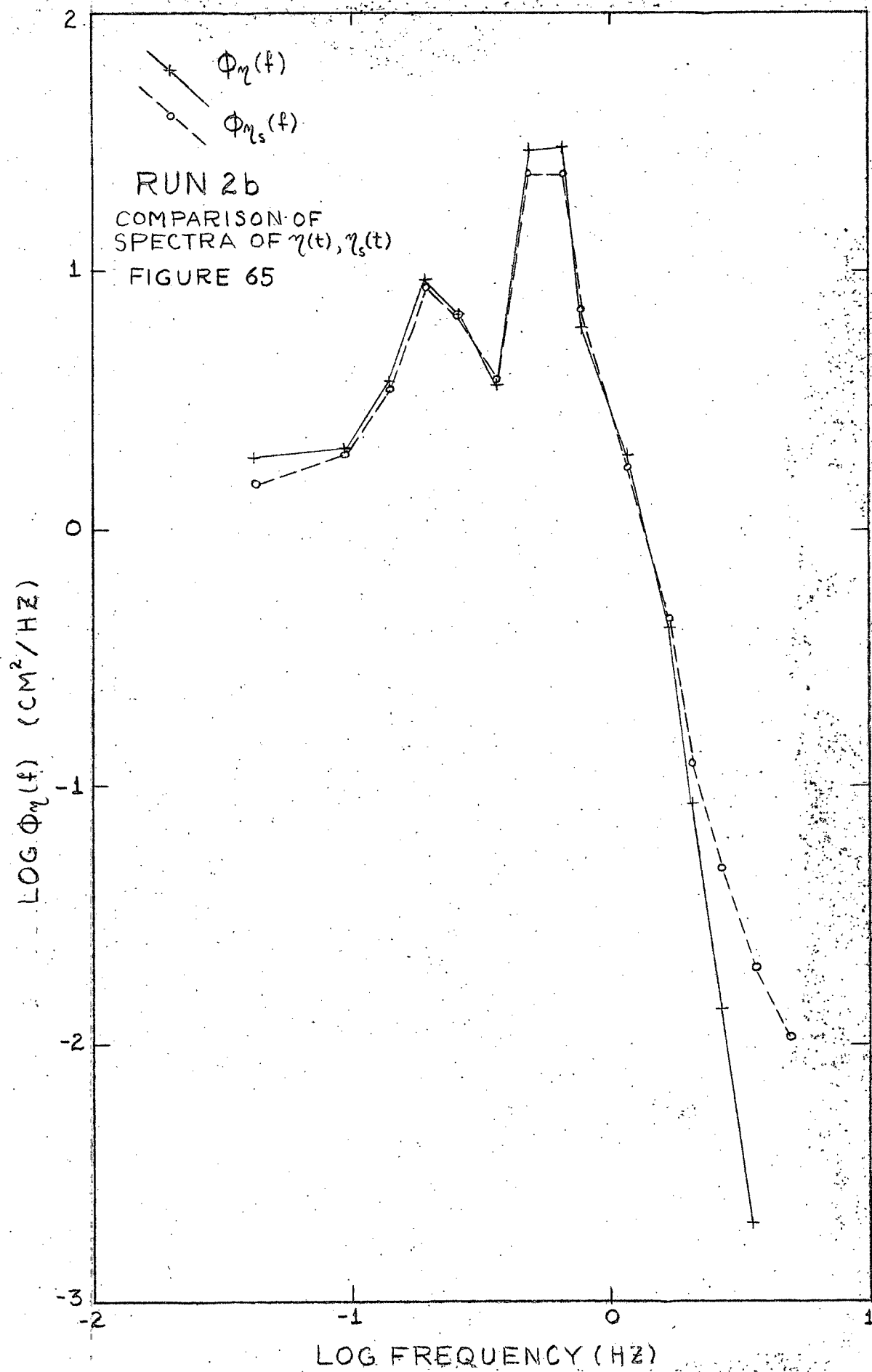
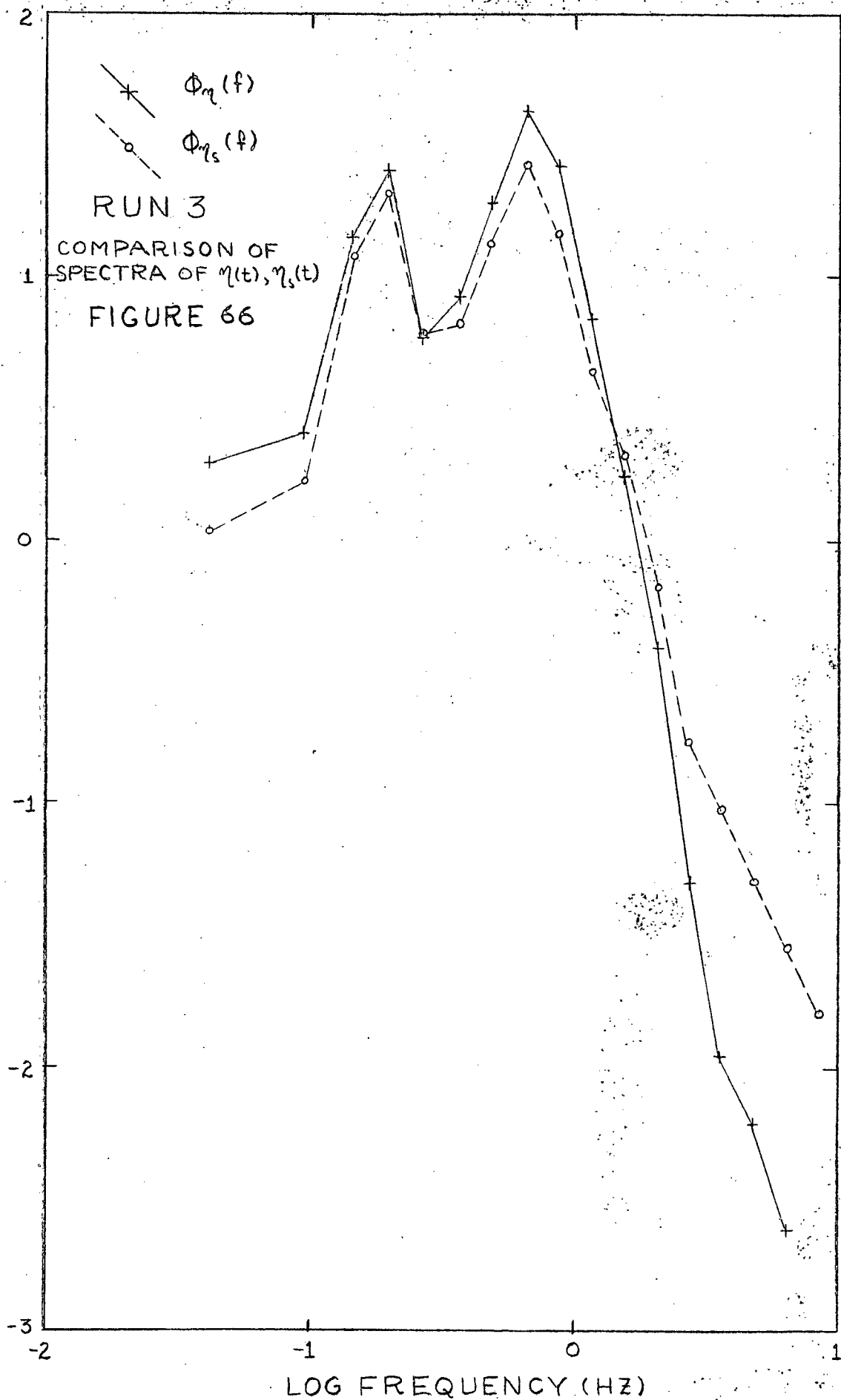


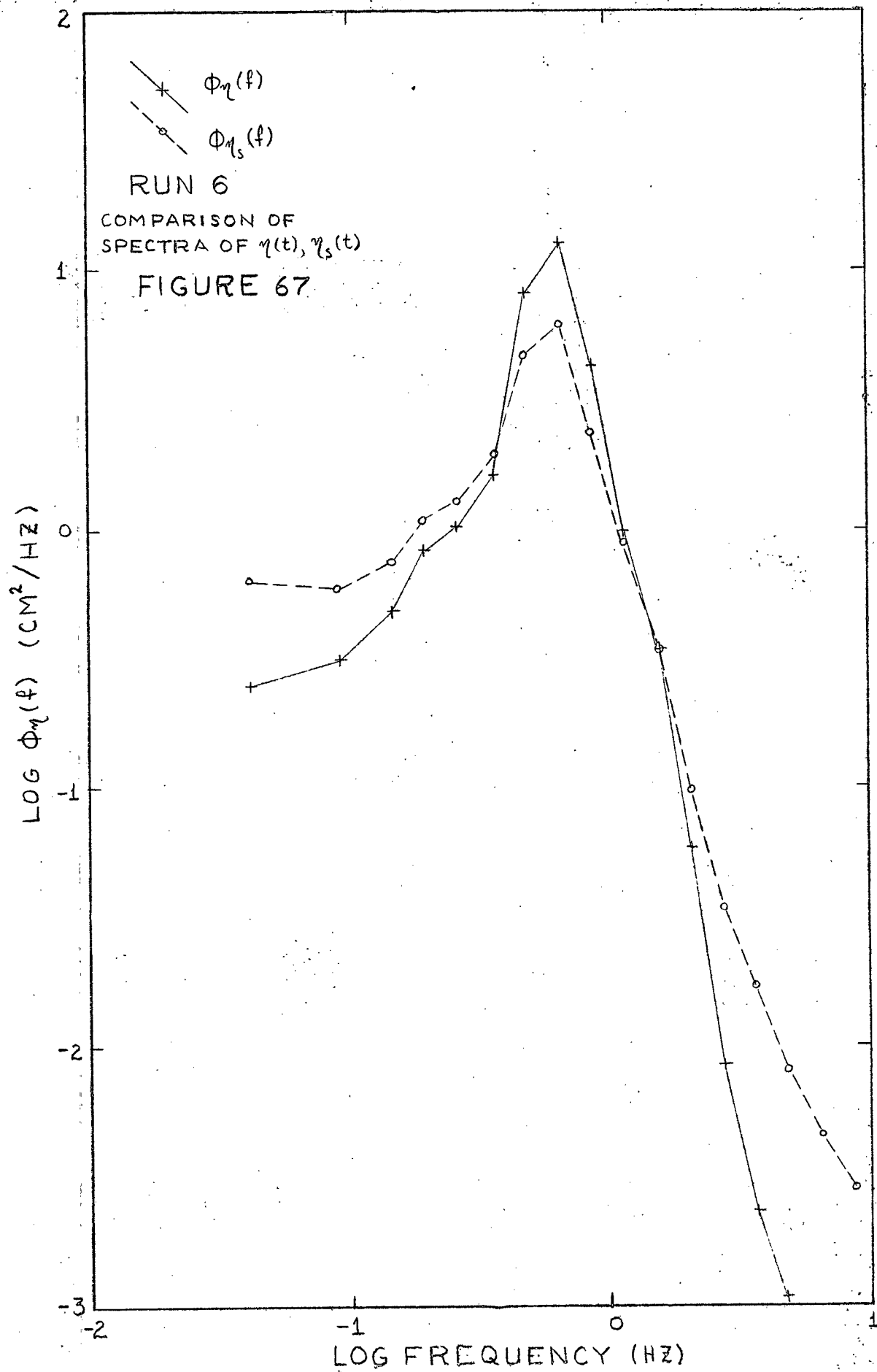
FIGURE 63.
POWER SPECTRUM OF $\eta_s(t)$

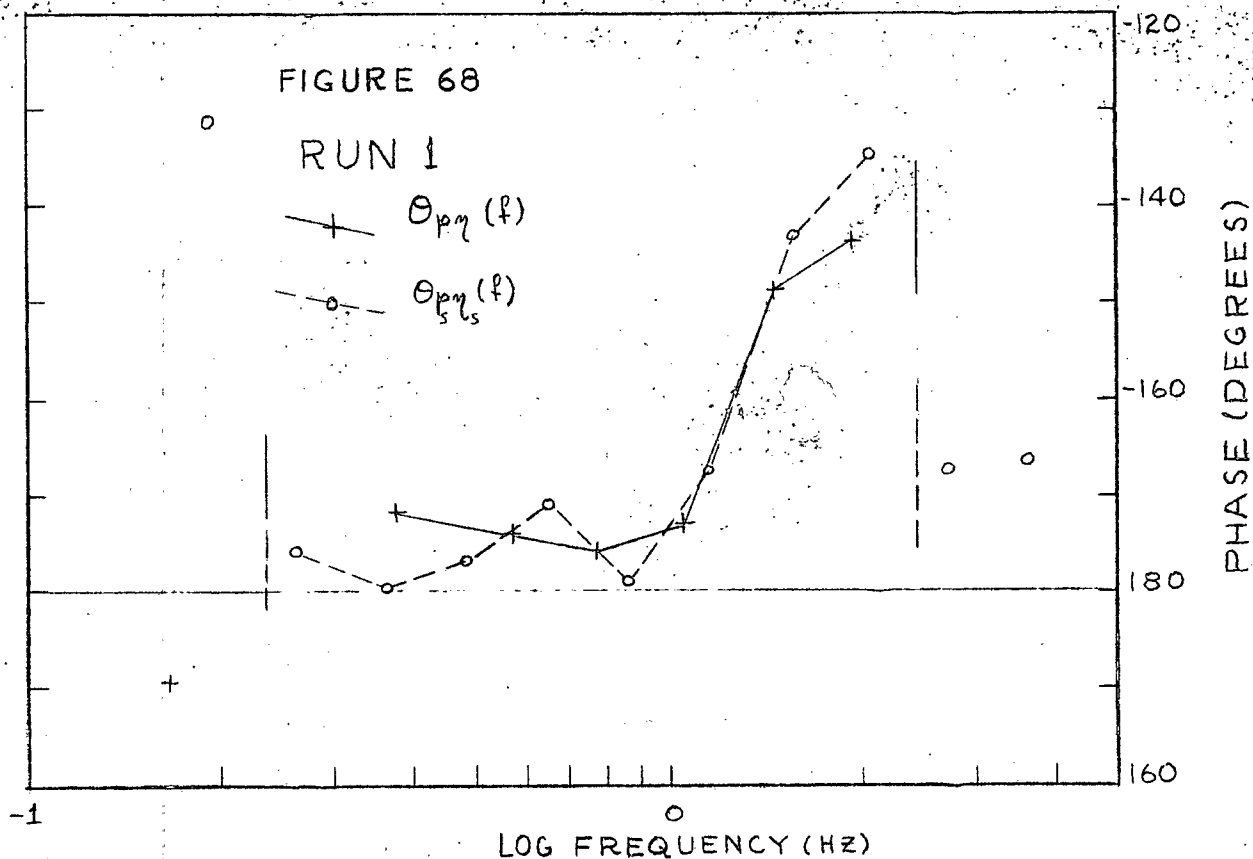




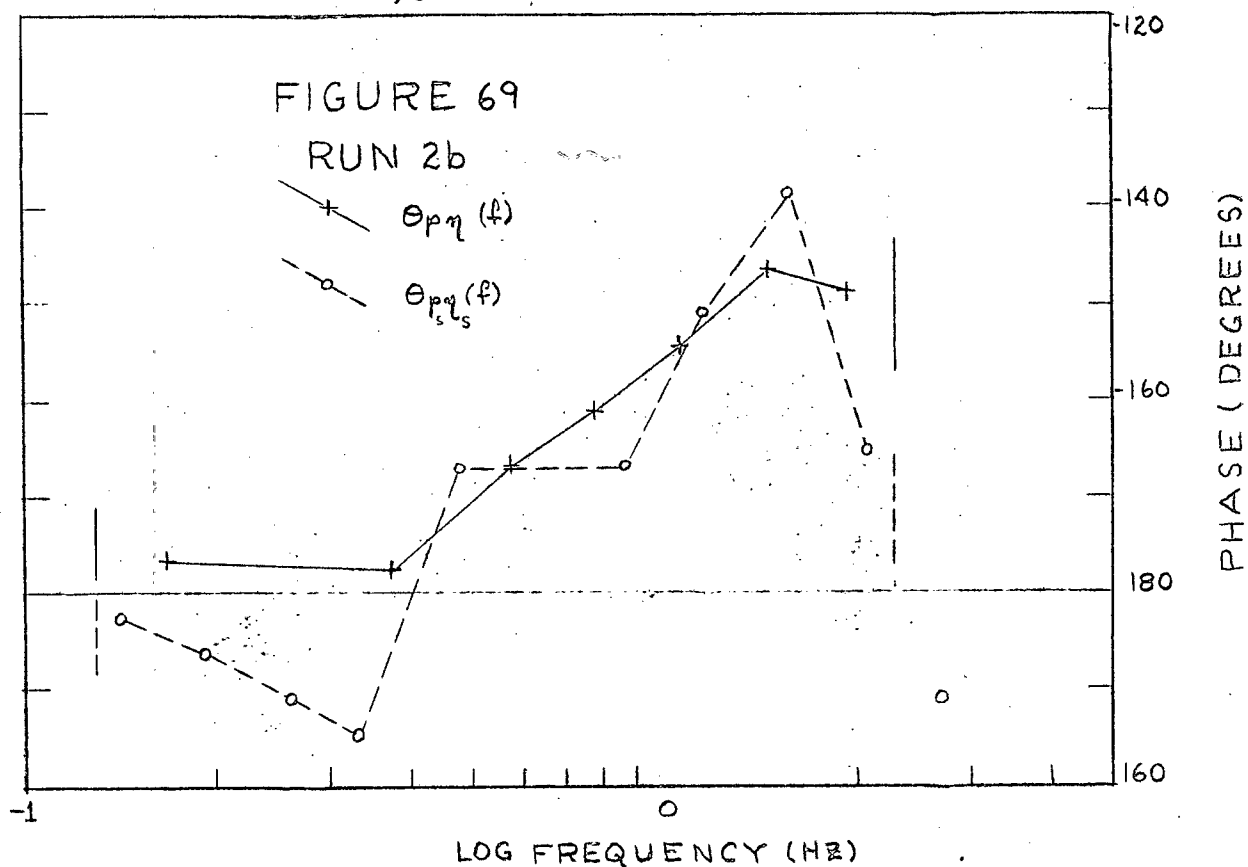
LOG $\Phi_{\eta}(f)$ (CM^2/HZ)

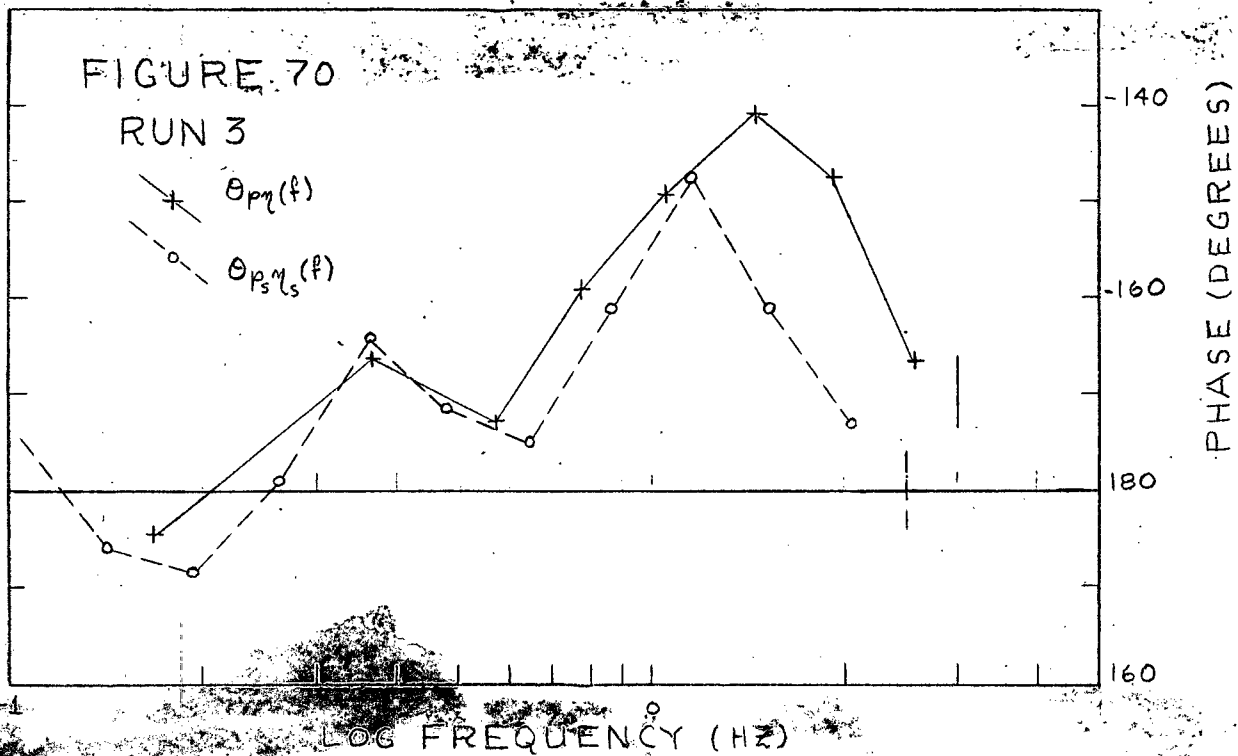




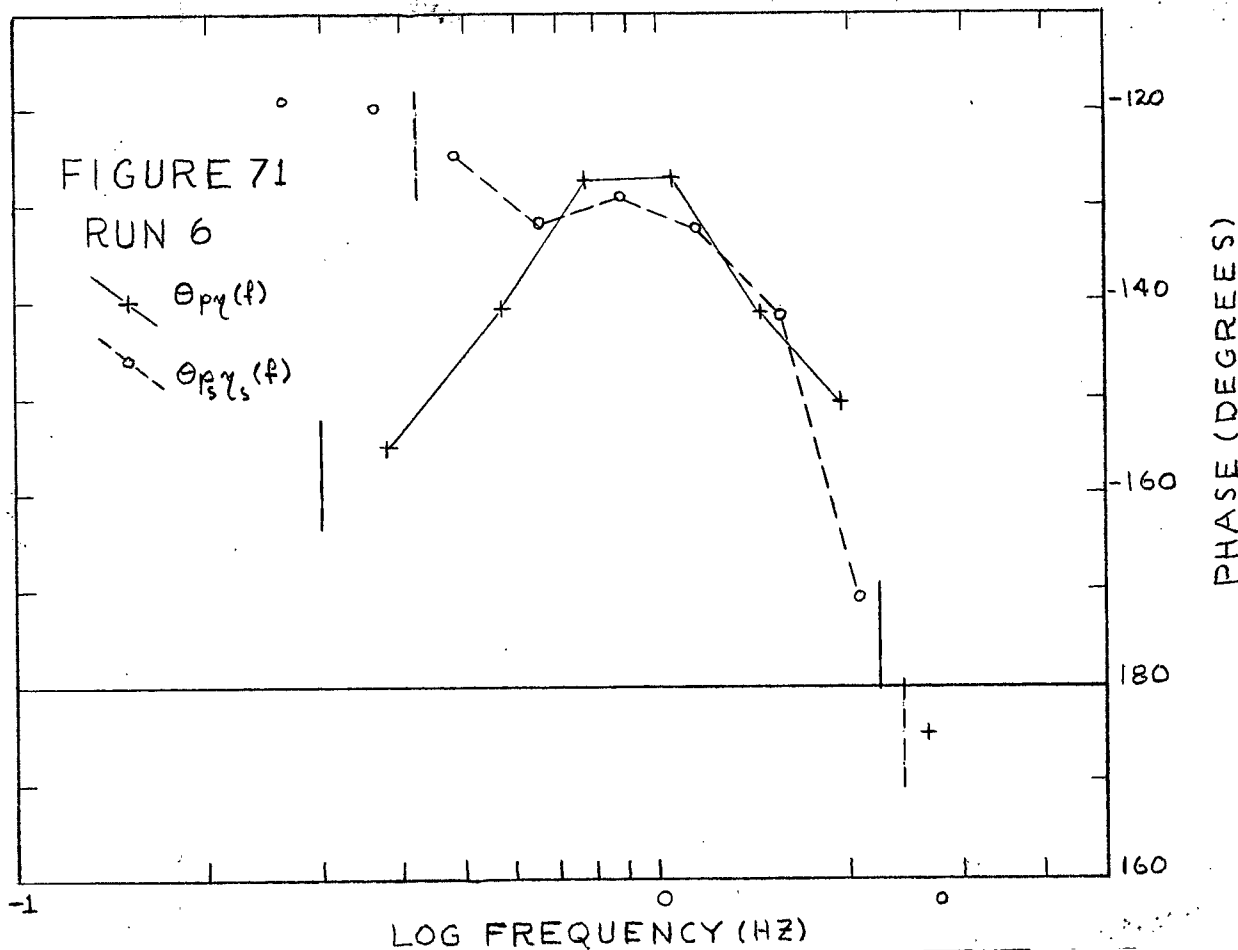


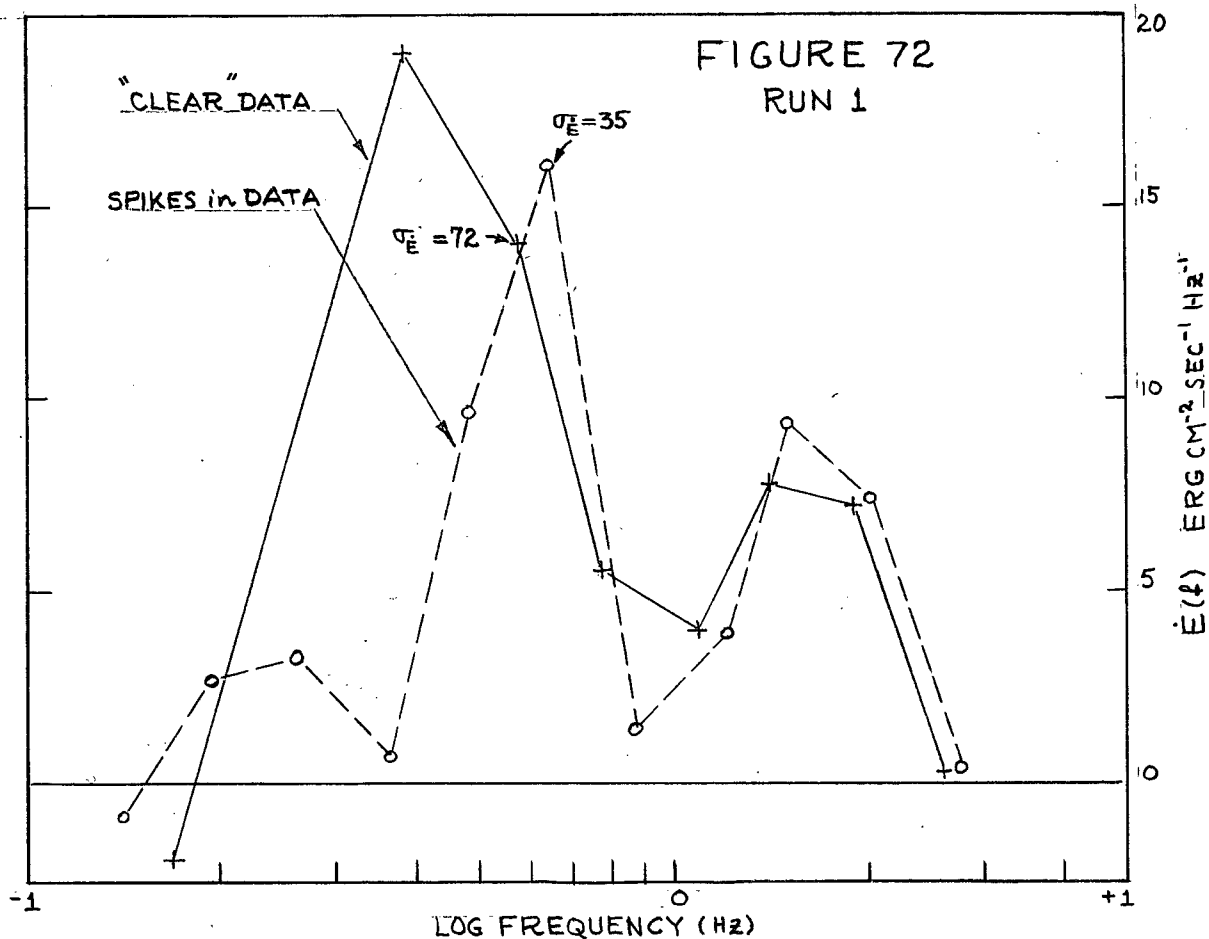
COMPARISON OF SPIKE-CONTAMINATED AND "CLEAR"
 p_η PHASE SPECTRA



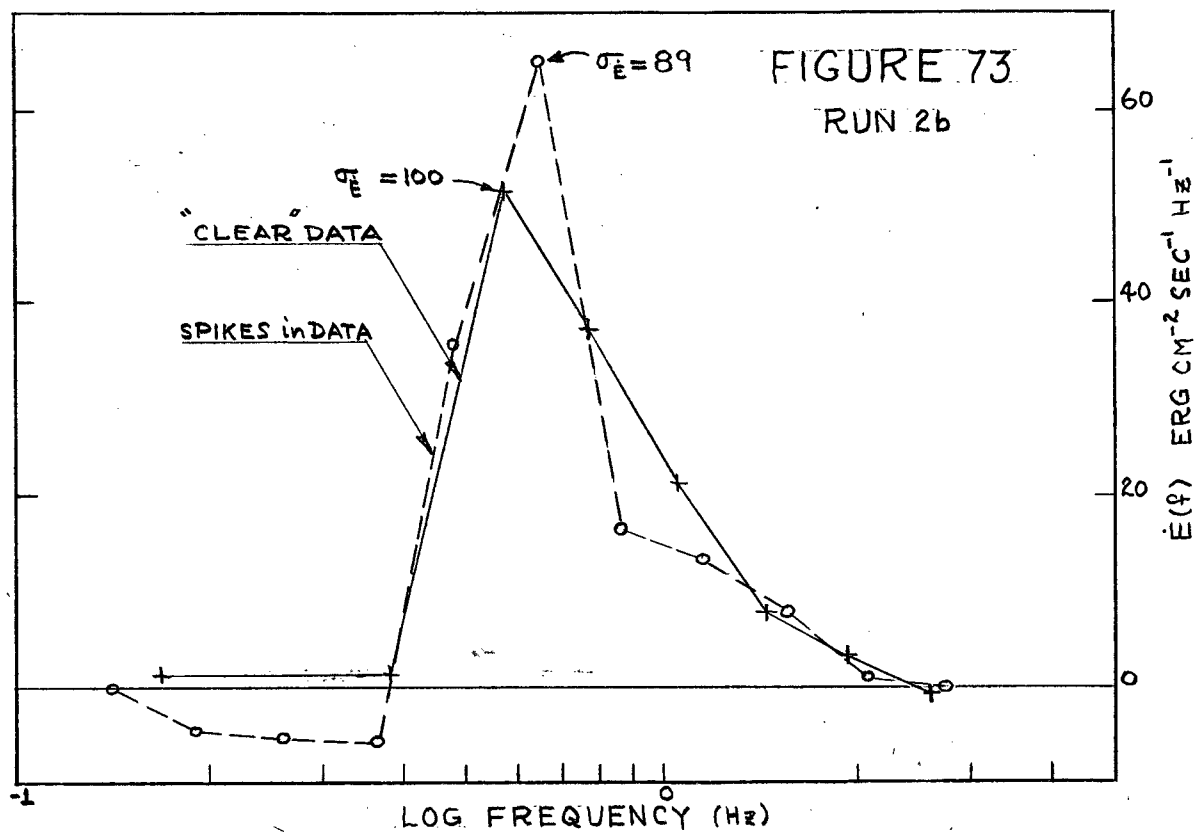


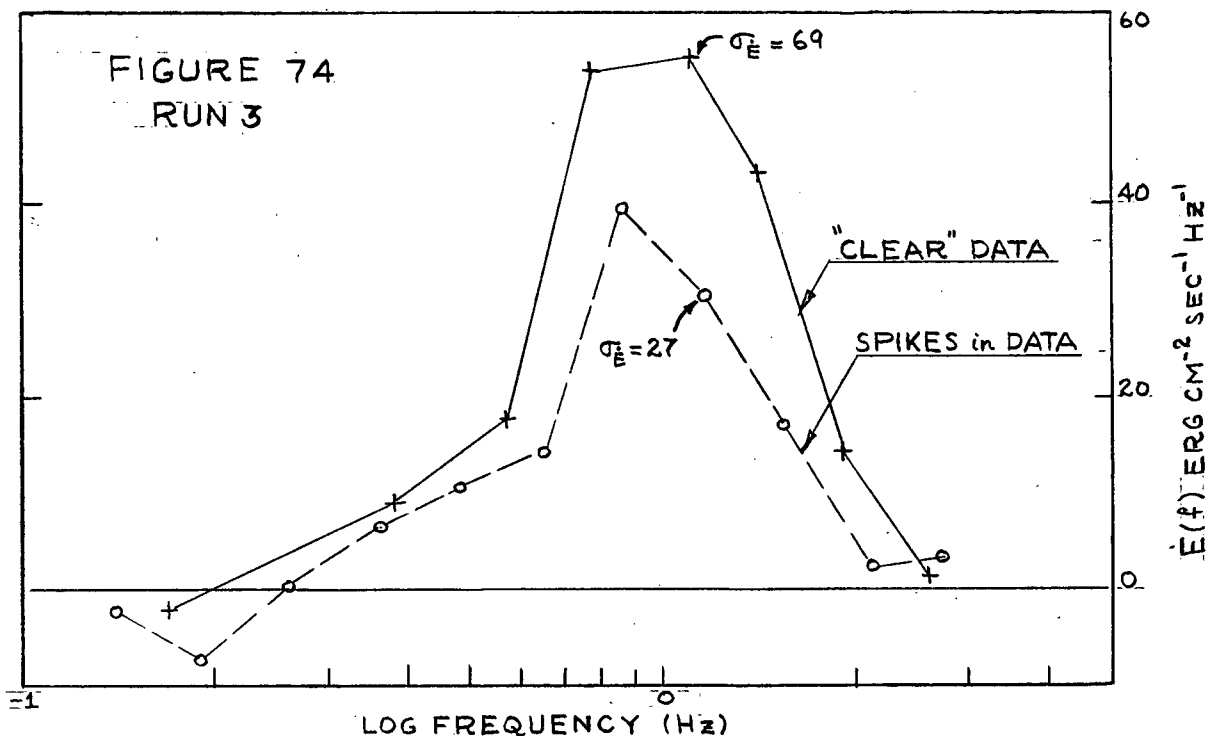
COMPARISON OF SPIKE-CONTAMINATED AND
"CLEAR" p, γ PHASE SPECTRA



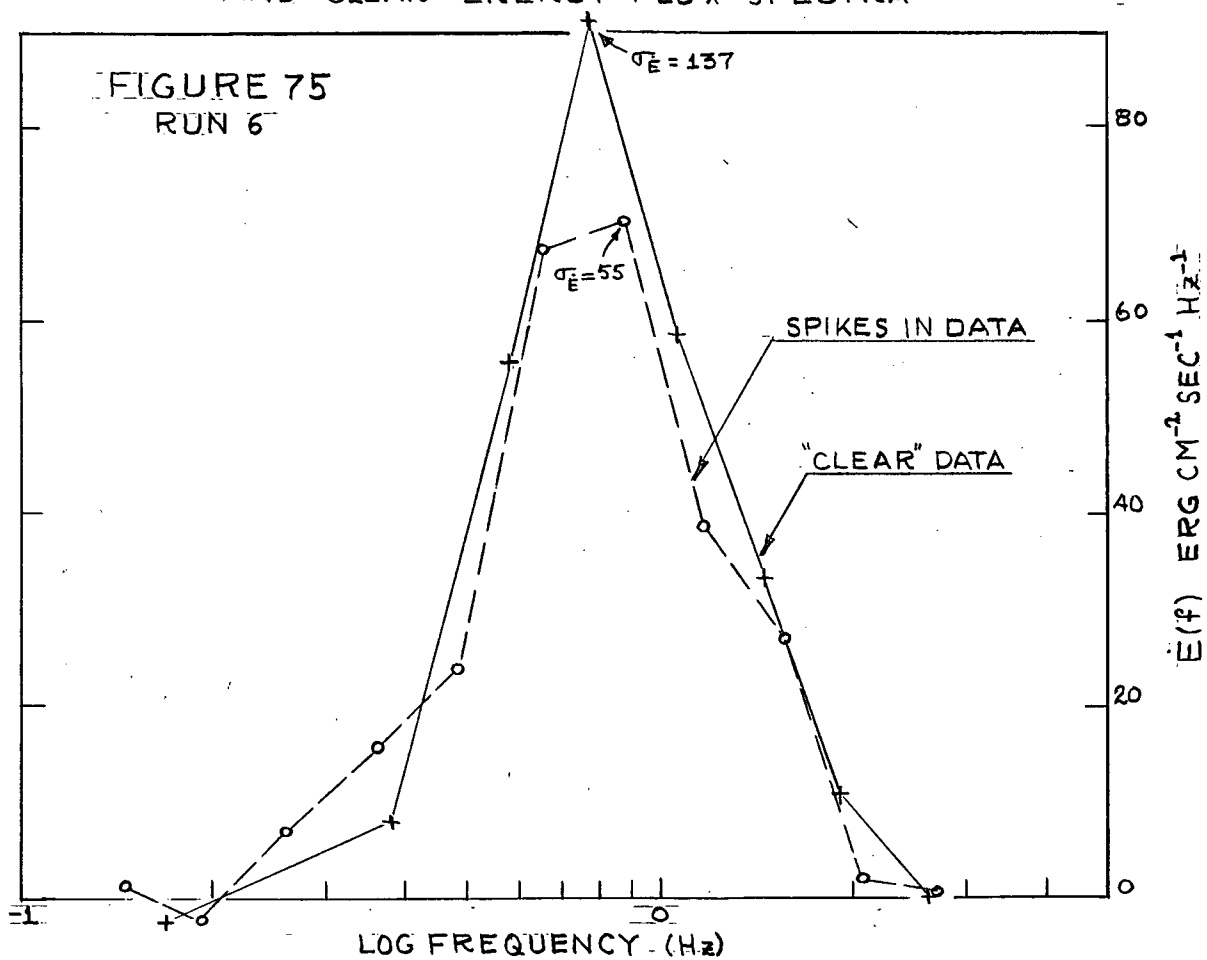


COMPARISON OF SPIKE-CONTAMINATED
AND "CLEAR" ENERGY FLUX SPECTRA





COMPARISON OF SPIKE-CONTAMINATED
AND "CLEAR" ENERGY FLUX SPECTRA



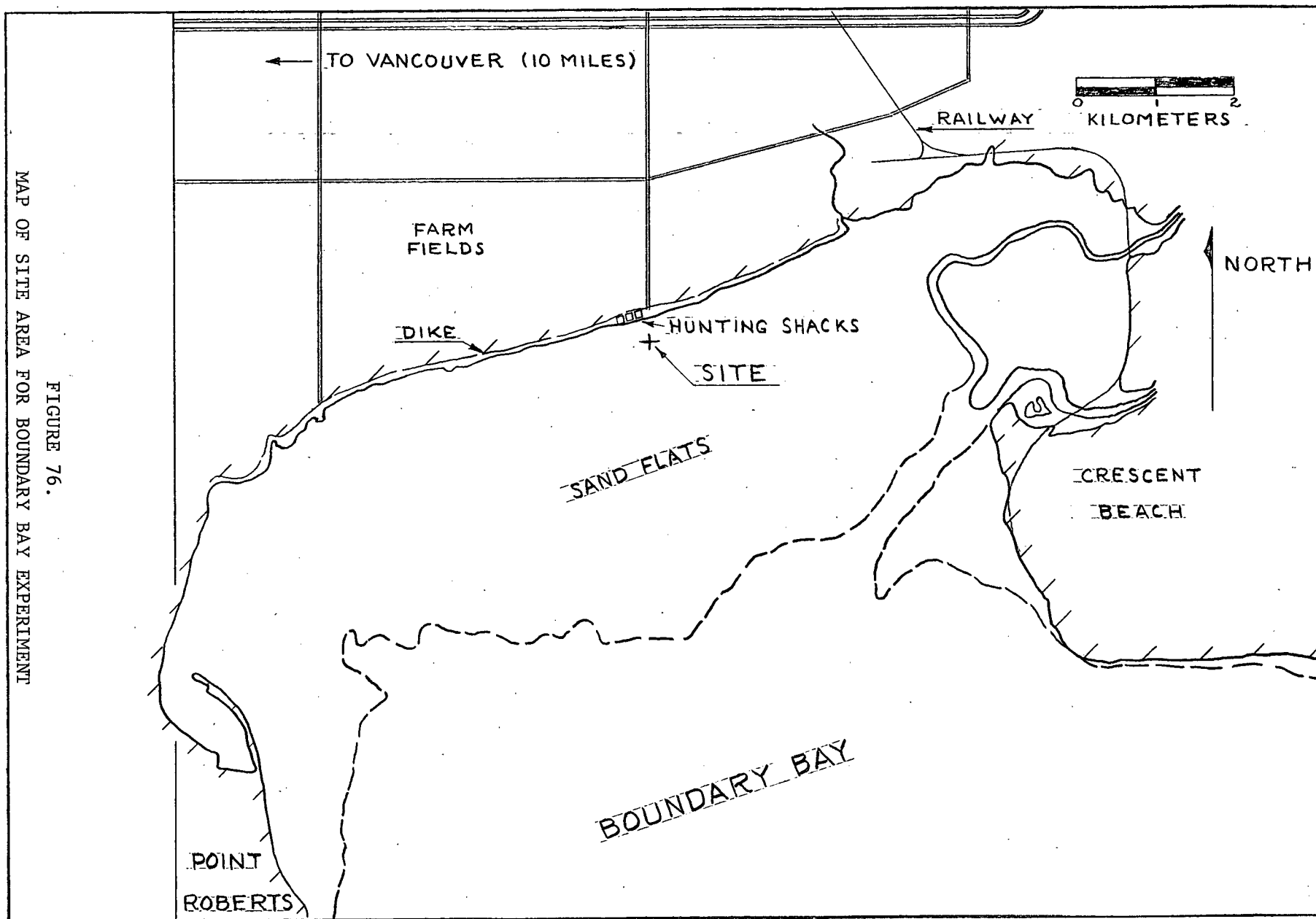


FIGURE 76.

MAP OF SITE AREA FOR BOUNDARY BAY EXPERIMENT

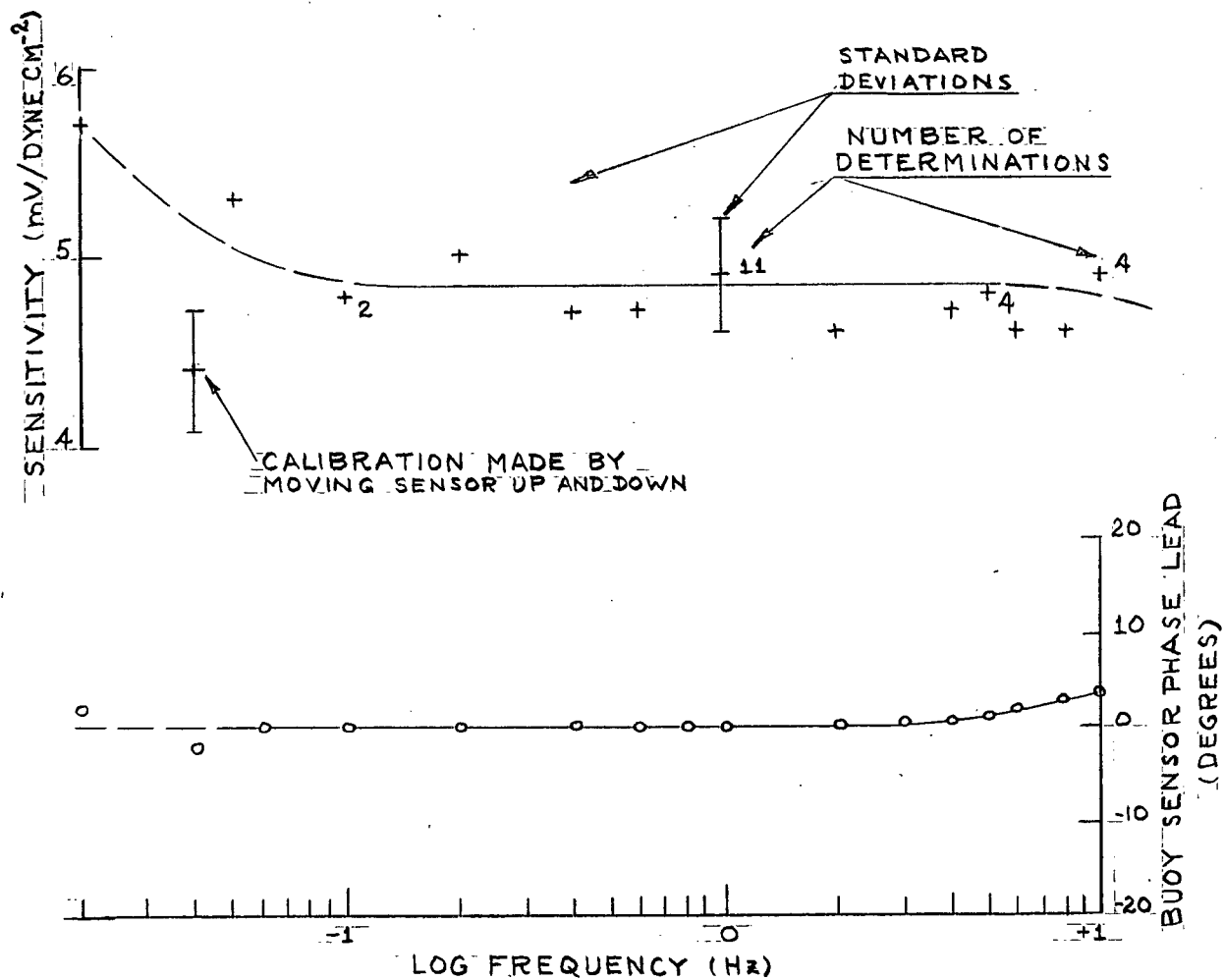


FIGURE 78.

BUOY SENSOR CALIBRATION FOR BOUNDARY BAY EXPERIMENT

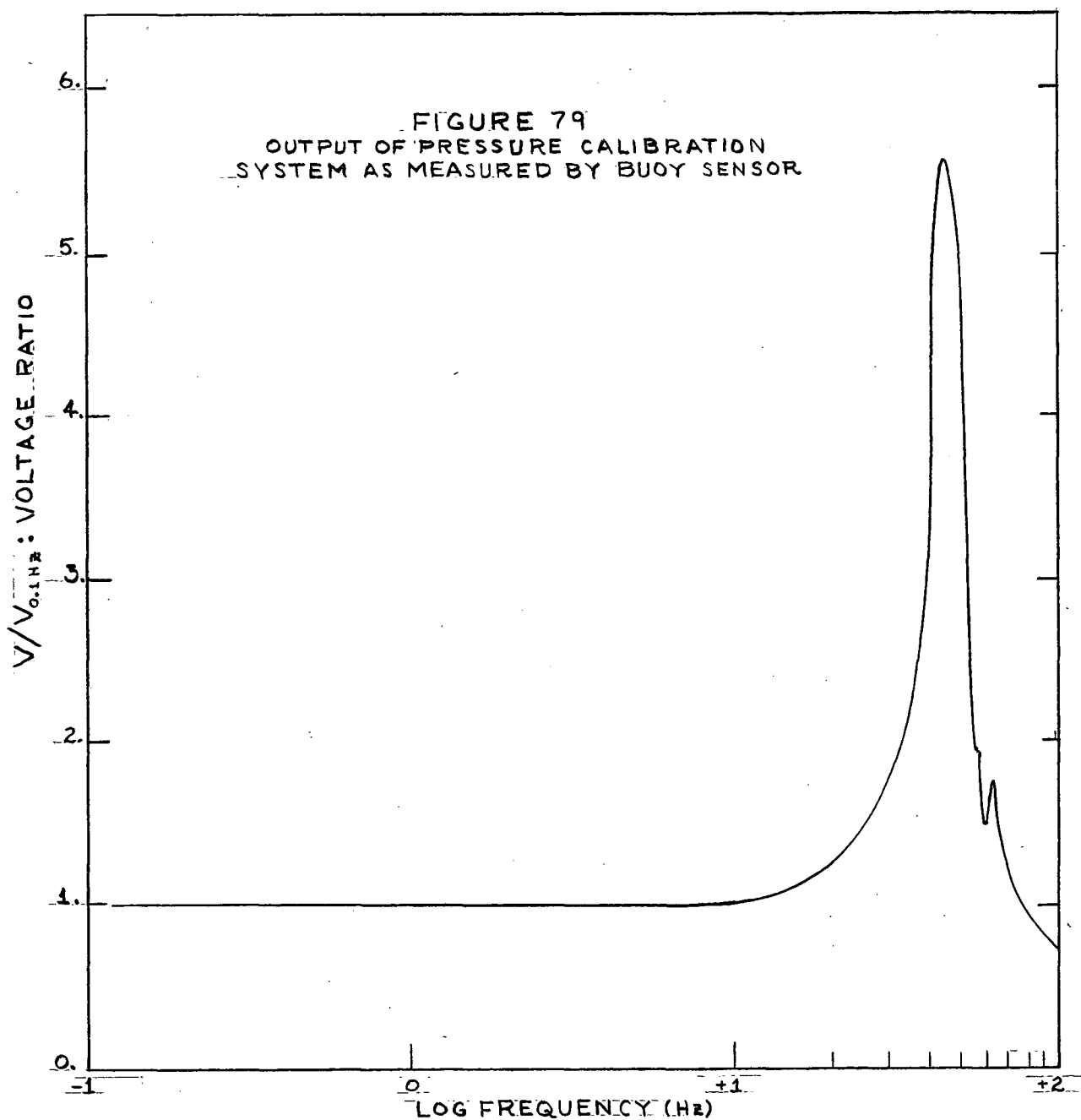


FIGURE 79.
FREQUENCY RESPONSE OF CALIBRATION DRUM

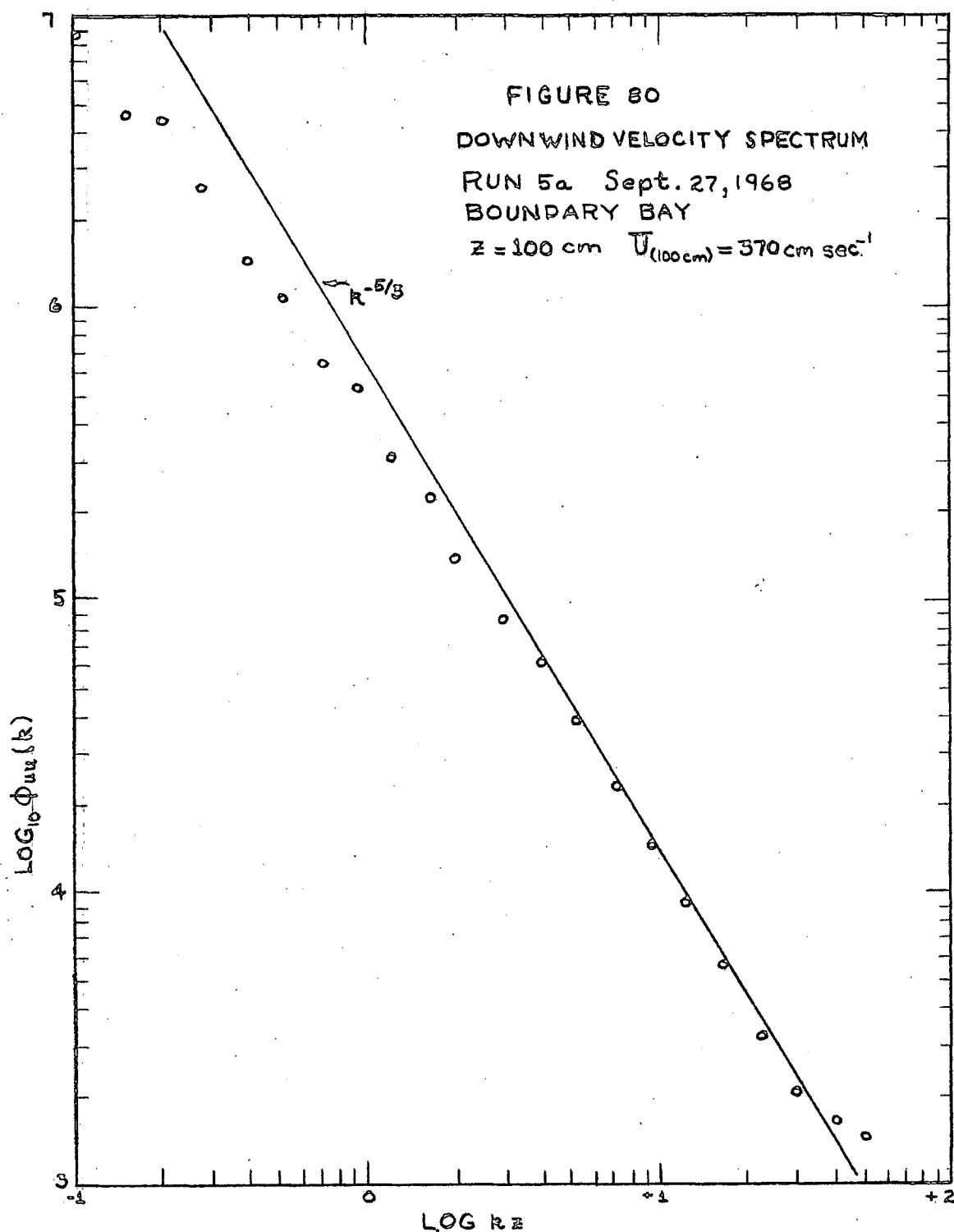
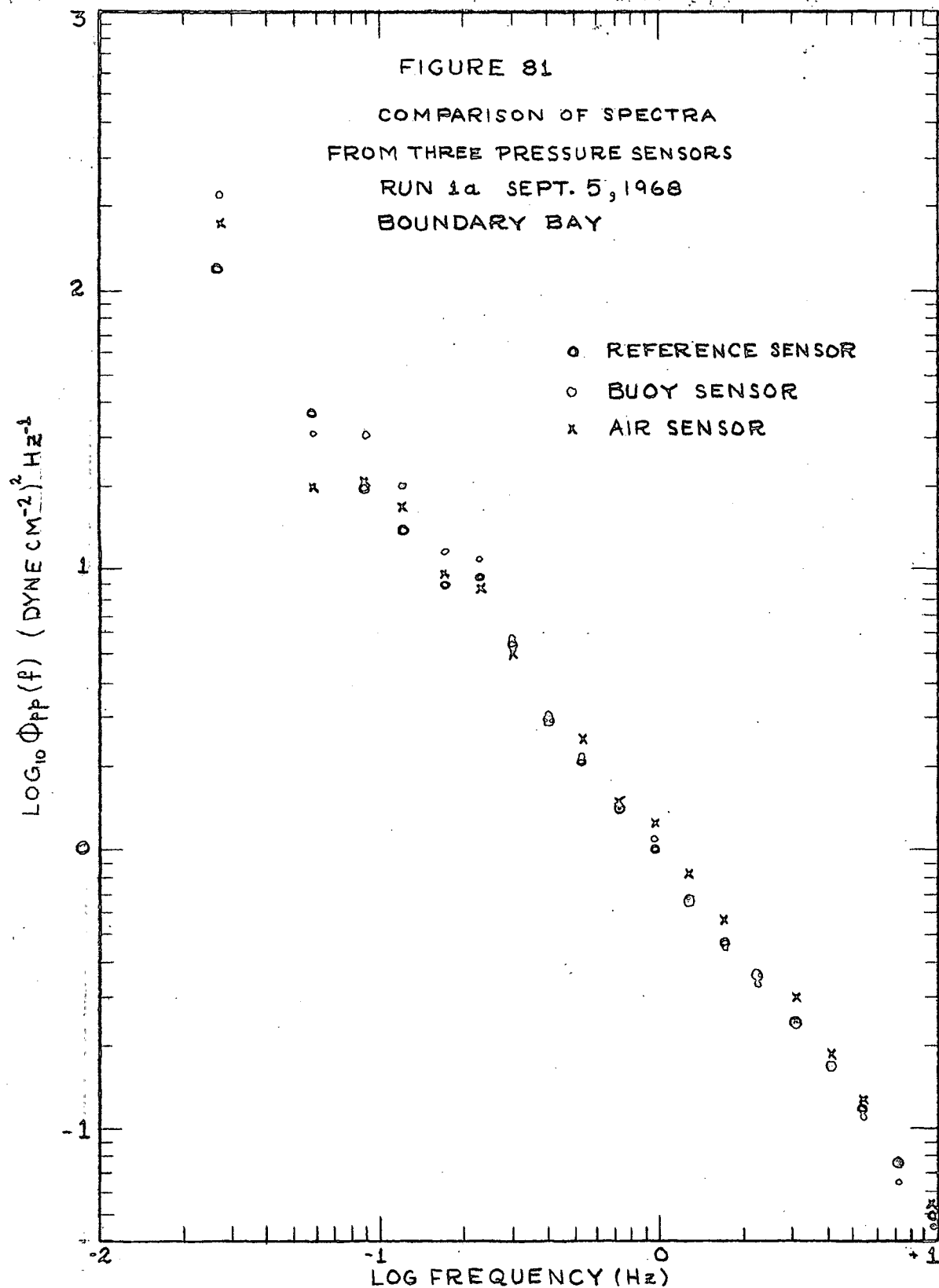
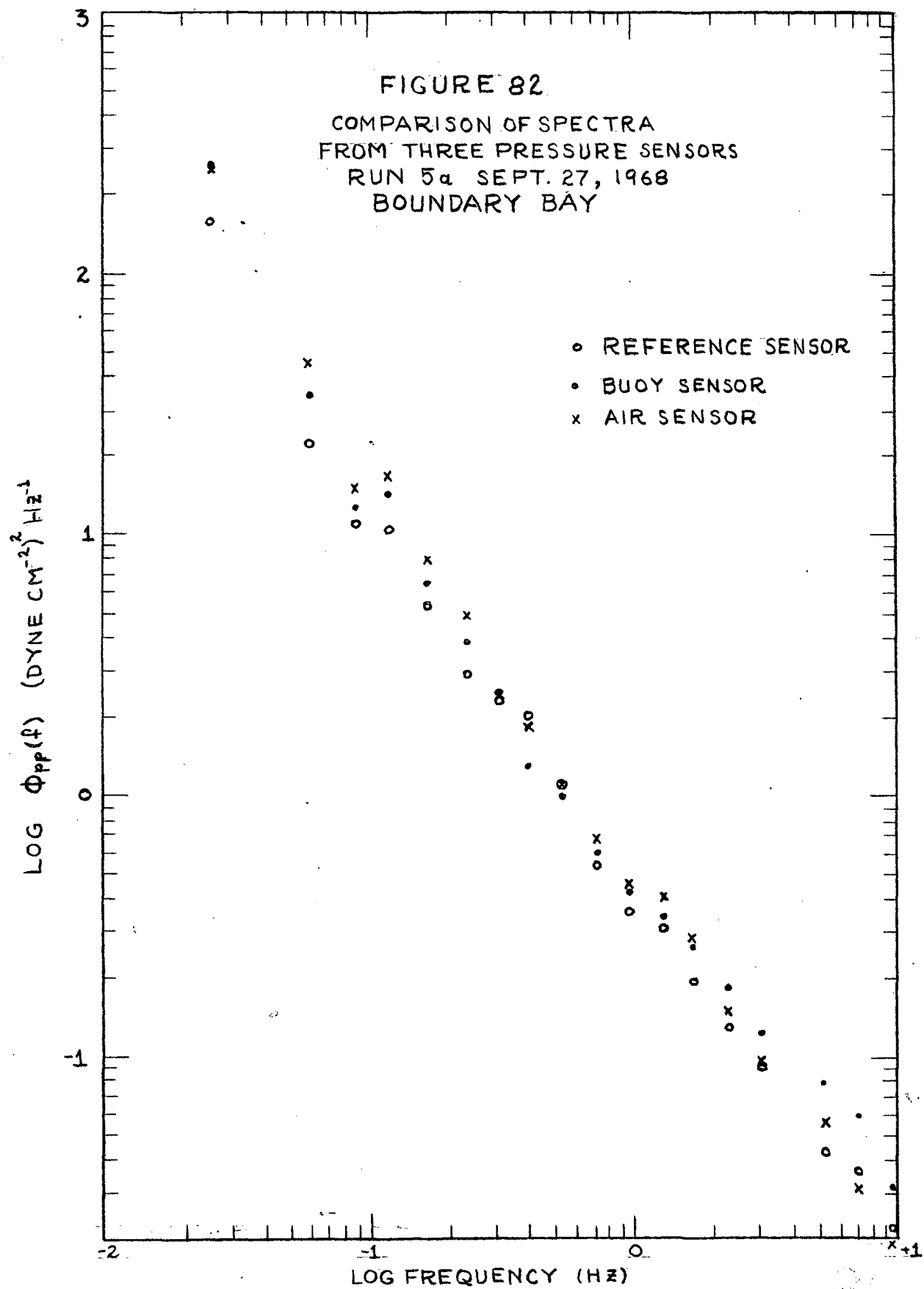


FIGURE 80.
TYPICAL POWER SPECTRUM OF DOWNWIND VELOCITY FLUCTUATIONS





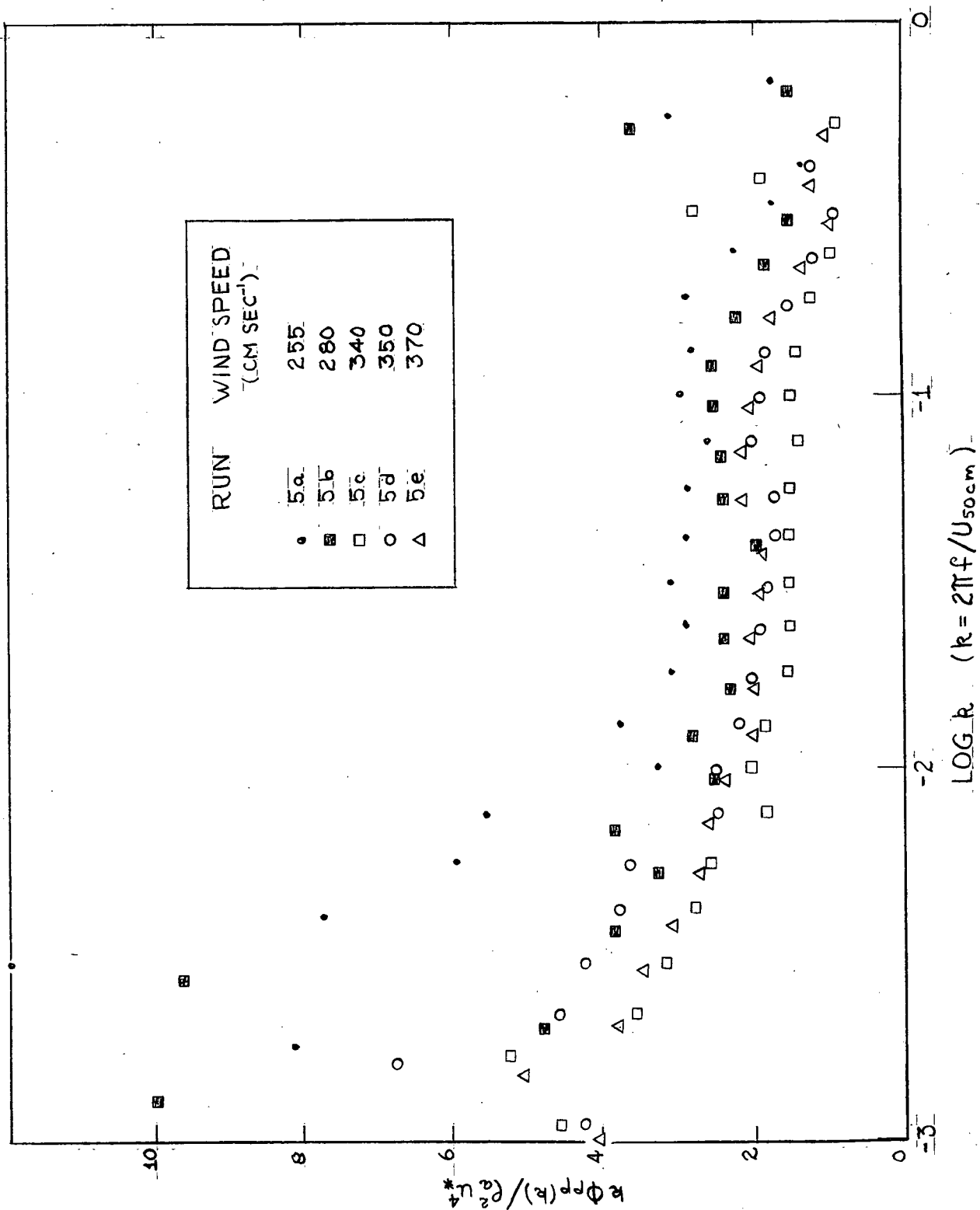


FIGURE 83.

NON-DIMENSIONAL PRESSURE SPECTRUM FROM BOUNDARY BAY

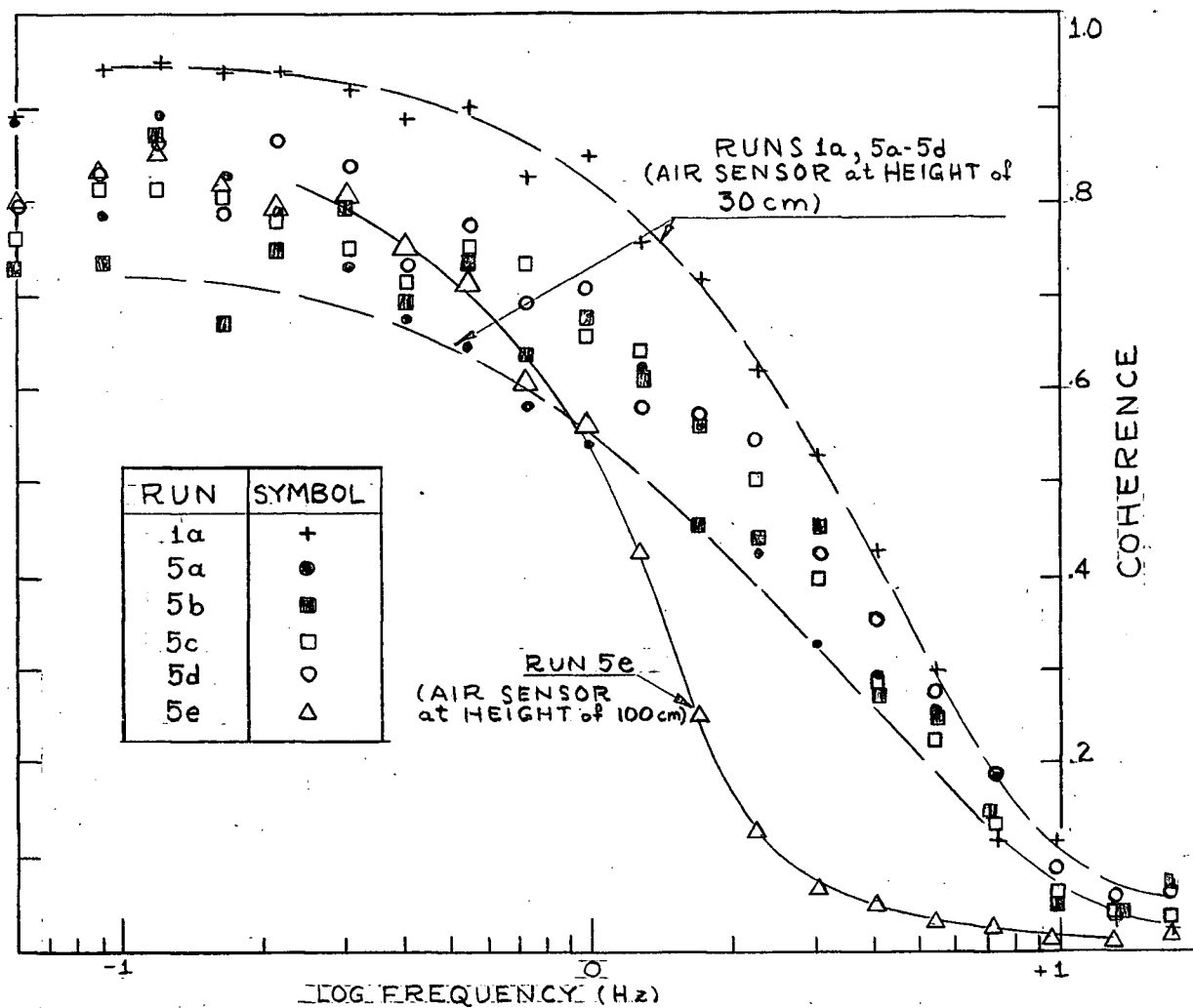


FIGURE 84. COHERENCE BETWEEN "BUOY" AND "AIR" PRESSURE SENSORS

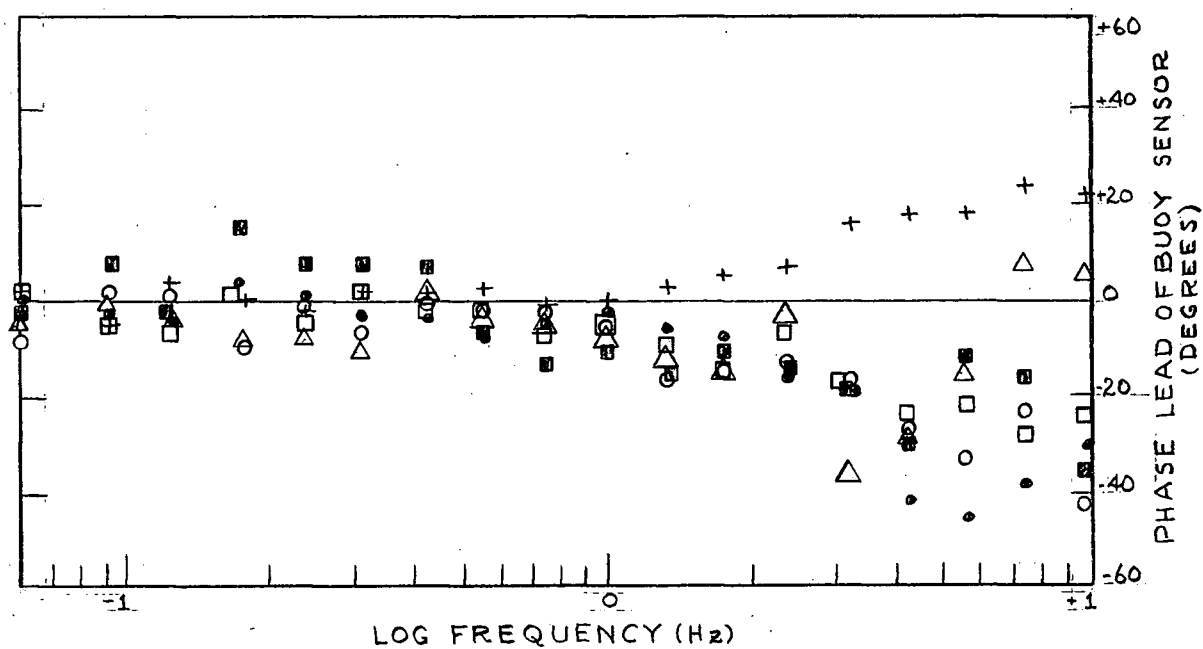


FIGURE 85. PHASE ANGLE BETWEEN "BUOY" AND "AIR" PRESSURE SENSORS

RUN	SYMBOL
1a	+
5a	•
5b	■
5c	□
5d	○
5e	△

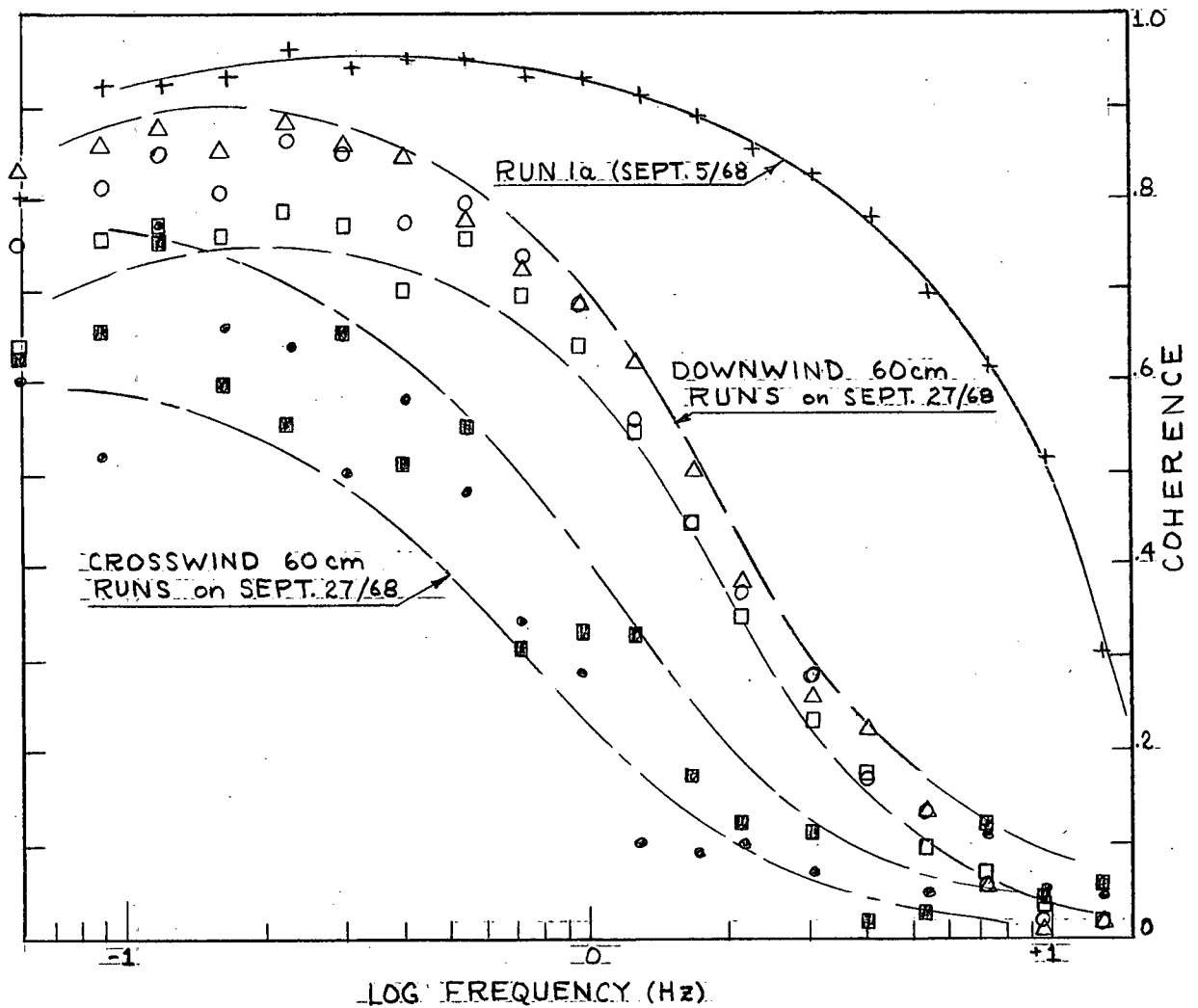


FIGURE 86.

COHERENCE BETWEEN "BUOY" AND "REFERENCE" PRESSURE SENSORS

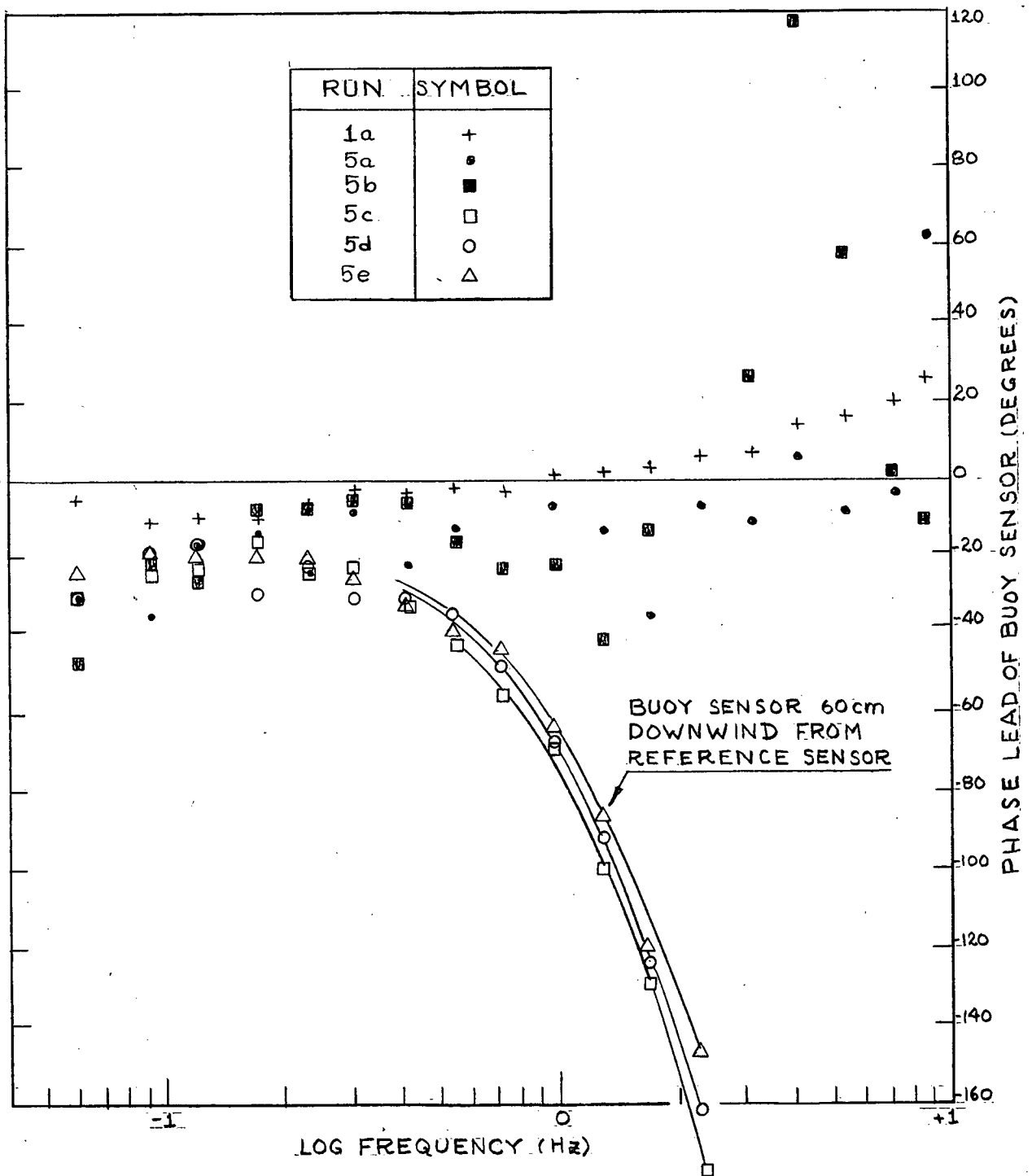


FIGURE 87.

PHASE ANGLE BETWEEN "BUOY" AND "REFERENCE" PRESSURE SENSORS

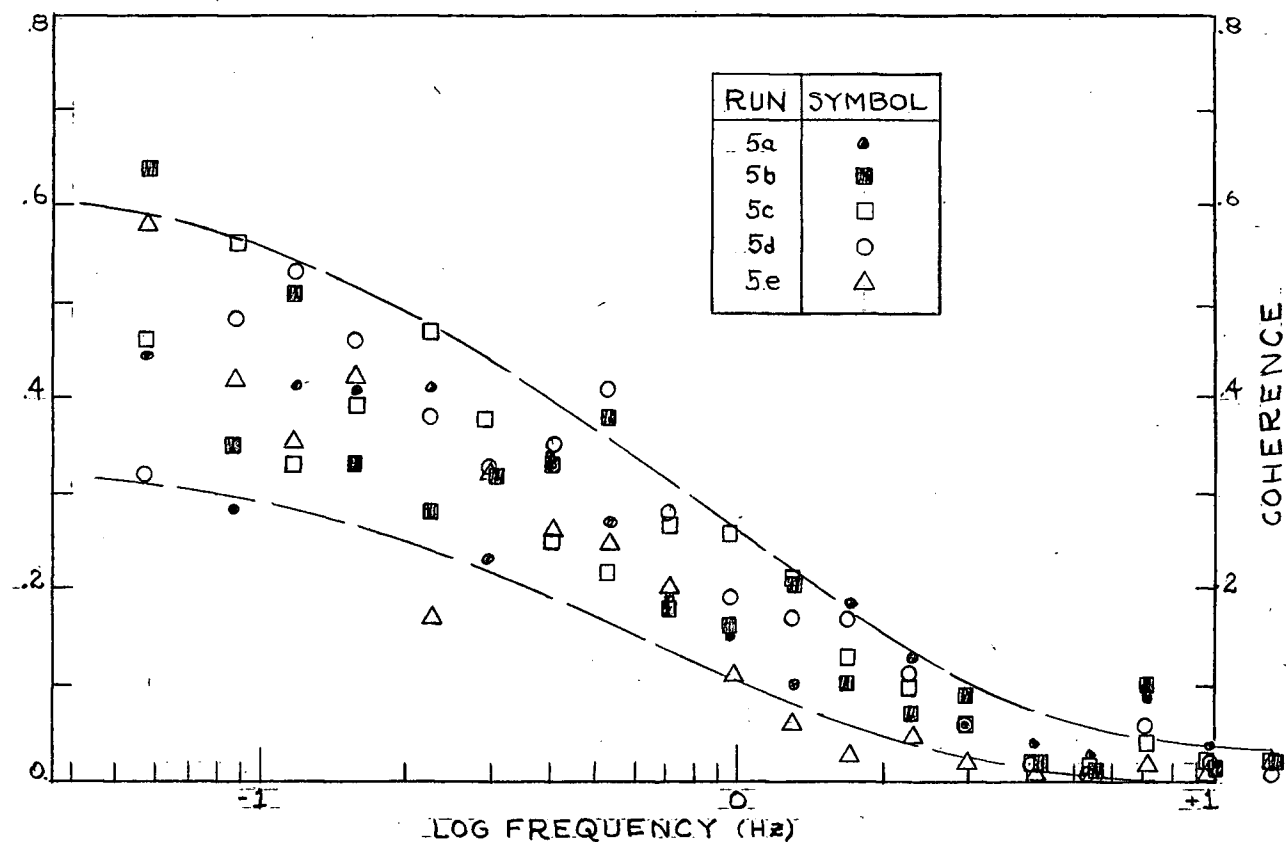


FIGURE 88. COHERENCE BETWEEN "BUOY" PRESSURE SENSOR AND HOT-WIRE AIR SPEED

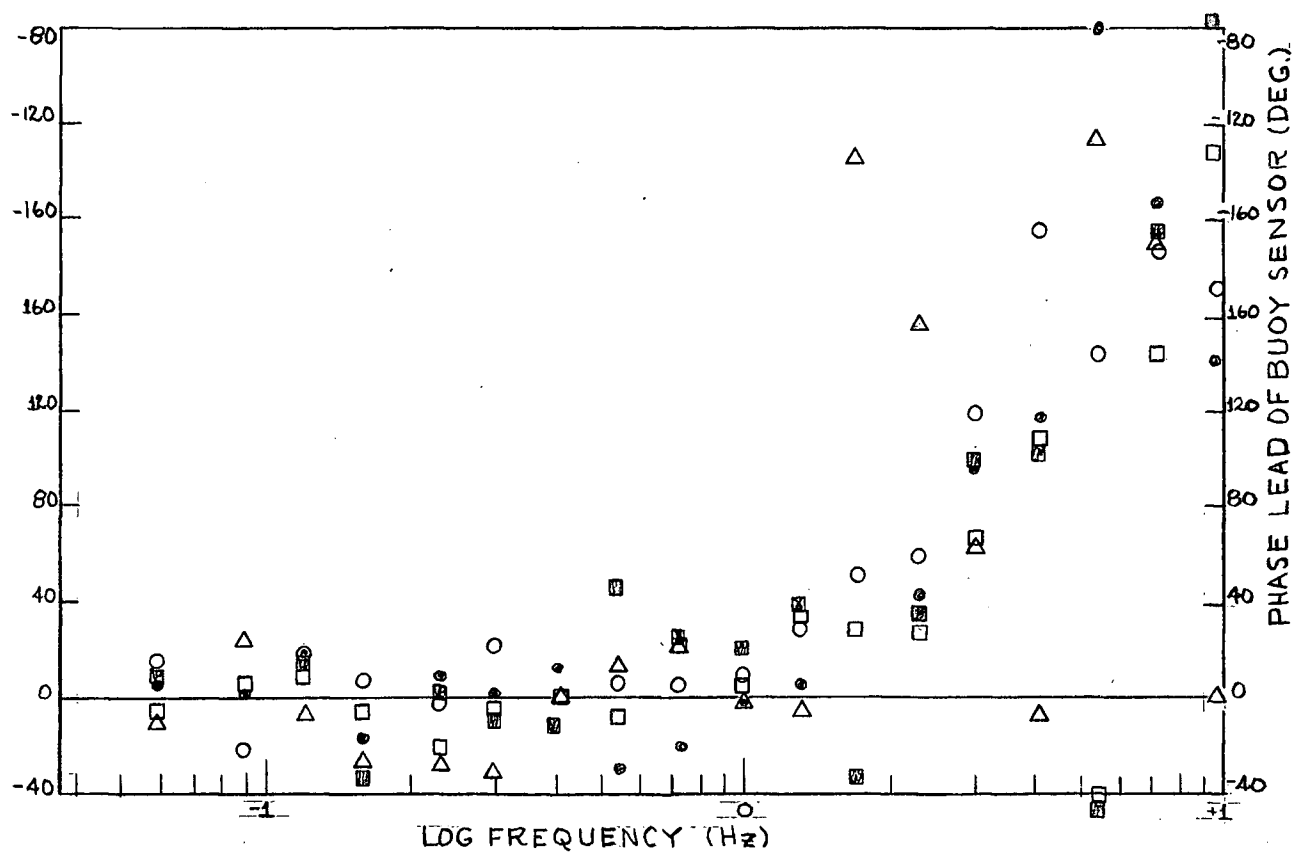


FIGURE 89.

PHASE ANGLE BETWEEN "BUOY" PRESSURE SENSOR AND HOT-WIRE AIR SPEED

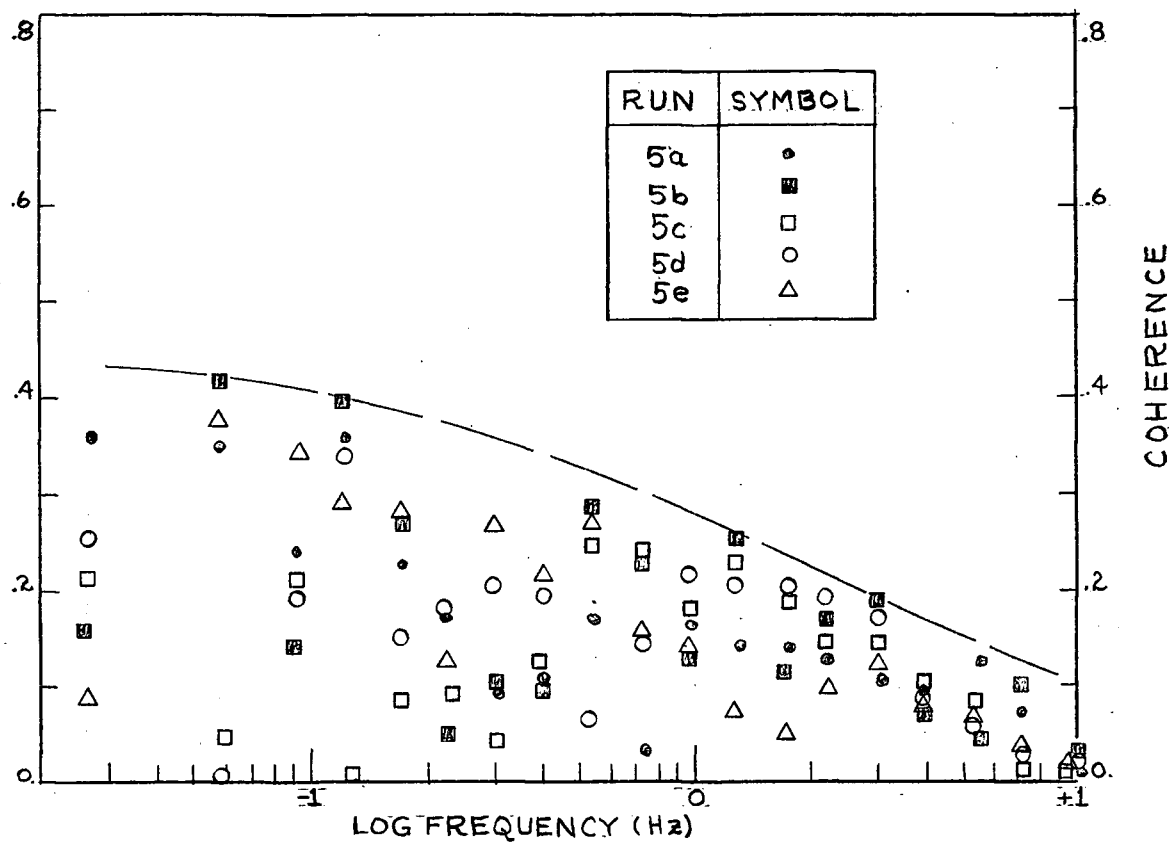


FIGURE 90.

COHERENCE BETWEEN "AIR" PRESSURE SENSOR AND HOT-WIRE AIR SPEED

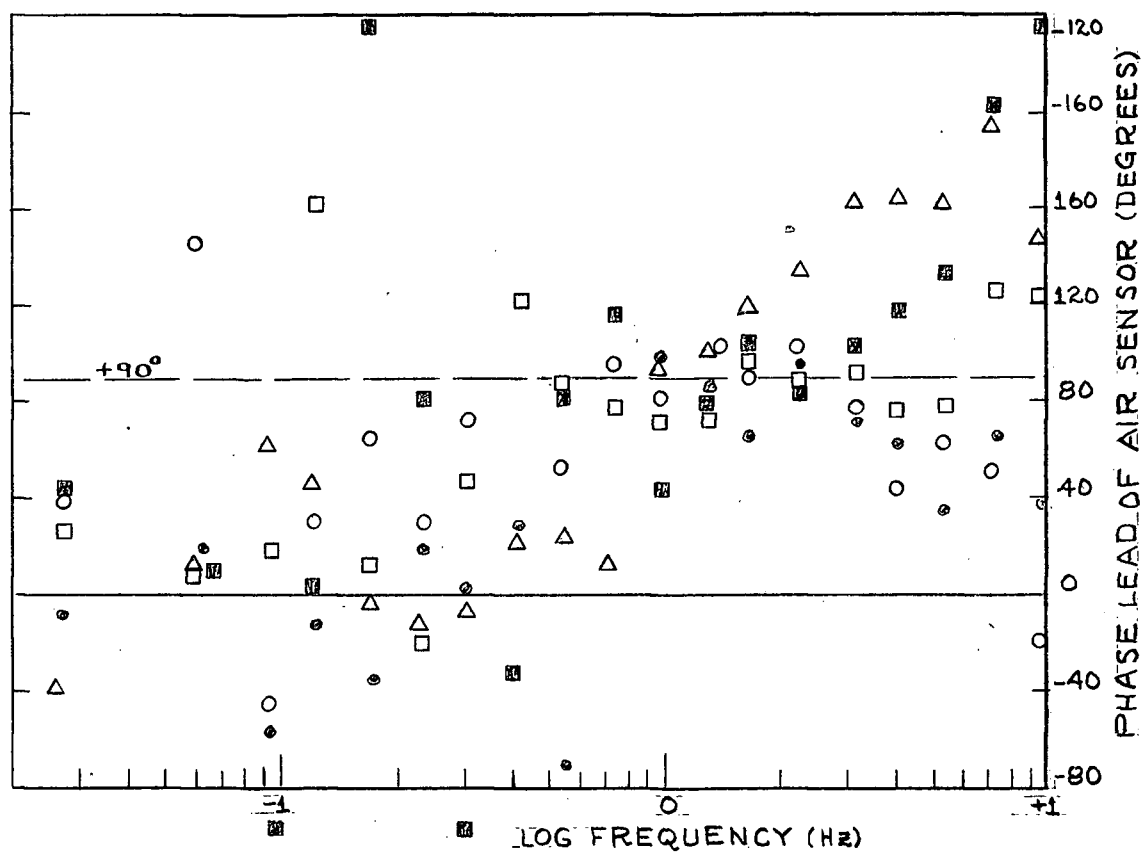


FIGURE 91.

PHASE ANGLE BETWEEN "AIR" PRESSURE SENSOR AND HOT-WIRE AIR SPEED

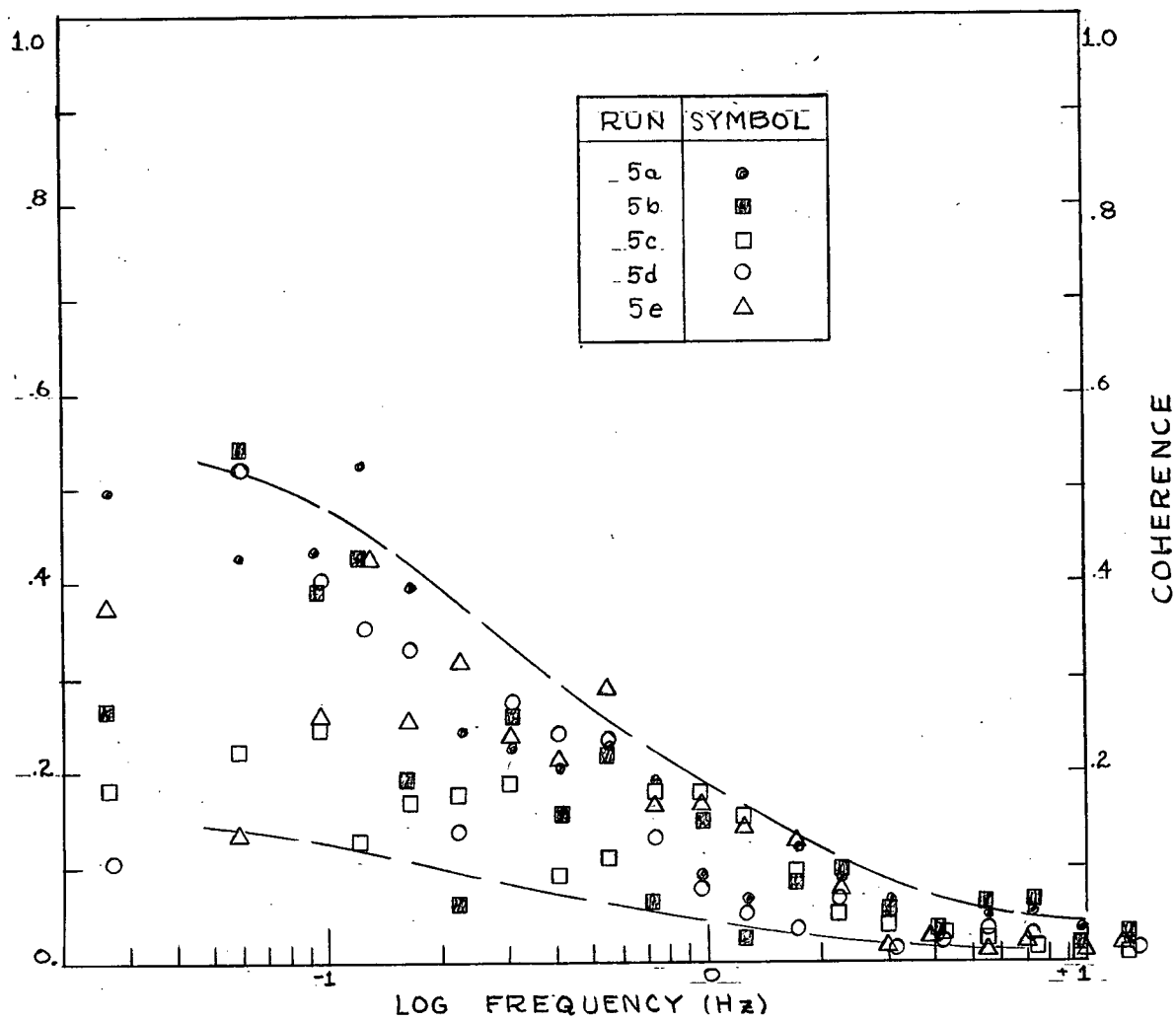


FIGURE 92.

COHERENCE BETWEEN "REFERENCE" PRESSURE SENSOR
AND HOT-WIRE AIR SPEED

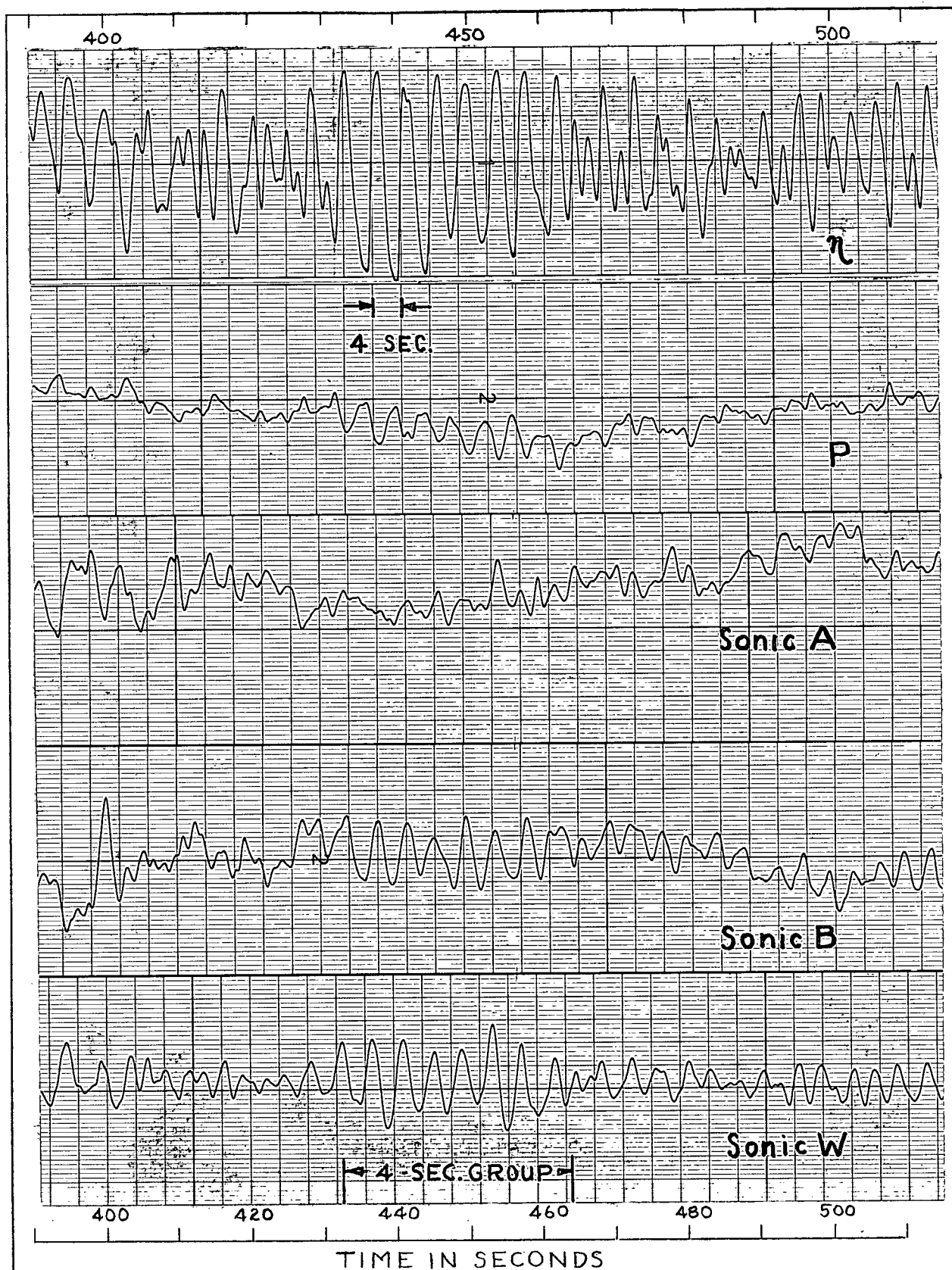


FIGURE 93.

CHART RECORDING OF WAVE, PRESSURE AND SONIC ANEMOMETER
SIGNALS DURING PASSAGE OF 4-SECOND SWELL GROUP

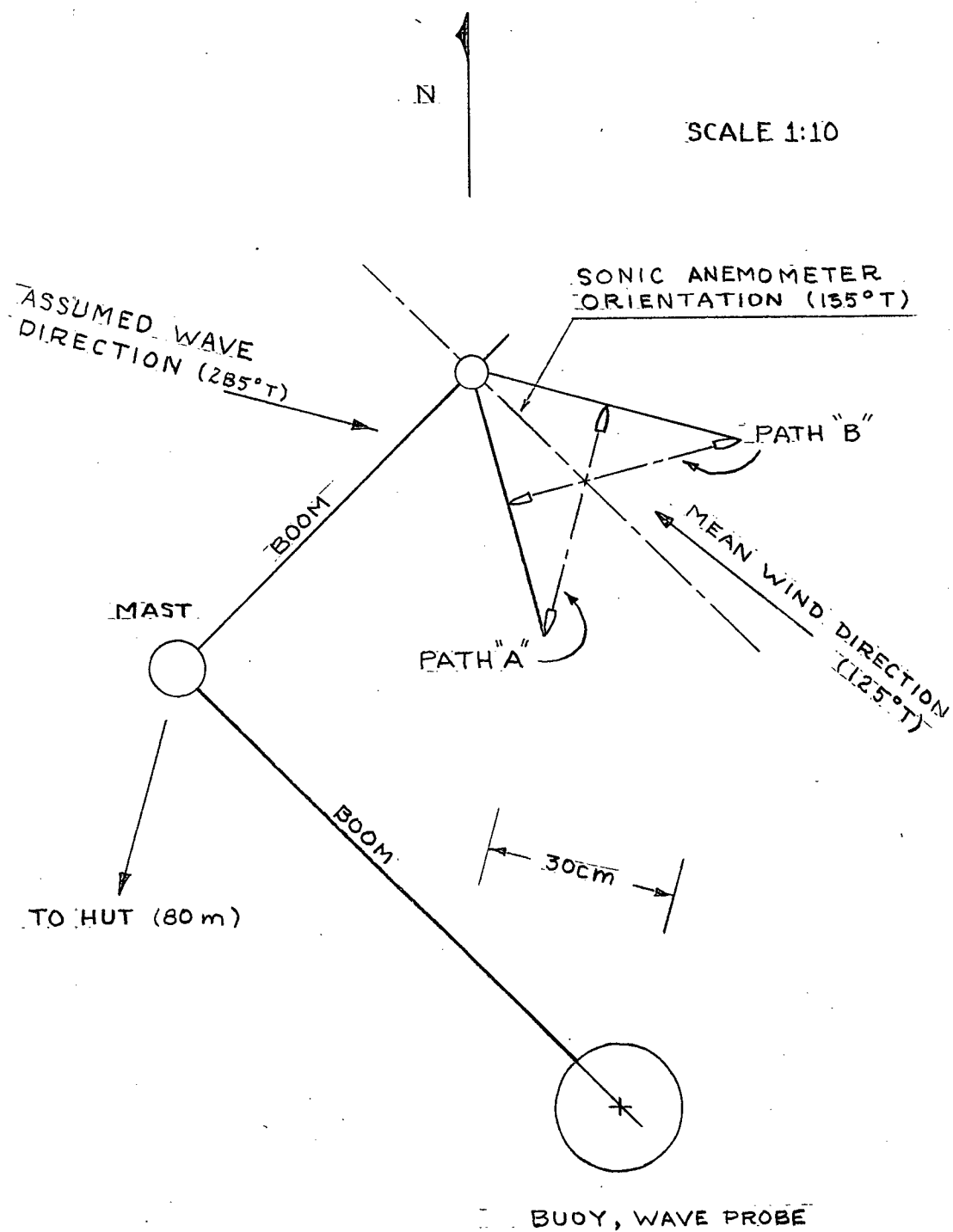


FIGURE 94.

SCALE DRAWING OF INSTRUMENT SETUP FOR RUN 5

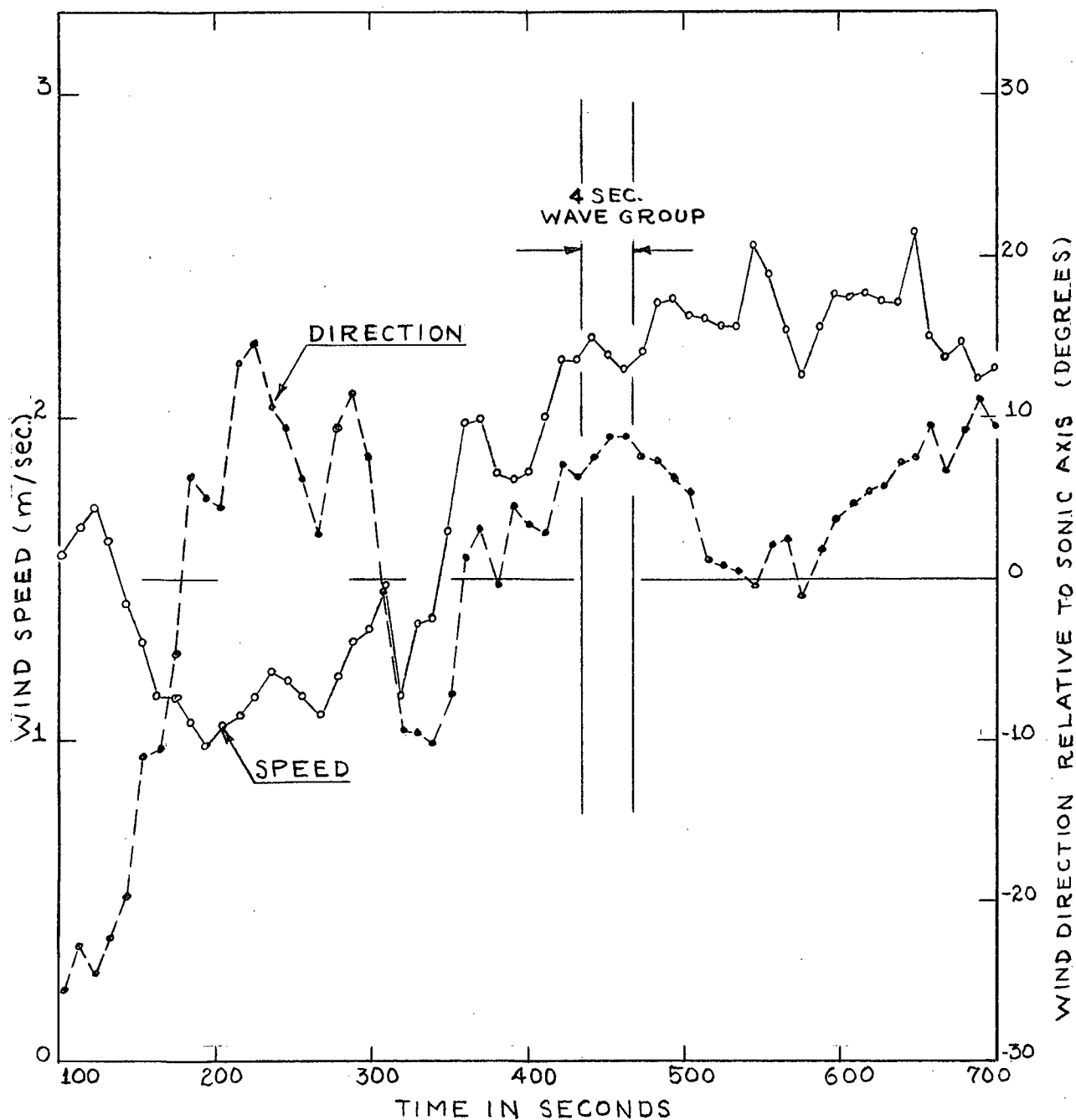


FIGURE 95.

TIME VARIATION OF U, θ FROM SONIC ANEMOMETER
(MEANS OVER TEN-SECOND INTERVALS) FOR RUN 5

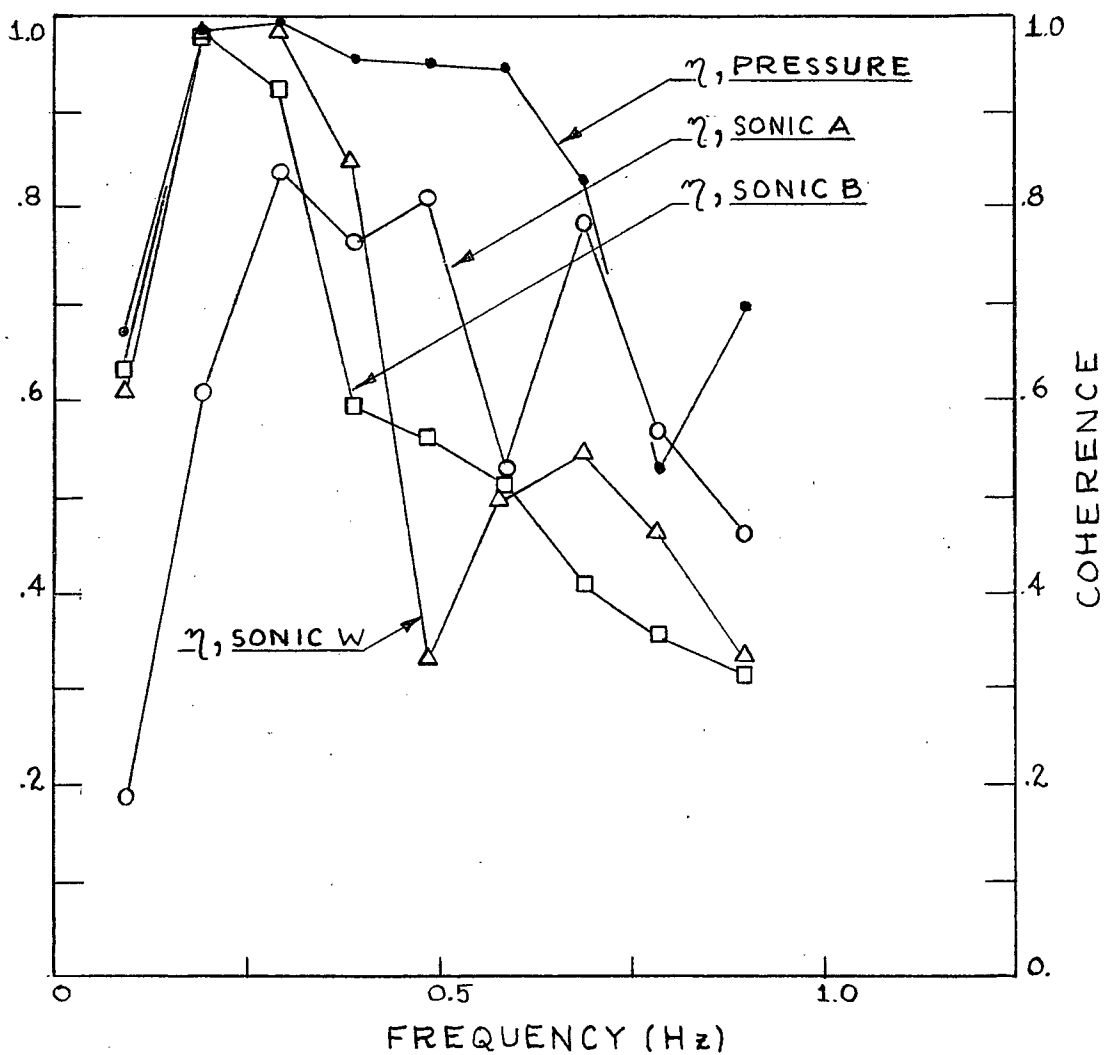


FIGURE 96.

COHERENCE SPECTRA DURING PASSAGE OF SWELL GROUP

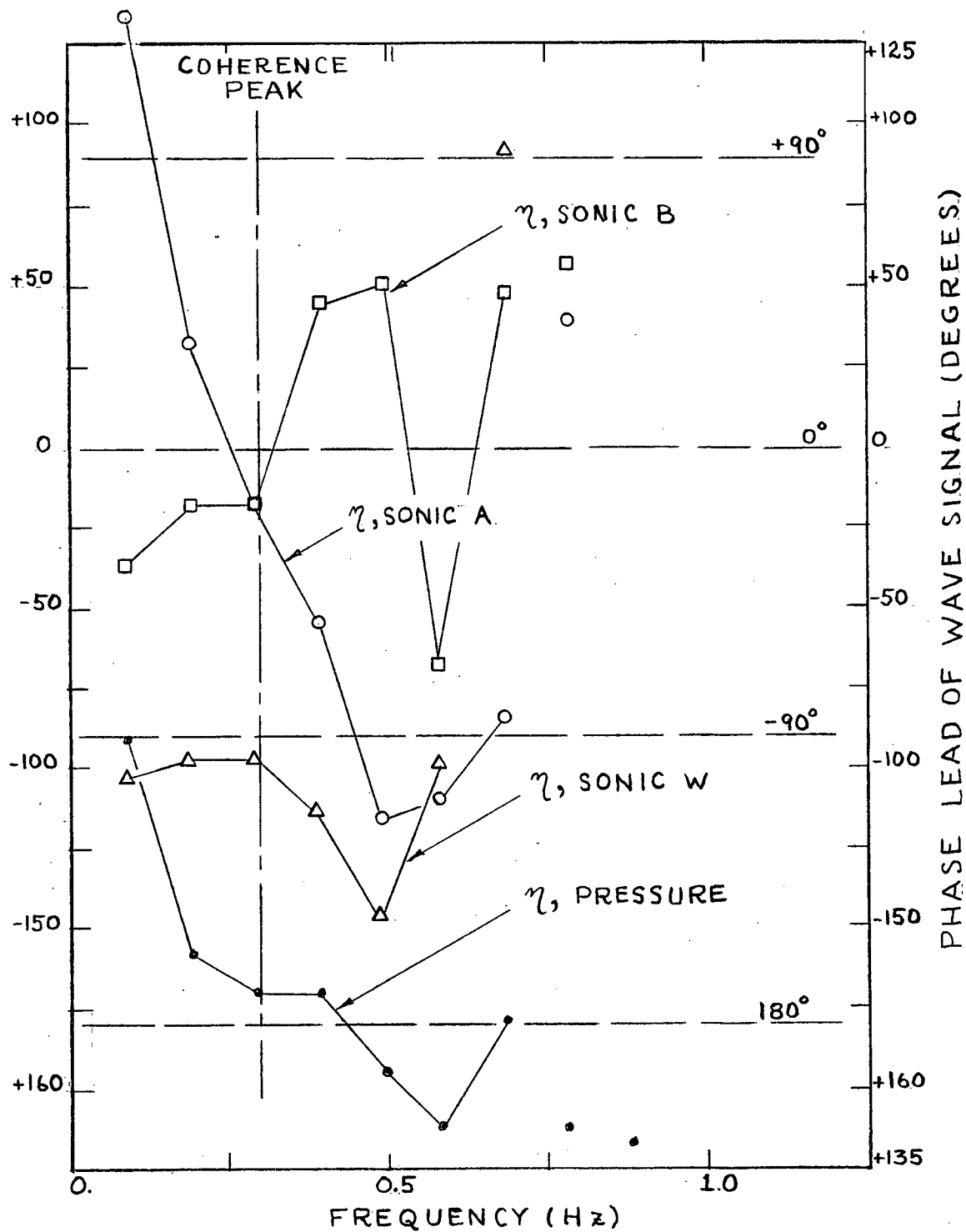


FIGURE 97.

PHASE SPECTRA DURING PASSAGE OF SWELL GROUP